Free boundary problems in the design of novel microfluidic devices



Simon N. Calver
Pembroke College
University of Oxford

A thesis submitted for the degree of
Doctor of Philosophy

March 2021

Abstract

This thesis will focus on understanding the flows within a novel microfluidic device, which is constructed by exploiting the interfacial properties of two immiscible liquids. While first-generation microfluidic technology is still far from fulfilling its potential in the life sciences because of substantial capital costs, high failure rates, and problems with biocompatibility, a new microfluidic technology developed by collaborators at the University of Oxford is able to sidestep these difficulties. This system prints liquid channels of cell culture medium on a surface that is overlaid by another biocompatible fluid. Flow through these devices is driven passively via surface tension, eliminating the need for additional equipment, although external pumps can also be used. The disparate length scales of the fluid geometry in these devices will be exploited to develop asymptotic models to inform their design for use in cell biology and many other prospective applications.

Contents

1 Introduction **1**

1.1 Microfluidic devices 1

1.1.1 PDMS-based devices 2

1.1.2 Open microfluidics 3

1.1.3 How Freestyle Fluidics works 3

1.2 Models relevant to Freestyle Fluidics 7

1.2.1 Current models of Freestyle Fluidics devices 7

1.2.2 Similar devices 9

1.2.3 Pendant drops 10

1.2.4 Rivulet flow 12

1.2.5 Fluid junctions 12

1.3 Thesis summary and overview 13

2 Fundamental principles for modelling Freestyle Fluidics **16**

2.1 Introduction 16

2.2 Freestyle Fluidics: governing equations 16

2.2.1 Geometric setup 16

2.2.2 Governing equations, boundary conditions and initial conditions 18

2.2.3 Physical and geometrical parameter values 21

2.2.4 Global mass conservation 21

3 Thin film modelling **25**

3.1 Introduction 25

3.2 Scales and non-dimensionalisation 26

3.2.1 Global mass conservation 32

3.3 Asymptotic analysis for a long, narrow conduit of constant width . . 33

3.3.1 Asymptotic structure and timescales 33

3.3.2 Quasi-steady solution in the drops 35

3.3.3 Quasi-steady solution in the conduit 38

3.3.4 Quasi-steady solution in the junction regions 39

3.3.5 Conduit relaxation 49

3.3.6 Droplet drainage 50

3.3.7 Numerical validation 53

3.3.8 Maintaining a pinned contact line 57

3.3.9 A survey of fluxes and shear stresses 59

3.4 Model extensions 64

3.4.1 Active pumping 64

3.4.2 Controlling the flow by altering the conduit width 66

3.5 Discussion 69

4 Thick drops and thin conduits **72**

4.1 Velocity and time scales 72

4.2 The dimensionless governing equations 75

4.3 Quasi-steady solution in the drops 77

4.3.1 Formulation 77

4.3.2 Small Bond number 79

4.3.3 Order unity Bond numbers 82

4.3.4 Non-uniqueness of solutions 85

4.3.5 Summary 87

4.4 Quasi-steady solution in the conduit 88
4.5 Quasi-steady problem in the junction region 90
4.6 Droplet drainage 95
4.7 Comparison with the thin-film asymptotics 97
4.8 Pinning and pinch off 99
4.9 Multiple steady states 102
4.10 Discussion 103

5 Generalisations: networks, corrections, thick conduits and comparisons to data 106

5.1 Networks 107
5.1.1 Network geometry 108
5.1.2 Node asymptotics in the thin-film limit 109
5.1.3 Kirchhoff-type laws for networks 113
5.1.4 Numerical validation of the thin-film networks 115
5.1.5 Network dynamics 118
5.1.6 The network GUI 119
5.1.7 Further applications 120
5.1.8 Discussion 122
5.2 Higher order solutions for the thin-film drop and conduit 123
5.2.1 Correction to the thin-film drop volume 123
5.2.2 Numerical validation of the volume correction 127
5.2.3 Higher order solutions for the thin-film conduit 129
5.2.4 Large Bond numbers in the thin-film analysis 132
5.2.5 Discussion 134
5.3 Analysis of a long, thick conduit 134
5.3.1 Geometry and governing equations 135
5.3.2 The leading-order problem 137

5.3.3 Zero Bond number: circular cross-sections 140
5.3.4 Leading-order flow problem 141
5.3.5 Incorporating gravity into the cross-section 146
5.3.6 Flow in the conduit 148
5.3.7 Discussion 151
5.4 Comparison to experimental data 152
5.5 An elastic interface 154
5.5.1 A preliminary model incorporating an elastic interface 155
5.5.2 Quasi-steady conduit solution 157
5.5.3 Elasticity in the junction region 159
5.5.4 Returning to the experimental data 161
5.5.5 Discussion 162
5.6 Summary 162

6 Concluding remarks and future work **164**
6.1 Conclusions 164
6.2 Future work 167

Bibliography **168**

List of Figures

1.1 The side view of the new device with a simple geometry consisting of two printed fluid drops and a fluid conduit connecting them. The height of the conduit is much less than the drops and is barely visible in the images. The left- and right-hand drops initially contained 10 µl and 20 µl of fluid; 10 µl of blue dye was then added to the left-hand drop. The fluid is pumped from the left-hand drop to the right-hand one due to their pressure difference. (a)–(c) The fluid in the left drop (containing blue dye) flows into the right, the images were taken at times 0 min, 33 min and 66 min after the blue dye was added. Reproduced with permission from Walsh *et al.* [127] under the creative commons licence, `http://creativecommons.org/licenses/by/4.0/`. 5

1.2 Images from experiments showing some possible networks of drops and conduits. (a) A stable concentration is maintained across two laminar streams. (b) The fluids in the outer drops are mixed in the central drop. (c) Serial dilutions are created in the four central drops. (d) Fluid is pumped directly into the conduits and collects in the drop. Reproduced with permission from Walsh *et al.* [127] under the creative commons licence, `http://creativecommons.org/licenses/by/4.0/`. 6

2.1 (a) The footprint of a dumbbell shaped circuit, Ω_1^*, in a Petri dish of base radius L_D, where Ω_2^* denotes the base of the Petri dish outside of the dumbbell footprint. (b) A close up of the footprint showing the different regions: the base radii of the two drops are denoted $\alpha_L L$ and $\alpha_R L$, the drops are connected by a conduit of width $2a^*(x^*)$, where the length L is the distance between the two junction regions. The side views (c) and (d) show a cross-section of the device on the line of symmetry, $y^* = 0$, with the origin at the start of the conduit (either where it exits the left drop (c) or where the fluid is pumped in (d)). The region occupied by the fluid in the circuit is denoted Γ_1^* and the region occupied by the overlaying fluid is denoted by Γ_2^*. The overlay/circuit interface is denoted S_1^* and the air/overlay interface is denoted S_2^*. The depth of the overlay is denoted H_O, the height scale of the drops is denoted H_D and the height scale of the conduit is denoted H_C. . . 17

3.1 (a) The dimensionless contact set with each of the regions labelled: Ω_L and Ω_R are the bases of the drops; Ω_C is the conduit contact set with a width of $2a(x)$ and straight edges at $x = 0, 1$; Ω_{JL} and Ω_{JR} are the junction regions where the drops intersect the conduit and $\partial\Omega$ is the pinned contact line. (b) The dimensionless fluid domains and interfaces: Γ_L and Γ_R are the fluid drops with footprints Ω_L and Ω_R respectively; Γ_C denotes the fluid contained in the conduit with footprint Ω_C; S_1 is the interface between $\Gamma_1 = \Gamma_L \cup \Gamma_C \cup \Gamma_R$ and Γ_2 with Γ_2 the region occupied by fluid above the interface, and S_2 the interface of the overlay with the air above. 28

3.2 The dimensionless contact set with each of the domains labelled: Ω_L and Ω_R are the bases of the drops; Ω_C is the rectangular conduit, with a length of 1 along its outer edge and a width of 2ϵ; Ω_{JL} and Ω_{JR} are the junction regions where the drops intersect the conduit and $\partial\Omega$ is the pinned contact line. 34

3.3 (a) Plots of the interface profile in the drop region for $\alpha_L^2 \mathrm{Bo} = -50$, -20, 0, 6, 14, with $\widehat{v}_L = \alpha_L^3$. The profiles corresponding to the positive and negative Bond numbers are given by (3.31a) (dashed lines) and (3.35a) (dotted lines) respectively. For Bo = 0 the profile is given by (3.38a) (solid line). (b) The contact angle given by (3.34a) and (3.37a) with the values corresponding to the profiles in (a) indicated. 38

3.4 (a) The leading-order problem in the junction region. (b) The second-order problem in the junction region, where $\widetilde{h}_\infty = \widetilde{\theta}_L \left(\widetilde{x}^2 - \widetilde{y}^2\right) / \left(2\,\alpha_L\right) - p_L \widetilde{x}^2/2$. The junction region is defined as $\Omega_J = \{(\widetilde{x}, \widetilde{y}) : \ \widetilde{x} < 0\} \cup \{(\widetilde{x}, \widetilde{y}) : \ |\widetilde{y}| < 1, \ \widetilde{x} \geq 0\}$. See text for details and the derivation of the boundary conditions. 41

3.5 The map given by (3.53) maps the upper half ζ-plane (a) to the junction region in the ω-plane (b). The solid line corresponds to the edge of the drop and the dashed line to the edge of the conduit. In the ζ-plane the line of symmetry is on $\xi = 0$ and in the ω-plane the line of symmetry is on $\widetilde{y} = 0$ with the conduit extending along the $\widetilde{x}$-axis. 44

3.6 Plots of the leading-order solution and the second-order correction in the junction region for Bo = 8 and $\alpha_L = 0.5$. The location of the substrate is indicated by the grid with the conduit extending in the positive $\widetilde{y}$-direction. (a) The leading-order solution given by (3.59). (b) The second-order solution given by (3.65) and (3.80). 46

3.7 Numerical solution of the conduit relaxation problem given by (3.89)–(3.91) for different boundary conditions (drop pressures), where the initial profile is linear. The dashed line is the steady-state solution given by (3.92). In (a) $\tau = 0, 0.0064, 0.0320$, whereas in (b) $\tau = 0, 0.0005, 0.0020$. 51

3.8 The evolution of the left-hand drop volume given by (3.100) for $\widehat{v}_L(T = 0)/\widehat{v}_T = \mathscr{V} = 0.4, 0.7, 0.9$ with $\widehat{v}_T$ the total volume, $\alpha = \beta_L/\beta_R = 0.25$ and noting (3.99) shows these solutions tend to 0.8 for large time. . . 52

3.9 (a) Examples of the geometry when the corner is rounded for $n = 0, 1, 2$, the changes are on the length scale of the conduit width. (b) The corresponding contact angle as a function of $\widetilde{x}$ for $n = 0, 1, 2$ at equilibrium. (c) The maximum relative difference in the drop volume as a function of n for $n = 0, 1/2, 1, 2, 4, 8$, where V_0 is the volume with $n = 0$. 54

3.10 Comparison of COMSOL solutions with model predictions for different values of the small parameter ϵ. In each case the calculations were performed using $\alpha_L = \alpha_R = 1$ and Bo $= 2$ with the initial volumes $\widehat{v}_L(0) = 0.2$ and $\widehat{v}_L(0) = 0.1$. (a)–(c) The solid lines show the numerical solution for $\epsilon = 0.01, 0.1, 0.2$ and the dashed line shows the asymptotic approximation. We compare (a) the drop volumes, given by (3.100); (b) the maximum shear stress on the substrate given by (3.102) with $y = 0$ and $x = 1$; and (c) the flux given by (3.93) and (3.103). (d) The root mean squared difference of the flux over a unit time interval for different values of ϵ, where $\mathcal{Q}_N$ is the numerical solution. 55

3.11 The composite solution for the interface. The dimensionless parameters used are Bo $= 20$, $\alpha_L = 0.5$, $\alpha_R = 0.4$, $\epsilon = 0.05$, $\widehat{v}_L = 0.03$ and $\widehat{v}_R = 0.03$. 57

3.12 Comparison of COMSOL solution with the composite solution described in §3.3.7 on $y = 0$. The calculations were performed using $\alpha_L = \alpha_R = 1$ and Bo $= 4$ with the initial volumes $\widehat{v}_L(0) = 0.1$ and $\widehat{v}_L(0) = 0.05$. The solid lines show the numerical solutions and the dashed lines the corresponding asymptotic approximation. We compare the solutions on the drainage timescale, *i.e.* $t \gg \epsilon^{-4}$. From top to bottom we have $t \approx 2.4 \times 10^8,\ 3.9 \times 10^9,\ 1.5 \times 10^{11}$. The solutions for the left- and right-hand drop regions are shown on the left- and right-hand sides respectively, the conduit region is shown in the middle panels; note that the height scales with ϵ^2 in the conduit. . . 58

3.13 (a) As a function of drop radius, α_L, we plot β_L, the ratio of the dimensionless drop pressure to volume for the left-hand drop given by (3.33), (3.34) and (3.36) for Bo $= -20, -8, 0, 2, 4, 10, 20$. The dashed line shows the boundary on which Bo $=$ Bo$_C$ (defined in §3.3.2 as the Bond number below which either the drop height or pressure are no longer positive). (b) The time taken for an initial flux $\mathcal{Q}_I$ to reduce by 50% as a function of $\alpha = \beta_R/\beta_L$. The initial fluxes are $\mathcal{Q}_I = 0.01, 1, 4, 10$. The dashed line shows the minimum value of α for which there is a solution with a particular initial flux. 61

3.14 In this figure and the following one we show the effect of changing a single model parameter on the flux and maximum shear stress in the conduit as functions of time. The geometries are shown on the left-hand side, in each case we modify the geometry with parameters $R_R = R_L = 3.2\,\text{mm}$, $a^* = 0.8\,\text{mm}$, $v_L = 8\,\mu\text{l}$ and $v_R = 7\,\mu\text{l}$ (shaded red). The dumbbells are labelled 1–4 with the corresponding fluxes and maximum shear stresses shown on the right-hand side. The parameters we modify are (a) the base radius of the left-hand drop $R_L = 3, 3.1, 3.2, 3.3\,\text{mm}$; (b) the base radius of the right-hand drop $R_R = 3.2, 3.1, 3, 2.9\,\text{mm}$; and (c) the width of the conduit $a = 0.9, 0.8, 0.7, 0.6\,\text{mm}$. 62

3.15 See caption to Figure 3.14. In this figure the parameters we modify are (a) the volume of the left-hand drop $v_L = 8, 9, 10, 11\,\mu\text{l}$; (b) the volume of the right-hand drop $v_R = 10, 9, 7, 6\,\mu\text{l}$; and (c) the length of the conduit $L = 10, 15, 20, 25\,\text{mm}$. 63

3.16 (a) The shear stress along the centre of the conduit found from the numerical solution of (3.18) and (3.20)–(3.22) with the conduit width given by (3.123) for $\mathcal{S} = 2.5$ and $\mathcal{Q} = 8.5714$ (chosen so that the conduit width doubles) with $\epsilon = 0.2, 0.05, 0.01$, the dashed line shows the value of $\mathcal{S}$. (b) Comparison of the two asymptotic solutions for shear stress, s, given by (3.120), (3.122) and (3.123) in a conduit of constant width, and a conduit with its width given by (3.123) for $\mathcal{S} = 2.5$ and $\mathcal{Q} = 8.5714$, note the logarithmic scaling for the straight conduit shear stress. 69

4.1 The new coordinate system: s is the arc length from the apex at $(0, H_A)$ and Ψ is the angle the curve makes with the horizontal. On the contact line $R = \alpha_L$ and the angle with the horizontal is the contact angle θ_L. 78

4.2 (a) Comparison of the thin-film drop profile (3.31) with the numerical solution of (4.44) and (4.52) for $V_L/\alpha_L^3 = 0.2, 0.4, 0.8$. (b)–(d) Comparison of the small Bond number asymptotics from §4.3.2 to the numerical solution of (4.44) and (4.52) for $\alpha_L^2 \mathrm{Bo} = -0.4, -0.2, 0.2, 0.4$. The dashed line in the middle is the exact solution for $\mathrm{Bo} = 0$. In each case the dashed lines are the asymptotic solution and solid lines the numerical. (b) The asymptotic drop profiles are given by (4.27), (4.28), (4.37) and (4.38). (c) The asymptotic solution pressure as a function of volume given by (4.31), (4.41) and (4.42). (d) The asymptotic solution for the contact angle as a function of drop volume given by (4.31), (4.40) and (4.43). 84

4.3 Numerical solution of (4.14) and (4.15) fixing either the pressure or the volume and finding the other as part of the solution for $\mathrm{Bo} = 1.2$ and $\alpha_L = 1$. A variety of profiles are shown each with the same volume ($V_L = 3$) but a different pressure. Beyond $V_{\max} \approx 4.5$ solutions do not appear to exist and between $V_{\mathrm{crit}} \approx 2.2$ and $V_{\max}$ multiple solutions exist. 86

4.4 The regime diagram showing when there are multiple solutions for a given drop volume and Bond number. The lower line forming the boundary between single and multiple solutions is given by V_{crit} and the upper line is given by $V_{\max}$. 87

4.5 The maximum contact angle in a drop as a function of the Bond number. 92

4.6 (a) The leading-order problem in the junction region. (b) The second-order problem in the junction region, where $\widetilde{h}_\infty$ is the $\mathrm{O}(\epsilon)$ term in (4.77). 94

4.7 The drop pressure as a function of drop volume for the droplet drainage model with $\alpha_L = 1$ and $\mathrm{Bo} = 0, 0.8, 1.4, 2, 3, 4$. 97

4.8 Comparison of numerical solutions of (4.86) and (4.87) with the thin-film asymptotics. (a) The volume in the left drop given by (4.86) and (4.87) (solid lines) and the asymptotic solution given by (3.101) (dashed line), with $\mathrm{Bo} = 2$, $\alpha_L = \alpha_R = 1$ and an initial volume of $V_L = 3/4V_T$ for $V_T = 0.1, 0.4, 0.8$. (b) The corresponding fluxes given numerically by (4.83) for thick drops (solid lines) and by the right-hand side of (3.97) for thin drops (dashed line). 98

4.9 Generally there are multiple equilibrium solutions to (4.86). (a) The right-hand side of (4.86) is plotted as a function of V_L with $\mathrm{Bo} = 1$, $\alpha_L = 1$ and $\alpha_R = 0.8$. The system has three non-trivial equilibria, at $V_L \approx 0.39, 1.7, 3.7$, as indicated by the circles. The equilibrium $V_L \approx 1.7$ is clearly unstable. (b) The flux and both left and right drop volumes, as functions of time, are shown for the initial conditions $(V_L, V_R) = (1.7, 2.2)$ (dashed lines) and $(1.65, 2.25)$ (solid lines), *i.e.* they have the same total volume. 103

5.1 (a) The footprint of a network is defined as the union of rectangles and circles; nodes are the regions where the rectangles intersect. (b) The geometry in the node region showing the coordinates along each conduit where $a = j+1, i+4$, $b = j+1, i+7$ and $c = j+1, i+6$. (c) The geometric parameters in the drops and conduits, where $d = i+1$, $i+2$ 109

5.2 Comparison of the drop volumes for solutions to the asymptotic problem (5.18) and (5.19) (dashed lines) to the full numerical problem (3.18) and (3.20)–(3.22) (solid lines) for the geometry shown in (a). The physical parameters are taken from Table 2.1. The two lower drops (2 and 3) both have an initial volume of 11 µl, while the upper drop has an initial volume of 21 µl. (b) The solutions for the volume of drop 2 for $\epsilon \approx 0.27, 0.14, 0.069$. 116

5.3 Comparison of the drop volumes for solutions to the asymptotic problem (5.18) and (5.19) (dashed lines) to the full numerical problem (3.18) and (3.20)–(3.22) (solid lines) for the geometry shown in (a). The physical parameters are taken from Table 2.1. The left- and rightmost drops (2 and 7) have an initial volume of 10 µl and the remaining drops have an initial volume of 1 µl. (b)–(d) The volumes of drops 1, 2 and 3 respectively for $\epsilon \approx 0.12, 0.061, 0.031$. 117

5.4 The network GUI, created in MATLAB, allows the user to rapidly design and test potential networks. 119

5.5 Solving mazes using microfluidic networks; the 20 µl drop has the higher pressure and is the "entrance" to the maze, the 10 µl drop is the exit. (a) A maze with lots of dead ends. (b) The same maze with multiple possible routes to the exit. 121

5.6 Streamlines in a node computed in COMSOL. The arrows on the base of the node show the pressure gradient there. 123

5.7 (a) The geometries used in the numerical simulations with $n = 2, 4, 6, 8$ conduits. (b) Comparison of the numerical solutions (solid lines) on the domains shown in (a) to (5.44) (dashed lines) for different values of ϵ with $\alpha = 1/8$, $\mathrm{Bo} = 256$ and $\mathcal{P} = 1/\beta$, where β is given by (5.36). 128

5.8 (a) Plots of the conduit cross-section profile for $\epsilon^2\text{Bo} = -50$, -20, 0, 4, π^2, with $\widehat{A} = 1$. The profiles corresponding to negative Bond numbers are given by (5.67) (dotted lines). The profiles corresponding to positive Bond numbers are found by replacing the hyperbolic cosines with cosines and multiplying by -1 in (5.67) (dashed lines). For $\text{Bo} = 0$ the profile is given by (3.42) (solid line). (b) The relative difference in $\mathcal{A}_0$ and $\mathcal{M}_0$ compared to the values in (3.43) as a function of the Bond number. 133

5.9 (a) The geometry of the conduit showing the different fluid regions, Γ^*_{C1}, Γ^*_{C2}, and the dividing interface S^*_{C1}. (b) The cross-section of the conduit, Π^*_1, Π^*_2 and the relevant length scales. 136

5.10 The coordinate system for the conduit cross-section: s is the arc length from the top of the profile, θ_C is the contact angle and Φ is the angle the curve makes with the horizontal. The regions inside and outside of the conduit are denoted Π_1 and Π_2 respectively. 140

5.11 (a) In τ-σ space the fluid interface is a straight line with the infinite strips, bounded by $0 < \sigma < \beta$ and $\beta < \sigma < \pi$, mapping to the overlay and circuit cross-section respectively. (b) The transformed coordinates given by (5.106), constant values of σ are transformed to circles in Y-Z space. The shading represents the same region. 143

5.12 (a) The convergence of the Fourier series solution for the flux (5.128) as a function of N for $\mathcal{L} = 3, 4, 10, 15, 20, 25$, with $\mu = 4$ and $\theta_C = 1$. (b) The cross-sectional area (5.104) as a function of the contact angle. (c) The flux given by (5.128) as a function of θ_C for $\mu = 0, 4, 1000$. (d)–(f) The velocity in the cross-section of the conduit $\overline{U}_1$ and overlay $\overline{U}_2$ given by (5.118) and (5.119) with $\theta_C = 1.4$, $\mathcal{L} = 20$, and $N = 100$, where the viscosity ratio μ is given by $\mu = 0$ in (d), $\mu = 4$ in (e) and $\mu = 1000$ in (f). We note that the velocity outside of the conduit is effectively zero in (f). 144

5.13 Numerical solutions of (5.130) and (5.132) with the initial condition $\widetilde{P}_1(X, 0) = 0.1$ for (a) $\mathcal{Q}_0 = 0.01$, where the solid lines show the solution at $T = 0, 92, 194, 500$, and (b) $\mathcal{Q}_0 = 0.001$, where the solid lines show the solution at $T = 0, 18, 39, 100$. The dashed red line shows the steady state solution. 146

5.14 Numerical solutions of (5.133) and (5.134) for $a^2\widetilde{\mathrm{Bo}} = -15$, -8, 0, 3, 5.1962 for a fixed area $\widetilde{\mathcal{A}} = 1$. For clarity, dashed lines have been used for profiles with $a^2\widetilde{\mathrm{Bo}} < 0$, dotted lines have been used for $a^2\widetilde{\mathrm{Bo}} > 0$ and the solid line shows the profile for $a^2\widetilde{\mathrm{Bo}} = 0$. 147

5.15 (a) Pressure and (b) area of a conduit cross-section as a function of contact angle θ_C given by (5.133)–(5.135) for $a^2\widetilde{\mathrm{Bo}} = -4$, -1, -0.5, -0.1, 0, 0.1, 0.5. The dashed red lines show the exact solution when $a^2\widetilde{\mathrm{Bo}} = 0$ given by (5.103) in (a) and by (5.104) in (b). (c) The convergence of the COMSOL solution as $\mathcal{N}$ is increased and the mesh size is decreased for $\theta_C = 1$, $\mu = 4$ and $a^2\widetilde{\mathrm{Bo}} = 0$. (d) The flux in each cross-section given by (5.96) corresponding to the solutions in (a) and (b), with $\mu = 4$. 149

5.16 The geometry and governing equations for the finite element problem in the conduit cross-section, where the interface S_{C1} between Π_1 and $\widetilde{\Pi}_2$ is found by solving (5.133) and (5.134) 150

5.17 Plots of the conduit interface cross-section given by (5.133) and (5.134) (thick black lines) and the corresponding velocity profiles given by (5.137)–(5.143) for (a) $a^2\widetilde{\mathrm{Bo}} = -15$; (b) $a^2\widetilde{\mathrm{Bo}} = 0$ and (c) $a^2\widetilde{\mathrm{Bo}} = 5.1962$ with $\mu = 4$ and $\mathcal{A} = 1$. 151

5.18 Comparison of the maximum conduit interface height given by (5.144) (red dashed lines) with experimental data for different imposed flow rates. The flow is from left to right and the final six data points for each experiment are not included in the comparison since they are in the junction region. The solid green lines show the interface height with interface elasticity, as derived later (see (5.175) where the parameter value $\mathscr{E} = 3.4$ has been used). 153

5.19 (a) The velocity in the conduit measured using PIV. The dashed line shows the location of the interface found by fitting (5.102) to data. (b) The height of the velocity maximum as a function of the viscosity ratio μ computed with (5.118). 154

5.20 The water serum mixture used in the devices forms wrinkles on its surface as demonstrated by sucking fluid out of a suspended drop. In (a)-(c) the decreasing volume causes the drop to shrink but in (d) the elastic properties of the surface cause it to wrinkle. Unpublished figures kindly supplied by Prof. Walsh. 155

Chapter 1

Introduction

1.1 Microfluidic devices

The technologies used in the fabrication of microfluidic devices have been utilised for nearly two decades [129] and their potential to revolutionise many areas of medicine, biology, and chemistry have been widely discussed [128]. Microfluidic devices have been used to facilitate protein crystallisation, genome sequencing, drug discovery, cancer diagnostics, studies of microbiological ecology and are of growing importance in the life sciences [57, 63, 88, 128]. The current global pandemic highlights a further area in which microfluidic devices are of great importance. Rapid, large-scale testing for Covid-19 has been shown to be an important factor in limiting its spread [105]. In the past, microfluidic devices have been used to test for similar viral strains [133] and there is currently a lot of research going into developing new microfluidic devices capable of providing rapid diagnostics [95, 116].

One of the key advantages of microfluidic devices is their ability to facilitate both massively high throughput assays and minimise reagent costs by manipulating exceedingly small volumes of liquids [97]. Moreover, the peculiar low Reynolds number hydrodynamics within these devices can be harnessed to generate carefully controlled environments that allow for systematic handling of biological samples and for mixing chemicals [114]. Nevertheless, the development of microfluidics has largely fallen short of the promises made twenty years ago, especially in the life sciences. There are

many reasons why a large scale "microfluidic revolution" has not yet occurred [101], but chief among them are that (i) the materials commonly used for microfabrication are toxic to sensitive eukaryotic cell lines; (ii) most microfluidic devices are highly sensitive to small perturbations and air bubbles, which means that the success rate of experiments in even the most capable of hands can be abysmal; and (iii) the fabrication of devices typically requires highly specialised equipment, advanced training and a dedicated clean room [14, 52, 76]. All of these factors have come to create a significant barrier to uptake by researchers from across different disciplines. While first-generation microfluidic systems have revealed the many applications that can benefit from this technology, the challenge ahead is to remove the barriers discussed above and, in doing so, increase the penetration of microfluidic assays across the life sciences and chemistry. Therefore, there is a need to develop a new class of devices that are quick to produce, flexible and non-toxic.

1.1.1 PDMS-based devices

Early microfluidic devices were typically constructed by making a pattern of channels in a polymer (although glass and silicon have also been widely used [59]), either by engraving or moulding [81]. Fluid would then be pumped through the channels by an external pump. The most commonly used material in the fabrication of microfluidic devices is Polydimethylsiloxane — PDMS [9]. It has several advantages for use in microfluidics: it is transparent, inexpensive and largely biocompatible. In addition, PDMS structures as small as a few nanometres can be moulded [10].

The small length scales of microfluidic devices are of further use to biologists as they can be used to study individual cells [4], for instance, in studies of chemotaxis [1]. Despite its advantages, there are some drawbacks to the use of PDMS in biology. For example, small hydrophobic molecules can be absorbed, which can bias results in experiments [119]. PDMS is also permeable to water which can make it difficult

to control evaporation [131]. Differences in cellular responses have been observed between macro-scale cultures in Petri dishes and microfluidic cultures in PDMS-based devices. Some of these differences can be attributed to the issues of PDMS outlined above [89]. There exist numerous methods for treating the surface of PDMS to remedy these issues, and this is an active area of research [47, 48, 90]. Another approach may be to avoid using this material entirely. Freestyle Fluidics is an approach which has recently been developed by Walsh *et al.* [127] that does not rely on the use of PDMS. Their new method of fabricating microfluidic devices is capable of sidestepping many of the barriers of traditional devices.

1.1.2 Open microfluidics

The devices constructed using the Freestyle Fluidics approach belong to a class of microfluidic device referred to as open microfluidics. In these devices, at least one fluid-fluid interface exists. Often, this is achieved by having the liquid in the device exposed to the surrounding air, although more complex interfaces can also exist. This makes the fluid in the device much more accessible, which is of particular use in biotechnology and biology [15]. It is common in open microfluidic devices for the flow in the channels to be driven by capillary forces [12, 26, 61], removing the need for external energy. Though there is generally still a reliance on etching, patterning of surfaces with hydrophobic and hydrophilic stripes or the use of solid walls to maintain stable channels [70, 132]. The advantage of the novel device studied in this thesis is that none of these methods are required to keep the channel in place. Throughout this thesis, we refer to the fluid-interface channels as conduits to differentiate them from their solid-walled counterparts.

1.1.3 How Freestyle Fluidics works

Using the new method of Freestyle Fluidics, a microfluidic device is created by printing a partially wetting liquid (*i.e.* a liquid that will spread on a surface until an equilibrium

contact angle is reached) on the base of an unpatterned Petri dish. The partially wetting liquid is then covered with an immiscible fluid to prevent evaporation. The surface of the Petri dish covered by the partially wetting liquid forms a footprint that remains fixed when the contact angle is maintained between the advancing and receding values.

Using Freestyle Fluidics, a variety of different experimental designs have been developed, with varying degrees of complexity. Some examples of these are shown in Figure 1.1 and Figure 1.2. As illustrated in Figure 1.1, the simplest circuit consists of two drops connected by a single conduit so that the contact set has a dumbbell shape. Here, the pressure is initially higher in the left-hand drop (which contains a blue dye) so the fluid flows through the conduit, which is just visible as a line connecting the drops, into the right-hand drop. The pressure in each drop depends on both the volume and base radius of the drop. In general, decreasing the base radius or increasing the volume will increase the pressure in the drop. In Figure 1.1, due to the smaller base radius, the left-hand drop has the higher pressure. A key part of the work of this thesis will be to quantify the relationship between drop size and pressure.

The three-drop network in Figure 1.2a demonstrates, using different coloured dyes, how a chemical concentration gradient can be maintained across the width of a conduit. The control of chemical gradients is important in many applications of microfluidic devices, in particular in biological assays [111]. Fluid flows out of each of the left-hand drops (indicated by the arrows). Due to the low Reynolds number, the flow is laminar in the conduits and the fluid from each drop does not significantly mix where they join in the middle conduit. Such a setup can be used to control chemical gradients, enabling more refined studies of chemotaxis for example. In Figure 1.2b, the fluids in the eight outer drops flow into the central drop and mix together because, as we mentioned above, the smaller drops have the higher pressure. Fig-

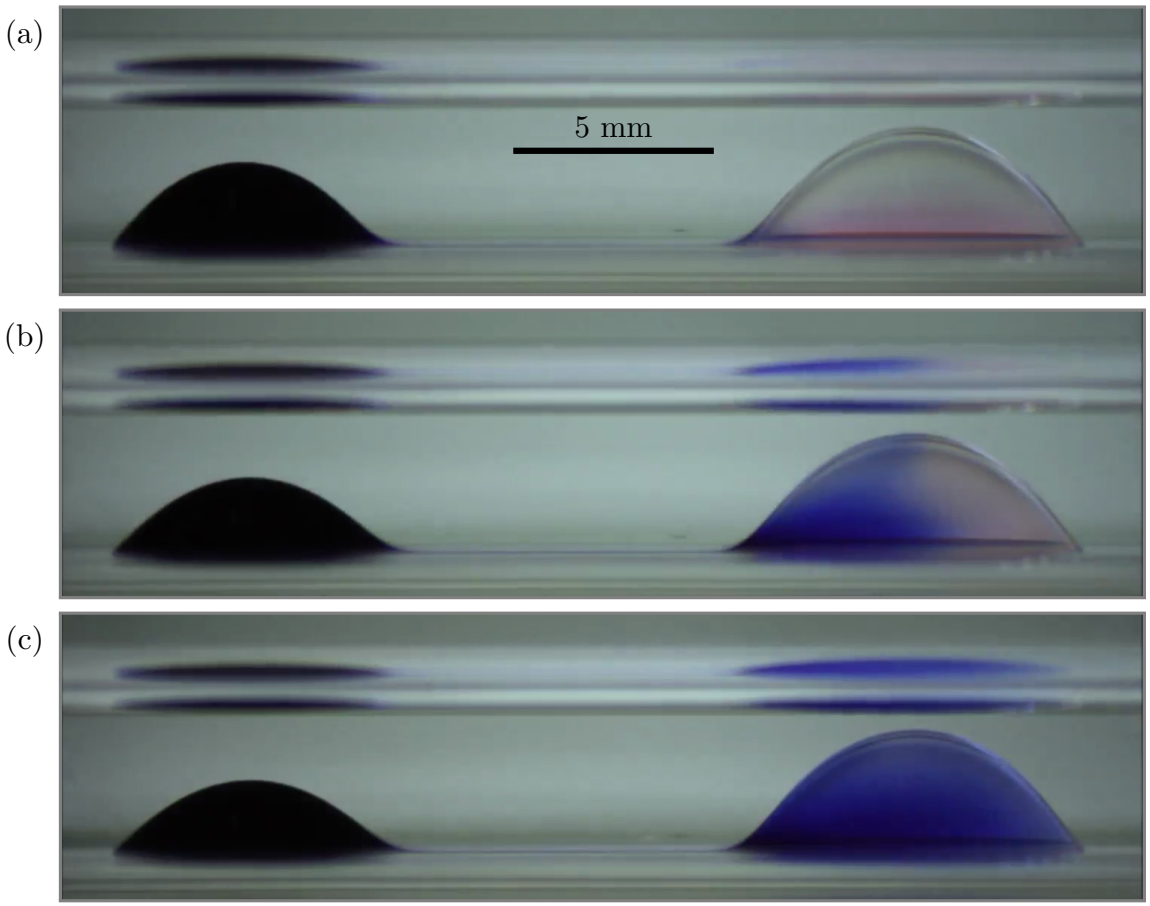


Figure 1.1: The side view of the new device with a simple geometry consisting of two printed fluid drops and a fluid conduit connecting them. The height of the conduit is much less than the drops and is barely visible in the images. The left- and right-hand drops initially contained 10 µl and 20 µl of fluid; 10 µl of blue dye was then added to the left-hand drop. The fluid is pumped from the left-hand drop to the right-hand one due to their pressure difference. (a)–(c) The fluid in the left drop (containing blue dye) flows into the right, the images were taken at times 0 min, 33 min and 66 min after the blue dye was added. Reproduced with permission from Walsh *et al.* [127] under the creative commons licence, `http://creativecommons.org/licenses/by/4.0/`.

ure 1.2c demonstrates, with coloured dyes again as a surrogate for the chemicals of interest, how different concentrations can be achieved in different drops. As well as maintaining concentration gradients in a conduit, it is also useful to have different concentrations in different drops. The left- and rightmost drops (indicated by the arrows) contain more fluid than the remaining drops, so that as the device equilibrates different quantities of the fluids are delivered to each of the central drops. Such serial

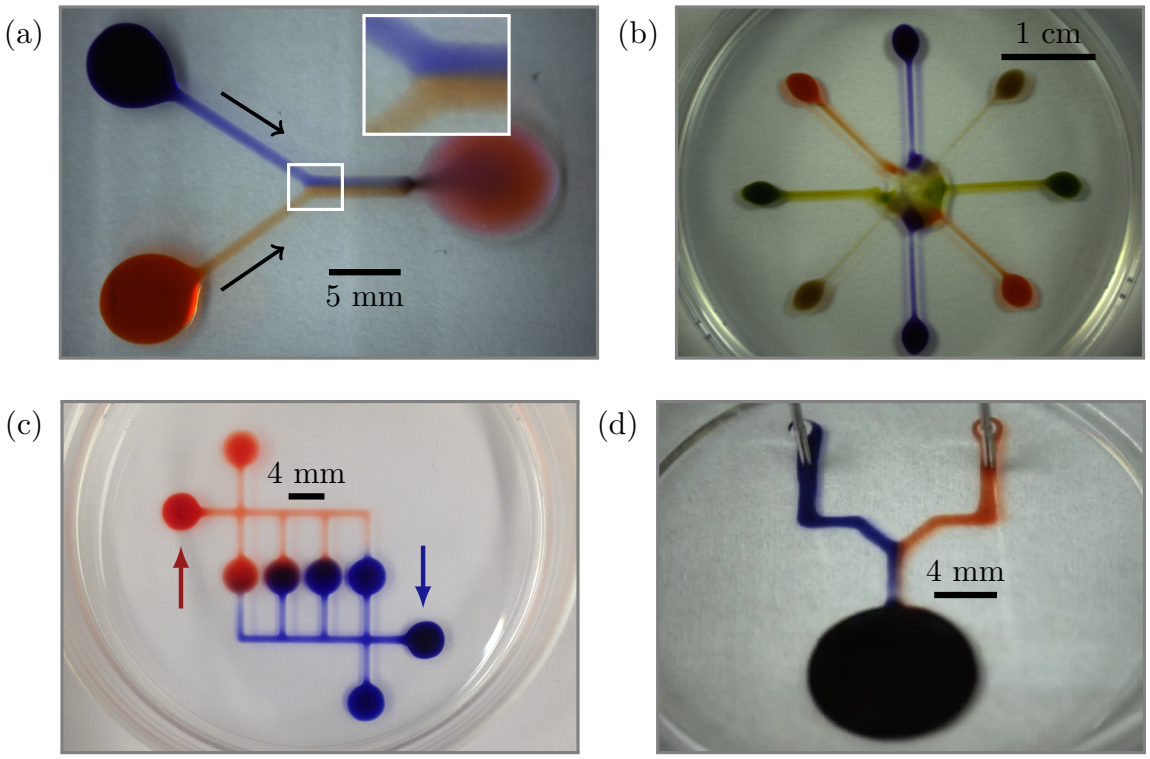


Figure 1.2: Images from experiments showing some possible networks of drops and conduits. (a) A stable concentration is maintained across two laminar streams. (b) The fluids in the outer drops are mixed in the central drop. (c) Serial dilutions are created in the four central drops. (d) Fluid is pumped directly into the conduits and collects in the drop. Reproduced with permission from Walsh *et al.* [127] under the creative commons licence, `http://creativecommons.org/licenses/by/4.0/`.

dilutions can then be used to test the effect of different chemical concentrations on cells placed within the drops. Walsh *et al.* [127] demonstrate this with human embryonic kidney (HEK) cells. A similar configuration to Figure 1.2a is shown in Figure 1.2d, illustrating how the drops can be replaced with needles (visible at the top of the image) through which fluid can be pumped. A fundamental aim in the development of free surface microfluidics, and also this thesis, is the evidence-based design of such devices to obtain flow characteristics that are suitable for the experiment at hand. In contrast with conventional microfluidic devices, where fluid is pumped through solid channels with a fixed geometry, in these new devices, the shape of the interface between the two liquids and the flow is dependent on the complex interplay between

surface tension, buoyancy, and viscosity.

1.2 Models relevant to Freestyle Fluidics

There are a wide variety of uses and designs for microfluidic devices and, as such, there has been a lot of interest in developing mathematical models for microfluidics [21, 96]. The difficulties involved in prototyping new designs of microfluidic devices also make mathematical modelling an attractive means of testing design ideas [20, 40]. Typically, numerical methods are required to model all but the simplest microfluidic devices [41, 42, 65]. Given the wide variety of modelling that has been previously undertaken, we will focus on the models that have the most relevance to Freestyle Fluidics.

1.2.1 Current models of Freestyle Fluidics devices

The disparity of length scales evident in Figures 1.1 and 1.2 has important implications for the numerical solution of the free boundary problem using computational fluid dynamics (CFD) software. It is reasonable to expect that the discretised equations will become increasingly stiff, and therefore more expensive to run and less likely to converge, as the disparity of length scales is increased to that required in practice or for more complicated geometries. Thus, we anticipate CFD to be impractical because of the need for either extensive software development or expensive proprietary software and the desire for real-time analysis of experiments and device design across large numbers of prospective geometries. However, the disparity of length scales is to the advantage of an asymptotic analysis, which we will use to derive systematically reduced models that retain all of the essential physics but are sufficiently simple to be analytically or computationally tractable. Reduced models, with controlled approximations and the essential physics, will give valuable insight into the physics governing the evolution of the fluid interface and will have the po-

tential to be generalised to more complex geometries. Our aim of evidence-based device design, as discussed above, can be broken down into a series of simple objectives, namely analysing and classifying the dynamics of (i) drops, (ii) conduits, (iii) drop-conduit junctions and (iv) conduit-conduit junctions followed by integrating this understanding to allow for informed – circuit level – device design. In particular, the mathematical and modelling concepts needed to model the fundamental components of the microdevices of Walsh *et al.* [127] are well known: pendant drops and rivulets have been studied extensively. However, their study in the context of device design for free surface microfluidic platforms, and the integration of drops and conduits into circuits of increasing complexity for these platforms, constitutes the novel aspects of this thesis.

In the limit of small gravity, a sessile drop of fluid will take on the shape of a spherical cap, and simple expressions can be found for the contact angle and radius of curvature. Using this approximation, Walsh *et al.* [127] estimate the pressure at the base of a drop to be given by

$$P_{base(drop)} = \frac{2\gamma}{R} + \rho_{FC40} g h_0 + \rho_{water} g h_1, \tag{1.1}$$

where γ is the interfacial tension, R is the radius of curvature of the drop, ρ_{FC40} is the density of the overlaying fluid, ρ_{water} is the density of the drop fluid, g is the acceleration due to gravity, h_1 is the height of the drop and h_0 is the depth of the overlay above the drop. The first term on the right-hand side of (1.1) is the Laplace pressure and two following terms are the hydrostatic pressures due to the two fluids. This expression can be used to approximate the pressure difference driving the flow. Then, assuming that the pressure at the base of the drop and in the conduit near the inlet are equal, the shape of the conduit can be determined using

$$\frac{\gamma}{R_{conduit}} = \frac{2\gamma}{R} + \left(\rho_{FC40} - \rho_{water}\right) g h_1, \tag{1.2}$$

where $R_{conduit}$ is the radius of curvature at the inlet of the conduit. Using simple geometry, Walsh *et al.* [127] also compute the drop volume in terms of these parameters to be

$$V_{drop} = \frac{\pi h_1^2}{3}\left(3R - h_1\right). \tag{1.3}$$

These expressions can be used to determine whether the contact angles are expected to be within the advancing and receding angles and thus whether the contact line will be fixed for a given geometry. However, there is still a need to extensively analyse the dynamics of such a device to be able to address further specific design questions.

1.2.2 Similar devices

There are a wide variety of microfluidic devices that use surface tension to drive the fluid flow [80]. Devices with a similar geometry to that shown in Figure 1.1 have been developed over the past two decades [13, 98, 126]. The key drawback of these is that they still rely on solid PDMS channels to connect the fluid drops. The pressure in the drops is modelled with the Young-Laplace equation – which we shall discuss further in the next section – and an ODE for the drop volumes can be written in the form

$$\frac{\mathrm{d}V_1}{\mathrm{d}t} = -\frac{\mathrm{d}V_2}{\mathrm{d}t} = Q, \tag{1.4}$$

where V_i is the volume of drop i and Q is the flux in the channel [60, 126]. Assuming Poiseuille flow the flux can be written as

$$Q = K_{ch}\left(\frac{2\gamma}{R_1} - \frac{2\gamma}{R_2}\right), \tag{1.5}$$

where once more γ is the interfacial tension, R_i is the radius of curvature of drop i and the constant K_{ch} depends on the geometry of the channel. In general, numerical modelling is required to analyse the flow in these devices [61, 62]. Multiple channels can be connected to create networks. Lee *et al.* (2019) [74] model this by making an analogy with Kirchhoff's current law; we shall make a similar analogy for networks of drops and conduits.

Another similar device is modelled by Darhuber *et al.* (2001) [26]. In these devices there are no solid channels, instead the fluid is constrained by hydrophilic stripes on a hydrophobic surface. The pressure exerted by a fluid drop is used to drive fluid along the hydrophilic stripe; this results in a dumbbell shaped geometry, though the drops have square bases. By considering stripe widths that are much less than the base size of the drops, the two regions can be analysed separately. The evolution of the fluid height h_c along the microstripe is governed by

$$\frac{\partial h_c}{\partial t} - \frac{64}{35}\frac{\gamma}{\mu w^2}\frac{\partial}{\partial x}\left(h_c^3\frac{\partial h_c}{\partial x}\right) = 0, \tag{1.6}$$

where w is the width of the stripe and μ the viscosity of the fluid used [26]. This may be recognisable as the thin-film equation with one spatial dimension. The main focus of the modelling of these devices is on the spreading of the liquid front along the hydrophilic stripe [25]. Yang *et al.* (2011) [130] also look at the travelling fluid fronts using a similar configuration, with the fluid additionally confined by a solid channel.

The above mentioned devices all have at least one free surface and rely on surface tension to drive the fluid flow, although none of them use an overlaying fluid. As with the modelling of these similar devices, we will be able to split the geometry of the devices shown in Figures 1.1 and 1.2 into multiple regions and analyse them each individually. So we now proceed to review some of the modelling relevant to each of the individual regions.

1.2.3 Pendant drops

The shape of a static fluid drop hanging under gravity is governed by the Young-Laplace equation, a second order partial differential equation [29]. The term pendant drop usually refers to a drop of fluid hanging under gravity, whereas a sessile drop refers to a drop of fluid resting on a surface. In either case, the equations governing the interface shape are the same. In the new devices, the overlay is typically denser than

the cell culture medium used in the circuit, so the force of gravity pushes the drops upwards and they behave like pendant drops. The shape of pendant drops has been studied extensively for more than a century [46, 118]. This has been particularly useful in determining fluid properties. For instance, the interfacial tension can be determined by fitting the solution of the Young-Laplace equation to two-dimensional images of fluid drops hanging under gravity [11]. There have been numerous tables drawn up for this purpose [8] and extended over time [44, 79, 113], although with the advent of cheap computing, the fitting can be done much more easily [5]. Similar methods can also be used to calculate the contact angle of sessile drops [50], particularly when direct measurements cannot be made. Traditionally, gravity and surface tension alone determine the shape of pendant drops, but other forces have also been incorporated, for instance electric fields [7].

The impact of overlying fluid is particularly relevant to our modelling of Freestyle Fluidics. This has not been investigated as extensively, but it has been shown that, when the depth of the overlay is large compared to the drop height, the shape of the drop is not affected by the free surface of the overlay [121]. Our main aim in studying pendant drops is to understand how the pressure depends on the volume and how this affects the flow in the conduits. Analytic expressions relating the pressure, volume and contact angle can easily be derived, but finding the relation between them for arbitrarily sized drops requires numerical simulation. Exact solutions of the Young-Laplace equation can be found [19, 51], and perturbations to these give asymptotic solutions when, for example, the effects of gravity are small [82, 84]. Although we are considering static drops, there may be experimental regimes in which the dynamics are important. For instance, with a large enough volume, a portion of the fluid may detach from the base; this phenomenon is known as pinch off [39]. The conditions under which the fluid will experience pinch off have been well studied, but determining the volume of fluid that will remain requires numerical simulation and

is beyond the scope of this thesis [54, 86]. Thus, it will be important to understand when the solutions are stable to small perturbations, which has been studied for both sessile and pendant drops [77, 78]. Additionally, there can be multiple solutions to the Young-Laplace equation for a given contact angle and Bond number [83, 118]. Several of these solutions may be stable to small perturbations and determining the appropriate solution would again require consideration of the full dynamics [94]. Another phenomenon that is beyond the scope of this thesis, but is nevertheless an interesting question, is the effect of Marangoni flows [122].

1.2.4 Rivulet flow

Rivulets are also well understood and, like pendant drops, their shape is governed by the Young-Laplace equation, though the fluid motion also needs to be considered via the Navier-Stokes equations. A common problem is flow down an inclined plane; such gravity driven flows have relevance in coating surfaces and instabilities in a liquid film can cause rivulets to form [37, 56, 91]. In their simplest form, gravity-driven flows have a constant pressure gradient and pinned contact line. In this case, the problem is reduced to one dimension [120]; in the limiting cases of small contact angle and small gravity, analytic solutions can be found for the interface shape. The static model has been generalised to allow for moving contact lines and an analysis of the stability of the rivulet [28]. Rivulets with varying widths have also been studied [38]. The breakup of the rivulet into droplets can then be modelled [33]. Another area in which rivulets are important, and which has some similarity to the devices we are modelling, is in inkjet printing. For instance, modelling the motion of the contact line at a corner between two straight rivulets [58].

1.2.5 Fluid junctions

All of the pendant drop modelling mentioned thus far has assumed axisymmetric drops. In the Freestyle Fluidics devices, the junctions where the drops and conduits

meet introduces an asymmetry into the drops. Asymmetry has been modelled in the context of static drops on inclined planes [71, 72], for which numerical methods are required. More often, it is the motion of a drop on an inclined plane that is of interest [73]. Such problems may also involve the formation of a rivulet behind the drop as it moves and asymptotic methods can be used [106].

1.3 Thesis summary and overview

As discussed in the previous section, some of the key components needed to model the novel microfluidic device of this thesis have been studied extensively in the past, particularly the building blocks of pendant drops and rivulets. However, the analysis of open fluidic microdevices requires the analysis of not only junctions between these building blocks, but also large networks of drops and rivulets, all within a single modelling framework. Thus, and in summary, the overarching aim of this thesis is the development of systematic and rational asymptotic analyses to derive reduced models of the flow in novel free surface microfluidic devices formed by pendant drops and rivulets, together with the subsequent investigation and characterisation of these flows. To break this aim down, in chapter 2 we lay out the equations governing the flow in the microfluidic device. These equations are based on reasonable physical assumptions embedded in classical fluid mechanics. In chapter 3, we set out to derive a reduced model for the long-time behaviour of the fluid in a surface tension driven microdevice using the standard thin-film equations (see e.g. Oron *et al.* (1997) [87]). The main focus is on the simple "dumbbell" geometry in which two thin fluid drops connected by a long, thin and narrow conduit are printed on a planar substrate and overlayed with an immiscible fluid to prevent evaporation, as shown in Figure 1.1. We will determine the asymptotic structure of the dumbbell problem in which the flow is driven by the pressure difference between the drops. This will show that there are three distinct spatial regions we need to consider, and we identify the relevant

timescales in each, as well as the timescale over which the free surface of the whole device relaxes. We also identify the extent to which the geometry can be tuned to control the flux through the conduit and the shear stress on the substrate, both of which can be important considerations in experiments. On the longest identified timescale, we find solutions of the lubrication equations in each region and form a composite solution for the thickness of the liquid over the whole domain. The asymptotic predictions are shown to be in excellent agreement with numerical simulations even for moderate aspect ratios. The implications of the current work, and possible directions for future development will then be discussed.

In chapter 4, we consider the regime in which the lubrication equations are no longer valid. As before, the simple dumbbell setup (passive pumping) is analysed, but we also allow for the fluid to be pumped directly into the conduit (active pumping) so that we only need a single drop to act as a reservoir. This introduces different timescales depending on whether the fluid in the conduit is actively or passively pumped. Quasi-steady equations are found in the drop and conduit regions, though these require numerical solution. We are unable to find an analytical expression for the interface height in the junction, but analysis of this region shows that, at leading order, the pressure is transmitted straight through it. We are thus able to construct an ODE model for the equilibration of the device. The ODE is solved numerically since explicit expressions cannot be found for the flux or volume (except in the thin-film regime). As anticipated, the full numerical problem is difficult to solve, so validation of the results in this chapter is implemented via comparison with the thin-film model from chapter 3.

In chapter 5, we examine several extensions and generalisations of the models developed in the previous chapters. In §5.1, networks of drops and conduits are considered. Here, the analysis of the previous chapters is generalised to obtain Kirchhoff-type laws for the flow through more complicated networks of drops and conduits. Us-

ing the network model, a graphical user interface (GUI) that permits the rapid testing of candidate networks for experimental design is developed. In §5.2 we consider the next order correction to the drop volume with the aim of improving the predictive capability of the network model. Active pumping in isolated conduits — without the constraints imposed by matching with the drop — is modelled in §5.3, this will allow for conduits with comparable width and height scales. In §5.4, we compare the models developed in the previous chapters to experimental data. We show that the there are some disagreements when the models of chapters 3 and 4 are compared to experimental data. The devices are particularly useful for experiments involving cells, which require printing the circuit with a culture medium. Proteins from such media are deposited on the fluid interface, causing it to behave like an elastic solid. This is particularly noticeable in the conduits, where the fluid velocity is observed to be zero on the interface. The model is modified so that it captures this additional important physics, while still retaining as much simplicity as possible.

Note that a paper based on the results from chapter 3 and §5.1 has recently been published in the Journal of Fluid Mechanics [18].

Chapter 2

Fundamental principles for modelling Freestyle Fluidics

2.1 Introduction

In the this chapter we derive, summarise and non-dimensionalise the governing equations for Freestyle Fluidics. This will form the fundamental basis for the following chapters on Freestyle Fluidics, where we initially consider thin film limits in the simple setting of dumbbell geometries. In later chapters, we will analyse the model in distinguished limits where the thin film limit no longer holds, once more in the context of a simple dumbbell geometry, before generalising to consider networks.

2.2 Freestyle Fluidics: governing equations

We start by stating the equations governing the full problem, namely the incompressible Navier-Stokes equations together with the usual solid-fluid and fluid-fluid boundary conditions. Though Walsh *et al.* [127] have developed more complicated designs, we will first focus on the relatively simple configurations illustrated in Figure 2.1.

2.2.1 Geometric setup

The simplicity of the new devices means that complex circuits can be easily and quickly made by printing multiple drops and conduits in a Petri dish. We will start

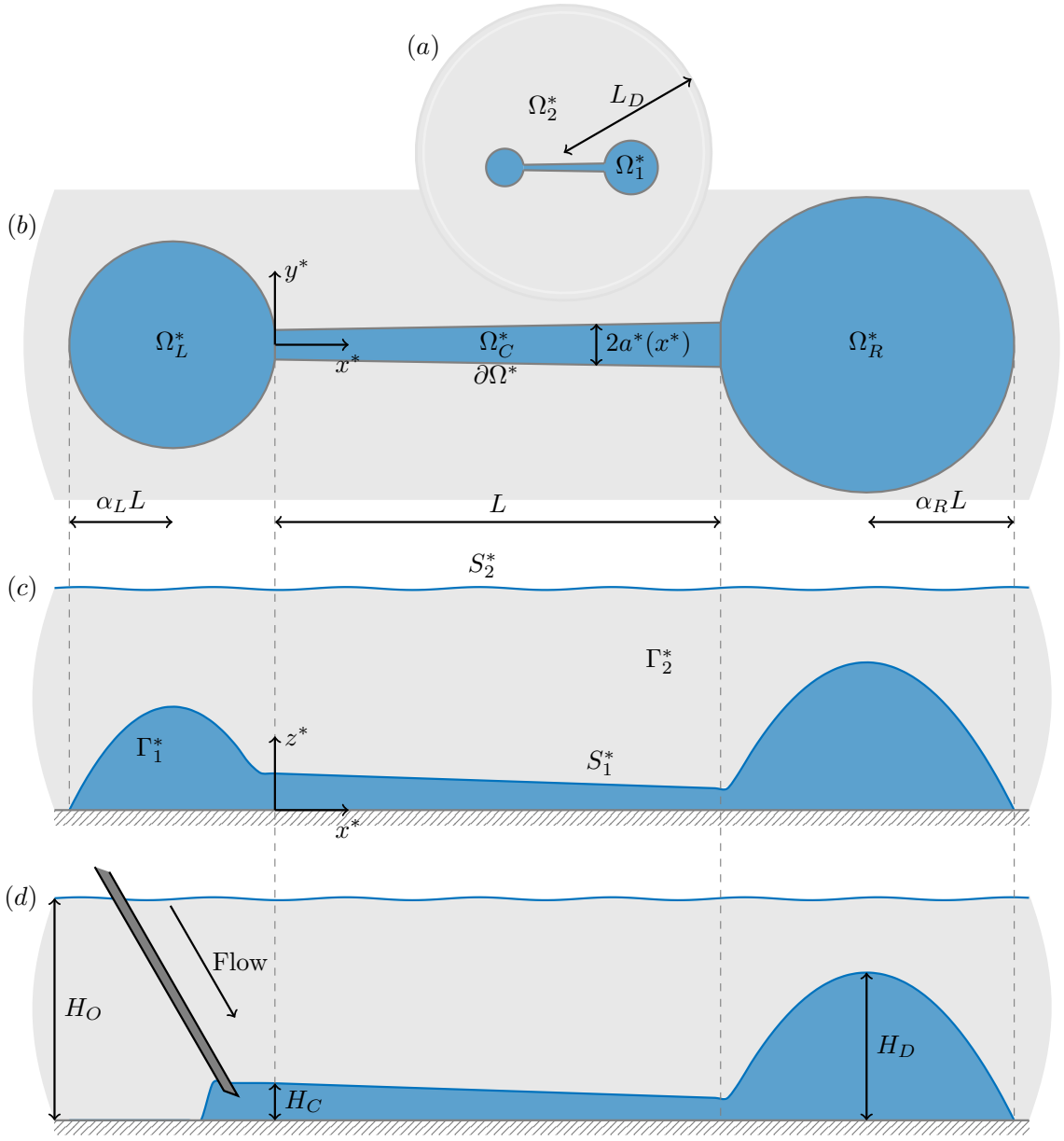


Figure 2.1: (a) The footprint of a dumbbell shaped circuit, Ω_1^*, in a Petri dish of base radius L_D, where Ω_2^* denotes the base of the Petri dish outside of the dumbbell footprint. (b) A close up of the footprint showing the different regions: the base radii of the two drops are denoted $\alpha_L L$ and $\alpha_R L$, the drops are connected by a conduit of width $2a^*(x^*)$, where the length L is the distance between the two junction regions. The side views (c) and (d) show a cross-section of the device on the line of symmetry, $y^* = 0$, with the origin at the start of the conduit (either where it exits the left drop (c) or where the fluid is pumped in (d)). The region occupied by the fluid in the circuit is denoted Γ_1^* and the region occupied by the overlaying fluid is denoted by Γ_2^*. The overlay/circuit interface is denoted S_1^* and the air/overlay interface is denoted S_2^*. The depth of the overlay is denoted H_O, the height scale of the drops is denoted H_D and the height scale of the conduit is denoted H_C.

by considering the simplest passive and active experimental set-ups as illustrated in Figure 2.1. The passive circuit consists of a conduit of length L with a base width of $2a^*$ (which may vary along its length), with fluid drops of base radius $R_L = \alpha_L L$ and $R_R = \alpha_R L$ at either end; the subscripts $_L$ and $_R$ correspond to the left- and right-hand drops, respectively. The initial volumes deposited in each drop and their base radii can be chosen so that there is a difference in pressure between the two drops. This pressure difference then drives the fluid along the conduit until the drop pressures are equalised. For the actively driven circuit, Figure 2.1d, there is a needle connected to an external pump in place of the left-hand drop. The fluid is then driven along the conduit by the pump to be collected by the fluid drop at the other end, which acts thereby as a reservoir. In either case the circuit is then overlaid with an immiscible fluid with depth H_O as shown in Figure 2.1c for the passive case and in Figure 2.1d for the active case. We let H_D denote the height scale of a drop and H_C the height scale of the conduit. The diameter of the Petri dish is denoted L_D and we assume that the circuit is printed sufficiently far away from its edges that this boundary has a negligible impact on the flow in the circuit. The media are chosen to ensure a large advancing and small receding contact angle and hence the contact line $\partial\,\Omega^*$ is pinned almost everywhere for the duration of most experiments. It is only near the corners where a conduit meets a drop that the contact angle will exceed the advancing angle. But, as we shall discuss in depth in chapter 3, this will not have a significant impact on our analysis, and we can therefore only consider pinned contact lines.

2.2.2 Governing equations, boundary conditions and initial conditions

We introduce the Cartesian coordinates $\boldsymbol{x}^* = (x^*, y^*, z^*)$ with the associated basis vectors $(\mathbf{e_x}, \mathbf{e_y}, \mathbf{e_z})$ and time t^*, where the asterisks denote variables that are dimensional. The rigid, impermeable base is on the plane $z^* = 0$ and x^* is the distance along the conduit from the intersection with the left drop as shown in Figure 2.1,

noting that we initially focus on the passive circuit, Figure 2.1c. The location of the free surface of the fluid in the circuit is denoted by $z^* = h^*(x^*, y^*, t^*)$, where the film thickness h^* may be multi-valued. The location of the free surface open to the air is denoted by $z^* = h_O^*(x^*, y^*, t^*)$. The velocity for each fluid is denoted by $\boldsymbol{u}_i^*(x^*, y^*, z^*, t^*) = (u_i^*, v_i^*, w_i^*)$ and $p_i^*(x^*, y^*, z^*, t^*)$ denotes the pressure field for $i = 1, 2$, where the subscript $_1$ refers to the liquid in the circuit Γ_1^* and the subscript $_2$ refers to the overlaying liquid in Γ_2^*. The liquids in the device are assumed to be incompressible viscous fluids with constant densities ρ_1 and ρ_2 and constant dynamic viscosities μ_1 and μ_2 (and hence constant kinematic viscosities ν_1 and ν_2). With the assumption of Newtonian flow, both fluids satisfy the incompressible Navier-Stokes equations, so that

$$\frac{\partial \boldsymbol{u}_i^*}{\partial t^*} + (\boldsymbol{u}_i^* \cdot \boldsymbol{\nabla})\boldsymbol{u}_i^* - \nu_i \nabla^2 \boldsymbol{u}_i^* = -\frac{\boldsymbol{\nabla} p_i^*}{\rho_i} - g\mathbf{e_z}, \tag{2.1a}$$

$$\boldsymbol{\nabla} \cdot \boldsymbol{u}_i^* = 0, \tag{2.1b}$$

for $(x^*, y^*, z^*) \in \Gamma_i^*$, $i = 1, 2$, where g is the acceleration due to gravity.

The fluids used are immiscible, so there is no mass transfer across the interface S_1^* between the circuit and overlay. We also assume that the velocities of the two fluids are continuous across the interface S_1^*. There is no-slip on the base and walls of the Petri dish. The jump in traction on the interface between the two fluids, S_1^*, is assumed to be due to a constant surface tension γ (*i.e.* we assume no surfactant gradients are present). The kinematic condition on this surface is given by

$$\boldsymbol{u}_i^* \cdot \mathbf{n} = v_n^* \quad \text{on } S_1^* \text{ for } i = 1, 2, \tag{2.2}$$

where $\mathbf{n}$ is the unit normal to S_1^*, pointing out of Γ_2^* and v_n^* is the velocity of the free boundary S_1^* in that direction. Continuity of velocity is assumed for all unit vectors $\mathbf{t}$ tangent to S_1^*:

$$\boldsymbol{u}_1^* \cdot \mathbf{t} = \boldsymbol{u}_2^* \cdot \mathbf{t} \quad \text{on } S_1^*. \tag{2.3}$$

No-slip conditions hold for each liquid on the substrate so that

$$\boldsymbol{u}_i^* = \mathbf{0} \quad \text{on } z^* = 0 \text{ for } (x^*, y^*) \in \Omega_i^* \ (i = 1, 2). \tag{2.4}$$

As mentioned earlier, the entire device is printed on a Petri dish, so we must also take account of the walls of the dish in contact with the overlay, with the fluid in the circuit assumed to be far away from the edges of the dish. No-slip boundary conditions are imposed on the walls of the Petri dish, but we make the simplifying assumption that the length scale of the Petri dish is much larger than the length scale of the printed circuit ($L_D \gg L$). Thus, we define $\Gamma_2^* = \{(x^*, y^*, z^*) : 0 < z^* < h_O^*(x^*, y^*, t^*), (x^*, y^*, z^*) \notin \Gamma_1^*\}$ and impose the condition

$$\boldsymbol{u}_2^* \to \mathbf{0} \quad \text{as } x^{*2} + y^{*2} \to \infty \text{ for } (x^*, y^*, z^*) \in \Gamma_2^*. \tag{2.5}$$

For a constant surface tension γ, the balance of stress across the interface gives

$$(\boldsymbol{\sigma}_2^* \cdot \mathbf{n} - \boldsymbol{\sigma}_1^* \cdot \mathbf{n}) = -\gamma \kappa^* \mathbf{n} \quad \text{on } S_1^*, \tag{2.6}$$

where the Cauchy stress tensor is given by

$$\boldsymbol{\sigma}_i^* = -p_i^* \mathbf{I} + \mu_i \left(\nabla \boldsymbol{u}_i^* + (\nabla \boldsymbol{u}_i^*)^{\mathrm{T}} \right) \quad \text{for } i = 1, 2, \tag{2.7}$$

and the mean curvature of the circuit/overlay $\kappa^*(x^*, y^*, z^*, t^*)$ is defined as

$$\kappa^* = -\boldsymbol{\nabla} \cdot \mathbf{n}. \tag{2.8}$$

A positive curvature means that the surface is upwardly concave at that point. A similar condition holds on the quiescent free surface of the overlay S_2^*. The kinematic condition on this interface is given by

$$\boldsymbol{u}_2^* \cdot \mathbf{n} = v_{n_a}^* \quad \text{on } S_2^*, \tag{2.9}$$

where $v_{n_a}^*$ is the outward normal velocity of the free boundary. We assume that the air is essentially inviscid and thus exerts only atmospheric pressure in the normal direction, so that

$$\boldsymbol{\sigma}_2^* \cdot \mathbf{n}_a = \gamma_a \kappa_a^* \mathbf{n}_a - p_{\mathrm{atm}} \mathbf{n}_a \quad \text{on } S_2^*, \tag{2.10}$$

where κ_a^* is the curvature, $\mathbf{n}_a$ the outward normal, γ_a the surface tension of the air/overlay interface and p_{atm} is atmospheric pressure. The contact line $\partial\,\Omega^*$ is assumed to be pinned, so that the contact set between each liquid and the substrate is fixed. The problem is closed by prescribing three initial conditions: the location of the free boundaries S_1^* and S_2^*, which also fixes the contact line and hence the location of the contact set, and the initial velocities $\boldsymbol{u}_i^*(\boldsymbol{x}^*, 0)$ for $\boldsymbol{x}^* \in \Omega_i^*$ $(i = 1, 2)$.

So far we have not mentioned the effect of the needle in the active pumping case, Figure 2.1d. For a complete analysis we would have to take account of the change to the interface shape due to the needle and of the flow through the pump. Instead we make the simplifying assumption that we can restrict ourselves to the domain $x^* > 0$ and impose suitable inlet boundary conditions at $x^* = 0$ having reduced the model using long-wavelength asymptotics.

2.2.3 Physical and geometrical parameter values

In Table 2.1 we summarise the physical and geometrical parameter values that characterise the free surface microfluidic devices of Walsh *et al.* [127], treating the medium as Newtonian with the viscosity of water. Typically the covering fluid is FC40, a biocompatible and viscous fluorocarbon, and a range of geometrical scales are typically considered, as detailed in the table.

2.2.4 Global mass conservation

Focusing on the passive dumbbell shaped circuit in Figure 2.1b, we divide the contact set Ω_1^* into three regions: the conduit region is defined by $\Omega_C^* = \{(x^*, y^*) :\ 0 < x^* < L,\ |y^*| < a^*(x^*)\}$, where $a^*(x^*)$ is depicted in Figure 2.1b, the left-hand drop region Ω_L^* which is bounded by a circular arc of radius $R_L = \alpha_L L$ centred at $(x^*, y^*) = (-\sqrt{R_L^2 - a_0^2}, 0)$, and intersects the conduit at $(x^*, y^*) = (0, \pm a_0)$, where $a_0 = a^*(0)$. Similarly, the right-hand drop region is bounded by a circular arc of radius $R_R = \alpha_R L$ centred at $(x^*, y^*) = (L + \sqrt{R_R^2 - a^*(L)^2}, 0)$, which intersects the conduit at $(x^*, y^*) =$

Symbol	Definition	Typical values	Units
μ_1	Dynamic viscosity (water)	1×10^{-3}	$\mathrm{kg\,m^{-1}\,s^{-1}}$
μ_2	Dynamic viscosity (FC40)	4.05×10^{-3}	$\mathrm{kg\,m^{-1}\,s^{-1}}$
γ	Surface tension (water/FC40)	4×10^{-2}	$\mathrm{kg\,s^{-2}}$
γ_A	Surface tension (FC40/air)	1.6×10^{-2}	$\mathrm{kg\,s^{-2}}$
ρ_1	Density (water)	1×10^{3}	$\mathrm{kg\,m^{-3}}$
ρ_2	Density (FC40)	1.85×10^{3}	$\mathrm{kg\,m^{-3}}$
ρ_a	Density (air)	1.2	$\mathrm{kg\,m^{-3}}$
g	Gravitational acceleration	9.81	$\mathrm{m\,s^{-2}}$
H_O	Depth of overlaying liquid	3	mm
H_D	Maximum height of drop	0.2–3	mm
L	Conduit length	1.5–30	mm
a_0	Half conduit width at the inlet	0.15–0.75	mm
R_L, R_R	Base radii of left and right drops	1–4	mm
v_L^*, v_R^*	Volume of fluid in left and right drops	2–20	µl

Table 2.1: The physical parameters for water and FC40 (the typical overlaying fluid) at room temperature and pressure, and the typical range of geometric parameters. All values are from Walsh *et al.* [127].

$(0, \pm a^*(L))$ as shown in Figure 2.1b. Here we have assumed that the drops do not impinge on the conduit region $0 < x^* < L$, which is usually the case in practice.

The fluid domains corresponding to each of these contact sets can be similarly defined as follows: the conduit domain is defined by $\Gamma_C^* = \{(x^*, y^*, z^*) \in \Gamma_1^* : 0 < x^* < L\}$; the left and right drops are defined by $\Gamma_L^* = \{(x^*, y^*, z^*) \in \Gamma_1^* : x^* < 0\}$ and $\Gamma_R^* = \{(x^*, y^*, z^*) \in \Gamma_1^* : x^* > L\}$ as shown in Figure 2.1b. We define the volumes in the left drop, conduit and right drop v_L^*, v_C^* and v_R^* respectively, to be given by

$$v_i^*(t^*) = \iiint_{\Gamma_i^*} \mathrm{d}x^* \,\mathrm{d}y^* \,\mathrm{d}z^* \quad \text{for } i = L, C, R. \tag{2.11}$$

For a passive circuit the total volume is fixed since there is no flux of liquid through the pinned contact line. In this case the total volume in the circuit is given by the initial volume, v_T^* say, so that

$$v_L^* + v_C^* + v_R^* = v_T^*. \tag{2.12}$$

We define the conduit cross-section $\Pi_1^*(x^*, t^*)$ to be the intersection of Γ_1^* and a plane with constant x^* for $0 < x^* < L$, then the cross-sectional area A^* and flux Q^* in the

conduit are given by

$$A^*(x^*,t^*) = \iint_{\Pi_1^*} \mathrm{d}y^*\,\mathrm{d}z^*, \quad Q^*(x^*,t^*) = \iint_{\Pi_1^*} u_1^*\,\mathrm{d}y^*\,\mathrm{d}z^*. \tag{2.13a,b}$$

Integrating the incompressibility condition (2.1b) over the cross-section and using (2.2) and (2.4) gives the conservation of mass condition in the conduit:

$$\frac{\partial A^*}{\partial t^*} + \frac{\partial Q^*}{\partial x^*} = 0. \tag{2.14}$$

Integrating (2.1b) instead over each of the domains Γ_R^*, Γ_L^* and Γ_C^* shows how the volume is changing in each region over time:

$$\frac{\mathrm{d}v_L^*}{\mathrm{d}t^*} = -Q_L^*(t^*), \quad \frac{\mathrm{d}v_R^*}{\mathrm{d}t^*} = Q_R^*(t^*), \quad \frac{\mathrm{d}v_C^*}{\mathrm{d}t^*} = Q_L^*(t^*) - Q_R^*(t^*), \tag{2.15a–c}$$

where we have defined $Q_L^*(t^*) = Q^*(0,t^*)$ and $Q_R^*(t^*) = Q^*(L,t^*)$ to be the fluxes where the conduit connects to the left and right drop, respectively. With active pumping (2.15a) and (2.15c) are no longer applicable (since there is no left-hand drop); instead, the flux at $x^* = 0$ is taken to be equal to the flow rate imposed by the pump.

In summary, for the model given by (2.1)–(2.4) and (2.6)–(2.8) we have defined seven key geometric quantities: the depth of the overlaying fluid H_O; the conduit length L; the conduit width $2a^*(x^*)$; the base radii of the drops R_L and R_R and the initial drop volumes $v_L^*(0)$ and $v_R^*(0)$. In the following three chapters we will focus on different distinguished limits and thus we start each of these chapters by non-dimensionalising the governing equations. For reference, we give a brief overview of the dimensionless parameters that will be important for our modelling, with more detailed explanations being given throughout the text. In each chapter we will define a different Reynolds number: Re_1, Re_2 and Re_3 for the lubrication approximation (chapter 3), thick drops model (chapter 4) and conduit model (§5.3) respectively. The Reynolds number gives a measure of the importance of inertial forces compared to viscous ones. The Reynolds numbers as we have defined them in Table 2.2 can be

Symbol	Definition	Typical values
Re_1	$\delta^3 \rho_1 \gamma L/\mu_1^2$	7.5×10^{-3}–9.6×10^{6}
Re_2	$\epsilon^4 \rho_1 \gamma L/\mu_1^2$	3.8×10^{-5}–7.5×10^{4}
Re_3	$\epsilon \rho_1 \gamma L/\mu_1^2$	2×10^{3}–6×10^{5}
Ca_1	δ^3	1.25×10^{-7}–8
Ca_2	ϵ^4	6.25×10^{-10}–6.25×10^{-2}
Ca_3	ϵ	0.005–0.5
Bo	$(\rho_2 - \rho_1) g L^2/\gamma$	0.5–188
μ	μ_2/μ_1	≈ 4
α_L, α_R	$R_L/L, R_R/L$	0.03–2.7
δ	H_D/L	0.005–2
ϵ	a_0/L	0.005–0.5

Table 2.2: The dimensionless parameters and their typical ranges.

large. However, as with standard lubrication theory, inertia will be governed by reduced Reynolds numbers, these will be introduced as we examine the model in detail. We also provide the corresponding capillary numbers, Ca_1, Ca_2, Ca_3: these give the relative effect of viscous and surface tension forces for the lubrication approximation, thick drops model and conduit model respectively. The remaining dimensionless parameters summarised in Table 2.2 are: the Bond number Bo, which gives a measure of the importance of gravitational forces compared to surface tension; the viscosity ratio of the fluids used $\mu = \mu_2/\mu_1$; and the dimensionless radii of the bases of the two drops denoted by α_L and α_R. The final parameters are the aspect ratios of the entire circuit: the ratio of drop height to conduit length $\delta = H_D/L$ and the ratio of the conduit width to length, defined as $\epsilon = a_0/L$.

Chapter 3

Thin film modelling

Numerous elements of this chapter have recently been published in the Journal of Fluid Mechanics by Calver *et al.* [18].

3.1 Introduction

In this chapter we set out to derive the simplest asymptotic model for the long-term behaviour of the fluid in the surface tension driven microdevice of Figure 1.1. We analyse the thin-film regime in which the vertical length scales of the circuit are much smaller than the horizontal ones, even for the drops, which is often the case in practice. Thus, we define the parameter $\delta = H_D/L$ and begin our analysis of (2.1)–(2.4) and (2.6)–(2.8) for $\delta \ll 1$. This assumption will greatly simplify the governing equations allowing us to find an analytic solution for the drop volumes and flow rate when the conduit is long and narrow.

In §3.2 we begin with a concise formulation of the lubrication equations governing the flow in a dumbbell configuration. In §3.3.1 we will determine the asymptotic structure of the dumbbell problem in the distinguished limit in which the flow is driven by the pressure difference between drops. This will show that there are three distinct regions we need to consider, and we identify the relevant time scales in each and the time scale over which the free surface of the whole device relaxes. It is the last of these time scales which will be most relevant for determining the duration

of an experiment. On this time scale we find solutions of the lubrication equations in each region and form a composite solution for the thickness of the liquid over the whole domain. Verification will be carried out via comparison of our asymptotic predictions with numerical simulations of the thin-film equations. We will then be able to illustrate qualitative trends in §3.3.8 and §3.3.9. For much of this chapter we will focus on the dumbbell geometry, shown in Figure 2.1b, with a constant conduit width. Following a study of the associated fluid flows, fluxes and stresses we also develop our analysis to consider variable conduit widths and active pumping, rather than driving fluid via the pressure differences between two drops.

3.2 Scales and non-dimensionalisation

We suppose that the drops may be large enough that we must account for the effects of gravity, but not so large that gravity dominates the effects of surface tension. We then use the drop height and conduit length to non-dimensionalise the vertical and horizontal components respectively. In the thin film model the height in the circuit scales with δL and we further assume that the height is single valued. The mean curvature of the circuit/overlay interface (2.8) scales with $1/R_C$, where R_C is the radius of curvature of the drop. The typical radius of curvature of the left-hand drop is as if it were a spherical cap of base radius α_L and height δL for which

$$R_C^2 = (R_C - \delta L)^2 + \alpha_L^2 L^2, \tag{3.1}$$

giving $R_C = \alpha_L^2 L/\delta + \mathrm{O}(\delta)$. Throughout, we assume $\alpha_R, \alpha_L = \mathrm{O}(1)$, so that the mean curvature scales with δ/L. We choose the pressure scale in the circuit so that curvature and pressure balance in (2.6), which shows that the pressure in the circuit, in excess of hydrostatic pressure, scales with $\delta\gamma/L$. We define U_0 to be a typical horizontal velocity scale in the circuit. Balancing the terms in the incompressibility condition (2.1b) shows that the horizontal velocity components u_1^* and v_1^* scale with

U_0 and the vertical component w_1^* scales with δU_0. We thus choose a velocity scale which balances the pressure gradient with the dissipative viscous term in (2.1a); we find the velocity scale to be $U_0 = \delta^3\gamma/\mu_1$.

The depth of the overlaying fluid is necessarily greater than the maximum height of the circuit: $H_D < H_O$. We further assume that $H_O \sim L$ so that $H_D \ll H_O$ and non-dimensionalise the vertical and horizontal components in the overlay with L. We assume that the fluid in the overlay is driven solely by the flow in the circuit, so the same velocity scale is used in the overlay as for the horizontal velocity scale in the circuit. Balancing the pressure gradient with the dissipative viscous term in (2.1a); we find the pressure scale in the overlay to be $\delta^3\gamma/L$. A much larger overlay depth, $H_O \gg L$, would not alter the leading-order equations, whereas for a shallow overlay, $H_D \sim H_O$, we would need to model both the fluid in the circuit and overlay at leading order.

The equations are rescaled with

$$\begin{gathered} x^* = L\,x, \quad y^* = L\,y, \quad z^* = \begin{cases} \delta L\,z & \text{for } (x^*, y^*, z^*) \in \Gamma_1^*, \\ L\,Z & \text{for } (x^*, y^*, z^*) \in \Gamma_2^*, \end{cases} \\ a^* = L\,a, \quad h^* = \delta L\,h, \quad t^* = \frac{3L}{U_0}t, \quad \kappa^* = \frac{\delta}{L}\kappa, \quad \boldsymbol{u}_i^* = U_0\,(u_i, v_i, \delta w_i)\,, \\ p_1^* = \frac{\delta\gamma}{L}\,p_1 + p_{\text{atm}} + \rho_2 g H_O - \rho_1 g L Z, \\ p_2^* = \frac{\delta^3\gamma}{L}\,p_2 + p_{\text{atm}} + \rho_2 g H_O - \rho_2 g L Z, \end{gathered} \tag{3.2}$$

for $i = 1, 2$, where p_{atm} is atmospheric pressure. The factor of 3 in the time scaling has been included so as to simplify the leading-order equations. We similarly drop the asterisks from the dimensional domains Ω^*, $\partial\,\Omega^*$, S_i^* and Γ_i^* to denote the rescaled contact set Ω, contact line $\partial\Omega$, fluid interfaces S_i and fluid domains Γ_i for $i = 1, 2$ as illustrated in Figure 3.1. In the circuit the governing equations (2.1) are now given by

$$\delta^2\,\mathrm{Re}_1\left(\frac{1}{3}\frac{\partial u_1}{\partial t} + (\boldsymbol{u}_1 \cdot \boldsymbol{\nabla})\,u_1\right) - \left(\delta^2\widetilde{\nabla}^2 u_1 + \frac{\partial^2 u_1}{\partial z^2}\right) = -\frac{\partial p_1}{\partial x}, \tag{3.3a}$$

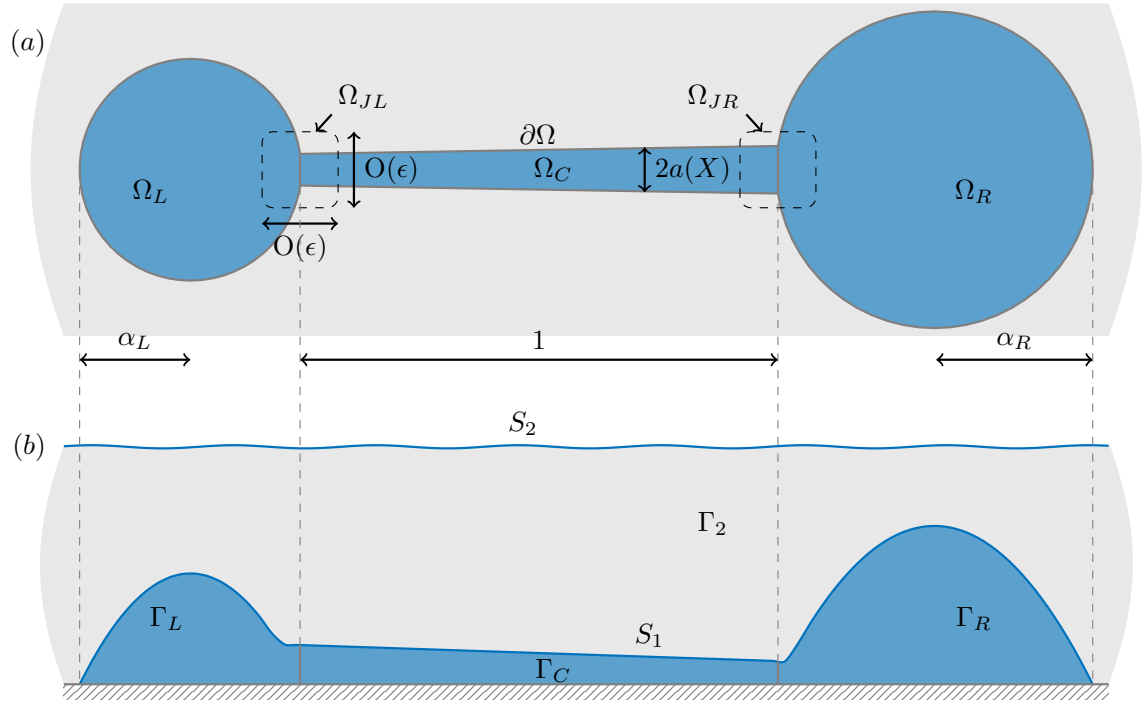


Figure 3.1: (a) The dimensionless contact set with each of the regions labelled: Ω_L and Ω_R are the bases of the drops; Ω_C is the conduit contact set with a width of $2a(x)$ and straight edges at $x = 0, 1$; Ω_{JL} and Ω_{JR} are the junction regions where the drops intersect the conduit and $\partial\Omega$ is the pinned contact line. (b) The dimensionless fluid domains and interfaces: Γ_L and Γ_R are the fluid drops with footprints Ω_L and Ω_R respectively; Γ_C denotes the fluid contained in the conduit with footprint Ω_C; S_1 is the interface between $\Gamma_1 = \Gamma_L \cup \Gamma_C \cup \Gamma_R$ and Γ_2 with Γ_2 the region occupied by fluid above the interface, and S_2 the interface of the overlay with the air above.

$$\delta^2 \operatorname{Re}_1 \left(\frac{1}{3}\frac{\partial v_1}{\partial t} + (\boldsymbol{u}_1 \cdot \boldsymbol{\nabla})\, v_1 \right) - \left(\delta^2 \widetilde{\nabla}^2 v_1 + \frac{\partial^2 v_1}{\partial z^2} \right) = -\frac{\partial p_1}{\partial y}, \tag{3.3b}$$

$$\delta^4 \operatorname{Re}_1 \left(\frac{1}{3}\frac{\partial w_1}{\partial t} + (\boldsymbol{u}_1 \cdot \boldsymbol{\nabla})\, w_1 \right) - \left(\delta^4 \widetilde{\nabla}^2 w_1 + \delta^2 \frac{\partial^2 w_1}{\partial z^2} \right) = -\frac{\partial p_1}{\partial z}, \tag{3.3c}$$

$$\frac{\partial u_1}{\partial x} + \frac{\partial v_1}{\partial y} + \frac{\partial w_1}{\partial z} = 0, \tag{3.3d}$$

for $(x, y) \in \Omega_1$ and $0 < z < h(x, y, t)$, where $\widetilde{\nabla}^2 = \partial^2/\partial x^2 + \partial^2/\partial y^2$, $\boldsymbol{\nabla} = (\partial/\partial x, \partial/\partial y, \partial/\partial z)$ and $\boldsymbol{u}_i = (u_i, v_i, w_i)$. In the overlaying liquid the different height scale gives instead the governing equations

$$\operatorname{Re}_1 \left(\frac{1}{3}\frac{\partial u_2}{\partial t} + \left((u_2, v_2) \cdot \widetilde{\boldsymbol{\nabla}} \right) u_2 + \delta\, w_2 \frac{\partial u_2}{\partial Z} \right) - \frac{\nu_2}{\nu_1} \overline{\nabla}^2 u_2 = -\frac{\rho_1}{\rho_2}\frac{\partial p_2}{\partial x}, \tag{3.4a}$$

$$\operatorname{Re}_1 \left(\frac{1}{3}\frac{\partial v_2}{\partial t} + \left((u_2, v_2) \cdot \widetilde{\boldsymbol{\nabla}} \right) v_2 + \delta\, w_2 \frac{\partial v_2}{\partial Z} \right) - \frac{\nu_2}{\nu_1} \overline{\nabla}^2 v_2 = -\frac{\rho_1}{\rho_2}\frac{\partial p_2}{\partial y}, \tag{3.4b}$$

$$\delta \mathrm{Re}_1 \left(\frac{1}{3} \frac{\partial w_2}{\partial t} + \left((u_2, v_2) \cdot \widetilde{\boldsymbol{\nabla}} \right) w_2 + \delta^2 \, w_2 \frac{\partial w_2}{\partial Z} \right) - \delta \frac{\nu_2}{\nu_1} \, \overline{\nabla}^2 w_2 = - \frac{\rho_1}{\rho_2} \frac{\partial p_2}{\partial Z}, \tag{3.4c}$$

$$\frac{\partial u_2}{\partial x} + \frac{\partial v_2}{\partial y} + \delta \, \frac{\partial w_2}{\partial Z} = 0 \tag{3.4d}$$

for $(x, y, Z) \in \Gamma_2$, where $\overline{\nabla}^2 = \partial^2/\partial x^2 + \partial^2/\partial y^2 + \partial^2/\partial Z^2$, $\widetilde{\boldsymbol{\nabla}} = (\partial/\partial x, \partial/\partial y)$ and $\mathrm{Re}_1 = U_0 L/\nu_1$ is the Reynolds number. The kinematic boundary condition on the fluid interface (2.2) is given by

$$w_1 = \frac{1}{3} \frac{\partial h}{\partial t} + u_1 \frac{\partial h}{\partial x} + v_1 \frac{\partial h}{\partial y} \quad \text{on } z = h(x, y, t) \text{ for } (x, y) \in \Omega_1, \tag{3.5a}$$

$$w_2 = \frac{1}{3} \frac{\partial h}{\partial t} + u_2 \frac{\partial h}{\partial x} + v_2 \frac{\partial h}{\partial y} \quad \text{on } Z = \delta \, h(x, y, t) \text{ for } (x, y) \in \Omega_1, \tag{3.5b}$$

The velocity is continuous across the interface, so

$$\boldsymbol{u}_1(x, y, h, t) = \boldsymbol{u}_2(x, y, \delta \, h, t) \quad \text{ for } (x, y) \in \Omega_1, \tag{3.6}$$

where Ω_1 is the contact set of Γ_1. Since the velocities on the interface are equal (3.5a) and (3.5b) are equivalent. The no-slip conditions are now given by

$$\boldsymbol{u}_1 = \mathbf{0} \quad \text{on } z = 0 \text{ for } (x, y) \in \Omega_1. \tag{3.7}$$

$$\boldsymbol{u}_2 = \mathbf{0} \quad \text{on } Z = 0 \text{ for } (x, y) \notin \Omega_1. \tag{3.8}$$

The far-field condition for the velocity in the overlaying fluid (2.5) is now given by

$$\boldsymbol{u}_2 \to \mathbf{0} \quad \text{as } x^2 + y^2 \to \infty. \tag{3.9}$$

The dynamic boundary condition (2.6) becomes

$$\widehat{\boldsymbol{\sigma}}_2 \cdot \mathbf{n} - \widehat{\boldsymbol{\sigma}}_1 \cdot \mathbf{n} = -\delta \, (\widehat{\kappa} + \mathrm{Bo} \, h) \, \mathbf{n} \quad \text{on } S_1, \tag{3.10}$$

where the Bond number is defined as $\mathrm{Bo} = (\rho_2 - \rho_1) g L^2/\gamma$ and the rescaled stress tensors are given by

$$\widehat{\boldsymbol{\sigma}}_1 = -\delta \, p_1 \mathbf{I} + \delta^2 \, \boldsymbol{\tau}_1, \tag{3.11}$$

$$\widehat{\boldsymbol{\sigma}}_2 = -\delta^3 \, p_2 \mathbf{I} + \delta^2 \mu \, \boldsymbol{\tau}_2, \tag{3.12}$$

where $\mu = \mu_2/\mu_1$ and $\boldsymbol{\tau}_i$ depends on the fluid; for the fluid in the circuit (the drops and conduit) it is given by

$$\boldsymbol{\tau}_1 = \begin{bmatrix} 2\,\delta\,\dfrac{\partial u_1}{\partial x} & \delta\left(\dfrac{\partial v_1}{\partial x} + \dfrac{\partial u_1}{\partial y}\right) & \delta^2\,\dfrac{\partial w_1}{\partial x} + \dfrac{\partial u_1}{\partial z} \\ \delta\left(\dfrac{\partial v_1}{\partial x} + \dfrac{\partial u_1}{\partial y}\right) & 2\,\delta\,\dfrac{\partial v_1}{\partial y} & \delta^2\dfrac{\partial w_1}{\partial y} + \dfrac{\partial v_1}{\partial z} \\ \delta^2\,\dfrac{\partial w_1}{\partial x} + \dfrac{\partial u_1}{\partial z} & \delta^2\dfrac{\partial w_1}{\partial y} + \dfrac{\partial v_1}{\partial z} & 2\,\delta\,\dfrac{\partial w_1}{\partial z} \end{bmatrix}, \tag{3.13}$$

while for the fluid in the overlay we have

$$\boldsymbol{\tau}_2 = \delta \begin{bmatrix} 2\,\dfrac{\partial u_2}{\partial x} & \dfrac{\partial v_2}{\partial x} + \dfrac{\partial u_2}{\partial y} & \delta\,\dfrac{\partial w_2}{\partial x} + \dfrac{\partial u_2}{\partial Z} \\ \dfrac{\partial v_2}{\partial x} + \dfrac{\partial u_2}{\partial y} & 2\,\dfrac{\partial v_2}{\partial y} & \delta\dfrac{\partial w_2}{\partial y} + \dfrac{\partial v_2}{\partial Z} \\ \delta\,\dfrac{\partial w_2}{\partial x} + \dfrac{\partial u_2}{\partial Z} & \delta\,\dfrac{\partial w_2}{\partial y} + \dfrac{\partial v_2}{\partial Z} & 2\,\delta\,\dfrac{\partial w_2}{\partial Z} \end{bmatrix}, \tag{3.14}$$

and the mean non-dimensional curvature $\widehat{\kappa}$ is defined as

$$\widehat{\kappa} = \boldsymbol{\nabla} \cdot \frac{(h_x, h_y, -1)}{\sqrt{\delta^2 h_x^2 + \delta^2 h_y^2 + 1}}. \tag{3.15}$$

We define the reduced Reynolds number to be $\delta^2\mathrm{Re}_1$, as can be seen in Table 2.2 this will typically be small when $\delta \ll 1$. Assuming $\delta^2\mathrm{Re}_1 \ll 1$ we derive the leading-order approximation to (3.3)–(3.15). The Navier-Stokes equations (3.3) reduce at leading order in δ to the familiar lubrication equations given by

$$\frac{\partial p_1}{\partial x} = \frac{\partial^2 u_1}{\partial z^2}, \quad \frac{\partial p_1}{\partial y} = \frac{\partial^2 v_1}{\partial z^2}, \quad \frac{\partial p_1}{\partial z} = 0, \tag{3.16a,b,c}$$

$$\frac{\partial u_1}{\partial x} + \frac{\partial v_1}{\partial y} + \frac{\partial w_1}{\partial z} = 0 \tag{3.16d}$$

for $0 < z < h(x, y, t)$ and $(x, y) \in \Omega_1$. As shown in Table 2.1 the typical viscosities of the two fluids used are of a similar size, and when $\mu = \mathrm{O}(1)$ the tangential components of (3.10) give, at leading order,

$$\frac{\partial u_1}{\partial z} = 0, \quad \frac{\partial v_1}{\partial z} = 0 \quad \text{on } z = h(x, y, t) \text{ for } (x, y) \in \Omega_1 \tag{3.17a,b}$$

while the normal component is, at leading order

$$p_1 = -\nabla^2 h - \mathrm{Bo}\, h \quad \text{for } (x, y) \in \Omega_1, \tag{3.18}$$

where $\nabla^2 = \partial^2/\partial x^2 + \partial^2/\partial y^2$. Thus, at leading order, the only effect of the upper liquid layer is via the hydrostatic pressure in the normal stress boundary condition, *i.e.* it only has an effect through the Bond number. We note that for $\mu = \mathrm{O}(1)$, the shear stress exerted by the upper liquid is of a higher-order than that generated by the flow in the circuit. In chapter 5 we will consider the effects of a much higher viscosity ratio on the flow.

Integrating (3.16a,b) twice with respect to z and applying the boundary conditions (3.7) and (3.17) gives

$$u_1 = \frac{1}{2}\left(z^2 - 2hz\right)\frac{\partial p_1}{\partial x}, \quad v_1 = \frac{1}{2}\left(z^2 - 2hz\right)\frac{\partial p_1}{\partial y}. \tag{3.19a,b}$$

Thus, we can combine this with (3.5a), (3.7) and (3.16d) to give in the usual manner (see e.g. Oron *et al.* [87]) Reynolds lubrication equation in the form

$$\frac{\partial h}{\partial t} = \nabla \cdot \left(h^3 \nabla p_1\right) \quad \text{for } (x, y) \in \Omega_1. \tag{3.20}$$

The interface height is zero on the contact line and there is no flux through the contact line, so we impose the boundary conditions

$$h = 0, \quad \left(h^3 \nabla p_1\right) \cdot \boldsymbol{\nu} = 0 \quad \text{for } (x, y) \in \partial\Omega, \tag{3.21a,b}$$

where $\boldsymbol{\nu}$ denotes the outward pointing normal on $\partial\Omega$ in the (x, y)-plane. Finally an initial condition $\mathscr{H}(x, y)$ needs to be prescribed for the interface height at time $t = 0$, *i.e.*

$$h(x, y, 0) = \mathscr{H}(x, y) \quad \text{for } (x, y) \in \Omega_1. \tag{3.22}$$

The leading-order model (3.18) and (3.20)–(3.22) is applicable for small $\delta = H_D/L$, which we recall to be the ratio of the vertical and horizontal length scales of the

drops. Further estimates of the non-dimensional parameters based on Table 2.1 are presented in Table 2.2 for reference and the resulting equations are of the form of the thin-film equation, which has a long history of study [87].

3.2.1 Global mass conservation

One of our main aims will be to predict the timescale over which the volumes of the two drops equilibrate; *i.e.* the timescale of drop drainage. Since the height of the fluid interface is single valued we can write

$$\widehat{v}_L(t) = \iint_{\Omega_L} h \, \mathrm{d}x \, \mathrm{d}y, \quad \widehat{v}_C(t) = \iint_{\Omega_C} h \, \mathrm{d}x \, \mathrm{d}y, \quad \widehat{v}_R(t) = \iint_{\Omega_R} h \, \mathrm{d}x \, \mathrm{d}y, \quad (3.23\text{a–c})$$

where $\widehat{v}_i = \delta L^3 v_i^*$ for $i = L, C, R$. The total volume in the circuit (2.12) is now given by

$$\widehat{v}_L + \widehat{v}_C + \widehat{v}_R = \iint_{\Omega_1} \mathscr{H}(x, y) \, \mathrm{d}x \, \mathrm{d}y = \widehat{v}_T, \quad (3.24)$$

where $v_T^* = \delta L^3 \widehat{v}_T$. Using (2.13), the dimensionless area of, and flux through, a cross-section of the conduit in an x-plane (with $0 < x < 1$) are given at leading order by

$$\widehat{A}\,(x,t) = \int_{-a(x)}^{a(x)} h \, \mathrm{d}y, \quad \widehat{Q}\,(x,t) = \int_{-a(x)}^{a(x)} \int_0^h u_1 \, \mathrm{d}z \, \mathrm{d}y, \quad (3.25\text{a,b})$$

where $A^* = \delta L^2 \, \widehat{A}$ and $Q^* = \delta L^3 U_0 / 3 \, \widehat{Q}$. Integrating (3.20) over the conduit cross-section then gives

$$\frac{\partial \widehat{A}}{\partial t} + \frac{\partial \widehat{Q}}{\partial x} = 0 \quad \text{for } 0 < x < 1. \quad (3.26)$$

Alternatively, integrating (3.20) over the three regions Ω_L, Ω_C and Ω_R shows that the volume of liquid in each region evolves according to the ordinary differential equations given by

$$\frac{\mathrm{d}\widehat{v}_L}{\mathrm{d}t} = -\widehat{Q}_L(t), \quad \frac{\mathrm{d}\widehat{v}_R}{\mathrm{d}t} = \widehat{Q}_R(t), \quad \frac{\mathrm{d}\widehat{v}_C}{\mathrm{d}t} = \widehat{Q}_L(t) - \widehat{Q}_R(t), \quad (3.27\text{a–c})$$

where we have defined $\widehat{Q}_L(t) = \widehat{Q}(0,t)$ and $\widehat{Q}_R(t) = \widehat{Q}(1,t)$ to be the fluxes where the conduit connects to the left and right drop respectively. The expressions in (3.26)

and (3.27) will play a key role in our scaling and subsequent asymptotic analysis, in which they will be used to close the leading-order governing equations (rather than proceeding to higher order).

3.3 Asymptotic analysis for a long, narrow conduit of constant width

We begin by considering conduits with a constant width $a(x) = \epsilon \ll 1$.

3.3.1 Asymptotic structure and timescales

The two main aims of the dumbbell set-up are (i) for the pressure difference between the two drops to be the dominant mechanism that drives fluid through the conduit; and (ii) for the flux through the conduit to vary slowly over time. To achieve aim (ii) we require the conduit to be long and narrow *i.e.* $\epsilon \ll 1$. To achieve aim (i) we require the pressure in the drops and conduit to be comparable, where the dimensionless pressure in a drop is of O(1). In the conduit we scale $y \sim \epsilon$, then balancing the pressure with the first term on the right-hand side of (3.18) shows that we must have liquid of thickness $h \sim \epsilon^2$ in the conduit in order for the pressures to balance. If the initially printed conduit is thicker than this there would be a higher pressure in the conduit and the fluid would flow from the conduit into both drops until the conduit height reaches $O(\epsilon^2)$. Throughout we assume that the conduits are initially printed with thickness $h \sim \epsilon^2$. We will show that the resulting asymptotic structure consists of five regions: two drops with contact sets Ω_L and Ω_R, a narrow and thin conduit with contact set Ω_C, and two small junction regions with contact sets Ω_{JL} and Ω_{JR} connecting together the drops and conduit, as illustrated in Figure 3.2.

Given our assumptions about the geometry of the device we can now describe the different physical timescales and show that drainage (the timescale on which the pressure equilibrates) acts on a much longer timescale than anything else in the model.

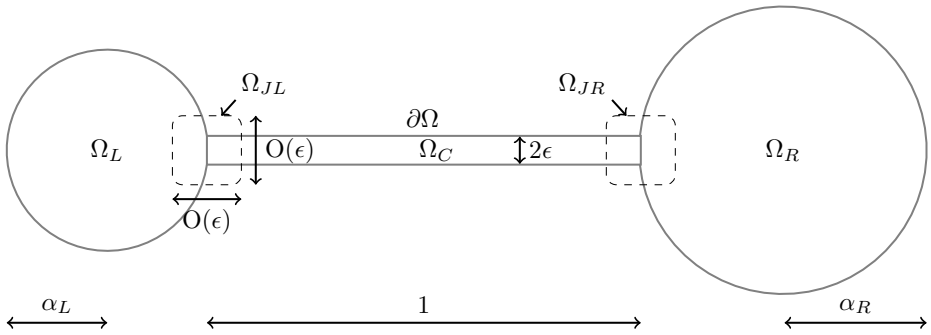


Figure 3.2: The dimensionless contact set with each of the domains labelled: Ω_L and Ω_R are the bases of the drops; Ω_C is the rectangular conduit, with a length of 1 along its outer edge and a width of 2ϵ; Ω_{JL} and Ω_{JR} are the junction regions where the drops intersect the conduit and $\partial\Omega$ is the pinned contact line.

In (3.2) the dimensional governing equations were initially rescaled with the capillary timescale, so we define $t_D \sim 1$ to be the timescale of relaxation in the drop region. In the three regions we have defined, we can use a dominant balance argument in the thin-film equation (3.20) to find the timescale of capillary action in each region. In the junction region we scale with $x, y, h \sim \epsilon$; these scalings and (3.18) then show that $p_1 \sim \epsilon^{-1}$. In the conduit region we scale with $y \sim \epsilon$ and $h \sim \epsilon^2$ and (3.18) shows that $p_1 \sim 1$. These scalings and (3.20) give us the dimensionless timescales of capillary action in the junction and conduit, respectively, as $t_J \sim \epsilon$ and $t_{CW} \sim \epsilon^{-2}$. Since we assume that the conduit is much longer than it is wide, t_{CW} is the timescale of relaxation of the free boundary across the width of the conduit. The timescale of relaxation of the free boundary along the length of the conduit is found by balancing the terms in (3.26). The cross-sectional area and flux in the conduit in (3.25) are also rescaled with $y \sim \epsilon$ and $h \sim \epsilon^2$, so that $\widehat{A} \sim \epsilon^3$ and $\widehat{Q} \sim \epsilon^7$; hence the timescale for relaxation along the length of the conduit is $t_{CL} \sim \epsilon^{-4}$. The drainage timescale is then found by balancing the terms in (3.27). With the same length scales as above for the flux, we still have $\widehat{Q} \sim \epsilon^7$, but the relevant length scale for the volume gives $\widehat{v}_L = \mathrm{O}(1)$ (since all the fluid is contained in the drop regions at leading order). Thus the timescale for drop drainage is $t_{DD} \sim \epsilon^{-7}$.

We have identified five timescales thus far, each depending on the conduit aspect ratio ϵ. They are, respectively, the relaxation timescales for the junction, drops, conduit width and conduit length and the drainage timescale:

$$t_J \sim \epsilon, \quad t_D \sim 1, \quad t_{CW} \sim \frac{1}{\epsilon^2}, \quad t_{CL} \sim \frac{1}{\epsilon^4}, \quad t_{DD} \sim \frac{1}{\epsilon^7}. \tag{3.28a–e}$$

To achieve slowly varying fluxes and stresses, we need t_{DD} to be much larger than t_{CL}, and we can also already see that the drainage timescale is very sensitive to ϵ, so that the geometry is an important factor in achieving a given flux.

3.3.2 Quasi-steady solution in the drops

The leading-order analysis is the same in each drop, so we give only the details for the left-hand one. The conduit is in the much smaller junction region, so at leading order the relevant contact set in the drop is the circular disc Ω_{L0} of radius α_L with centre $(x, y) = (-\alpha_L, 0)$. For $t \gg t_D \sim 1$, (3.20) and (3.21b) show that the profile is quasi-steady, with spatially uniform pressure at leading order. The boundary condition (3.21a) holds at leading order on the boundary of the contact set except at the origin (*i.e.* on $\partial\Omega_{L0}/\{(0,0)\}$); at the origin we must instead match with the junction region. Since the height scale in the junction region is of $\mathrm{O}(\epsilon)$, the relevant matching condition is that the leading-order film thickness tends to zero as $(x, y) \to (0, 0)$, with $(x, y) \in \Omega_{L0}$. Hence, at leading order the drop profile is as if there was no junction region and therefore axisymmetric.

We introduce the polar coordinate $r = \sqrt{(x + \alpha_L)^2 + y^2}$ measuring radial distance from the centre of the circular contact set of the left-hand drop. Then, expanding $h \sim h_L(r, t)$ and $p \sim p_L(t)$ as $\epsilon \to 0$, we deduce from (3.18) and (3.21) the familiar leading-order governing equations given by

$$\frac{\partial^2 h_L}{\partial r^2} + \frac{1}{r}\frac{\partial h_L}{\partial r} + \mathrm{Bo}\, h_L = -p_L \quad \text{for } 0 < r < \alpha_L, \tag{3.29}$$

with $|h_L(0,t)| < \infty$ and $h_L(\alpha_L, t) = 0$; the pressure is related to the leading-order drop volume by the conservation of mass constraint that

$$2\pi \int_0^{\alpha_L} r\, h_L \, \mathrm{d}r = \widehat{v}_L(t)\,, \tag{3.30}$$

where $\widehat{v}_L\,(t)$ now denotes the leading-order volume in the left-hand drop (for small ϵ). Thus the leading-order problem in the left-hand drop has been reduced to the classical one of finding the shape of a static liquid drop with constant surface tension and gravity, which has been well studied with well known interface shape when the contact angle is small [19]. Subject to the additional constraint that we require the drop thickness and pressure to be positive away from the contact line (as discussed below), the solution for $\mathrm{Bo} > 0$ is given by

$$h_L = \frac{p_L}{\mathrm{Bo}} \left(\frac{J_0\Big(\sqrt{\mathrm{Bo}}\, r\Big)}{J_0\Big(\sqrt{\mathrm{Bo}}\, \alpha_L\Big)} - 1 \right), \quad h_R = \frac{p_R}{\mathrm{Bo}} \left(\frac{J_0\Big(\sqrt{\mathrm{Bo}}\, r\Big)}{J_0\Big(\sqrt{\mathrm{Bo}}\, \alpha_R\Big)} - 1 \right), \tag{3.31a,b}$$

where J_n is the Bessel function of the first kind of order n and the pressures are a linear function of the volume given by

$$p_L = \beta_L\, \widehat{v}_L, \quad p_R = \beta_R\, \widehat{v}_R, \tag{3.32}$$

where $\widehat{v}_R(t)$ now denotes the leading-order volume in the right-hand drop for small ϵ. We note that the Bessel functions are oscillatory, but in general we seek solutions that are truncated so that their height decreases monotonically from the origin. The constants relating the pressure to the volume in the left- and right-hand drops are defined as

$$\beta_L = \frac{\mathrm{Bo}\, J_0\Big(\sqrt{\mathrm{Bo}}\, \alpha_L\Big)}{\pi \alpha_L^2 J_2\Big(\sqrt{\mathrm{Bo}}\, \alpha_L\Big)}, \quad \beta_R = \frac{\mathrm{Bo}\, J_0\Big(\sqrt{\mathrm{Bo}}\, \alpha_R\Big)}{\pi \alpha_R^2 J_2\Big(\sqrt{\mathrm{Bo}}\, \alpha_R\Big)}. \tag{3.33a,b}$$

The contact angles (as a function of the drop volumes) are given by

$$\theta_L = \delta \frac{\sqrt{\mathrm{Bo}}\, J_1\Big(\sqrt{\mathrm{Bo}}\, \alpha_L\Big)}{\pi \alpha_L^2 J_2\Big(\sqrt{\mathrm{Bo}}\, \alpha_L\Big)} \widehat{v}_L, \quad \theta_R = \delta \frac{\sqrt{\mathrm{Bo}}\, J_1\Big(\sqrt{\mathrm{Bo}}\, \alpha_R\Big)}{\pi \alpha_R^2 J_2\Big(\sqrt{\mathrm{Bo}}\, \alpha_R\Big)} \widehat{v}_R. \tag{3.34a,b}$$

Since the square root of the Bond number appears in the argument of the Bessel functions in (3.31), (3.33) and (3.34), they have an imaginary argument when the liquid in the circuit is denser than the overlaying liquid (*i.e.* Bo < 0). In this case the solution may be written in terms of modified Bessel functions; these give a profile which decreases monotonically from the origin, unlike the original Bessel functions which are oscillatory as described above. For Bo < 0 the solutions of (3.29) are given by

$$h_L = \frac{p_L}{|\mathrm{Bo}|}\left(1 - \frac{I_0\Big(\sqrt{|\mathrm{Bo}|}\, r\Big)}{I_0\Big(\sqrt{|\mathrm{Bo}|}\, \alpha_L\Big)}\right), \quad h_R = \frac{p_R}{|\mathrm{Bo}|}\left(1 - \frac{I_0\Big(\sqrt{|\mathrm{Bo}|}\, r\Big)}{I_0\Big(\sqrt{|\mathrm{Bo}|}\, \alpha_R\Big)}\right), \quad (3.35\text{a,b})$$

where I_n is the modified Bessel function of the first kind of order n and the constants relating the pressure to the volume in the left- and right-hand drops are now defined as

$$\beta_L = \frac{|\mathrm{Bo}|\, I_0\Big(\sqrt{|\mathrm{Bo}|}\, \alpha_L\Big)}{\pi \alpha_L^2 I_2\Big(\sqrt{|\mathrm{Bo}|}\, \alpha_L\Big)}, \quad \beta_R = \frac{|\mathrm{Bo}|\, I_0\Big(\sqrt{|\mathrm{Bo}|}\, \alpha_R\Big)}{\pi \alpha_R^2 I_2\Big(\sqrt{|\mathrm{Bo}|}\, \alpha_R\Big)}. \quad (3.36\text{a,b})$$

The contact angles (as a function of the drop volumes) are now defined as

$$\theta_L = \delta \frac{\sqrt{|\mathrm{Bo}|}\, I_1\Big(\sqrt{|\mathrm{Bo}|}\, \alpha_L\Big)}{\pi \alpha_L^2 I_2\Big(\sqrt{|\mathrm{Bo}|}\, \alpha_L\Big)} \widehat{v}_L, \quad \theta_R = \delta \frac{\sqrt{|\mathrm{Bo}|}\, I_1\Big(\sqrt{|\mathrm{Bo}|}\, \alpha_R\Big)}{\pi \alpha_R^2 I_2\Big(\sqrt{|\mathrm{Bo}|}\, \alpha_R\Big)} \widehat{v}_R. \quad (3.37\text{a,b})$$

For completeness we note that when Bo $= 0$ the profiles are given by

$$h_L = \frac{p_L}{4}\left(\alpha_L^2 - r^2\right), \quad h_R = \frac{p_R}{4}\left(\alpha_R^2 - r^2\right), \quad (3.38\text{a,b})$$

where $p_L = 8/\pi\, \widehat{v}_L$ and $p_R = 8/\pi\, \widehat{v}_R$ and the contact angles are $\theta_L = 4/\pi\delta\alpha_L\, \widehat{v}_L$ and $\theta_L = 4/\pi\delta\alpha_R\, \widehat{v}_R$.

Some examples of the possible drop profiles are shown in Figure 3.3a. When the Bond number is positive, the profile is flatter near the edges with a bulge in the middle; when Bo < 0 the profile tends to flatten out. We note that when Bo < 0, β_L and β_R are always positive, as are θ_L and θ_R. We do not allow for solutions with either negative drop thicknesses or negative pressures anywhere. Now it follows

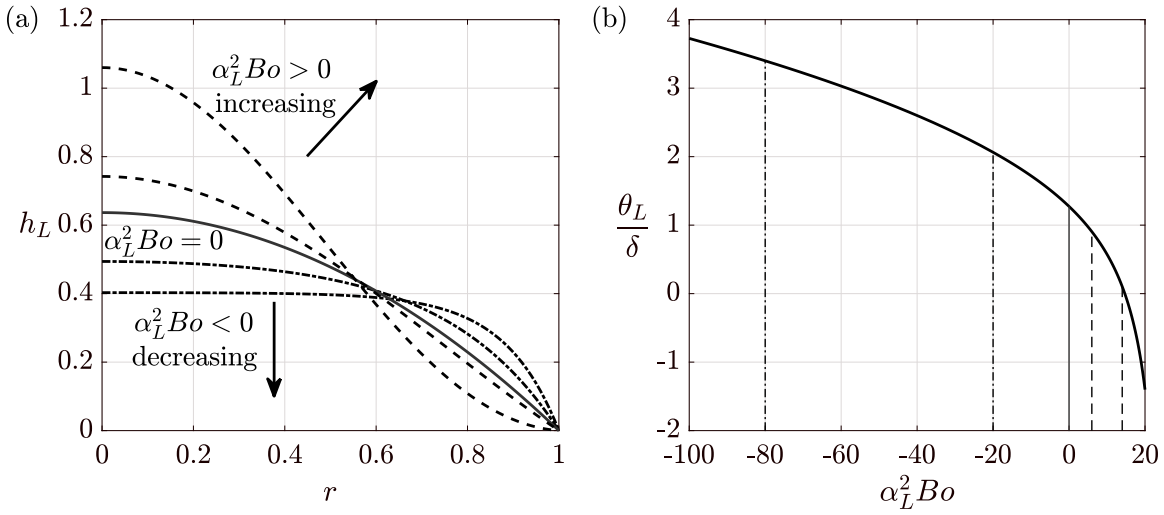


Figure 3.3: (a) Plots of the interface profile in the drop region for $\alpha_L^2 \mathrm{Bo} = -50$, -20, 0, 6, 14, with $\widehat{v}_L = \alpha_L^3$. The profiles corresponding to the positive and negative Bond numbers are given by (3.31a) (dashed lines) and (3.35a) (dotted lines) respectively. For $\mathrm{Bo} = 0$ the profile is given by (3.38a) (solid line). (b) The contact angle given by (3.34a) and (3.37a) with the values corresponding to the profiles in (a) indicated.

from (3.31) and (3.33) that h_L, h_R, p_L and p_R are everywhere positive if and only if $\alpha_L\sqrt{\mathrm{Bo}} < \lambda$ and $\alpha_R\sqrt{\mathrm{Bo}} < \lambda$, where $\lambda \approx 2.405$ is the smallest positive root of J_0. There is therefore a critical Bond number $\mathrm{Bo}_C = \min\left(\lambda^2/\alpha_R, \lambda^2/\alpha_L\right)$ beyond which at least one of the leading-order quasi-steady solutions above would cease to exist and we note that there is an entirely equivalent restriction on pendant rivulets [91]. However, we must also ensure that the contact line remains pinned, *i.e.* that the contact angle remains between the receding and advancing values. This constraint is even more restrictive than the one on the Bond number, and best addressed once we have derived the corresponding leading-order solutions in the conduit and junction region, so we defer a discussion until later (see section §3.3.8).

3.3.3 Quasi-steady solution in the conduit

The footprint of the conduit is a rectangle of width 2ϵ and length 1. On the long edges of the conduit the interface will have zero height where the contact line is pinned. The appropriate boundary condition at the ends will be derived below by matching with

the junction regions. As with the solution in the drops, we note that the problem of flow in a fluid rivulet has also been well studied, see, for example, [91, 120]. Earlier we deduced that we need $h \sim \epsilon^2$ in order for the pressure difference between the drops to be the dominant mechanism driving the flow. Thus, we rescale the governing equations with

$$y = \epsilon\,\widehat{y}, \quad h = \epsilon^2\,h_C. \tag{3.39}$$

Expanding $p_1 \sim p_C(x, \widehat{y}, t)$ for the conduit as $\epsilon \to 0$ in (3.20) then gives

$$\frac{\partial h_C}{\partial t} \sim \epsilon^4 \frac{\partial}{\partial x}\left(h_C^3 \frac{\partial p_C}{\partial x}\right) + \epsilon^2 \frac{\partial}{\partial \widehat{y}}\left(h_C^3 \frac{\partial p_C}{\partial \widehat{y}}\right). \tag{3.40}$$

Provided $t \gg t_{CW} \sim \epsilon^{-2}$ and requiring p_C regular as $h_C \to 0$, the pressure is then spatially uniform in each x-plane at leading order. Similarly expanding (3.18) then gives

$$\frac{\partial^2 h_C}{\partial \widehat{y}^2} = -p_C \quad \text{for } -1 < \widehat{y} < 1. \tag{3.41}$$

We note that the effects of gravity do not enter at leading order for $\mathrm{Bo} = \mathrm{O}(1)$. Since $h_C = 0$ at $\widehat{y} = \pm 1$ for $0 < x < 1$, we deduce that the interface height has a parabolic profile in each cross-section given by

$$h_C = \frac{p_C}{2}\left(1 - \widehat{y}^2\right). \tag{3.42}$$

It follows from (3.25) that the corresponding leading order expressions for the area and flux in the conduit are given by

$$\widehat{A} \sim \frac{2}{3}\epsilon^3 p_C, \quad \widehat{Q} \sim -\frac{1}{35}\epsilon^7 \frac{\partial}{\partial x}\left(p_C^4\right) \quad \text{as } \epsilon \to 0. \tag{3.43a,b}$$

3.3.4 Quasi-steady solution in the junction regions

The junction regions, which connect the conduit to the drops, are indicated by the boxes in Figure 3.2. Without loss of generality we will consider only the junction connecting the conduit to the left drop. Since the film thickness and contact angle are of O(1) in the drop and of $\mathrm{O}(\epsilon^2)$ in the conduit we choose an intermediate height

scale in the junction, the pertinent scalings in the left-hand junction region are given by

$$x = \epsilon\widetilde{x}, \quad y = \epsilon\widetilde{y}, \quad h = \epsilon\widetilde{h}. \tag{3.44}$$

The contact line of the left-hand drop then satisfies

$$\left(\epsilon\widetilde{x} + \sqrt{\alpha_L^2 - \epsilon^2}\right)^2 + \epsilon^2\widetilde{y}^2 = \alpha_L^2 \quad \text{for } \widetilde{x} \leq 0, \tag{3.45}$$

so that it lies at $\widetilde{x} = 0$ for $|\widetilde{y}| \geq 1$ at leading order as $\epsilon \to 0$ with $\widetilde{y} = \mathrm{O}(1)$. The leading-order geometry of the contact set in the junction region is therefore as illustrated in Figure 3.4: the contact set of the drop fills the left half-plane $\widetilde{x} < 0$, while that of the conduit fills the semi-infinite strip $|\widetilde{y}| < 1$, $\widetilde{x} \geq 0$. The interface height in the junction region is governed by (3.20), with the solution needing to match with the conduit solution (3.42) as $\widetilde{x} \to \infty$ and with the drop solution (3.31) as $\widetilde{x}^2 + \widetilde{y}^2 \to \infty$ in the left half-plane, with (3.21) still holding on the contact lines at $\widetilde{x} = 0$, $|\widetilde{y}| \geq 1$.

We consider the timescale $t \gg t_J \sim \epsilon$, so that the governing equation (3.20) is quasi-steady. The disparity in the film thicknesses in the drop, junction and conduit regions (where h is of O(1), of O(ϵ) and of O(ϵ^2), respectively) means that we must now proceed to second-order in the analysis to span these length scales: expanding $\widetilde{h} \sim \widetilde{h}_0(\widetilde{x}, \widetilde{y}, t) + \epsilon\widetilde{h}_1(\widetilde{x}, \widetilde{y}, t)$ and $p \sim p_{JL}(\widetilde{x}, \widetilde{y}, t)$ as $\epsilon \to 0$, we find that $\widetilde{h}_0$ and $\widetilde{h}_1$ satisfy the leading- and second-order problems summarised in Figure 3.4 in which we have also recorded the boundary conditions on the contact line and the far-field conditions that must be imposed in order to match with the adjoining drop and conduit. The mean curvature of the leading-order film thickness is equal to zero because the leading-order pressure appears first in the second-order problem for the correction to the film thickness. We note that if the leading-order pressure were an order of magnitude larger then it would not be possible to match it with the pressures in the adjoining drop and conduit (as shown below in (3.64)); nor would it be possible

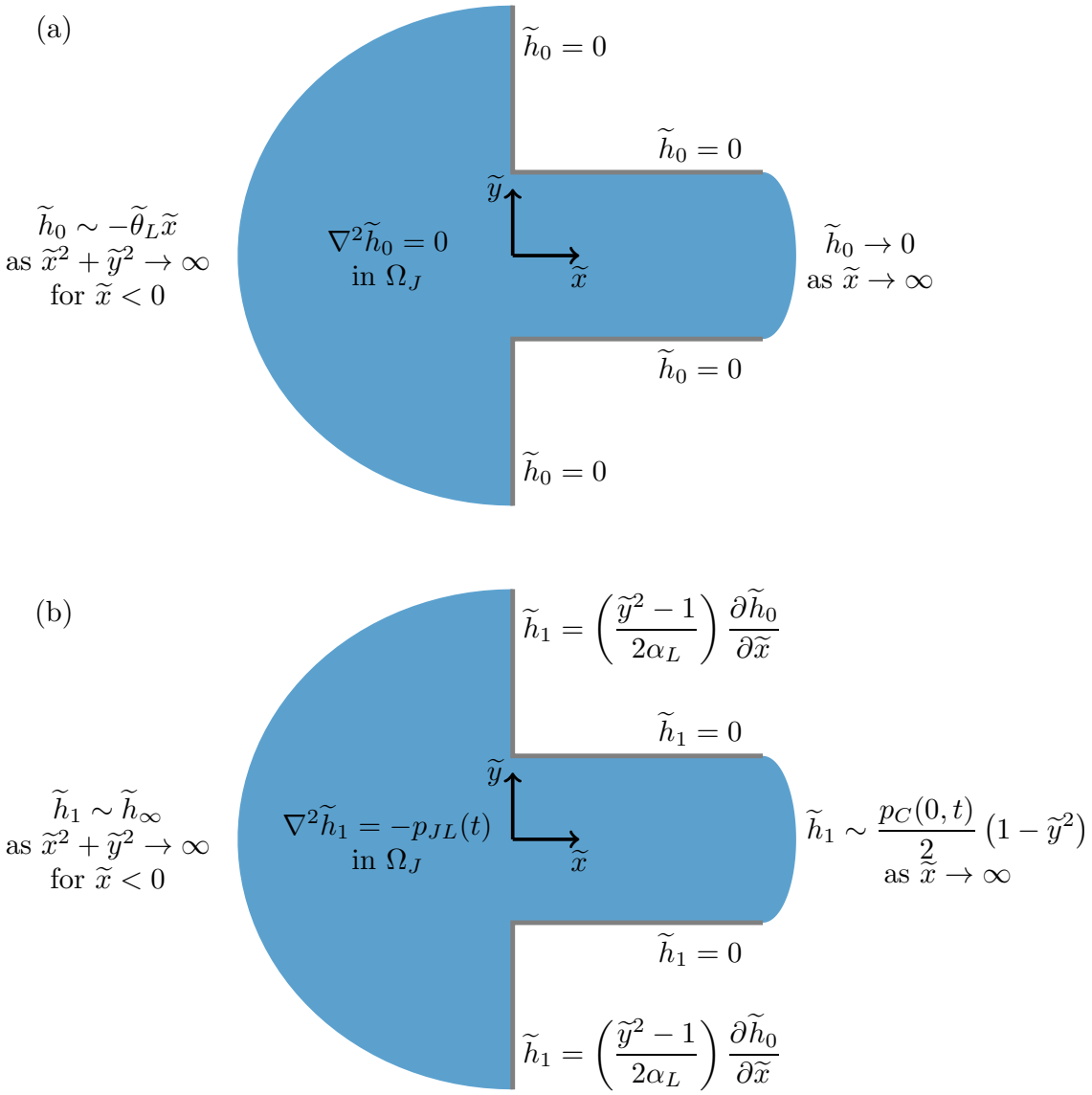


Figure 3.4: (a) The leading-order problem in the junction region. (b) The second-order problem in the junction region, where $\widetilde{h}_\infty = \widetilde{\theta}_L \left(\widetilde{x}^2 - \widetilde{y}^2\right) / \left(2\,\alpha_L\right) - p_L \widetilde{x}^2/2$. The junction region is defined as $\Omega_J = \{(\widetilde{x}, \widetilde{y}) : \ \widetilde{x} < 0\} \cup \{(\widetilde{x}, \widetilde{y}) : \ |\widetilde{y}| < 1, \ \widetilde{x} \geq 0\}$. See text for details and the derivation of the boundary conditions.

to match the leading-order film thickness with that in the drop (because this requires the leading-order film profile to be linear in the far-field).

At leading order the height is zero on the contact line (given by (3.21)) and also tends to zero in the conduit as $\widetilde{x} \to \infty$ since the interface height is of $\mathrm{O}(\epsilon)$ there. In the junction region, the radial distance from the centre of the circular contact set of

the drop (see (3.45)) can be written as

$$r = \sqrt{\left(\epsilon\widetilde{x} + \sqrt{\alpha_L^2 - \epsilon^2}\right)^2 + \epsilon^2\widetilde{y}^2}. \tag{3.46}$$

Substituting (3.46) into the left-hand drop solution (3.31a) and expanding as $\epsilon \to 0$ gives

$$h_L = -\epsilon\widetilde{\theta}_L\,\widetilde{x} + \epsilon^2\widetilde{\theta}_L\left(\frac{\widetilde{x}^2 - \widetilde{y}^2 + 1}{2\,\alpha_L} - \frac{p_L}{2}\,\widetilde{x}^2\right) + \mathrm{O}\big(\epsilon^3\big)\,, \tag{3.47}$$

where the leading-order contact angle $\widetilde{\theta}_L$ is given by

$$\widetilde{\theta}_L = \frac{J_1\Big(\sqrt{\mathrm{Bo}}\,\alpha_L\Big)}{\sqrt{\mathrm{Bo}}\,J_0\Big(\sqrt{\mathrm{Bo}}\,\alpha_L\Big)}p_L. \tag{3.48}$$

The leading-order far-field boundary condition is found by matching the interface height in the junction with the leading-term in (3.47) as $\widetilde{x}^2 + \widetilde{y}^2 \to \infty$ for $\widetilde{x} < 0$. Similarly, the next-order interface height in the junction $\widetilde{h}_1$ matches with the $\mathrm{O}(\epsilon^2)$ term in (3.47), noting that only the $\widetilde{x}$ and $\widetilde{y}$ terms are retained since we are just concerned with the limit $\widetilde{x}^2 + \widetilde{y}^2 \to \infty$.

At second order the interface height is still zero on the contact line in the conduit, but on $\widetilde{x} = 0$ we have to take account of the curvature of the contact line. For $\widetilde{x} \le 0$ the contact line (3.45) satisfies

$$\widetilde{x} = \frac{\sqrt{\alpha_L^2 - \epsilon^2\widetilde{y}^2} - \sqrt{\alpha_L^2 - \epsilon^2}}{\epsilon}. \tag{3.49}$$

Substituting this into $\widetilde{h}(\widetilde{x}, \widetilde{y}, t) = 0$ and expanding as $\epsilon \to 0$ gives the boundary condition

$$\widetilde{h}_0(0, \widetilde{y}, t) + \epsilon\left(\widetilde{h}_1(0, \widetilde{y}, t) - \left(\frac{\widetilde{y}^2 - 1}{2\alpha_L}\right)\frac{\partial\widetilde{h}_0}{\partial\widetilde{x}}\right) + \mathrm{O}\big(\epsilon^2\big) = 0 \quad \text{on } \widetilde{x} = 0. \tag{3.50}$$

In the conduit the far-field condition comes from matching with the conduit solution (3.42). To find the leading-order far-field condition in the drop we expanded (3.31a) as $r \to \alpha_L^-$: the next term in this expansion gives the far-field condition at second order, and thus the function $\widetilde{h}_\infty$.

The boundary value problems in Figure 3.4 may be solved using standard conformal mapping techniques. A Schwarz-Christoffel transformation maps the upper half of the ζ-plane to a polygon in the complex ω-plane, where we let $\omega = \widetilde{x} + i\widetilde{y}$ and $\zeta = \xi + i\eta$. As described in Driscoll (1996) [36], if the polygon has vertices $\omega_1, \ldots, \omega_n$ and interior angles $\alpha_1\pi, \ldots, \alpha_n\pi$ in counter-clockwise order, the transformation is given by

$$\omega = f(\zeta) = A + C \int \prod_{k=1}^{n-1} (\zeta - \zeta_k)^{\alpha_k - 1} \, \mathrm{d}\zeta, \tag{3.51}$$

for some complex constants A and C, where $\omega_k = f(\zeta_k)$ for $k = 1, \ldots, n-1$ and $f(\infty) = \omega_n$. Under a conformal mapping, harmonic functions remain harmonic, so solving Laplace's equation in the interior of a polygon is equivalent to solving Laplace's equation in the upper half-plane, where the boundary data on the real line is found by transforming the boundary conditions of the original problem. The junction can be thought of as a polygon with some of its vertices at infinity. The interior angles at the corners $\omega = \pm i$ are $3\pi/2$, while in the far-field of the conduit as $\widetilde{x} \to \infty$ the interior angle is zero. The transform $\omega = f(\zeta)$ maps the upper half ζ-plane to the junction region in the ω-plane and is then given by

$$\omega = f(\zeta) = A + C \int \frac{\sqrt{\zeta - 1}\sqrt{\zeta + 1}}{\zeta} \, \mathrm{d}\zeta \tag{3.52}$$

$$= \frac{2i}{\pi} \left(\sqrt{\zeta^2 - 1} + \sin^{-1}\left(\frac{1}{\zeta}\right) \right), \tag{3.53}$$

where A and C have been chosen so that $f(i) = 1$, $f(-i) = -1$ and $f(0) = \infty$, *i.e.* the origin in the ζ-plane is transformed to the far-field of the conduit. The transform is illustrated in Figure 3.5. The contact line in the junction region Ω_J is transformed to the real line $\eta = 0$ in the ζ-plane, where the far-field of the conduit ($\widetilde{x} \to \infty$) is transformed to the origin, the edge of the conduit ($|\widetilde{y}| = 1$ for $\widetilde{x} > 0$) is transformed to $0 < |\xi| \leq 1$ and the edge of the drop ($\widetilde{x} = 0$ for $|\widetilde{y}| > 1$) is transformed to $|\xi| > 1$.

Matching with the drop region requires us to expand the transform (3.53) at

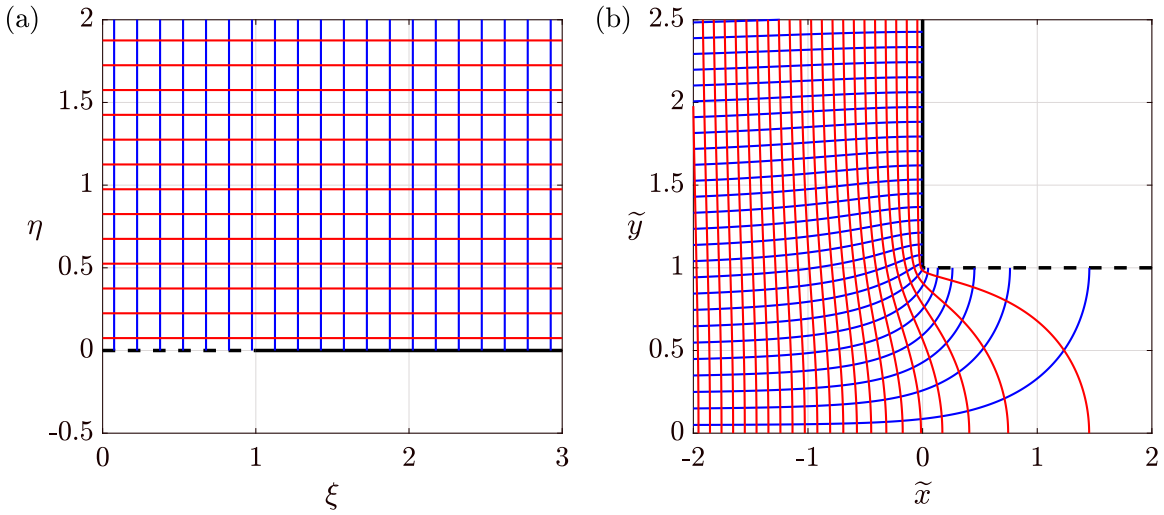


Figure 3.5: The map given by (3.53) maps the upper half ζ-plane (a) to the junction region in the ω-plane (b). The solid line corresponds to the edge of the drop and the dashed line to the edge of the conduit. In the ζ-plane the line of symmetry is on $\xi = 0$ and in the ω-plane the line of symmetry is on $\widetilde{y} = 0$ with the conduit extending along the $\widetilde{x}$-axis.

infinity which gives

$$\omega \sim \frac{2i}{\pi}\zeta \quad \text{as } |\zeta| \to \infty. \tag{3.54}$$

In the original geometry, the far-field drop boundary condition can be written as $\widetilde{h}_0 \sim -\widetilde{\theta}_L \widetilde{x} = \mathrm{Re}(-\widetilde{\theta}_L \omega)$. Thus, it follows the leading-order mapped problem is given by

$$\nabla^2 \widetilde{h}_0 = 0 \qquad \text{for } \eta > 0, \tag{3.55}$$

$$\widetilde{h}_0 = 0 \qquad \text{on } \eta = 0, \tag{3.56}$$

$$\widetilde{h}_0 \sim -\mathrm{Re}\left(\frac{2i\widetilde{\theta}_L}{\pi}\zeta\right) \quad \text{as } \xi^2 + \eta^2 \to \infty. \tag{3.57}$$

In the ζ-plane the solution is given by

$$\widetilde{h}_0 = \frac{2\widetilde{\theta}_L}{\pi}\eta. \tag{3.58}$$

Hence, in the ω-plane we find the leading-order solution to be given implicitly by

$$\widetilde{h}_0 = \frac{2\widetilde{\theta}_L}{\pi}\,\mathrm{Im}\left(f^{-1}(\omega)\right). \tag{3.59}$$

At leading order, for $t \gg t_J \sim \epsilon$, the thin-film equation (3.20) is given by

$$\nabla \cdot \left(\widetilde{h}_0^3 \nabla p_{JL} \right) = 0 \quad \text{for } (\widetilde{x}, \widetilde{y}) \in \Omega_J, \tag{3.60}$$

where $\Omega_J = \{(\widetilde{x}, \widetilde{y}) : \ \widetilde{x} < 0\} \cup \{(\widetilde{x}, \widetilde{y}) : \ |\widetilde{y}| < 1, \ \widetilde{x} \geq 0\}$ is illustrated in Figure 3.4. On the contact line (3.21b) gives

$$\left(h_0^3 \nabla p_{JL} \right) \cdot \boldsymbol{\nu} = 0 \quad \text{for } (\widetilde{x}, \widetilde{y}) \in \partial\Omega_J, \tag{3.61}$$

where $\partial\Omega_J = \{(\widetilde{x}, \widetilde{y}) : \ \widetilde{x} = 0, |\widetilde{y}| \geq 1\} \cup \{(\widetilde{x}, \widetilde{y}) : \ \widetilde{x} > 0, |\widetilde{y}| = 1\}$ as illustrated in Figure 3.4 and $\boldsymbol{\nu}$ is the outward pointing normal on $\partial\Omega_J$ in the $(\widetilde{x}, \widetilde{y})$-plane. The pressure matches with the drop and conduit pressures in the far-field as follows:

$$p_{JL} \to p_C(0, t) \quad \text{as } \widetilde{x} \to \infty, \tag{3.62}$$

$$p_{JL} \to p_L(t) \qquad \text{as } \widetilde{x}^2 + \widetilde{y}^2 \to \infty \text{ for } \widetilde{x} < 0. \tag{3.63}$$

Since the boundary value problem (3.60)–(3.63) has at most one solution, it is given by the obvious one, namely the spatially uniform one in which $p_{JL} = p_{JL}(t)$; we deduce that the pressure passes straight through the junction at leading order, *i.e.*

$$p_{JL}(t) = p_L(t) = p_C(0, t). \tag{3.64}$$

To find the next order solution we first subtract from $\widetilde{h}_1$ the far-field solution in the drop as $\widetilde{x}^2 + \widetilde{y}^2 \to \infty$, so that we are again solving Laplace's equation in the junction region, *i.e.* we set

$$\widetilde{h}_1 = \widetilde{H}_1 + \frac{\widetilde{\theta}_L}{2\alpha_L} \left(\widetilde{x}^2 - \widetilde{y}^2 + \frac{\pi^2 - 2}{\pi^2} \right) - \frac{p_L}{2} \widetilde{x}^2. \tag{3.65}$$

The governing equations are now

$$\nabla^2 \widetilde{H}_1 = 0 \qquad \text{in } \Omega_J, \tag{3.66}$$

$$\widetilde{H}_1 \sim \frac{\alpha_L p_L - \widetilde{\theta}_L}{2\alpha_L} \widetilde{x}^2 \qquad \text{as } \widetilde{x} \to \infty, \text{ for } |\widetilde{y}| < 1 \tag{3.67}$$

$$\widetilde{H}_1 = \frac{\alpha_L p_L - \widetilde{\theta}_L}{2\alpha_L} \widetilde{x}^2 + \frac{\widetilde{\theta}_L}{\pi^2 \alpha_L} \qquad \text{on } |\widetilde{y}| = 1 \text{ for } \widetilde{x} > 0, \tag{3.68}$$

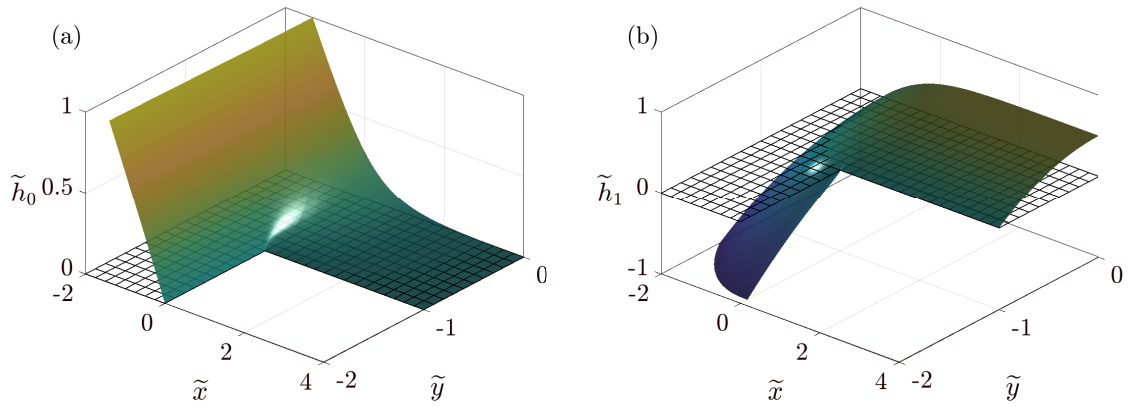


Figure 3.6: Plots of the leading-order solution and the second-order correction in the junction region for $\mathrm{Bo} = 8$ and $\alpha_L = 0.5$. The location of the substrate is indicated by the grid with the conduit extending in the positive $\widetilde{y}$-direction. (a) The leading-order solution given by (3.59). (b) The second-order solution given by (3.65) and (3.80).

$$\widetilde{H}_1 = \frac{\widetilde{y}^2 - 1}{2\alpha_L}\left(\widetilde{\theta}_L + \frac{\partial \widetilde{h}_0}{\partial \widetilde{x}}\right) + \frac{\widetilde{\theta}_L}{\pi^2 \alpha_L} \quad \text{on } \widetilde{x} = 0 \text{ for } |\widetilde{y}| > 1, \tag{3.69}$$

$$\widetilde{H}_1 \to 0 \qquad \text{as } \widetilde{x}^2 + \widetilde{y}^2 \to \infty \text{ for } \widetilde{x} < 0, \tag{3.70}$$

where $\widetilde{h}_0$ is given by (3.59) and the derivative on the boundary is given by

$$\frac{\partial \widetilde{h}_0}{\partial \widetilde{x}}(0, \widetilde{y}, t) = -\frac{\widetilde{\theta}_L |\xi|}{\sqrt{\xi^2 - 1}} \quad \text{for } |\xi| > 1, \tag{3.71}$$

where $\widetilde{y} = f(\xi)$. We then use the conformal mapping $\omega = f(\zeta)$ to transform this problem to the upper-half plane. To determine the boundary conditions in the ζ-plane we need to examine the transform (3.53) more closely. We first note that there is a logarithmic singularity near the origin: expanding (3.53) at the origin we find that

$$f(\zeta) = -\frac{2}{\pi}\log(\zeta) + i + \mathrm{O}\big(\zeta^2\big) \tag{3.72}$$

as $\zeta \to 0$. On $\eta = 0$ the map (3.53) can be split into real and imaginary parts as follows

$$f(\xi) = \begin{cases} -\dfrac{2}{\pi}\left(\sqrt{1-\xi^2} - \log\left(\dfrac{\sqrt{1-\xi^2}+1}{|\xi|}\right)\right) + i & \text{for } |\xi| \le 1, \\ \dfrac{2i}{\pi}\left(\sqrt{\xi^2 - 1} + \sin^{-1}\left(\dfrac{1}{|\xi|}\right)\right) & \text{for } |\xi| > 1. \end{cases} \tag{3.73}$$

Using (3.72) and (3.73) and the expression $\mathrm{Re}(\omega^2) = \mathrm{Re}(f(\zeta)^2)$, the problem (3.66)–(3.70) may then be mapped to the following problem in the upper-half ζ-plane:

$$\nabla^2 \widetilde{H}_1 = 0 \qquad \text{for } \eta > 0, \tag{3.74}$$

$$\widetilde{H}_1 = \mathscr{U}(\xi) \qquad \text{on } \eta = 0 \text{ for } \xi \neq 0, \tag{3.75}$$

$$\widetilde{H}_1 \sim \mathrm{Re}(\mathscr{W}(\zeta)) \quad \text{as } \xi^2 + \eta^2 \to 0, \tag{3.76}$$

$$\widetilde{H}_1 \to 0 \qquad \text{as } \xi^2 + \eta^2 \to \infty, \tag{3.77}$$

where $\mathscr{U}$ is given by

$$\mathscr{U}(\xi) = \begin{cases} \dfrac{2\left(\alpha_L p_L - \widetilde{\theta}_L\right)}{\pi^2 \alpha_L} \left(\sqrt{1-\xi^2} - \log\left(\dfrac{\sqrt{1-\xi^2}+1}{|\xi|} \right) \right)^2 + \dfrac{\widetilde{\theta}_L}{\pi^2 \alpha_L} \\ \qquad\qquad \text{for } |\xi| \leq 1, \\ \dfrac{2\widetilde{\theta}_L}{\pi^2 \alpha_L} \left(\left(\sqrt{\xi^2-1} + \sin^{-1}\left(\dfrac{1}{|\xi|} \right) \right)^2 - \dfrac{\pi^2}{4} \right) \left(1 - \dfrac{|\xi|}{\sqrt{\xi^2-1}} \right) + \dfrac{\widetilde{\theta}_L}{\pi^2 \alpha_L} \\ \qquad\qquad \text{for } |\xi| > 1 \end{cases} \tag{3.78}$$

and $\mathscr{W}$ is given by

$$\mathscr{W}(\zeta) = \frac{2\left(\alpha_L p_L - \widetilde{\theta}_L\right)}{\pi^2 \alpha_L} \left(\log(\zeta) - i\pi \right) \log(\zeta) \,. \tag{3.79}$$

The solution to Laplace's equation in a half-space with Dirichlet boundary data is well known [85]: using a Fourier transform the solution for $\eta > 0$ can be written as

$$\widetilde{H}_1(\xi, \eta, t) = \frac{\eta}{\pi} \int_{-\infty}^{\infty} \frac{\mathscr{U}(s)}{\eta^2 + (s-\xi)^2} \, \mathrm{d}s. \tag{3.80}$$

Numerical methods are required to evaluate the integral in (3.80). Since $\mathscr{U}(\xi)$ is an even function we can write the solution in the form

$$\widetilde{H}_1(\xi, \eta, t) = \frac{\eta}{\pi} \left(\mathcal{H}(\xi, \eta, t) + \mathcal{H}(-\xi, \eta, t) \right), \tag{3.81}$$

where

$$\mathcal{H}(\xi, \eta, t) = \int_{0}^{\infty} \frac{\mathscr{U}(s)}{\eta^2 + (s-\xi)^2} \, \mathrm{d}s. \tag{3.82}$$

We first split this integral at the points $\xi = 1$ and $\xi = N_\infty$, so that

$$\mathcal{H} = \int_0^1 \frac{\mathscr{U}(s)}{\eta^2 + (s-\xi)^2}\,\mathrm{d}s + \int_1^{N_\infty} \frac{\mathscr{U}(s)}{\eta^2 + (s-\xi)^2}\,\mathrm{d}s + \int_{N_\infty}^{\infty} \frac{\mathscr{U}(s)}{\eta^2 + (s-\xi)^2}\,\mathrm{d}s, \quad (3.83)$$

where $N_\infty \gg 1$ is some suitably chosen number as we shall shortly discuss. We evaluate each of the integrals in (3.83) separately.

On the interval $[0, 1]$ we write the integral as

$$\int_0^1 \frac{\mathscr{U}(s)}{\eta^2 + (s-\xi)^2}\,\mathrm{d}s = \int_0^1 \frac{\mathscr{U}(s)}{\eta^2 + (s-\xi)^2} - \frac{\mathscr{V}(s)}{\eta^2 + \xi^2}\,\mathrm{d}s + \int_0^1 \frac{\mathscr{V}(s)}{\eta^2 + \xi^2}\,\mathrm{d}s, \quad (3.84)$$

where the function $\mathscr{V}(s)/(\eta^2 + \xi^2)$ is the leading term in the small s expansion of the integrand in (3.80), namely

$$\mathscr{V} = \frac{2\alpha_L p_L - \widetilde{\theta}_L - 2\left(\alpha_L p_L - \widetilde{\theta}_L\right)\left(\log\left(\frac{s}{2}\right) + 2\right)\log\left(\frac{s}{2}\right)}{\pi^2 \alpha_L}. \quad (3.85)$$

Written in this form the first term on the right-hand side of (3.84) has a bounded integrand and can be computed numerically, more on which shortly. The second term on the right-hand side of (3.84) can be computed exactly and is given by

$$\int_0^1 \frac{\mathscr{V}(s)}{\eta^2 + \xi^2}\,\mathrm{d}s = \frac{2\alpha_L p_L - \widetilde{\theta}_L + 2\left(\alpha_L p_L - \widetilde{\theta}_L\right)\log(2)^2}{\pi^2 \alpha_L\,(\eta^2 + \xi^2)}. \quad (3.86)$$

On the interval $[1, N_\infty]$ the function $\mathscr{U}(s)$ is bounded for all N_∞ and the second integral in (3.83) must be computed numerically. On the interval $[1, N_\infty]$ we first find the far-field Laurent expansion of the integrand in (3.80); we can then integrate each of the terms in the expansion exactly. The first few terms in the expansion give

$$\int_{N_\infty}^{\infty} \frac{\mathscr{U}(s)}{\eta^2 + (s-\xi)^2}\,\mathrm{d}s = \frac{(\pi^2 - 7)\,\widetilde{\theta}_L}{4\pi^2 \alpha_L}\left(\frac{1}{3N_\infty^3} + \frac{\xi}{2N_\infty^4}\right) + \mathrm{O}\left(\frac{1}{N_\infty^5}\right). \quad (3.87)$$

The integrals that require quadrature, namely the first term on the right-hand side of (3.84) and the second term on the right-hand side of (3.83), are found in MATLAB using the *integral* function. The accuracy of these integrals is determined by setting the relative and absolute tolerances as part of the function input [103]. By choosing

N_∞ and the number of terms in the Laurent expansion (3.87), we can then compute (3.80) to the same accuracy.

An example of the leading- and second-order solutions are shown in Figure 3.6. As we approach the corner along the contact line the slope of both these solutions becomes infinite. Expanding (3.59) around the point $\omega = \widetilde{r}e^{i\phi} - i$ (*i.e.* the corner at $(\widetilde{x}, \widetilde{y}) = (0, -1)$) gives

$$\widetilde{h}_0 \sim \frac{3\widetilde{\theta}_L}{2\sqrt{2}}\widetilde{r}^{\frac{2}{3}} \sin\frac{2\phi}{3} \quad \text{as } \widetilde{r} \to 0. \tag{3.88}$$

The singularities in the gradient at the corners will have implications for the pinning of the contact line as we shall discuss in §3.3.8.

3.3.5 Conduit relaxation

As detailed in §3.3, the conduit is quasi-steady for $t_{CL} \gg \epsilon^{-4}$, *i.e.* it relaxes to its quasi-steady profile on the timescale $t_{CL} \sim \epsilon^{-4}$; this was derived from (3.25). Using (3.25) and (3.26) and making the rescaling $t = (70/3)\,\epsilon^{-4}\tau$, we derive an equation for the conduit pressure on the timescale of conduit relaxation:

$$\frac{\partial p_C}{\partial \tau} = \frac{\partial^2}{\partial x^2}\left(p_C^4\right) \quad \text{for } 0 < x < 1,\ \tau > 0. \tag{3.89}$$

This is an example of the porous medium equation in one spatial dimension [124].

In §3.3.4 we deduced that the leading-order pressure in the junction regions is spatially uniform and equal to the pressure in the adjacent drop and conduit as long as $t \gg t_J \sim \epsilon$. Since $t_{CL} \gg t_J$ as $\epsilon \to 0$, the pressure at the ends of the conduit will be equal to the pressure in the corresponding drop. Furthermore, since $t_{DD} \gg t_{CL}$ the leading-order pressure in the drops will not have changed, so the relevant boundary conditions for (3.89) are given by

$$p_C(0, \tau) = p_L(0), \quad p_C(1, \tau) = p_R(0) \quad \text{for } \tau > 0, \tag{3.90a,b}$$

where the pressures in the left- and right-hand drops, p_L and p_R, can be related to their respective volumes, $\widehat{v}_L$ and $\widehat{v}_R$, by (3.33). The problem is closed by prescribing

an initial pressure profile of the form

$$p_C(x,0) = \mathscr{P}(x) \quad \text{for } 0 < x < 1. \tag{3.91}$$

We note that (3.91) is equivalent to prescribing an initial film thickness (as we did initially in (3.22)) since the relationship between the pressure and film thickness in each cross-section is known and given by (3.42). For a positive and sufficiently regular initial profile, we anticipate the long-time attractor to be the steady-state solution, so that

$$p_C \to \left(\left(p_R^4 - p_L^4\right) x + p_L^4\right)^{\frac{1}{4}} \quad \text{as } \tau \to \infty. \tag{3.92}$$

To find the time dependent solution of (3.89) numerical methods are required, which we shall briefly describe. The spatial derivative is approximated using 2nd order central differences. This gives a system of time dependent ODEs which is solved in MATLAB using the built in ODE solver *ODE15s* [104] with the initial pressure given by a straight line. This solver is for stiff problems which this may be when pressure differences are large. Examples of the solution of the time-dependent problem are shown in Figure 3.8a and b (solid lines); they tend to (3.92) (dashed line) as τ increases, and we note that the steady state is reached much faster when the initial pressure gradient is increased.

3.3.6 Droplet drainage

On the timescale of drainage $t_{DD} \sim \epsilon^{-7}$, the pressure in the conduit is quasi-steady and therefore given by the right-hand side of the expressions in (3.92). We can then use relation (3.43b) to find that the flux in the conduit on this timescale is given by

$$\widehat{Q} \sim \epsilon^7 \frac{p_L^4 - p_R^4}{35} \quad \text{as } \epsilon \to 0. \tag{3.93}$$

We defined the fluid volumes in each region in (3.23). Using the leading-order solutions in the drops (3.31)–(3.33) and conduit (3.42) and (3.92) the volumes are given

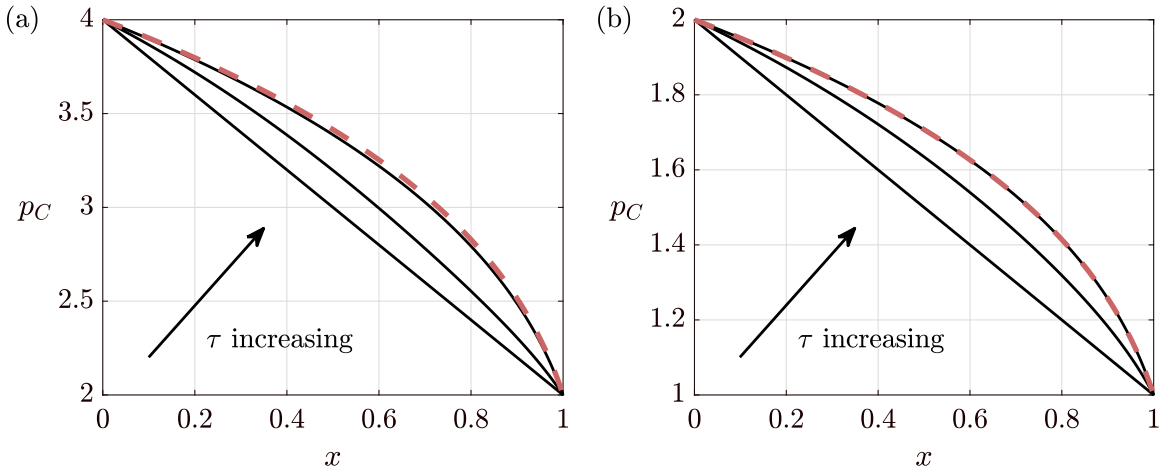


Figure 3.7: Numerical solution of the conduit relaxation problem given by (3.89)–(3.91) for different boundary conditions (drop pressures), where the initial profile is linear. The dashed line is the steady-state solution given by (3.92). In (a) $\tau = 0, 0.0064, 0.0320$, whereas in (b) $\tau = 0, 0.0005, 0.0020$.

by

$$\widehat{v}_L(t) \sim \frac{p_L}{\beta_L}, \quad \widehat{v}_C(t) \sim \epsilon^3 \frac{8\,(p_L^5 - p_R^5)}{15\,(p_L^4 - p_R^4)}, \quad \widehat{v}_R(t) \sim \frac{p_R}{\beta_R}, \tag{3.94a–c}$$

as $\epsilon \to 0$. Note $\widehat{v}_C$ arises from the integral $\int_{-\epsilon}^{\epsilon} \int_0^1 h_C \,\mathrm{d}y \,\mathrm{d}x$ with h_C given by (3.42) in terms of p_C and y, where p_C in turn is given by (3.92). We define V_J to be the volume of the junction region. The junction region scales used in (3.44) show that, at leading order, $V_J = \mathrm{O}(\epsilon^3)$. Thus, when $\epsilon \ll 1$, most of the fluid is contained in the drops, with the conduit containing very little. At leading order the total volume of fluid in the circuit (3.24) is given by

$$\widehat{v}_L + \widehat{v}_R = \widehat{v}_T. \tag{3.95}$$

We can therefore use (3.27) to find ODEs for the volume in each drop. Substituting (3.93) into (3.27) gives

$$\frac{\mathrm{d}\widehat{v}_L}{\mathrm{d}t} \sim -\epsilon^7 \frac{p_L^4 - p_R^4}{35}, \quad \frac{\mathrm{d}\widehat{v}_R}{\mathrm{d}t} \sim \epsilon^7 \frac{p_L^4 - p_R^4}{35} \quad \text{as } \epsilon \to 0. \tag{3.96a,b}$$

Since the drop pressure is a linear function of the volume (with the constants of proportionality given by (3.33)), we can write (3.96) entirely in terms of the drop

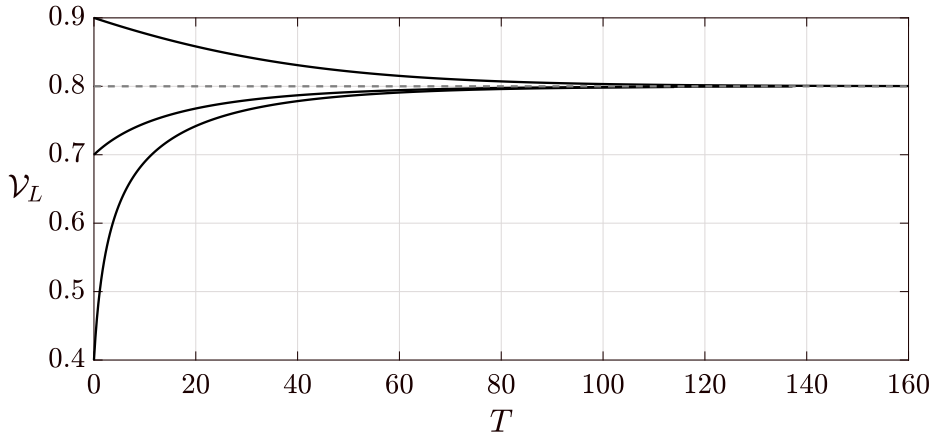


Figure 3.8: The evolution of the left-hand drop volume given by (3.100) for $\widehat{v}_L(T = 0)/\widehat{v}_T = \mathscr{V} = 0.4, 0.7, 0.9$ with $\widehat{v}_T$ the total volume, $\alpha = \beta_L/\beta_R = 0.25$ and noting (3.99) shows these solutions tend to 0.8 for large time.

volumes. If we then rescale time with $t = 35/(\widehat{v}_T^3\beta_R^4)\,\epsilon^{-7}T$, we need only solve a single ordinary differential equation given by

$$\frac{\mathrm{d}\mathcal{V}_L}{\mathrm{d}T} = (1 - \mathcal{V}_L)^4 - \alpha^4\mathcal{V}_L^4, \tag{3.97}$$

where $\alpha = \beta_L/\beta_R$ and $\mathcal{V}_L = \widehat{v}_L/\widehat{v}_T$ is the leading-order rescaled drop volume. To close this problem we will need an initial volume for the left drop of the form

$$\mathcal{V}_L(0) = \mathscr{V}. \tag{3.98}$$

The powers of four in (3.97) suggest that there could be multiple steady-state solutions, but we find that only one of them is real and in the range $[0, \widehat{v}_T]$, so the volume of the left drop can only tend to one value, given by

$$\mathcal{V}_L \to \frac{1}{1+\alpha} \quad \text{as } T \to \infty. \tag{3.99}$$

The equation governing the volume is separable, and with the help of the symbolic mathematics software MATHEMATICA we find an implicit solution of (3.97) to be

given by

$$\log\left(\frac{\left(\mathcal{V}_L-\frac{1}{1-\alpha}\right)^{\frac{(1-\alpha)^2}{4\alpha^3}}\left(\left(\mathcal{V}_L-\frac{2}{1+\alpha^2}\right)\mathcal{V}_L+\frac{1}{1+\alpha^2}\right)^{\frac{1}{2\alpha^2}}}{\left(\mathcal{V}_L-\frac{1}{1+\alpha}\right)^{\frac{(1+\alpha)^2}{4\alpha^3}}}\right) \\ +\frac{(1-\alpha^2)}{4\alpha^3}\arg\left(\frac{-\alpha\mathcal{V}_L+(1-\mathcal{V}_L)\,i}{1-\mathcal{V}_L-\alpha\mathcal{V}_L i}\right)+C=T, \tag{3.100}$$

where C is a constant found from the initial conditions. In the case where $\alpha = 1$, the volumes of the drops each tend to $1/2$ and the solution can be written explicitly as

$$\mathcal{V}_L=\frac{1}{2}\left(1+\frac{1}{\sqrt{Ae^{2T}-1}}\right),\quad A=1+\frac{1}{(2\mathscr{V}-1)^2}. \tag{3.101}$$

Some examples of the evolution of the left-hand drop volume are plotted in Figure 3.8 for different initial volumes.

3.3.7 Numerical validation

In this section we will describe our numerical simulations of the full thin-film boundary value problem given by (3.18) and (3.20)–(3.22) on the domain indicated in Figure 2.1a (for a conduit with a constant width), and compare the results with the asymptotic predictions we have obtained. The numerical simulations are performed in the finite element solver COMSOL Multiphysics® using the thin-film flow toolbox [23]. We specify the initial volumes of the two drops; with this we can form a piecewise approximation to the interface height and pressure using (3.31)–(3.33) in the drops and (3.42) and (3.92) in the conduit. There will be discontinuities in the interface height at either end of the conduit so we initially run the simulation on the junction relaxation timescale t_J to smooth out the initial condition. We use this piecewise construction of the initial condition rather than a composite solution because it is easier to implement and the junction regions relax on a much faster timescale than those we are interested in.

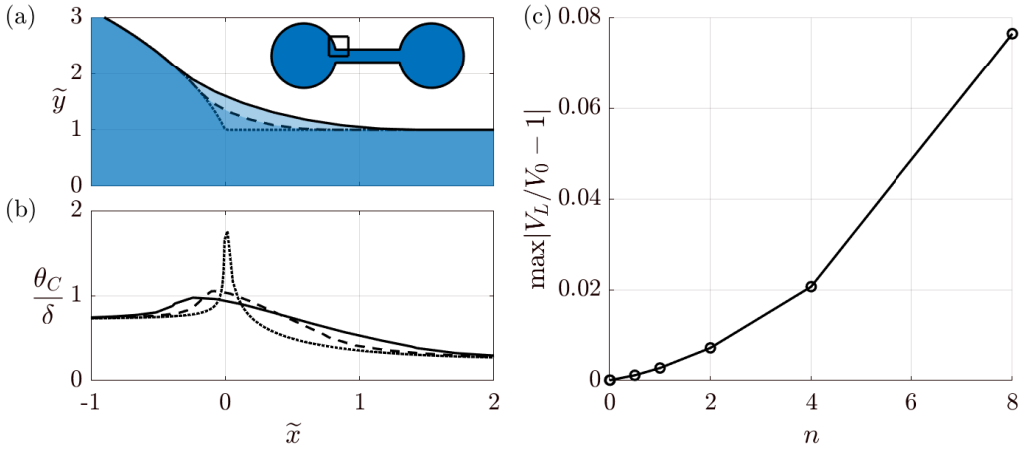


Figure 3.9: (a) Examples of the geometry when the corner is rounded for $n = 0, 1, 2$, the changes are on the length scale of the conduit width. (b) The corresponding contact angle as a function of $\widetilde{x}$ for $n = 0, 1, 2$ at equilibrium. (c) The maximum relative difference in the drop volume as a function of n for $n = 0, 1/2, 1, 2, 4, 8$, where V_0 is the volume with $n = 0$.

In §3.3.4 we showed that the gradient is singular near the corners in the junction region. We would also expect similar behaviour in the full numerical solution at these points. A tool is provided in COMSOL to fillet (round) corners in 2D [22]. We first demonstrate that the drainage timescale solution is not significantly altered when the corners in the geometry given in Figure 2.1a are rounded by a circular arc of radius $n\epsilon$. Figure 3.9a demonstrates how the corners are rounded for $n = 0, 1, 2$ and Figure 3.9b shows the corresponding contact angle as a function of $\widetilde{x}$. When $n = 0$ there is rapid variation at $\widetilde{x} = 0$ as expected; this disappears when the corner is rounded. Despite the change in geometry the dynamics on the drainage timescale are only slightly altered as shown in Figure 3.9c. This analysis shows that we are able to get meaningful solutions using the original, sharp cornered geometry, and that the smoothing of the corners described in §3.3.4 to accommodate transient movement of the contact line will not affect the leading-order dynamics. Thus, in the numerical simulations we use the geometry as shown in Figure 2.1.

For intermediate values of ϵ (typically $\epsilon = \mathrm{O}(10^{-1})$) the numerical solution can be

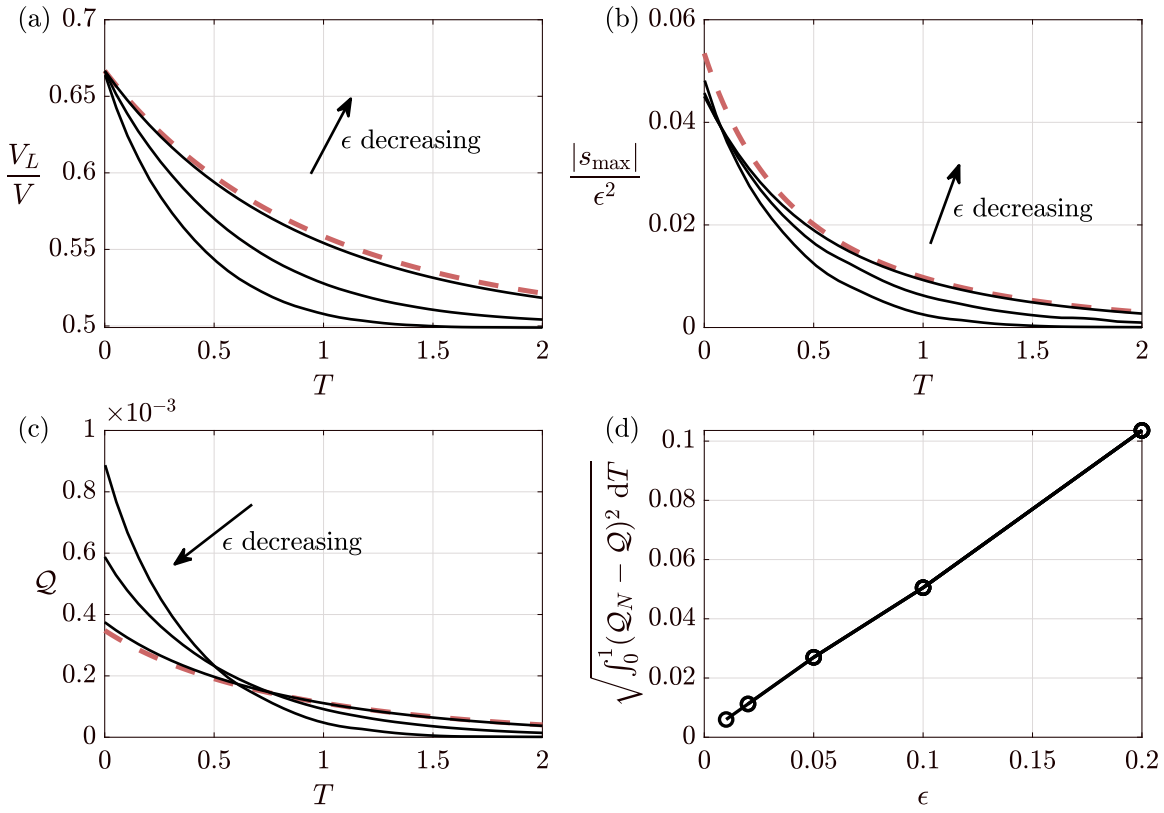


Figure 3.10: Comparison of COMSOL solutions with model predictions for different values of the small parameter ϵ. In each case the calculations were performed using $\alpha_L = \alpha_R = 1$ and $\mathrm{Bo} = 2$ with the initial volumes $\widehat{v}_L(0) = 0.2$ and $\widehat{v}_L(0) = 0.1$. (a)–(c) The solid lines show the numerical solution for $\epsilon = 0.01, 0.1, 0.2$ and the dashed line shows the asymptotic approximation. We compare (a) the drop volumes, given by (3.100); (b) the maximum shear stress on the substrate given by (3.102) with $y = 0$ and $x = 1$; and (c) the flux given by (3.93) and (3.103). (d) The root mean squared difference of the flux over a unit time interval for different values of ϵ, where $\mathcal{Q}_N$ is the numerical solution.

found in a matter of seconds, but as anticipated, for smaller values of ϵ we find run times can increase by multiple orders of magnitude even for the lubrication distinguished limit. This underlines how our asymptotic approach can facilitate the rapid prototyping of microfluidic system designs. In Figure 3.10 we compare numerical solutions of (3.18) and (3.20)–(3.22) to our asymptotic predictions for various small values of ϵ. In each simulation only the width of the conduit was altered and the initial drop volumes were fixed. In Figure 3.10a we see good agreement over a range of values of ϵ for the volumes of the left (upper dashed line) and right (lower dashed

line) drops as a function of time.

The drainage solution can also be used to find the shear stress in the conduit. In the x-direction the leading-order dimensionless shear stress on the substrate is given by

$$s = \left.\frac{\partial u_1}{\partial z}\right|_{z=0} = -h\frac{\partial p}{\partial x} = \frac{(\epsilon^2 - y^2)\,(p_L^4 - p_R^4)}{8\sqrt{p_L^4 - (p_L^4 - p_R^4)\,x}}, \tag{3.102}$$

where the dimensional shear stress is $s^* = \gamma/L\, s$. We define $s_{\max} = \max(s)$, where the maximum shear stress is on $y = 0$ at either $x = 0$ or $x = 1$ depending on the direction of the flow; the maximum will be at the junction near the conduit outlet. In Figure 3.10b we compare the absolute maximum of the shear stress found in COMSOL with the asymptotic prediction in (3.102). Again, as ϵ is decreased we see good agreement. We let $\widehat{Q}_0$ denote the leading-order flux, given by the right hand side of (3.93). This is rescaled with

$$\widehat{Q}_0 = \frac{\widehat{v}_T^4 \beta_R^4}{\epsilon^7 35}\mathcal{Q}; \tag{3.103}$$

then we find larger relative differences as can be seen in Figure 3.10c, especially on shorter timescales. Nevertheless there is still good agreement as ϵ is decreased. This is shown in Figure 3.10d, where the root mean squared difference of the flux over a unit time interval on the drainage timescale can be seen to decrease linearly with ϵ.

We are now in a position to compare our numerical predictions with a composite solution for the film height over the whole contact set Ω. Since the solutions found in the drop and conduit regions are only valid in those regions, we must find the composite solution in each of these regions and use these to form a composite solution for the whole domain Ω. In the left drop the composite solution is found by adding the junction solution to the drop solution and then subtracting the overlap; in this case the two leading terms in the limit $\widetilde{x}^2 + \widetilde{y}^2 \to \infty$ as shown in Figure 3.4. The solution in the right drop is found in a similar way. In the conduit, $0 < x < 1$, we must find the junction solutions at either end of the conduit and add them both to the conduit solution (given by (3.42) and (3.92)); the overlaps are then the conduit

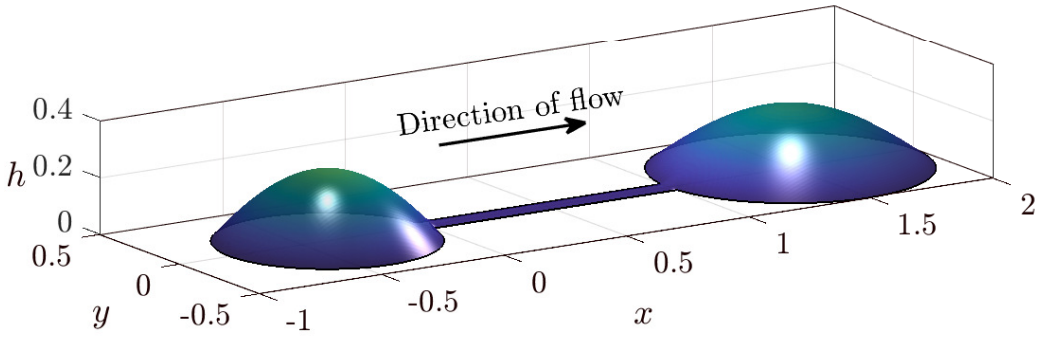


Figure 3.11: The composite solution for the interface. The dimensionless parameters used are Bo = 20, $\alpha_L = 0.5$, $\alpha_R = 0.4$, $\epsilon = 0.05$, $\widehat{v}_L = 0.03$ and $\widehat{v}_R = 0.03$.

solutions at $x = 0$ and at $x = 1$, so these are both subtracted. An example of the composite solution is shown in Figure 3.11 with an arrow indicating the direction of flow; since the base radii of the drops are different the same volumes will give different pressures. In Figure 3.12 we plot the composite interface height (dashed line) along the centre of the conduit, *i.e.* on $y = 0$ for different values of ϵ. The left and right panels show the profile in the respective drop regions and the central panels show the solution in the conduit region. The solid line shows the corresponding numerical solution; we see particularly good agreement in the drop regions for all values of ϵ plotted. In the conduit the composite solution is able to pick out the location of the dip in conduit height near the outlet (the flow is from left to right), although it predicts a less sharp decrease in profile height. This dip is where the maximum shear stress occurs in the numerical solution.

3.3.8 Maintaining a pinned contact line

An important feature of these devices are the large advancing and small receding contact angles, θ_a and θ_R respectively, which allows the volume of fluid in a drop to change significantly without the contact line moving. The particular values are highly dependent on the materials and fluids used, though Walsh *et al.* [127] have observed values of $\theta_r \approx 3^\circ$ and $\theta_a \approx 70^\circ$ in their experiments. Using the leading-order

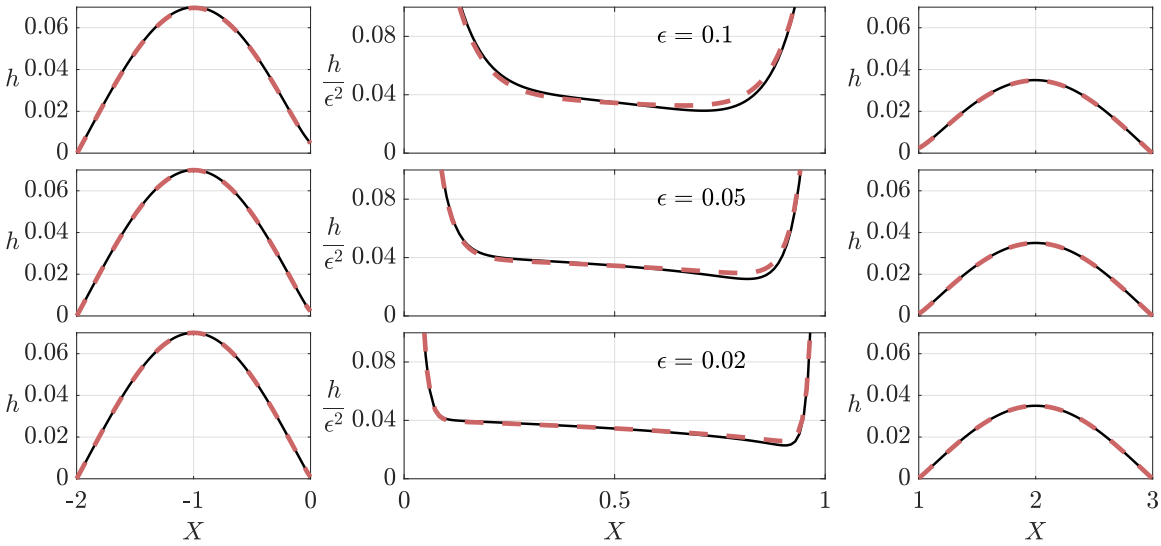


Figure 3.12: Comparison of COMSOL solution with the composite solution described in §3.3.7 on $y = 0$. The calculations were performed using $\alpha_L = \alpha_R = 1$ and $\mathrm{Bo} = 4$ with the initial volumes $\widehat{v}_L(0) = 0.1$ and $\widehat{v}_L(0) = 0.05$. The solid lines show the numerical solutions and the dashed lines the corresponding asymptotic approximation. We compare the solutions on the drainage timescale, *i.e.* $t \gg \epsilon^{-4}$. From top to bottom we have $t \approx 2.4 \times 10^8,\ 3.9 \times 10^9,\ 1.5 \times 10^{11}$. The solutions for the left- and right-hand drop regions are shown on the left- and right-hand sides respectively, the conduit region is shown in the middle panels; note that the height scales with ϵ^2 in the conduit.

solutions (3.31) and (3.42), the contact angles in the left- and right-hand drops and the conduit, denoted by $\theta_L(t)$, $\theta_R(t)$ and $\theta_C(x,t)$ respectively, are given by

$$\theta_L = \delta \frac{J_1\left(\sqrt{\mathrm{Bo}}\,\alpha_L\right)}{\sqrt{\mathrm{Bo}}\,J_0\left(\sqrt{\mathrm{Bo}}\,\alpha_L\right)} p_L, \quad \theta_R = \delta \frac{J_1\left(\sqrt{\mathrm{Bo}}\,\alpha_R\right)}{\sqrt{\mathrm{Bo}}\,J_0\left(\sqrt{\mathrm{Bo}}\,\alpha_R\right)} p_R, \quad \theta_C = \delta\epsilon\, p_C, \tag{3.104a–c}$$

where p_L, p_R, p_C are given by (3.32), (3.33) and (3.92). Since we are in the thin-film limit ($\delta \ll 1$) we will have $\theta_L, \theta_R, \theta_C < \theta_a$. The same, however, cannot be said of the contact angle in the junction regions; as we saw in §3.3.4 the contact angle tends to $\pi/2$ at the corners where the drop meets the conduit. In practice the contact line near this corner will move outwards until the contact angle falls to the advancing angle. We expect the smoothing of the corner to happen on a length scale of the width of the conduit and on a timescale not much larger than that of capillary action

in the junction regions. Furthermore, as we demonstrated numerically in Figure 3.9, smoothing the corner on this length scale does not significantly alter the drop volume and hence the flow rate in the conduit.

On the timescale $t \gg t_{CL} \sim \epsilon^{-4}$, the smallest contact angle in the conduit will occur at the outlet where $p_C = \min(p_L,\, p_R)$. As we are focusing on the distinguished limit in which $Bo, \alpha_L, \alpha_R = \mathrm{O}(1)$ as $\epsilon \to 0$ we deduce that the contact angle in the conduit is always less than in the drops, so that the leading-order contact angle is everywhere greater than or equal to the receding contact angle θ_r provided

$$\theta_{\min} = \delta\epsilon \min(p_L,\, p_R) \geq \theta_r, \tag{3.105}$$

where we have used (3.104c). Recall that in the lubrication distinguished limit we are currently studying the drop pressure varies linearly with the drop volume so that $p_L = \beta_L \widehat{v}_L$ and $p_R = \beta_R \widehat{v}_R$, where β_L and β_R are given by (3.33). It thus follows that, if (3.105) is satisfied for some $t \gg t_{CL}$, it will be satisfied for all $t \gg t_{CL}$. So that, on the drainage timescale, the contact line remains pinned only if it is pinned initially. We further note that in accordance with physical intuition it is easier to satisfy the constraint (3.105) the larger the volumes of the drops or the smaller the radii of their contact sets. As well as the drop volume, (3.105) depends on four geometric parameters, the conduit length L, the conduit width a_0, the drop base radius R_L and the drop height H_D, although the last of these will be set by the drop volume. Henceforth we shall assume that θ_r may be engineered to be sufficiently small that the constraint (3.105) pertains.

3.3.9 A survey of fluxes and shear stresses

We have already identified one way in which the footprint of the device can significantly alter the timescales involved: in §3.3 we showed that the timescale of drop drainage scales with ϵ^{-7}, where we recall $\epsilon = a_0/L \ll 1$ is the conduit width-to-length ratio. Two further parameters that affect the behaviour on this timescale are β_L and

β_R, the pressure-to-volume ratios in the left- and right-hand drops respectively defined in (3.33), as well as their ratio $\alpha = \beta_L/\beta_R$, which appeared first in (3.21). In Figure 3.13a we plot β_L as a function of the dimensionless radius α_L of the left-hand drop — a plot of β_R as a function of α_R would be identical — in which a log scale has been used to highlight that β_L varies over several orders of magnitude.

One of our main interests is in determining the conditions for an approximately constant flux in the conduit on the timescale of drainage. We approximate the initial flux $\mathcal{Q}_I$ using the right-hand side of (3.97), *i.e.*

$$\mathcal{Q}_I = -\left(1 - \mathcal{V}_L(0)\right)^4 - \alpha^4 \mathcal{V}_L(0)^4 . \tag{3.106}$$

If we prescribe the values of $\mathcal{Q}_I$ and α there is a single initial volume satisfying (3.106). Using (3.100) with this initial volume we then compute the time taken $T_{0.5}$ for the initial flux to reduce by 50%. The results of this analysis are shown in Figure 3.13b. This shows that large fluxes decay faster than small fluxes (the lower solid lines are the largest fluxes). In the examples in Figure 3.13b increasing the initial flux by 3 orders of magnitude (from 0.01 to 10) can similarly decrease $T_{0.5}$ by as much as 3 orders of magnitude. We can further see that decreasing α allows the fluxes to be maintained for longer. This corresponds to increasing the relative size of the base of the left-hand drop, as the base radius is increased a larger initial volume is needed to achieve the same initial flux, which consequently leads to a slower decay in flow rate. This shows that slowly varying fluxes can be achieved with either small initial flow rates or disparate base sizes.

A selection of solutions to the model for drainage of the drops (3.97) are shown in Figures 3.14 and 3.15, where the leading-order flux is given by the right-hand side of (3.93) and the shear stress is given by (3.102). In these figures we show the effect of changing a single model parameter on the flux and maximum shear stress in the conduit as functions of time. The geometries and volumes represent typical values

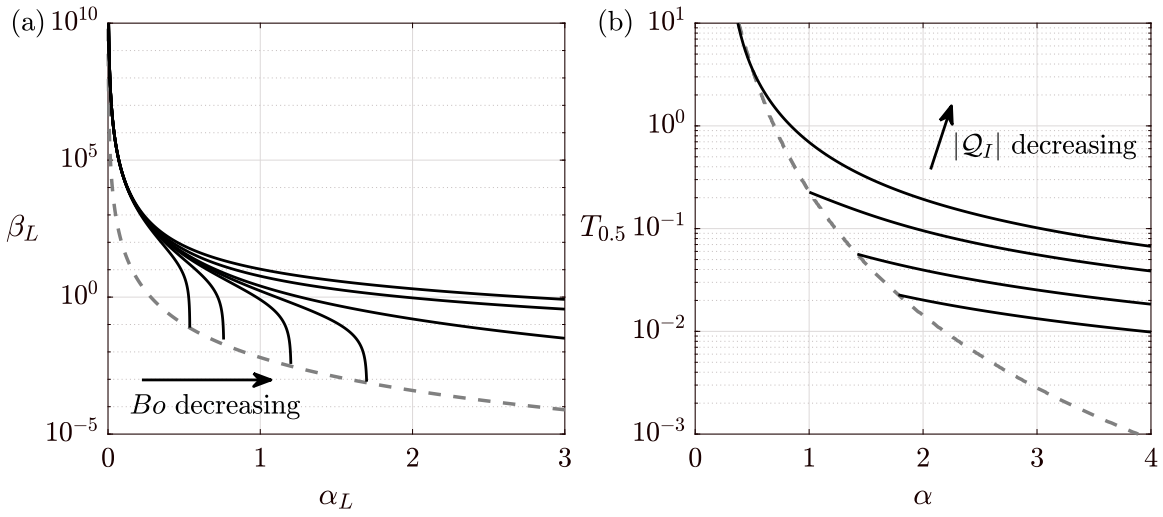


Figure 3.13: (a) As a function of drop radius, α_L, we plot β_L, the ratio of the dimensionless drop pressure to volume for the left-hand drop given by (3.33), (3.34) and (3.36) for $\mathrm{Bo} = -20, -8, 0, 2, 4, 10, 20$. The dashed line shows the boundary on which $\mathrm{Bo} = \mathrm{Bo}_C$ (defined in §3.3.2 as the Bond number below which either the drop height or pressure are no longer positive). (b) The time taken for an initial flux $\mathcal{Q}_I$ to reduce by 50% as a function of $\alpha = \beta_R/\beta_L$. The initial fluxes are $\mathcal{Q}_I = 0.01, 1, 4, 10$. The dashed line shows the minimum value of α for which there is a solution with a particular initial flux.

that are within the limits of the thin-film model with a timescale of minutes to hours as shown in Table 2.1. Figure 3.14a shows that changing the base radius of the inlet drop R_L (the drop that the fluid flows out of) by a few tenths of a millimetre can significantly alter the flow rate. Similarly Figure 3.14b shows that small decreases in the base radius of the right-hand drop can change the direction of the flow. This is an example of our earlier conclusion that the pressure in a drop is very sensitive to the base radius of the drop. In Figure 3.14c we see that decreasing the width of the conduit results in flows that are approximately uniform over a much longer timescale, though with lower fluxes. In Figure 3.15a and b we see that changing the volume of the left- and right-hand drops has a similar effect to changing their base radii, though a larger relative change in drop volume is required to see the same effect. Finally Figure 3.15c shows that increasing the length of the conduit results in smaller, slowly varying fluxes.

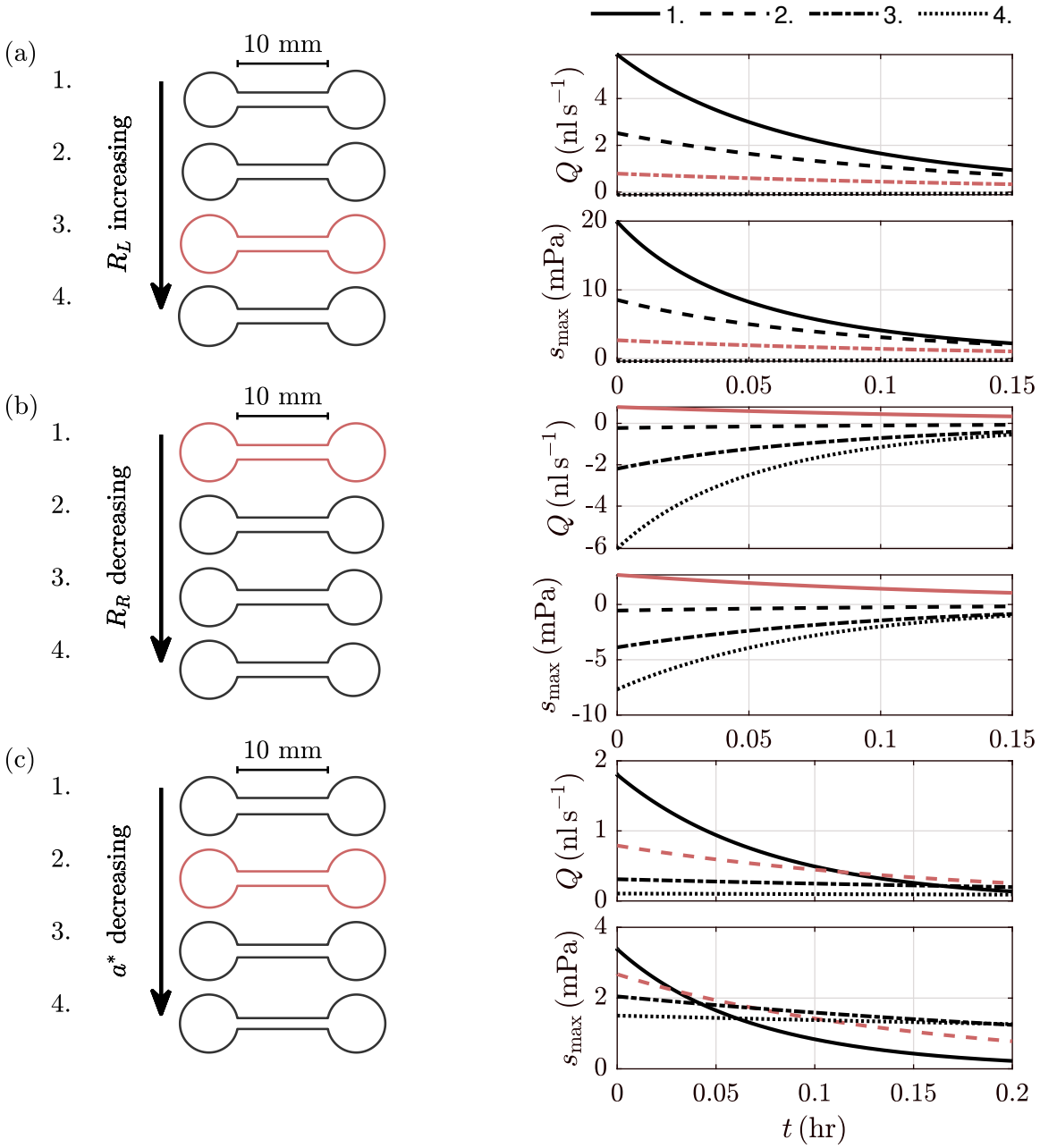


Figure 3.14: In this figure and the following one we show the effect of changing a single model parameter on the flux and maximum shear stress in the conduit as functions of time. The geometries are shown on the left-hand side, in each case we modify the geometry with parameters $R_R = R_L = 3.2\,\text{mm}$, $a^* = 0.8\,\text{mm}$, $v_L = 8\,\mu\text{l}$ and $v_R = 7\,\mu\text{l}$ (shaded red). The dumbbells are labelled 1–4 with the corresponding fluxes and maximum shear stresses shown on the right-hand side. The parameters we modify are (a) the base radius of the left-hand drop $R_L = 3, 3.1, 3.2, 3.3\,\text{mm}$; (b) the base radius of the right-hand drop $R_R = 3.2, 3.1, 3, 2.9\,\text{mm}$; and (c) the width of the conduit $a = 0.9, 0.8, 0.7, 0.6\,\text{mm}$.

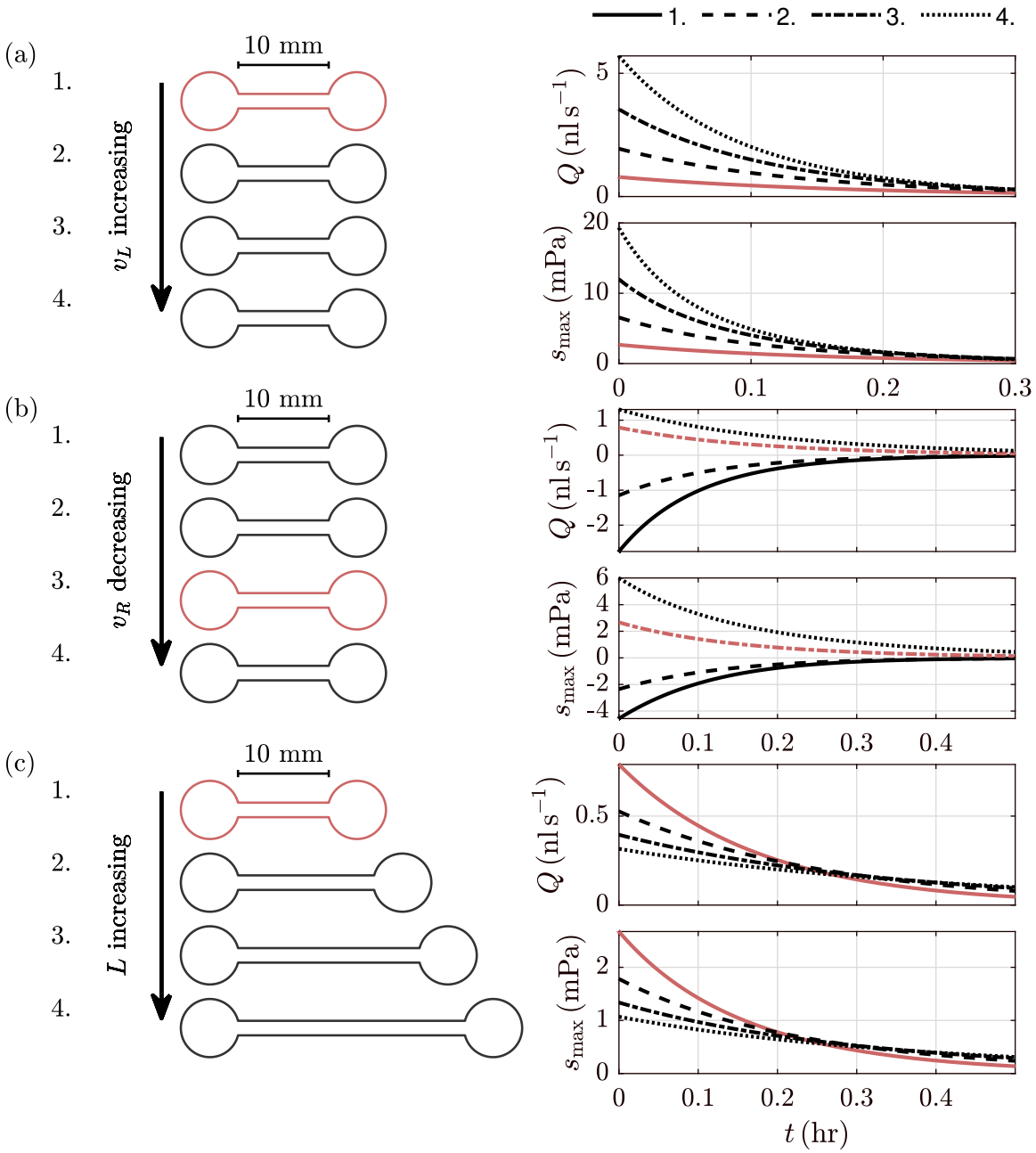


Figure 3.15: See caption to Figure 3.14. In this figure the parameters we modify are (a) the volume of the left-hand drop $v_L = 8, 9, 10, 11\,\mu\mathrm{l}$; (b) the volume of the right-hand drop $v_R = 10, 9, 7, 6\,\mu\mathrm{l}$; and (c) the length of the conduit $L = 10, 15, 20, 25\,\mathrm{mm}$.

The numerical solution of (3.18) and (3.20)–(3.22) has shown that the maximum shear stress occurs where the conduit has the smallest cross-section, the dip near the outlet of the conduit. As $\epsilon \to 0$ this dip moves closer to the drop as can be seen in the middle panels of Figure 3.12. Since the shear stress scales with ϵ^2, a narrow or long conduit will have lower shear stress. Walsh *et al.* [127] show that human embryonic kidney (HEK) cells can grow normally in their devices, though they did not directly measure shear stress in those experiments. Stathopoulos *et al.* (1985) [112] state that a shear stress greater than 2.6 Pa has a significant effect on the viability of HEK cells. As can be seen in Figures 3.14 and 3.15, our model predicts significantly smaller shear stresses for a range of parameters used experimentally (see Table 2.1). We further note that higher shear stresses are associated with higher flow rates. This means that large shear stresses, relative to that tolerated by cells, would be short lived if they did occur.

3.4 Model extensions

In this section we show how the model for the simple dumbbell can be extended to include a greater variety of mechanisms to control the flow.

3.4.1 Active pumping

So far we have focused on the passive circuit in which the flow through the conduit is driven by differences in pressure in the drops at either end as shown in Figure 2.1c. We will look at active pumping in more depth in the chapter 5, but for now we show how the pressure in the conduit is altered when a flow rate is imposed (as in Figure 2.1d). Since we began by considering the drop, junction and conduit regions separately, the analysis up to §3.3.4 remains unchanged. In §3.3.4 we showed that the leading-order pressure is transmitted straight through the junction regions for $t \gg t_J \sim \epsilon$ from which we deduced the appropriate boundary conditions in the

conduit for $t \sim t_{CL} \sim \epsilon^{-4}$: the pressure at the ends of the conduit is equal to the pressure in the connected drop. For actively driven flow there is only one drop and hence one junction (as illustrated in Figure 2.1d) which, without loss of generality, is taken to be the one on the right-hand side. So the pressure in the conduit is equal to the right-hand drop pressure at $x = 1$ and at $x = 0$ we impose the flow rate $\widehat{Q}_0(t)$. The flow rate may vary in time but we assume that it is quasi-steady on the timescale of conduit relaxation $t \sim t_{CL}$. In practice fluid is typically pumped into the circuit (rather than taken out) so we assume that the fluid is flowing in the positive x direction with the right-hand drop acting as a reservoir. In §3.3.3 we showed that the flux in the conduit satisfies (3.43b), which gives

$$\widehat{Q}_0 \sim -\frac{1}{35}\epsilon^7 \frac{\partial}{\partial x}\left(p_C^4\right) \quad \text{as } \epsilon \to 0. \tag{3.107}$$

Assuming that $\mathscr{Q}_0 = 35\widehat{Q}_0/\epsilon^7 = \mathrm{O}(1)$, the conduit relaxation problem for active pumping remains almost the same as the passive pumping case (3.89)–(3.91); the only difference being the boundary condition at $x = 0$. The equation for the pressure on the timescale of conduit relaxation (3.89) is given by

$$\frac{\partial p_C}{\partial \tau} = \frac{\partial^2}{\partial x^2}\left(p_C^4\right) \quad \text{for } 0 < x < 1,\ \tau > 0, \tag{3.108}$$

where $t = (70/3)\,\epsilon^{-4}\tau$. The boundary conditions for active pumping are

$$-\frac{\partial}{\partial x}\left(p_C^4\right)\bigg|_{x=0} = \mathscr{Q}_0, \quad p_C(1,\tau) = p_R(0) \quad \text{for } \tau > 0 \tag{3.109}$$

and, as in (3.91), we prescribe an initial condition of the form

$$p_C(x,0) = \mathscr{P}(x) \quad \text{for } 0 < x < 1. \tag{3.110}$$

We anticipate the long-time attractor (given sufficient regularity of the initial profile) to be the steady-state profile:

$$p_C \to \left(\mathscr{Q}_0\,(1-x) + p_R^4\right)^{\frac{1}{4}} \quad \text{as } \tau \to \infty. \tag{3.111}$$

In the next chapter we will see what happens when the scale of the imposed flow rate is much larger. In this case the pressure in the passive and active conduits will not be of the same order of magnitude. Since fluid is flowing into the circuit the total volume is no longer fixed; there will be no equilibration timescale, rather there will be a timescale on which the thin film model is no longer valid. Making the rescaling $t = \epsilon^7/35\widehat{T}$ in (3.27b), the volume in the right-hand drop is given by

$$\frac{\mathrm{d}\widehat{v}_R}{\mathrm{d}\widehat{T}} = \mathscr{Q}_0; \tag{3.112}$$

the flow rate is a known function of time so the volume of the reservoir drop is given by

$$\widehat{v}_R = \int_0^{\widehat{T}} \mathscr{Q}_0(\widehat{\tau})\ \mathrm{d}\widehat{\tau} + \widehat{v}_R(0)\,. \tag{3.113}$$

The model is not valid when $\widehat{v}_R = \mathrm{O}(1/\delta)$; (3.113) shows that this happens on the timescale $\widehat{T} \sim 1/\delta$. Using (3.32b) and (3.33b) we can write the conduit pressure as

$$p_C\left(x, \widehat{T}\right) = \left(\mathscr{Q}_0\left(\widehat{T}\right)(1-x) + \beta_R^4\left(\int_0^{\widehat{T}} \mathscr{Q}_0(\widehat{\tau})\ \mathrm{d}\widehat{\tau} + \widehat{v}_R(0)\right)^4\right)^{\frac{1}{4}} \tag{3.114}$$

on the timescale of drop drainage.

3.4.2 Controlling the flow by altering the conduit width

Active pumping allows for much greater control over the dynamics of the device and it further allows the geometry to be more finely tuned to give desired flow characteristics. For simplicity we have so far taken the conduit to have a fixed width. We will now demonstrate how we can choose the conduit width to reduce the variation in shear stress along the conduit. This objective only makes sense when the fluid is pumped actively; for passive flows the temporal variation in the flow rate means that some property that was initially constant would not remain so. Assuming that the conduit width varies on an O(1) length scale, the leading-order model given in §3.2 is largely

unchanged, only the flux and area in the conduit (given by (3.25)) are altered; we have instead

$$\widehat{A}\,(x,t) = \int_{-a}^{a} h\ \mathrm{d}y, \quad \widehat{Q}\,(x,t) = \int_{-a}^{a}\int_{0}^{h} u_1\ \mathrm{d}z\,\mathrm{d}y, \tag{3.115a,b}$$

where $2a(x)$ is the dimensionless width of the conduit, as shown in Figure 3.1. The analysis up to §3.3.3 is otherwise unchanged. In the conduit region we again rescale the governing equations with

$$y = \epsilon\,\widehat{y}, \quad h = \epsilon^2\,h_C, \quad a = \epsilon\widehat{a}, \quad p = p_C. \tag{3.116}$$

For $t \gg t_{CW} \sim \epsilon^{-2}$, the pressure is spatially uniform in each x-plane, and hence at leading order with respect to ϵ (3.18) gives

$$\frac{\partial^2 h_C}{\partial \widehat{y}^2} = -p_C \quad \text{for } \widehat{y} < |\widehat{a}|,\ 0 < x < 1, \tag{3.117}$$

The interface height is zero on the contact line which gives $h_C(x, \pm\widehat{a}, t) = 0$ for $0 < x < 1$, where $\widehat{a}$ is a function of x. The solution is readily found to be given by

$$h_C = \frac{p_C}{2}\left(\widehat{a}^2 - \widehat{y}^2\right). \tag{3.118}$$

Using (3.19) and (3.115) the flux in the conduit is then found to be given by

$$\widehat{Q} = -\frac{1}{35}\epsilon^7 a^7 \frac{\partial}{\partial x}\left(p_C^4\right). \tag{3.119}$$

We further note that the analysis in the junction regions is unchanged since the assumption that conduit width varies on a longer length scale than ϵ means that the geometry in the junction region is unaltered (although the width scale would be different in each junction).

The dimensionless shear stress on the base of the conduit was found in (3.102) to be

$$s(x,\, y,\, t) = -\epsilon^2 h_C \frac{\partial p_C}{\partial x}. \tag{3.120}$$

We define $\widehat{s}$ to be the dimensionless shear stress along the centre line of the conduit, *i.e.* $\widehat{s} = s\,(x,\,0,\,t)$. With the interface height given by (3.118), we find the shear stress to be

$$\widehat{s} = -\epsilon^2 \frac{\widehat{a}^2}{2} p_C \frac{\partial p_C}{\partial x}. \tag{3.121}$$

If constant values of $\widehat{s}$ and $\widehat{Q}$ are prescribed, then (3.119) and (3.121) give an ODE for the pressure in the conduit and an algebraic equation for the conduit width. Thus, we need to provide a single boundary condition to close the problem. We fix the width of the conduit at $x = 0$ so that $\widehat{a}(0) = 1$. The solution to (3.119) and (3.121) is then given by

$$p_C = \sqrt{\frac{\mathcal{Q}}{\mathcal{S}}} \left(1 - \frac{6}{5}\frac{\mathcal{S}^2}{\mathcal{Q}} x\right)^{\frac{5}{6}}, \tag{3.122}$$

$$\widehat{a} = \left(1 - \frac{6}{5}\frac{\mathcal{S}^2}{\mathcal{Q}} x\right)^{-\frac{1}{3}}, \tag{3.123}$$

where $\mathcal{Q} = 35\widehat{Q}/(4\epsilon^7)$ and $\mathcal{S} = 2\widehat{s}/\epsilon^2$. We can see that the solutions are only valid when $\mathcal{S}^2/\mathcal{Q} < 5/6$, so some care must be taken when choosing the desired flow rate and shear stress. We anticipate that the junction region will alter the shear stress significantly so we first demonstrate that the shear stress tends to $\widehat{s}$ in numerical solutions of the full governing equations (3.18) and (3.20)–(3.22) on the domain indicated in Figure 2.1d, where the width of the conduit is given by (3.123). We use the same numerical techniques as described in §3.3.7, with the slight difference that the flow rate is now imposed at $x = 0$. In Figure 3.16a we see good agreement away from the junction as ϵ is decreased. Near the junction region there is still a maximum in the shear stress as there was for the straight conduit, though it is not as extensive in space. The asymptotic solutions for the shear stress on the base of the conduit with a constant and varying width are shown in Figure 3.16b. This demonstrates that a small variation in the width of the conduit can make a big difference to the shear stresses. Furthermore, attempting to design a constant shear

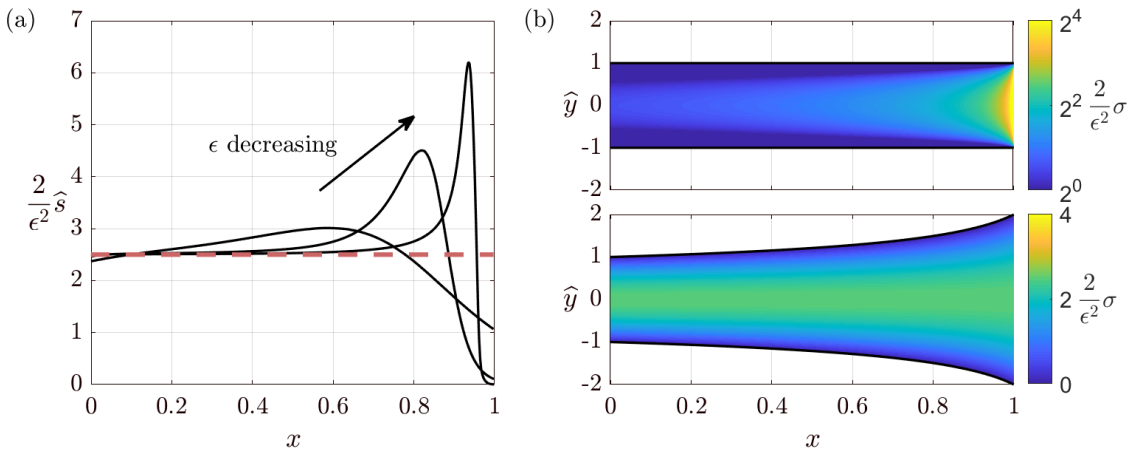


Figure 3.16: (a) The shear stress along the centre of the conduit found from the numerical solution of (3.18) and (3.20)–(3.22) with the conduit width given by (3.123) for $\mathcal{S} = 2.5$ and $\mathcal{Q} = 8.5714$ (chosen so that the conduit width doubles) with $\epsilon = 0.2, 0.05, 0.01$, the dashed line shows the value of $\mathcal{S}$. (b) Comparison of the two asymptotic solutions for shear stress, s, given by (3.120), (3.122) and (3.123) in a conduit of constant width, and a conduit with its width given by (3.123) for $\mathcal{S} = 2.5$ and $\mathcal{Q} = 8.5714$, note the logarithmic scaling for the straight conduit shear stress.

stress via the asymptotic conduit solution by changing conduit width also generates a shear stress spike on entering the junction region.

3.5 Discussion

In this chapter we set out to develop a model for the flow through a new class of free surface microfluidic device that relies on surface tension. The flow is governed by the standard thin film equations and the shape of the fluid interface is governed by the linearised Young-Laplace equation. There are several disparate length scales in a typical device geometry which allowed us to construct asymptotic solutions that are valid in different regions and over different timescales as the aspect ratio ϵ is decreased. In §3.3 we described each of the regions in a circuit with a dumbbell shaped footprint: the drop, conduit and junction regions. We focused on the limit in which the aspect ratio of the conduit ϵ is small, so that the conduits were long and thin. We also showed that each region is associated with a different relaxation timescale, which

vary over several orders of magnitude. In the junction region we showed that the contact angle near the corners will exceed the advancing angle; physically we would expect the sharp corners to be smoothed out over a length scale comparable to the conduit width. In Figure 3.9 we demonstrated that smoothing the corners in the numerical simulations did not have a significant effect on the flow rate and so we did not include this in our model.

In §3.3.6 we showed how the leading-order quasi-steady solutions in the drop and conduit regions can be combined to give a single ODE governing the time-dependent drop volumes. The ODE is separable and an implicit solution can be found; this then allowed us to predict the flux through the device given the initial drop volumes. When designing an experiment with a dumbbell configuration there are six dimensional parameters that can be modified for a given combination of fluids (a, L, α_L, α_R, v_L and v_R); the width and length of the conduit, the base radii of the two drops as well as the initial volume of fluid contained in each. Given a required flow rate, drainage time, shear stress (or other property), there is clearly a large solution space in which to search to find a circuit with the desired properties. Such an inverse problem is beyond the scope of this thesis, but the effect of modifying each of these parameters in turn on the leading-order drainage time solutions is easily determined. In §3.3.7 we found a composite solution for the interface height over the whole dumbbell shape. This allowed us to determine where the conduit cross-section area is smallest and hence where the fluid flow is fastest. Our asymptotic predictions for the drop volumes, conduit flux and interface height all show good agreement with our numerical simulations when the conduit aspect ratio is small.

In §3.3.8 we showed that maintaining an approximately constant flux in our distinguished limit is easier when the fluxes are small $\mathrm{O}(\mathrm{nl\,s^{-1}})$ or the timescales are relatively short O(h). Thus the geometries with $\epsilon \ll 1$ will be the most appropriate and also the most amenable to our analysis. The timescale of drainage has been

shown to be very sensitive to the aspect ratio of the conduit and thus it is the geometry that is the most important factor in achieving a given, approximately constant, flux over time. However, the height of the conduit is not constant over its length, so the velocity will vary along the length of the conduit. This difference in velocity will lead to differences in shear stress along the conduit as shown in the top panel of Figure 3.16b. In the context of cell handling experiments, shear stress impacts the expression of a wide range of different signalling pathways and this model may suggest a way of varying shear stresses within one device to test hypothesis using a single experiment. Alternatively, the variation in shear stress can be greatly reduced by printing a conduit with a gradually increasing width as shown in §3.4.2. However, the numerical modelling shown in Figure 3.16 indicates that there would still be a spike in shear stress in the junction region as there is with a conduit of constant width.

Finally, we note that if the conduit were printed with an initial height much less than this (*i.e.* $h \ll \epsilon^2$), then the pressure in the conduit would be much less than in the drops and fluid would initially flow into the conduit from both drops. Whereas, if $h \gg \epsilon^2$ initially in the conduit, then the pressure would be much higher in the conduit than in the drops and fluid would flow out of the conduit into both drops.

Chapter 4

Thick drops and thin conduits

In the previous chapter we derived an asymptotic model for the flow in the circuits shown in Figure 2.1 when the height of the drops is much less than their base radius, *i.e.* $H_D \ll L$. This allowed us to greatly simplify the governing equations. In this chapter we will consider the case in which H_D is comparable to L, *i.e.* for a so-called thick drop. We consider the same asymptotic structure as in §3.3.1, but with the full governing equations from chapter 2, in particular we only consider small conduit aspect ratios $a_0 \ll L$. Furthermore, as in chapter 3 we will focus our attention initially on the passive dumbbell setup before generalising to active pumping. As before we will split the geometry up into five regions: two drops, two junctions and the conduit. Solutions can be found in each of these regions, though we will have to rely more on numerical methods.

4.1 Velocity and time scales

In our analysis of the thin-film problem we found that there were five timescales of relaxation (see (3.28)) each associated with a different region of the geometry, though we were most interested in the longer timescales, namely those of conduit relaxation and drop drainage. We similarly expect there to be multiple timescales for the thick drop problem. We recall that the geometry consists of five regions: two drops with contact sets Ω_L and Ω_R, a narrow and thin conduit with contact set Ω_C, and two

Drop	$x^* \sim L$	$y^* \sim L$	$z^* \sim L$
Conduit	$x^* \sim L$	$y^* \sim a_0$	$z^* \sim \dfrac{a_0^2}{L}$
Junction	$x^* \sim a_0$	$y^* \sim a_0$	$z^* \sim a_0$

Table 4.1: The length scales in the three regions of the dumbbell shaped circuit, where a_0 is the scale of the conduit width and L is the conduit length with $a_0/L \ll 1$.

small junction regions with contact sets Ω_{JL} and Ω_{JR} connecting together the drops and conduit, as illustrated in Figure 3.1. With this geometry we can now describe the different physical timescales for the thick drop system. In this chapter we shall rescale the governing equations on the conduit relaxation timescale, but before doing so we will determine all of the relevant timescales. The dimensional length scales in the drop, conduit and junction are summarised in Table 4.1. The x^* and y^* length scales are the same as in §3.3 since we are considering the same device footprint. The only difference from the thin-film case is that the z^*-axis is scaled relative to L rather than δL.

For passively driven flows we still require the pressure in the drops and conduit to be comparable as described in §3.3. Thus, the pressure scales are given by $p_D^* \sim \gamma/L \sim p_C^* \sim \gamma H_C/a_0^2$ in the drop and conduit respectively, where H_C is the conduit height scale (as illustrated in Figure 2.1), and hence $H_C \sim a_0^2/L$. The velocity scales in each region are found by balancing the terms on the right-hand side of the stress tensor in (2.7). The timescales of capillary action are then found by dividing the relevant length scale by the velocity scale. There is only one relevant length scale in each of the drop and junction regions, the conduit length L and conduit width a_0, respectively, as shown in Table 4.1. Thus, by a balance in the stress boundary condition (2.6), we find the velocity scale to be γ/μ_1, which gives the timescales of capillary action in the drop and junction, respectively, as $t_D^* \sim L\mu_1/\gamma$ and $t_J^* \sim a_0\mu_1/\gamma$. Referring again to Table 4.1, we see that there are three length scales in the conduit region, of these, the z^*-scale dominates in (2.7) and the y^* scale dominates the mean curvature term

giving the velocity scale $a_0^2\gamma/(L^2\mu_1)$. To find the timescale we use the largest of the relevant length scales in the conduit L, which gives the timescale of relaxation of the free boundary across the width of the conduit as $t^*_{CW} \sim L^3\mu_1/(a_0^2\gamma)$. The remaining timescales for relaxation in the different regions are found by balancing the terms in the conservation of mass equation (2.14) and in the ODE for the drop volume (2.15). On these timescales the velocity scale is found by balancing the viscous term and the pressure gradient in (2.1a), which gives $U_0 \sim \gamma a_0^4/(\mu_1 L^4)$. Then, for example, the area and flux in the conduit scale with $A^* \sim a_0^3/L$ and $Q^* \sim \gamma a_0^7/(\mu_1 L^5)$, respectively. Balancing the terms in the conservation of mass expression (2.14),

$$\frac{\partial A^*}{\partial t^*} + \frac{\partial Q^*}{\partial x^*} = 0, \tag{4.1}$$

gives the timescale of relaxation along the conduit as $t^*_{CL} \sim L^5\mu_1/(a_0^4\gamma)$. Finally, we note that the drop volumes scale with L^3, so balancing the terms in the equations relating volumes to fluxes, (2.15), gives the timescale for drop drainage as $t^*_{DD} \sim L^8\mu_1/(a_0^7\gamma)$

Recall that in chapter 3 we defined the conduit aspect ratio as $\epsilon = a_0/L$. In terms of ϵ, the timescales of relaxation for the junction, drops, conduit width and conduit length and the drainage timescale, respectively, are given by

$$t^*_J \sim \epsilon\frac{L\mu_1}{\gamma}, \quad t^*_D \sim \frac{L\mu_1}{\gamma}, \quad t^*_{CW} \sim \frac{1}{\epsilon^2}\frac{L\mu_1}{\gamma}, \quad t^*_{CL} \sim \frac{1}{\epsilon^4}\frac{L\mu_1}{\gamma}, \quad t^*_{DD} \sim \frac{1}{\epsilon^7}\frac{L\mu_1}{\gamma}. \tag{4.1a–e}$$

As in chapter 3, each timescale can be written as a power of ϵ multiplied by the timescale of capillary action in the drop regions t^*_D, which we recall to be the timescale used in the initial non-dimensionalisation in (3.2). In particular the dependence on ϵ is the same as the corresponding thin-film timescales in (3.28). However, in the thin-film case the timescale of capillary action in the drops is given by $3L\mu_1/(\delta^3\gamma)$, where $\delta \ll 1$ and so we expect equilibration to happen much more quickly when the drops are thick.

4.2 The dimensionless governing equations

The governing equations (2.1)–(2.8) are initially rescaled with

$$(x^*, y^*, z^*) = L\,(X, Y, Z), \quad a^* = L\,a, \quad h^* = L\,H, \tag{4.2}$$

$$t^* = \frac{\mu_1}{\epsilon^4 \gamma} T, \quad \kappa^* = \frac{1}{L}\kappa, \quad \boldsymbol{u}_i^* = \frac{\gamma \epsilon^4}{\mu_1}\boldsymbol{U}_i, \tag{4.3}$$

$$p_i^* = \frac{\gamma}{L} P_i + p_{\text{atm}} + \rho_2 g H_O - \rho_i g L Z, \tag{4.4}$$

for $i = 1, 2$, where p_{atm} is atmospheric pressure and $\boldsymbol{U}_i = (U_i, V_i, W_i)$. The rescaled equations are

$$\epsilon^4 \text{Re}_2 \left(\frac{\partial \boldsymbol{U}_i}{\partial T} + (\boldsymbol{U}_i \cdot \boldsymbol{\nabla})\boldsymbol{U}_i \right) - \epsilon^4 \frac{\nu_i}{\nu_1} \nabla^2 \boldsymbol{U}_i = -\frac{\rho_1}{\rho_i} \boldsymbol{\nabla} P_i, \tag{4.5a}$$

$$\boldsymbol{\nabla} \cdot \boldsymbol{U}_i = 0, \tag{4.5b}$$

for $(X, Y, Z) \in \Gamma_i$, $i = 1, 2$ and where $\text{Re}_2 = \epsilon^4 \rho_1 \gamma / \mu_1$. We use the same notation as in Figure 3.1 for each of the dimensionless fluid regions. So, we let Γ_1 refer to the region containing the liquid in the circuit and Γ_2 refer to the region containing the overlaying liquid, as illustrated in Figure 3.1b, and we let S_1 denote the boundary separating these two regions. On S_1 the kinematic (2.2) and velocity continuity (2.3) boundary conditions are

$$\boldsymbol{U}_i \cdot \mathbf{n} = \widehat{v}_n \qquad \text{on } S_1 \text{ for } i = 1, 2. \tag{4.6}$$

$$\boldsymbol{U}_1 \cdot \mathbf{t} = \boldsymbol{U}_2 \cdot \mathbf{t} \quad \text{on } S_1, \tag{4.7}$$

where $\widehat{v}_n$ is the dimensionless velocity of the free boundary S_1 in the normal direction and $\mathbf{t}$ denotes any tangent vector on the interface. The no-slip conditions on the base and device walls, (2.4) and (2.5), are given by

$$\boldsymbol{U}_i = \mathbf{0} \quad \text{on } Z = 0 \text{ for } (X, Y) \in \Omega_i \ (i = 1, 2) \tag{4.8}$$

$$\boldsymbol{U}_2 \to \mathbf{0} \quad \text{as } X^2 + Y^2 \to \infty \text{ for } (X, Y, Z) \in \Gamma_2, \tag{4.9}$$

where (4.9) comes from the assumption that the walls of the device are sufficiently far from the circuit. The momentum balance across the interface in (2.6) becomes

$$(\boldsymbol{\sigma}_2 \cdot \mathbf{n} - \boldsymbol{\sigma}_1 \cdot \mathbf{n}) = -(\kappa + \mathrm{Bo}\, Z)\,\mathbf{n} \quad \text{on } S_1, \tag{4.10}$$

with

$$\boldsymbol{\sigma}_i = -P_i \mathbf{I} + \epsilon^4 \frac{\mu_i}{\mu_1}\left(\nabla \boldsymbol{U}_i + (\nabla \boldsymbol{U}_i)^{\mathrm{T}}\right) \quad \text{for } i = 1, 2, \tag{4.11}$$

where gravity, via the Bond number Bo, now may influence the interfacial mechanics given the change in physical scales. The capillary length, λ, is defined to be the length scale at which the Laplace and hydrostatic pressure are equal: for the interface open to the air it is given by

$$\lambda = \sqrt{\frac{\gamma_a}{(\rho_2 - \rho_a)g}}. \tag{4.12}$$

The typical values in Table 2.1 give $\lambda \simeq 1\,\mathrm{mm}$. When the characteristic length is less than λ, surface tension dominates gravity. The entire device needs to be large enough to fit several drops and conduits, so the length scale for the air/overlay interface will be on the order of several centimetres; much larger than the capillary length. Thus, it is gravity that is the most important factor determining the shape of S_2 and we neglect the effects of surface tension on the air/overlay interface, so that $h_O^*(x^*, y^*, t^*) = H_O$. Then (2.10) gives

$$P_2 \mathbf{n}_a = \epsilon^4 \frac{\mu_2}{\mu_1}\left(\nabla \boldsymbol{U}_2 + (\nabla \boldsymbol{U}_2)^{\mathrm{T}}\right) \cdot \mathbf{n}_a, \tag{4.13}$$

assuming $\mu = \mu_2/\mu_1 = \mathrm{O}(1)$, (4.13) shows that the pressure in the overlay satisfies $P_2 = \mathrm{O}(\epsilon^4)$.

We will find asymptotic solutions to (4.5)–(4.11) in the limit $\epsilon \to 0$. Throughout we assume that $\epsilon^4 \mathrm{Re}_2 \ll 1$; this assumption will be valid for most parameter values as shown in Table 2.1.

4.3 Quasi-steady solution in the drops

4.3.1 Formulation

The leading-order analysis is the same in each drop, so we give only the details for the left-hand one. The geometry of the contact set remains the same as in Figure 3.1. At leading order the relevant contact set in the drop is the circular disc Ω_{L0} of radius α_L with centre $(X, Y) = (-\alpha_L, 0)$. At leading order with respect to ϵ, and on timescales much greater than t_D^*, equation (4.5a) shows that the profile is quasi-steady, with spatially uniform pressure. The overlay/circuit interface is pinned to the circular footprint except at the origin (*i.e.* on $\partial\Omega_{L0}/\{(0,0)\}$); at the origin we must instead match with the junction region. Since the height scale in the junction region is of $\mathrm{O}(\epsilon)$, the relevant matching condition is that the leading-order overlay/circuit interface approaches the origin as $(X, Y) \to (0, 0)$, with $(X, Y) \in \Omega_{L0}$. We note that the problem of finding the shape of a static pendant drop with constant gravity and constant surface tension has been well studied, in particular the interface profiles we will find have been documented in, e.g., [118].

We denote by $P_L(T)$, $P_R(T)$ and $V_L(T)$, $V_R(T)$ the leading-order pressures and volumes in the left- and right-hand drops, respectively. We introduce the polar co-ordinate $R = \sqrt{(X + \alpha_L)^2 + Y^2}$ measuring radial distance from the centre of the circular contact set of the left-hand drop (see Figure 3.2).

Since we are considering axisymmetric drops, the drop profile can be described by a curve in (R, Z)-space. We define s to be the distance along this curve from the apex (the drop height on the axis of symmetry) and Ψ to be the angle with the horizontal as shown in Figure 4.1. In this coordinate system and as described in e.g. [82], the problem for the new unknowns $\Psi(s, T)$, $R(s, T)$ and $H_L(s, T)$ the drop height, may be written in the form

$$\frac{\mathrm{d}\Psi}{\mathrm{d}s} = \mathrm{Bo}\, H_L - \frac{\sin\Psi}{R} + P_L, \tag{4.14a}$$

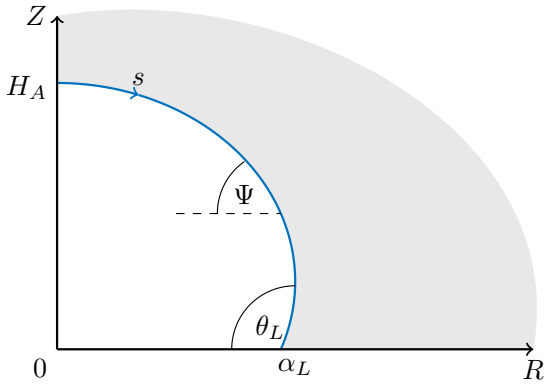


Figure 4.1: The new coordinate system: s is the arc length from the apex at $(0, H_A)$ and Ψ is the angle the curve makes with the horizontal. On the contact line $R = \alpha_L$ and the angle with the horizontal is the contact angle θ_L.

$$\frac{\mathrm{d}R}{\mathrm{d}s} = \cos\Psi, \tag{4.14b}$$

$$\frac{\mathrm{d}H_L}{\mathrm{d}s} = -\sin\Psi, \tag{4.14c}$$

for $0 < s < s^*$, where s^* corresponds to the point where the fluid boundary meets the base. The last equations (4.14b) and (4.14c) come from the geometry illustrated in Figure 4.1, while (4.14a) is found by substituting (4.14b) and (4.14c) into the normal component of the quasi-static balance of traction on the interface (4.10). The problem is axisymmetric so the interface makes an angle of zero with the horizontal at $s = 0$. The drop meets the pinned contact line at $s = s^*$, so the radius is zero at $s = 0$ and equal to α_L at s^*. As the drop problem is quasi-steady we will suppress the time dependence in what follows, thus the boundary conditions are now given by

$$\begin{aligned} \Psi(0) &= 0, \qquad R(0) = 0, \\ H_L(s^*) &= 0, \qquad R(s^*) = \alpha_L. \end{aligned} \tag{4.15}$$

There are five unknowns to solve for: the angle, radius and drop height Ψ, R and H_L respectively and two constants P_L and s^*. The problem is closed by prescribing the volume V_L. It will be convenient to write the volume constraint as an ODE, particularly when we come to find numerical solutions of this problem. In terms of

the new independent variable s the volume constraint becomes

$$V_L = -\pi \int_0^{s^*} R^2 \frac{\mathrm{d}H_L}{\mathrm{d}s}\, \mathrm{d}s. \tag{4.16}$$

We then define the function $v_L(s)$ satisfying

$$\frac{\mathrm{d}v_L}{\mathrm{d}s} = \pi R^2 \sin\Psi. \tag{4.17}$$

By comparison of with (4.17) with (4.16) we see that the boundary conditions are given by

$$v_L(0) = 0, \quad v_L(s^*) = V_L. \tag{4.18}$$

As was previously mentioned, we will not consider solutions for which H_L is negative, thus we only allow for contact angles in the range $[0, \pi]$, where the contact angle θ_L is defined as the angle the interface makes with the horizontal on the contact line, as shown in Figure 4.1. But as in the thin-film case, the advancing and receding contact angles will give a much more restrictive range of values. For general values of Bo, we look for numerical solutions of (4.14), (4.15), (4.17) and (4.18), as we shall describe in §4.3.3, but we begin by looking for analytic solutions when the Bond number is small.

4.3.2 Small Bond number

As $\mathrm{Bo} \to 0$ the effects of surface tension dominate those due to gravity and the drop forms a spherical cap [82]. We consider solutions to (4.14), (4.15), (4.17) and (4.18) which are perturbations to the spherical cap; this is a problem which has been well studied previously [19, 99]. When $\mathrm{Bo} \ll 1$, the angle Ψ increases monotonically with s, so we can use (4.14a) to eliminate s from the remaining equations (4.14b), (4.14c) and (4.17) to give

$$\frac{\mathrm{d}R}{\mathrm{d}\Psi} = \frac{R\cos\Psi}{(\mathrm{Bo}\, H_L + P_L)R - \sin\Psi}, \tag{4.19a}$$

$$\frac{\mathrm{d}H_L}{\mathrm{d}\Psi} = -\frac{R\sin\Psi}{(\mathrm{Bo}\, H_L + P_L)R - \sin\Psi}, \tag{4.19b}$$

$$\frac{\mathrm{d}v_L}{\mathrm{d}\Psi} = \frac{\pi R^3 \sin\Psi}{(\mathrm{Bo}\, H_L + P_L)R - \sin\Psi}, \tag{4.19c}$$

for $0 < \Psi < \theta_L$. In terms of the arc length s, the contact angle θ_L is defined as $\Psi(s^*) = \theta_L$, thus the boundary conditions (4.15) and (4.18) are now given by

$$R(0) = 0, \quad v_L(0) = 0, \tag{4.20}$$

$$H_L(\theta_L) = 0, \quad R(\theta_L) = \alpha_L, \quad v_L(\theta_L) = V_L. \tag{4.21}$$

We expand

$$R = R_0(\Psi) + \mathrm{Bo}\, R_1(\Psi) + \mathrm{O}\big(\mathrm{Bo}^2\big)\,, \tag{4.22}$$

$$H_L = H_{L0}(\Psi) + \mathrm{Bo}\, H_{L1}(\Psi) + \mathrm{O}\big(\mathrm{Bo}^2\big)\,, \tag{4.23}$$

$$v_L = v_{L0}(\Psi) + \mathrm{Bo}\, v_{L1}(\Psi) + \mathrm{O}\big(\mathrm{Bo}^2\big)\,, \tag{4.24}$$

$$P_L = P_{L0} + \mathrm{Bo}\, P_{L1} + \mathrm{O}\big(\mathrm{Bo}^2\big)\,, \tag{4.25}$$

$$\theta_L = \theta_{L0} + \mathrm{Bo}\, \theta_{L1} + \mathrm{O}\big(\mathrm{Bo}^2\big) \tag{4.26}$$

as $\mathrm{Bo} \to 0$. It follows from (4.19) that the leading-order solution corresponding to a spherical cap is given by

$$R_0 = \alpha_L \frac{\sin\Psi}{\sin\theta_{L0}}, \tag{4.27}$$

$$H_{L0} = \alpha_L \frac{\cos\Psi - \cos\theta_{L0}}{\sin\theta_{L0}}, \tag{4.28}$$

$$v_{L0} = \alpha_L^3 \frac{\pi\,(\cos^3\Psi - 3\cos\Psi + 2)}{3\sin^3\theta_{L0}}, \tag{4.29}$$

for $0 < \Psi < \theta_{L0}$. The corresponding leading-order pressure is given by

$$P_{L0} = \frac{2\sin\theta_{L0}}{\alpha_L}, \tag{4.30}$$

where θ_{L0} is determined from the volume constraint given by

$$V_L = \alpha_L^3 \frac{\pi\,(\cos^3\theta_{L0} - 3\cos\theta_{L0} + 2)}{3\sin^3\theta_{L0}}. \tag{4.31}$$

At O(Bo), (4.19) gives

$$(P_{L0}\,R_0 - \sin\Psi)\,\frac{\mathrm{d}R_1}{\mathrm{d}\Psi} + (P_{L0}\,R_1 + (H_0 + P_{L1})\,R_0)\,\frac{\mathrm{d}R_0}{\mathrm{d}\Psi} = R_1\cos\Psi, \tag{4.32}$$

$$(P_{L0}\,R_0 - \sin\Psi)\,\frac{\mathrm{d}H_1}{\mathrm{d}\Psi} + (P_{L0}\,R_1 + (H_0 + P_{L1})\,R_0)\,\frac{\mathrm{d}H_0}{\mathrm{d}\Psi} = -R_1\sin\Psi, \tag{4.33}$$

$$(P_{L0}\,R_0 - \sin\Psi)\,\frac{\mathrm{d}v_{L1}}{\mathrm{d}\Psi} + (P_{L0}\,R_1 + (H_0 + P_{L1})\,R_0)\,\frac{\mathrm{d}v_{L0}}{\mathrm{d}\Psi} = 3\pi R_0^2 R_1\sin\Psi, \tag{4.34}$$

for $0 \leq \Psi \leq \theta_{L0}$, with the boundary conditions

$$R_1(0) = 0, \quad v_{L1}(0) = 0, \tag{4.35a,b}$$

and

$$\theta_{L1}\frac{\mathrm{d}H_{L0}}{\mathrm{d}\Psi} + H_{L1} = 0, \quad \theta_{L1}\frac{\mathrm{d}R_0}{\mathrm{d}\Psi} + R_1 = 0, \quad \theta_{L1}\frac{\mathrm{d}v_{L0}}{\mathrm{d}\Psi} + v_{L1} = 0 \tag{4.36a–c}$$

on $\Psi = \theta_{L0}$. Using the boundary conditions (4.35) and (4.36a) the solutions of the O(Bo) equations (4.32)–(4.34) are given by

$$R_1 = \alpha_L\frac{2\,\cos^3\Psi - 3\cos\theta_{L0}\,\cos^2\Psi + 3\,\cos\theta_{L0} - 2 - 3P_{L1}\sin^2\Psi\,\sin\theta_{L0}}{6\sin^3\theta_{L0}\,\sin\Psi}, \tag{4.37}$$

$$\begin{aligned} H_{L1} = \alpha_L\frac{1}{6\sin^3\theta_{L0}}\Bigg[&2\log\left(\frac{1+\cos\Psi}{1+\cos\theta_{L0}}\right) + 6\theta_{L1}\sin^3\theta_{L0} \\ &- (\cos\Psi - \cos\theta_{L0})\,(3P_{L1}\sin\theta_{L0} - \cos\theta_{L0} + 2\cos\Psi)\Bigg], \end{aligned} \tag{4.38}$$

$$v_{L1} = \alpha_L^3\frac{\pi\,(\cos\Psi - 1)^2}{6\sin^5\theta_{L0}}\Bigg[(\cos\Psi + 2)\,(3\cos\theta_{L0} - 3P_{L1}\sin\theta_{L0} - 2\cos\Psi) - 3\Bigg]. \tag{4.39}$$

Our main interests are in determining how the pressure, volume and contact angle of the drop are related since these will determine the dynamics on the drainage timescale. The remaining boundary conditions (4.36b,c) and the solutions (4.37)–(4.39) then give next order terms for the pressure and contact angle

$$\theta_{L1} = \frac{\cos\theta_{L0} - 1}{6\sin\theta_{L0} + 3\sin(2\theta_{L0})}, \tag{4.40}$$

$$P_{L1} = \frac{2\,(\cos\theta_{L0} - 1)}{3\alpha_L\sin\theta_{L0}}. \tag{4.41}$$

The two term solutions are written with θ_{L0} as a parameter, which is determined from (4.31) for a fixed volume V_L. The pressure and contact angle are given by

$$P_L = \frac{2\sin\theta_{L0}}{\alpha_L} + \mathrm{Bo}\,\frac{2\alpha_L\,(\cos\theta_{L0}-1)}{3\sin\theta_{L0}} + O(\mathrm{Bo}^2), \tag{4.42}$$

$$\theta_L = \theta_{L0} + \mathrm{Bo}\,\frac{\cos\theta_{L0}-1}{6\sin\theta_{L0}+3\sin(2\theta_{L0})} + O(\mathrm{Bo}^2) \tag{4.43}$$

as $\mathrm{Bo}\to 0$. The O(Bo) terms in (4.42) and (4.43) are both negative for $0<\theta_{L0}<\pi$, so increasing the Bond number will reduce the drop pressure and contact angle. This observation is consistent with the thin-film asymptotics where the drop profile was given by a Bessel function (see (3.31)). As in §3.3.2, increasing the Bond number above zero tends to flatten the drop edges whereas decreasing it below zero has the reverse effect. The drop profile and the pressure and contact angle as a function of the drop volume are plotted in Figure 4.2 for a selection of Bond numbers (the red dashed lines)–the corresponding numerical solutions are also shown; we shall comment further on the agreement after first describing how the numerical solutions were obtained.

4.3.3 Order unity Bond numbers

We have just seen that, when $\mathrm{Bo}\ll 1$, approximate analytic solutions can be found for the volume, pressure and contact angle in an isolated drop. But, as can be seen in Table 2.2, the typical Bond numbers will often not be small. Now we turn our attention to finding numerical solutions of (4.14), (4.15), (4.17) and (4.18). Numerical solution of the Young-Laplace equation is well understood [51, 118], in particular, such solutions are used to determined the interfacial properties of fluids by comparing the numerical solutions with observations of real pendant drop profiles [11, 31, 68]. We begin by transforming the problem to a fixed domain; the equations are rescaled with s^* so that the boundary conditions can be imposed on $\hat{s}=0$ and $\hat{s}=1$, where $s=s^*\hat{s}$. To simplify the setup for our numerical solution the equations are rescaled so that the drop height at the origin is zero, as we shall now describe. Recall that

H_D is defined as the maximum dimensional drop height (as shown in Figure 2.1), the dimensionless height of the drop apex is then $H_A = H_D/L$. We let $\widetilde{H}_L = H_L - H_A$ so that $\widetilde{H}_L(0) = 0$. Defining $\widetilde{P}_L = P_L - \mathrm{Bo}\, H_A$, the system (4.14), (4.15), (4.17) and (4.18) becomes

$$\frac{\mathrm{d}\Psi}{\mathrm{d}\hat{s}} = s^* \left(\mathrm{Bo}\, \widetilde{H}_L - \frac{\sin\Psi}{R} + \widetilde{P}_L \right), \tag{4.44a}$$

$$\frac{\mathrm{d}R}{\mathrm{d}\hat{s}} = s^* \cos\Psi, \tag{4.44b}$$

$$\frac{\mathrm{d}\widetilde{H}_L}{\mathrm{d}\hat{s}} = -s^* \sin\Psi, \tag{4.44c}$$

$$\frac{\mathrm{d}v_L}{\mathrm{d}\hat{s}} = s^* \pi R^2 \sin\Psi, \tag{4.44d}$$

for $0 < \hat{s} < 1$, with the boundary conditions

$$\Psi(0) = 0, \quad R(0) = 0, \quad v_L(0) = 0, \quad \widetilde{H}_L(0) = 0, \tag{4.45}$$

$$R(1) = \alpha_L, \quad v_L(1) = V_L. \tag{4.46}$$

As $R \to 0^+$ the numerical solution will break down due to the singularity in (4.44a). This can be avoided by exploiting a Taylor expansion at $\hat{s} = 0$ which yields a system of algebraic equations for the coefficients that can be easily solved to give, as $\hat{s} \to 0^+$

$$\Psi \sim \Psi_{\hat{s}}(\hat{s}) = \frac{s^* \widetilde{P}_L}{2}\hat{s} - \frac{s^{*3}\mathrm{Bo}\, \widetilde{P}_L}{16}\hat{s}^3 + \frac{s^{*5}\mathrm{Bo}\, \widetilde{P}_L(\widetilde{P}_L^2 + 5\mathrm{Bo})}{1920}\hat{s}^5, \tag{4.47}$$

$$R \sim R_{\hat{s}}(\hat{s}) = s^*\hat{s} - \frac{s^{*3}\widetilde{P}_L^2}{24}\hat{s}^3 + \frac{s^{*5}\widetilde{P}_L^2(\widetilde{P}_L^2 + 12\mathrm{Bo})}{1920}\hat{s}^5, \tag{4.48}$$

$$\widetilde{H}_L \sim \widetilde{H}_{L\hat{s}}(\hat{s}) = \frac{s^{*2}\widetilde{P}_L}{4}\hat{s}^2 + \frac{s^{*4}\widetilde{P}_L(\widetilde{P}_L^2 + 3\mathrm{Bo})}{192}\hat{s}^4 \tag{4.49}$$

$$- \frac{s^{*6}\widetilde{P}_L(10\mathrm{Bo}^2 + 32\mathrm{Bo}\widetilde{P}_L^2 + \widetilde{P}_L^4)}{23040}\hat{s}^6, \tag{4.50}$$

$$v_L \sim v_{L\hat{s}}(\hat{s}) = \frac{\pi s^{*4}\widetilde{P}_L}{8}\hat{s}^4 - \frac{\pi s^{*6}\widetilde{P}_L(\widetilde{P}_L^2 + \mathrm{Bo})}{96}\hat{s}^6, \tag{4.51}$$

with error terms of order $\hat{s}^7$, $\hat{s}^7$, $\hat{s}^8$ and $\hat{s}^8$, respectively. There are still two degrees of freedom in these local expansions, namely $\widetilde{P}_L$ and s^*, which need to be found as part of the solution. We can now shift the boundary at $\hat{s} = 0$ away from the singularity

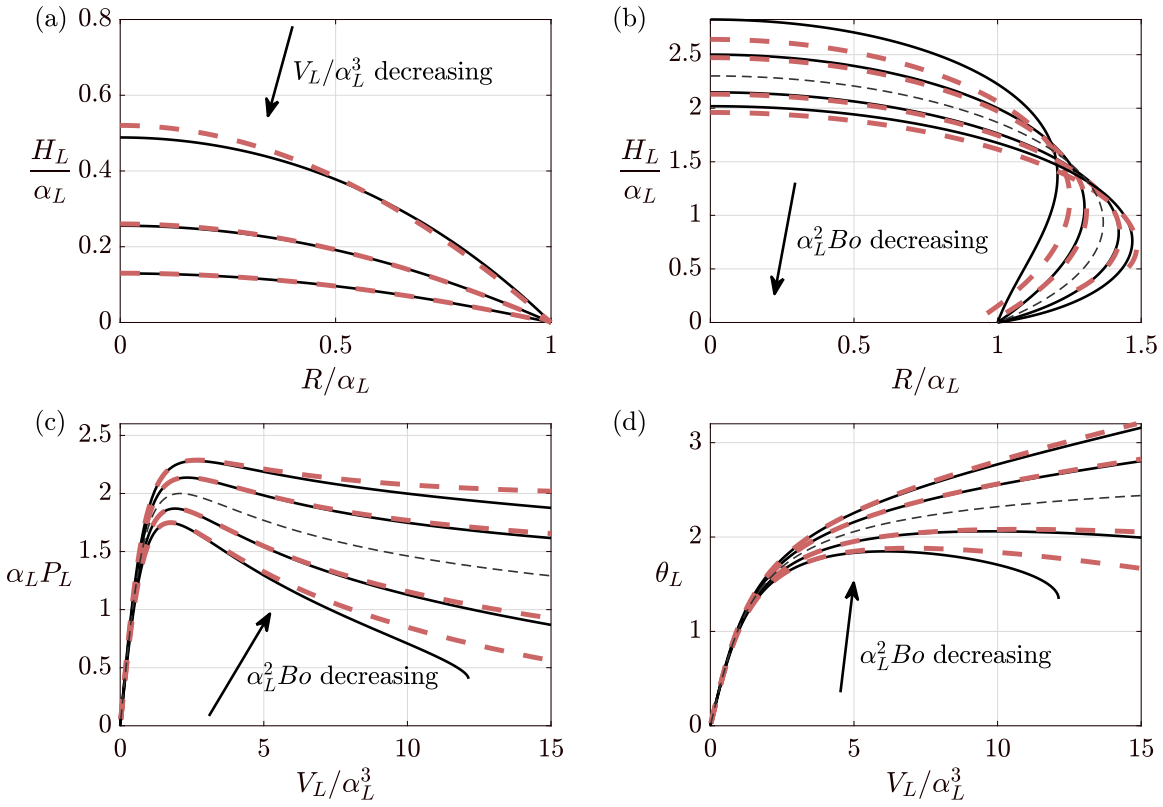


Figure 4.2: (a) Comparison of the thin-film drop profile (3.31) with the numerical solution of (4.44) and (4.52) for $V_L/\alpha_L^3 = 0.2, 0.4, 0.8$. (b)–(d) Comparison of the small Bond number asymptotics from §4.3.2 to the numerical solution of (4.44) and (4.52) for $\alpha_L^2 \mathrm{Bo} = -0.4, -0.2, 0.2, 0.4$. The dashed line in the middle is the exact solution for $\mathrm{Bo} = 0$. In each case the dashed lines are the asymptotic solution and solid lines the numerical. (b) The asymptotic drop profiles are given by (4.27), (4.28), (4.37) and (4.38). (c) The asymptotic solution pressure as a function of volume given by (4.31), (4.41) and (4.42). (d) The asymptotic solution for the contact angle as a function of drop volume given by (4.31), (4.40) and (4.43).

to $s^* = \varepsilon$ for some $\varepsilon \ll 1$ and solve in the range $\hat{s} \in (\varepsilon, 1)$. The boundary conditions are then replaced by

$$\Psi(\varepsilon) = \Psi_{\hat{s}}(\varepsilon), \quad R(\varepsilon) = R_{\hat{s}}(\varepsilon), \quad v_L(\varepsilon) = v_{L\hat{s}}(\varepsilon), \quad \widetilde{H}_L(\varepsilon) = \widetilde{H}_{L\hat{s}}(\varepsilon),$$
$$R(1) = \alpha_L, \quad v_L(1) = V_L. \tag{4.52}$$

The system (4.44) together with the boundary conditions (4.52) is now in a form in which it can be solved numerically. This is undertaken in MATLAB using the *BVP5C* boundary value problem solver, where the unknown parameters s^* and $\widetilde{P}_L$ are found as part of the solution. The solver *BVP5C* is fifth order accurate [64] and

we impose relative and absolute tolerances of 10^{-8}. The boundary value problem (BVP) solver also requires an initial guess at the solution for which we use the small Bond number solutions from §4.3.2. We first note that, when $\mathrm{Bo} > 0$, the volume of the drops cannot be increased indefinitely. Eventually the mass of fluid will be greater than can be held together by surface tension. In practice some of the fluid would detach from the drop, referred to as pinch off [54, 86]. Our numerical solutions fail to converge beyond a maximum volume $V_{\max}$. Beyond this threshold we are unable to find any steady-state solutions. The numerical value for $V_{\max}$ is found by solving (4.44) and (4.52) for increasing values of V_L until the solution fails to converge despite careful control of the continuation parameter V_L. Figure 4.2 shows how the numerical solution compares with the small Bond number asymptotics; we see good agreement below $V_{\max}$ as the Bond number is decreased. But the small Bond number asymptotics are unable to tell us anything about the maximum volume since (4.31) is valid for all $\theta_{L0} > 0$.

4.3.4 Non-uniqueness of solutions

In §4.3.3 we saw that, for positive Bond numbers, the numerical solutions only converge below a maximum volume, beyond which we expect the assumption of equilibrium to no longer be valid. While this non-equilibrium behaviour is outside the scope of this thesis, we have been able to find more solutions below the maximum volume by careful continuation as we shall shortly describe. The solutions we will describe are well known and have been studied in some of the earliest work on the Young-Laplace equation [115, 118], though the implications of these solutions on the flow in a microfluidic device appears to be novel. The central panel of Figure 4.3 shows an example of how the pressure and volume are related for $\alpha_L = 1$, $\mathrm{Bo} = 1.2$, with the panels either side showing some of the possible profiles for $V_L = 3$. The shape of the curve in the central panel is typical for all $\mathrm{Bo} > 0$; as the Bond number

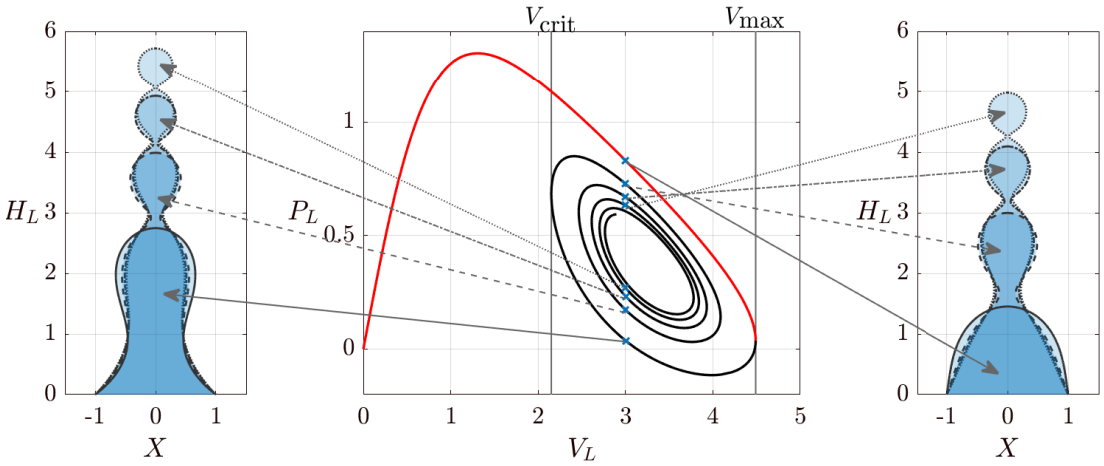


Figure 4.3: Numerical solution of (4.14) and (4.15) fixing either the pressure or the volume and finding the other as part of the solution for Bo $= 1.2$ and $\alpha_L = 1$. A variety of profiles are shown each with the same volume ($V_L = 3$) but a different pressure. Beyond $V_{\text{max}} \approx 4.5$ solutions do not appear to exist and between $V_{\text{crit}} \approx 2.2$ and V_{max} multiple solutions exist.

is increased the maxima in both V_L and P_L decrease. The extra solutions in Figure 4.3 require more effort to find. The trajectory near the extrema is difficult to track as the problem becomes increasingly stiff. As a local maximum or minimum in V_L is approached, we instead prescribe $\widetilde{P}_L$ in (4.44a) and solve only (4.44a)–(4.44c); the volume is then found by solving (4.16). As a local extrema in $\widetilde{P}_L$ is approached we switch back to solving the full system. In either case we need to use a previous solution for the initial guess in the BVP solver. The picture is more complicated than for a thin drop as in the previous chapter; a given volume may have many steady states each with a different pressure. There may in fact be infinitely many solutions for a given drop volume and parameter set [83]. As indicated in Figure 4.3, for a fixed volume, new solutions can be found with increasing numbers of bulges, or "lobes", as more lobes are added the volume of each decreases, while the total remains the same. For a given Bond number Bo there appears to be a volume V_{crit} beyond which there will be multiple steady-state solutions, though we would not expect them all to be stable to small perturbations. The critical volume as a function of the Bond number

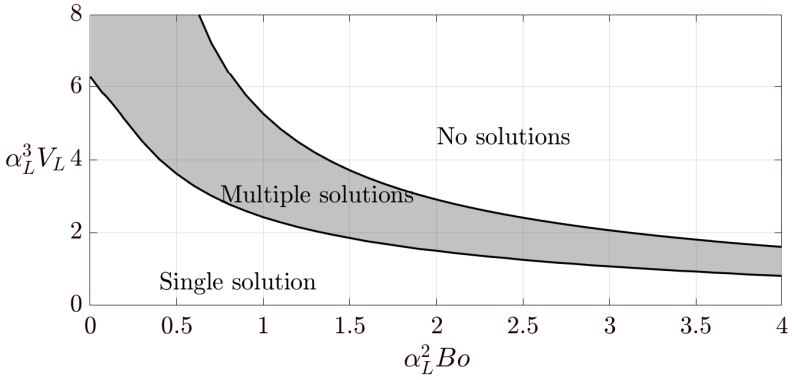


Figure 4.4: The regime diagram showing when there are multiple solutions for a given drop volume and Bond number. The lower line forming the boundary between single and multiple solutions is given by V_{crit} and the upper line is given by $V_{\max}$.

is calculated by finding the smallest volume V_L for which there are two solutions. Combining this with the numerical maximum $V_{\max}$ divides the parameter space into three regions in which there are: no solutions, one solution and multiple solutions. The corresponding regime diagram is plotted in Figure 4.4. We note that as $\text{Bo} \to 0^+$ the critical volume tends to a constant $V_{\text{crit}} \to 2\pi$. We can see why this is the case by considering what happens to a two lobed solution as $\text{Bo} \to 0^+$. Each of the lobes will tend to a circular arc as $\text{Bo} \to 0^+$, while the neck region (the region that connects the lobes) will shrink; with the profile ultimately resembling a circle of radius one on top of a semicircle of radius one, which corresponds to a volume of 2π. However, we note that when $\text{Bo} = 0$ this two lobed solution would not exist since the free boundary would not be smooth. Asymptotic solutions can be found for the neck regions [83], but they are beyond the scope of this thesis. In fact we find that there will not be multiple solutions for any volume if $\text{Bo} \leq 0$. When $\text{Bo} < 0$ the profiles tend to flatten out and we do not see the formation of neck regions.

4.3.5 Summary

We have seen in this section that there are several cases where our analysis cannot determine the pressure for a given volume; this may be because our steady state

assumption is no longer valid or because there are multiple possible steady state solutions for a given volume. In either case we would need to consider the dynamics. To give an accurate prediction of the flow rate it will be important to keep the volumes in either drop below $V_{\rm crit}$, as shown in Figure 4.3 and in practice this may represent an important working constraint. Violating this constraint entails in general access to an extensive number of profiles as predicted by the numerical solution of (4.44) and (4.46), though these are not necessarily all stable and may result in pinch off.

4.4 Quasi-steady solution in the conduit

We recall that the footprint of the non-dimensional conduit is a rectangle of width 2ϵ and length 1 and that the interface has zero height on the long edges of the conduit. In §4.1 we deduced that the height in the conduit scales with ϵ^2. Hence the leading-order problem and solution must be identical to that in §3.3.3, but to see this here we shall derive the solution directly from the Navier-Stokes equations (rather than from the thin-film equations as in chapter 3). The flow in the overlaying fluid is driven entirely by the flow in the conduit and we assume that this flow decays on the length scale of the conduit width. Thus we rescale with

$$Y = \epsilon\,\widehat{y}, \quad Z = \begin{cases} \epsilon^2\,\widehat{z} & \text{for } Z \in \Gamma_1, \\ \epsilon\widehat{Z} & \text{for } Z \in \Gamma_2, \end{cases} \qquad H = \epsilon^2\,h_C. \tag{4.53}$$

We then make the expansions

$$\begin{aligned} P_1 &\sim p_{C0}(X,\widehat{y},T) + \epsilon p_{C1}(X,\widehat{y},T), \\ h_C &\sim h_{C0}(X,\widehat{y},T) + \epsilon h_{C1}(X,\widehat{y},T), \\ U_i &\sim U_{i0}(X,\widehat{y},\widehat{z},T) + \epsilon U_{i1}(X,\widehat{y},\widehat{z},T), \\ V_i &\sim V_{i0}(X,\widehat{y},\widehat{z},T) + \epsilon V_{i1}(X,\widehat{y},\widehat{z},T), \\ W_i &\sim W_{i0}(X,\widehat{y},\widehat{z},T) + \epsilon W_{i1}(X,\widehat{y},\widehat{z},T), \end{aligned} \tag{4.54}$$

as $\epsilon \to 0$ for $i = 1, 2$. Assuming that $\epsilon^4 \mathrm{Re}_2 \ll 1$, at leading order (4.5a) gives

$$\frac{\partial^2 U_{10}}{\partial \widehat{z}^2} = \frac{\partial p_{C0}}{\partial X}, \quad \frac{\partial p_{C0}}{\partial \widehat{y}} = 0, \quad \frac{\partial p_{C0}}{\partial \widehat{z}} = 0 \tag{4.55}$$

for $0 < X < 1$, $0 < \widehat{y} < 1$, $0 < \widehat{z} < h_{C0}$. Thus p_{C0} is a function of X and T only. As can be seen in Table 2.1, the typical viscosities of the liquids used are within a multiplicative factor of about four. Thus, we assume that $\mu_2/\mu_1 = \mathrm{O}(1)$ as $\epsilon \to 0$. Considering just the flow in the conduit, the no-slip boundary condition on the base and the tangential component of the stress balance (4.10) give the boundary conditions

$$U_{10} = 0 \quad \text{on } \widehat{z} = 0, \tag{4.56}$$

$$\frac{\partial U_{10}}{\partial \widehat{z}} = 0 \quad \text{on } \widehat{z} = h_{C0}. \tag{4.57}$$

The leading-order velocity in the conduit is then given by

$$U_{10} = \frac{1}{2}\left(\widehat{z}^2 - 2\,h_{C0}\widehat{z}\right)\frac{\partial p_{C0}}{\partial X} \quad \text{for } 0 < X < 1. \tag{4.58}$$

Assuming that $\epsilon^2\mathrm{Bo} \ll 1$, the normal component of the stress balance (4.10) gives

$$\frac{\partial^2 h_{C0}}{\partial \widehat{y}^2} = -p_{C0} \quad \text{for } -1 < \widehat{y} < 1, \tag{4.59}$$

where the height is zero on $|\widehat{y}| = 1$. The equations we have just derived are the same governing equations for the fluid velocity and interface height in the conduit encountered in §3.3.3, although we recall that the dimensionless height and velocity in the circuit were additionally rescaled with δ in the thin-film case as can be seen in (3.2), whereas now $\delta = \mathrm{O}(1)$. In §4.1 we showed that the conduit cross-section area and flux are rescaled with $A^* = a_0^3/L\widehat{A}$ and $Q^* = \gamma a_0^7/(\mu_1 L^5)\widehat{Q}$, respectively, where $\widehat{A}$ and $\widehat{Q}$ are defined as

$$\widehat{A}\,(X,T) = \int_{-\epsilon}^{\epsilon} H \,\mathrm{d}Y, \quad \widehat{Q}\,(X,t) = \int_{-\epsilon}^{\epsilon}\int_{0}^{H} U_1 \,\mathrm{d}Z\,\mathrm{d}Y. \tag{4.60a,b}$$

Making the further expansions $\widehat{A} \sim \widehat{A}_0 + \epsilon\widehat{A}_1$ and $\widehat{Q} \sim \widehat{Q}_0 + \epsilon\widehat{Q}_1$ as $\epsilon \to 0$, it follows that the leading-order expressions for the interface height and the area and flux in the conduit are given by

$$h_{C0} = \frac{p_{C0}}{2}\left(1 - \widehat{y}^2\right), \quad \widehat{A}_0 = \frac{2}{3}\epsilon^3 p_{C0}, \quad \widehat{Q}_0 = -\frac{1}{35}\epsilon^7\frac{\partial}{\partial X}\left(p_{C0}^4\right). \tag{4.61a–c}$$

Hence we recover the thin-film results as in chapter 3.

4.5 Quasi-steady problem in the junction region

The junction regions connecting the conduit to the drops are indicated by the boxes in Figure 3.1. Without loss of generality we will consider only the junction connecting the conduit to the left-hand drop. As shown in Table 4.1 we use the width scale of the conduit to rescale in the junction region:

$$\boldsymbol{X} = \epsilon\,(\widetilde{x}, \widetilde{y}, \widetilde{z})\,, \quad H = \epsilon\,\widetilde{h}. \tag{4.62}$$

The velocity scale in the junction is the same as the velocity scale in the conduit and the pressure scale is the same as in the drops, *i.e.* the scales that we have already used to non-dimensionalise the governing equations via (4.62). Thus, the resulting problem in the junction region is very similar to the problem in §3.3.4. We began this chapter by rescaling the governing equations on the timescale of relaxation along the conduit length $t^* = t^*_{CL}T$, where $t^*_{CL} \sim \mu_1/(L\gamma)\,\epsilon^{-4}$. Since the junction region relaxes on the much faster timescale $t^*_J \sim \mu_1/(L\gamma)\,\epsilon$ the equations that we derive will be quasi-steady.

The contact set is as illustrated in Figure 4.6; the support of the drop fills the left half-plane while that of the conduit fills the semi-infinite strip $|\widetilde{y}| < 1$, $\widetilde{x} \geq 0$. The interface height in the junction region is governed by the normal component of (4.10) and (4.11), with the solution needing to match with the conduit solution as $\widetilde{x} \to \infty$ and with the drop solution as $\widetilde{x}^2 + \widetilde{y}^2 \to \infty$ in the left half-plane, with zero height on the contact line. Matching the film thickness of the drop and the conduit will require us to proceed to second order, so we expand $\widetilde{h} \sim \widetilde{h}_0(\widetilde{x}, \widetilde{y}, T) + \epsilon\widetilde{h}_1(\widetilde{x}, \widetilde{y}, T)$, $P \sim p_{J0}(\widetilde{x}, \widetilde{y}, T) + \epsilon p_{J1}(\widetilde{x}, \widetilde{y}, T)$ and $\kappa \sim \kappa_0(\widetilde{x}, \widetilde{y}, T) + \epsilon\kappa_1(\widetilde{x}, \widetilde{y}, T)$ as $\epsilon \to 0$. For ease of analysis we consider the case $\theta_L < \pi/2$, so that the drop does not impinge on the junction region, which is typical in practice. We thus assume that the interface height in the junction is single valued. Expanding (4.5a) with these expansions and using

the length scales in (4.62) shows that

$$\boldsymbol{\nabla} p_{J0} = \mathbf{0}, \quad \boldsymbol{\nabla} p_{J1} = \mathbf{0}. \tag{4.63}$$

Since there is zero flux through the boundary and the pressure matches with the constant pressure in the drop as $\widetilde{x}^2 + \widetilde{y}^2 \to \infty$ for $\widetilde{x} < 0$ we deduce that the pressure in the junction region is spatially uniform at leading- and next-to-leading-order and thus the pressures in the drop and conduit match at the junctions as before.

The equations governing the interface height are found by expanding the normal component of (4.10). When the interface height is single-valued, we can write the mean curvature as

$$\kappa = \boldsymbol{\nabla} \cdot \left(\frac{\nabla (Z - H)}{|\nabla (Z - H)|} \right). \tag{4.64}$$

Using the scalings in (4.62) and expanding $\kappa \sim \kappa_0/\epsilon + \kappa_1$ as $\epsilon \to 0$ we find the leading- and next-order curvature to be given by

$$\kappa_0 = \boldsymbol{\nabla} \cdot \left(\frac{\nabla \Phi}{|\nabla \Phi|} \right), \quad \kappa_1 = \boldsymbol{\nabla} \cdot \left(\nabla \widetilde{h}_1 \left(\frac{1}{|\nabla \Phi|} + \frac{\nabla \Phi \cdot \nabla \Phi}{|\nabla \Phi|^3} \right) \right) \tag{4.65}$$

where $\Phi = (\widetilde{z} - \widetilde{h}_0)$. The interface height in the junction is then governed by

$$\kappa_0 = 0, \quad \kappa_1 = -p_{J0}, \tag{4.66}$$

the thick drop generalisation of the equations for $\widetilde{h}_0$ and $\widetilde{h}_1$ in Figure 3.4. At leading order the interface meets the pinned contact line and its height also tends to zero in the conduit as $\widetilde{x} \to \infty$ since the interface height is $\mathrm{O}(\epsilon)$ there. The matching condition in the drop is found by expanding the system of ODEs governing the drop height (4.14) and (4.15) close to the contact line. In general we cannot find analytic solutions to the expanded equations since the drop height may be multi-valued, as shown in Figure 4.3. As shown in Figure 4.5 the maximum contact angle for which solutions to (4.14) and (4.15) exist only exceeds $\pi/2$ when $\alpha_L^2 \mathrm{Bo} \lessapprox 0.8$. Further, for smaller positive Bond numbers there is a greater range of volumes for which solutions

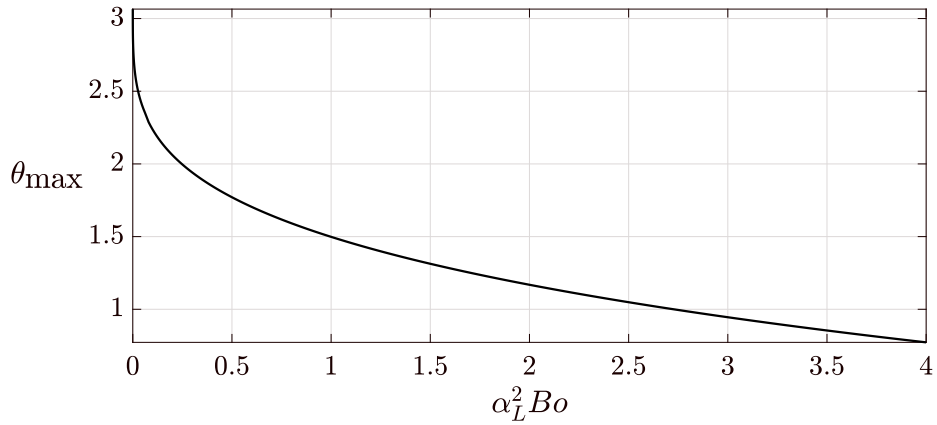


Figure 4.5: The maximum contact angle in a drop as a function of the Bond number.

to (4.14) and (4.15) exist with contact angles less than $\pi/2$. On the other hand, when the Bond number is large and negative, the contact angle will often be greater than $\pi/2$ (as illustrated for small negative Bond numbers in Figure 4.2). We anticipate that for the typical physical parameters used in experiments (see Table 2.1) the constraint $\theta_L < \pi/2$ will not be too restrictive.

The equations governing the drop height are given by (4.14) and (4.15). Close to the contact line the radius R increases monotonically with s and we can rewrite the equations as

$$\frac{\mathrm{d}\Psi}{\mathrm{d}R} = \frac{1}{\cos\Psi}\left(\mathrm{Bo}\, H_L - \frac{\sin\Psi}{R} + P_L\right), \tag{4.67a}$$

$$\frac{\mathrm{d}H_L}{\mathrm{d}R} = -\tan\Psi, \tag{4.67b}$$

subject to the boundary conditions

$$\Psi(\alpha_L) = \theta_L, \quad H_L(\alpha_L) = 0. \tag{4.68}$$

We rescale the drop radius with $R = \alpha_L + \epsilon\widetilde{r}$ and the drop height with $H_L = \epsilon\widetilde{h}_L$ and expand $\Psi(\widetilde{r}) \sim \Psi_0(\widetilde{r}) + \epsilon\Psi_1(\widetilde{r})$ and $H_L(\widetilde{r}) \sim \widetilde{h}_{L0}(\widetilde{r}) + \epsilon\widetilde{h}_{L1}(\widetilde{r})$ as $\epsilon \to 0$. At leading order (4.67) gives

$$\frac{\mathrm{d}\Psi_0}{\mathrm{d}\widetilde{r}} = 0, \tag{4.69}$$

$$\frac{\mathrm{d}\widetilde{h}_{L0}}{\mathrm{d}\widetilde{r}} = -\tan\Psi_0, \tag{4.70}$$

and the boundary conditions (4.68) become $\widetilde{h}_{L0}(0) = 0$ and $\Psi_0(0) = \theta_L$. The leading-order solutions are readily found to be given by

$$\Psi_0 = \theta_L, \quad \widetilde{h}_{L0} = -\tan\Psi_0\,\widetilde{r}. \tag{4.71}$$

At $\mathrm{O}(\epsilon)$ the governing equations (4.68) give

$$\frac{\mathrm{d}\Psi_1}{\mathrm{d}\widetilde{r}} = \frac{1}{\cos\Psi_0}\left(P_L - \frac{\sin\Psi_0}{\alpha_L}\right), \tag{4.72}$$

$$\frac{\mathrm{d}\widetilde{h}_{L1}}{\mathrm{d}\widetilde{r}} = -\left(1+\tan^2\Psi_0\right)\Psi_1, \tag{4.73}$$

with the boundary conditions $\widetilde{h}_{L1}(0) = 0$ and $\Psi_1(0) = 0$. The solutions are then found to be given by

$$\Psi_1 = \frac{1}{\cos\Psi_0}\left(P_L - \frac{\sin\Psi_0}{\alpha_L}\right)\widetilde{r}, \quad \widetilde{h}_{L1} = -\frac{1+\tan^2\Psi_0}{2\cos\Psi_0}\left(P_L - \frac{\sin\Psi_0}{\alpha_L}\right)\widetilde{r}^2. \tag{4.74}$$

In the terms of the junction variables $\widetilde{x}$ and $\widetilde{y}$ we can write $\widetilde{r}$ as

$$\widetilde{r} = \frac{\sqrt{\left(\epsilon\widetilde{x}+\alpha_L\right)^2 + \epsilon^2\widetilde{y}^2} - \alpha_L}{\epsilon}, \tag{4.75}$$

$$\widetilde{r} \sim \widetilde{x} + \epsilon\frac{\widetilde{y}^2}{2\,\alpha_L} \quad \text{as } \epsilon \to 0. \tag{4.76}$$

Expanding $\widetilde{h}_{L0}$ and $\widetilde{h}_{L1}$ gives the two term expansion of the far field drop boundary condition in the junction region:

$$\widetilde{h}_L \sim -\tan(\theta_L)\,\widetilde{x} + \epsilon\left(\frac{\tan(\theta_L)}{2\alpha_L}\left(\widetilde{x}^2 - \widetilde{y}^2\right) + \frac{\sin^3(\theta_L) - \alpha_L P_L}{2\alpha_L\cos^3(\theta_L)}\widetilde{x}^2\right). \tag{4.77}$$

As $\theta_L \to 0$ we recover the expansion used for the thin-film asymptotics in §3.3.4. At second order the interface height is still zero on the contact line in the conduit, but on $\widetilde{x} = 0$ we have to take account of the curvature of the contact line. In the conduit the far-field condition for the junction comes from matching with the conduit solution given by (4.61a). The leading- and second-order problems are summarised in Figure 4.6.

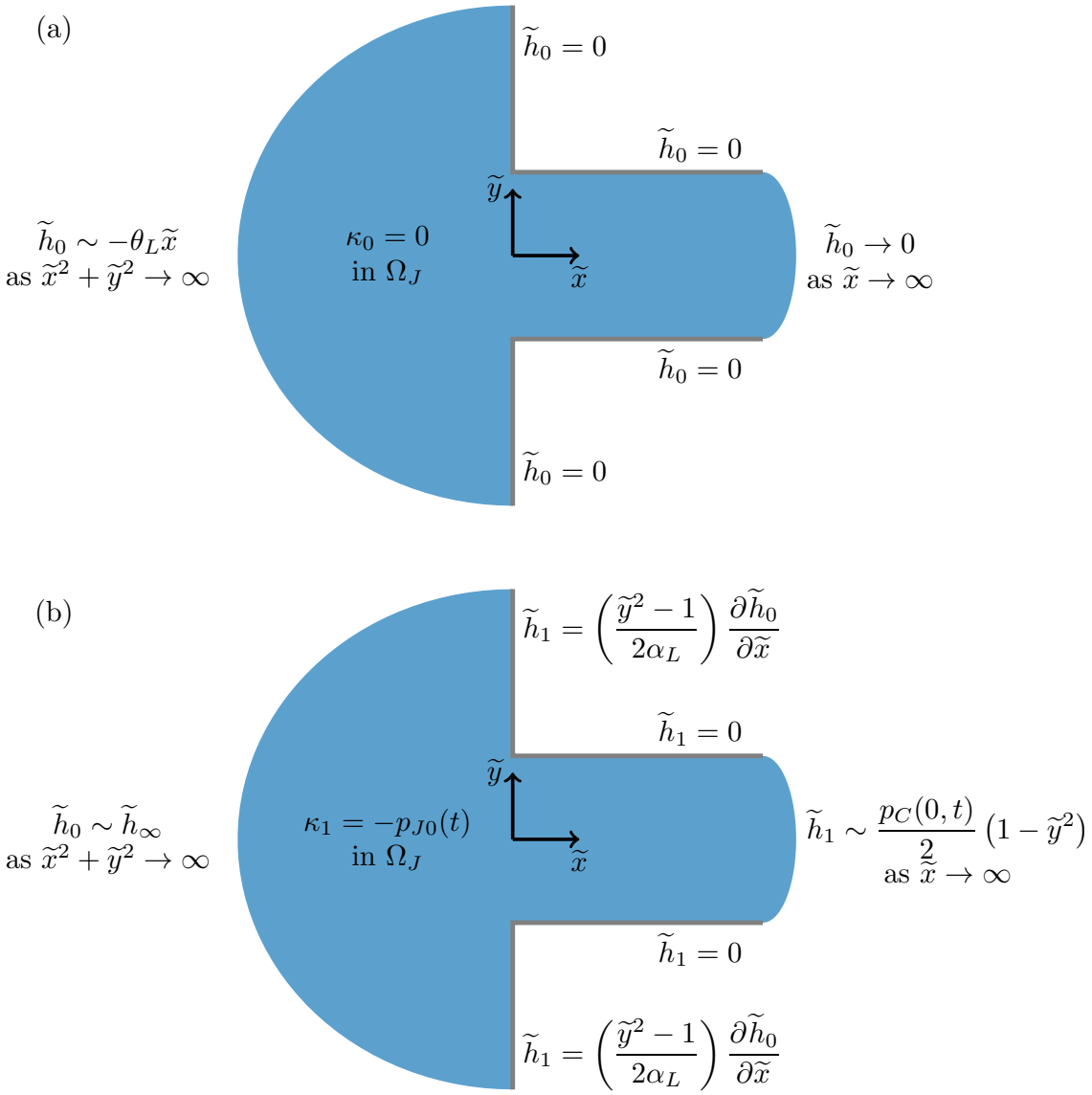


Figure 4.6: (a) The leading-order problem in the junction region. (b) The second-order problem in the junction region, where $\widetilde{h}_\infty$ is the O(ϵ) term in (4.77).

This junction problem does not present such a clear method of solution as we found for the thin-film asymptotics in §3.3.4 (see (3.64)) and will not be investigated further. We can proceed to consider the volume balances on the drop drainage timescale simply by noting that the pressure is spatially uniform in the junction, so that

$$p_{J0}(T) = P_L(T) = p_C(\widetilde{x} = 0, T). \tag{4.78}$$

In addition, in the thin-film model in chapter 3 our analysis of the junction region

showed that there are singularities in the gradient of the interface at the corners. We anticipate the same behaviour when the drops are thick. Therefore, the contact line in the junction region will smooth out on the length scale of the conduit width so that the contact angle is everywhere between the receding and advancing values, but this will not affect the leading-order dynamics.

4.6 Droplet drainage

In §4.4 we showed that, on the timescale of conduit relaxation, the rescaled conduit area and flux are given by the same expressions as in the thin-film asymptotics of chapter 3 via (4.61). Thus, we can also write the conservation of mass equation (2.14) in the same form as in chapter 3:

$$\frac{\partial p_{C0}}{\partial \tau} = \frac{\partial^2}{\partial X^2}\left(p_{C0}^4\right) \quad \text{for } 0 < X < 1,\, \tau > 0, \tag{4.79}$$

where $T = (70/3)\,\tau$. In (4.78) we summarised that the pressure at left- and right-hand ends of the conduit will be equal to the corresponding drop pressure, and since $T_{DD} \gg T_{CL}$, the leading-order drop pressures will be equal to their initial values, the boundary conditions for (4.79) are given by

$$p_{C0}(0,\tau) = P_L(0), \quad p_{C0}(1,\tau) = P_R(0) \quad \text{for } \tau > 0. \tag{4.80a,b}$$

We close the problem by prescribing an initial profile consistent with (4.80) and of the form

$$p_{C0}(X,0) = \mathscr{P}(X) \quad \text{for } 0 < X < 1. \tag{4.81}$$

The dimensionless conduit relaxation problem (4.79)–(4.81) is identical to the dimensionless problem in the thin-film limit (see (3.89)–(3.91)) and hence the long-time attractor is given by

$$p_{C0} \to \left(\left(P_L^4 - P_L^4\right) X + P_L^4\right)^{\frac{1}{4}} \quad \text{as } \tau \to \infty. \tag{4.82}$$

Thus, on the drainage timescale, the flux is given by

$$\widehat{Q}_0 \sim \epsilon^7 \frac{P_L^4 - P_R^4}{35} \quad \text{as } \epsilon \to 0. \tag{4.83}$$

Difficulty arises when we try to write (4.83) as a function of the left- and right-hand drop volumes. As illustrated in Figure 4.3, the dependence of the drop pressure on the volume is not as simple as it was in the thin-film case; there may be multiple profiles corresponding to a given volume when Bo > 0. However, as discussed in §4.3.4, we anticipate that most of these solutions are unlikely to be physically relevant. Without modelling the dynamics on the timescale of capillary action in the drops we cannot say for certain which shape the drop will take. We make the physically justified assumption that the disturbances to the drop shape are small enough that the pressure changes continuously with the volume. We further assume that the initial drop profiles lie on the upper part of the curve illustrated in Figure 4.3, centre, for $0 < V_L < V_{\max}$, so we only need to consider this part of the curve. This may be controlled for in practice when the drop is printed. We define the functions $\mathcal{P}_L(V_L;\, \alpha_L, \mathrm{Bo})$ and $\mathcal{P}_R(V_R;\, \alpha_R, \mathrm{Bo})$ to be the positive pressures on the uppermost branch of the volume pressure relation in the left- and right-hand drops respectively. Further examples of $\mathcal{P}_L(V_L;\, \alpha_L, \mathrm{Bo})$ are shown in Figure 4.7 for a range of Bond numbers. The leading-order volumes in the left- and right-hand drops in (2.15) are then given by

$$\frac{\mathrm{d}V_L}{\mathrm{d}T} \sim -\epsilon^3 \frac{\mathcal{P}_L(V_L)^4 - \mathcal{P}_R(V_R)^4}{35}, \quad \frac{\mathrm{d}V_R}{\mathrm{d}T} \sim \epsilon^3 \frac{\mathcal{P}_L(V_L)^4 - \mathcal{P}_R(V_R)^4}{35}. \tag{4.84a,b}$$

A very similar argument to the one given in (3.94) shows that when $\epsilon \ll 1$, most of the fluid is contained in the drops and the total volume in the circuit, governed by (3.24), reduces to

$$V_L + V_R = V_T \tag{4.85}$$

at this level of approximation. We therefore only need to solve one of the ODEs given in (4.84): making the rescaling $T = 35\epsilon^{-3}\mathcal{T}$ we solve

$$\frac{\partial V_L}{\partial \mathcal{T}} = -\left(\mathcal{P}_L(V_L)^4 - \mathcal{P}_R(V_T - V_L)^4\right), \tag{4.86}$$

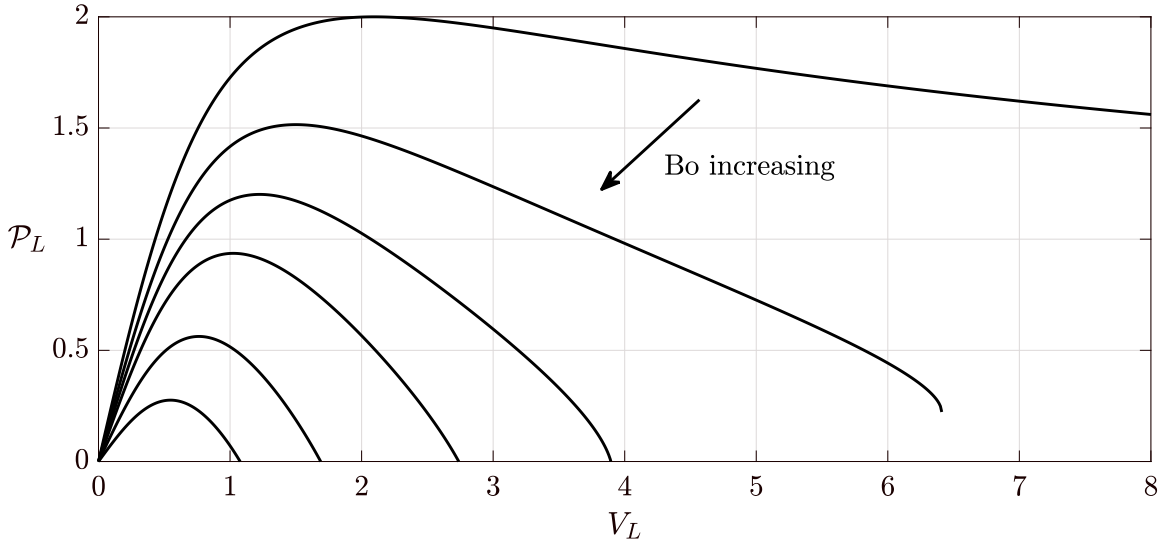


Figure 4.7: The drop pressure as a function of drop volume for the droplet drainage model with $\alpha_L = 1$ and $\mathrm{Bo} = 0, 0.8, 1.4, 2, 3, 4$.

subject to the initial condition

$$V_L(0) = \mathscr{V}. \tag{4.87}$$

Via (3.99) from §3.3.6 we showed that in the thin-film regime the drop volumes tend to a single steady state which depends on the relative base radii of the drops. This steady state occurs when the pressures in the two drops are equal, but Figure 4.7 shows that, for a given pressure, there are typically two possible volumes. Since there may be multiple steady states, the state that the system ends in may depend on the initial conditions.

Since the pressure as a function of the volume needs to be found numerically, solutions of (4.86) and (4.87) also need to be found numerically as we shall now describe.

4.7 Comparison with the thin-film asymptotics

In chapter 3 we derived a model for a device with a dumbbell shaped footprint valid in the limit $\delta = H_D/L \ll 1$. This was shown to be in good agreement with numerical simulations of the full thin-film problem on the dumbbell geometry for small values

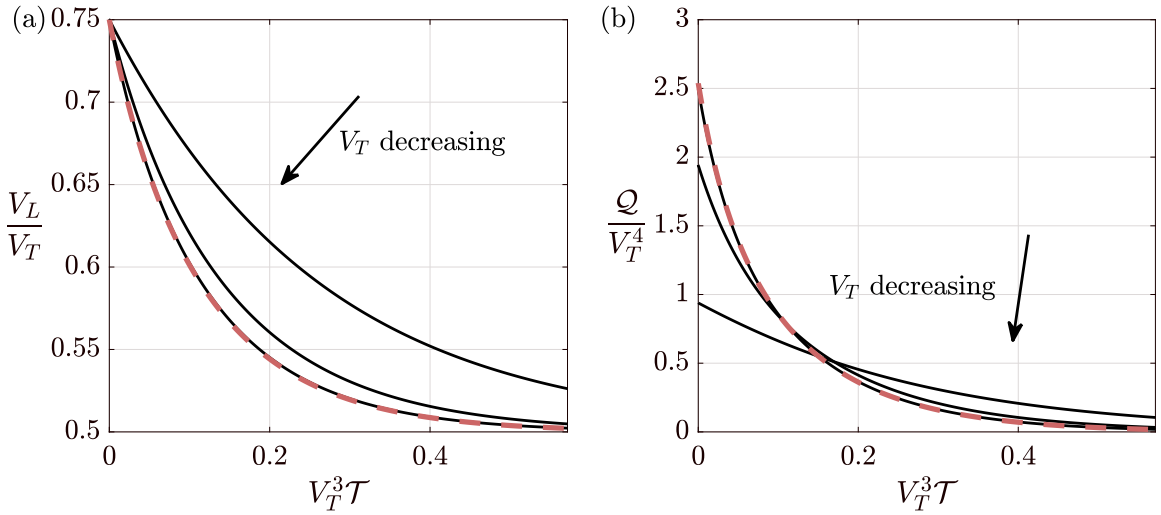


Figure 4.8: Comparison of numerical solutions of (4.86) and (4.87) with the thin-film asymptotics. (a) The volume in the left drop given by (4.86) and (4.87) (solid lines) and the asymptotic solution given by (3.101) (dashed line), with Bo $= 2$, $\alpha_L = \alpha_R = 1$ and an initial volume of $V_L = 3/4V_T$ for $V_T = 0.1, 0.4, 0.8$. (b) The corresponding fluxes given numerically by (4.83) for thick drops (solid lines) and by the right-hand side of (3.97) for thin drops (dashed line).

of ϵ. A similar comparison in this chapter would require numerical solution of the full Navier-Stokes equations with a free boundary between two immiscible fluids. This presents some significant technical difficulties and so we opt instead to show that the models presented in this chapter compare favourably with the thin-film model as $V_T \to 0$ (this is equivalent to $H_D/L = \delta \to 0$). We described the numerical method used to find the pressure in a thick drop for a given volume in §4.3.3. To solve (4.86) we compute the pressure for a range of volumes, we then use interpolation to determine the right-hand side of (4.86) as a function of V_L, assuming the drop pressure volume relation between P_L, P_R and V_L is on its primary branch, as depicted in red in Figure 4.3, centre. The ODE can then be solved numerically: we use the stiff ODE solver *ode15s* in MATLAB. Figure 4.3 shows that there may be multiple steady state solutions for a given volume when Bo > 0. In Figure 4.8 we compare solutions of (4.86) with the thin-film solution (3.101). Figure 4.8a shows the volume of the left-hand drop as a function of time. The solid lines are solutions to (4.86) and the

dashed line shows the thin-films solution (3.101); as the total volume is decreased the solutions converge to each other. Figure 4.8b shows the corresponding flux in the conduit, defined to be

$$\mathcal{Q} = P_L^4 - P_R^4, \tag{4.88}$$

we see similarly good agreement as the total volume is decreased. We note that, as in the thin-film regime, the drop volumes are always monotonic increasing or decreasing functions of time and hence the direction of flow does not change. This is not necessarily the case when there are networks of drops and conduits. Since the thin-film ODE can be derived readily from the thick-film ODE by taking its small aspect ratio limit, our analysis here serves as verification of our numerical simulations.

4.8 Pinning and pinch off

We noted in chapter 1 that the large advancing and small receding contact angles, θ_a and θ_r respectively, ensure that the volume of fluid in the drops can change significantly without the contact line moving, although in §3.3.4 we showed that the corners of the junction regions will be smoothed out. In chapter 3 we only needed to consider the receding angle since all the contact angles were small (other than in the corners of the junction regions). We demonstrated in (3.105) that the minimum contact angle occurs in the conduit near the outlet. We further showed that if the minimum contact angle is initially above the receding angle it will remain so. For the following analysis, the contact angle is defined by

$$\tan\theta = -\frac{\partial H}{\partial n} \quad \text{for } (X, Y) \in \partial\Omega, \tag{4.89}$$

where $\partial/\partial n$ now denotes the outward normal derivative on the contact line, Ω_1, in the (X, Y)-plane. In the drop region numerical methods are required to find the contact angle in most cases, but a relationship between the drop contact angle, pressure and volume has previously been derived, see e.g. Hajirahimi *et al.* [51], of which we give

a brief outline. Initially assuming that the drop height is single valued and axisymmetric, so that $Z = H_L(R)$ in the left-hand drop, where $R = \sqrt{(X+\alpha_L)^2 + Y^2}$ as in §4.3, we find that the curvature in (4.10) can be written as

$$\kappa = \frac{1}{R}\frac{\partial}{\partial R}\left(\frac{R\dfrac{\mathrm{d}H_L}{\mathrm{d}R}}{\sqrt{1+\left(\dfrac{\mathrm{d}H_L}{\mathrm{d}R}\right)^2}}\right). \tag{4.90}$$

The drop volume is then given by

$$V_L = 2\pi \int_0^{\alpha_L} R H_L \, \mathrm{d}R. \tag{4.91}$$

Integrating (4.10) over the drop radius using the boundary conditions $H_L(\alpha_L) = 0$ and $\mathrm{d}H_L/\mathrm{d}R = 0$ on $R = 0$, and equations (4.90) and (4.91) gives

$$\sin\theta_L = \frac{\alpha_L P_L}{2} + \frac{\mathrm{Bo} V_L}{2\pi\alpha_L}. \tag{4.92}$$

Although this expression has been derived assuming the function $H_L(R)$ is single valued, Hajirahimi *et al.* [51] go on to show that it generalises readily to the multi-valued case. Recall that the pressure is a non-linear function of the volume so (4.92) cannot be expressed any more simply in general. The numerical solutions of the drop problem show that there is a volume beyond which the contact angle will decrease as shown in Figure 4.2d. We can, however, write an analytic expression for the contact angle in the conduit. For a conduit of constant width the normal to $\partial\Omega_1$ is in the $\widehat{y}$ direction and so (4.89) and (4.61a) give

$$\tan\theta_C = \epsilon\, p_{C0}, \quad \text{for } 0 < X < 1. \tag{4.93}$$

Since $\epsilon \ll 1$, the minimum contact angle is in the conduit at the outlet, where the pressure is equal to the corresponding drop pressure. Thus, if the initial contact angle is above the receding angle once the system is quasi-steady, then we will have $\theta > \theta_r$ for the duration of an experiment, though with the added caveat that this

is only valid for drops with profiles on the upper branch illustrated in Figure 4.3 and with volumes which remain below $V_{\max}$ for the duration the experiment. Since the minimum contact angle is in the conduit we only need to consider the drop and junction regions to determine if there is a contact angle greater than the advancing angle on the drainage timescale. We anticipate that there will be large contact angles in the junction region on the timescale $t_J^* = \mathrm{O}(\epsilon)$. Such large contact angles were observed in the numerical solution of the full thin-film problem as shown in Figure 3.9, where the contact line was fixed. While we assume the corners in the junction region will initially be smoothed out until they are below the advancing angle we still anticipate that the largest contact angles will occur in the junction region, though changes to the drop footprint will have further influence on the dynamics via the Bond number compared to the considerations of chapter 3.

Numerical methods are required to determine the contact angle in the drop. When solving for the drop profile, as described in §4.3, we introduced the dependent variable Ψ giving the angle with the horizontal (see Figure 4.1). The contact angle was then defined to be the value of Ψ on the contact line. In Figure 4.5 we plot the resulting prediction for the maximum possible contact angle for a given Bond number. This shows that we can choose the base radius of a drop to ensure that the contact angle stays below the advancing angle for any volume. However, as shown in Figure 4.4 for larger Bond numbers the maximum volume for which solutions exist is decreased. Beyond this volume the quasi-steady approximation is no longer valid and we expect some of the liquid in the drop to detach if the volume is increased any further. Predicting how much fluid will detach is beyond the scope of this thesis although such analyses have been undertaken elsewhere [54, 86]. For most passively driven flows the volumes used experimentally will be small enough that pinch off does not occur. This will clearly need not be the case with actively driven flows since the volume of fluid in the circuit may not be fixed. We further note that pinch off is only

a problem when the Bond number is positive; when the Bond number is negative the liquid in the circuit is denser than in the overlay and will not detach, though the fluid in the circuit will eventually exceed the advancing contact angle and spread.

4.9 Multiple steady states

As Figures 4.3 and 4.7 illustrate, the relationship between pressure and volume in a drop is not a simple linear one as it was in chapter 3. As the drop volume increases the pressure initially increases before reaching a maximum and decreasing again. Recall that, in the drainage timescale model, we only consider the upper part of the curve, the shape of which is typical of all Bond numbers. Thus, for a given dumbbell geometry and total volume, multiple equilibrium solutions may exist to (4.86). The modelling of similar surface-tension driven devices has typically focused on regimes in which gravity can be ignored [62, 98] or in which the geometry is designed to ensure the flow is in one direction [30, 61]. In general multiple steady states have not been considered. The steady states are found by setting the right-hand side of (4.86) to zero, so that $P_L^4 - P_R^4 = 0$, subject to the volume constraint given in (4.85). Since we additionally require positive drop pressures (otherwise the conduit height would be negative, as shown by (4.61a)), the steady states are found by solving

$$P_L = P_R, \quad V_L + V_R = V_T. \tag{4.94}$$

Since there may be multiple volumes with the same pressure, there may be as many equilibria as highlighted in Figure 4.9a, where we show an example of the behaviour of the right-hand side of (4.86) as a function of V_L for a geometry with $\mathrm{Bo} = 1$, $\alpha_L = 1$ and $\alpha_R = 0.8$ and a total volume of $V_T = 3.9$. The left-hand drop volumes at which $P_L^4 - P_R^4 = 0$ are indicated by the circles. We deduce the stability of the equilibria by looking at the sign of $\partial V_L / \partial \mathcal{T}$. We can see that the equilibrium close to $V_L = 1.7$ is unstable; small perturbations to the left-hand drop volume will cause the system to

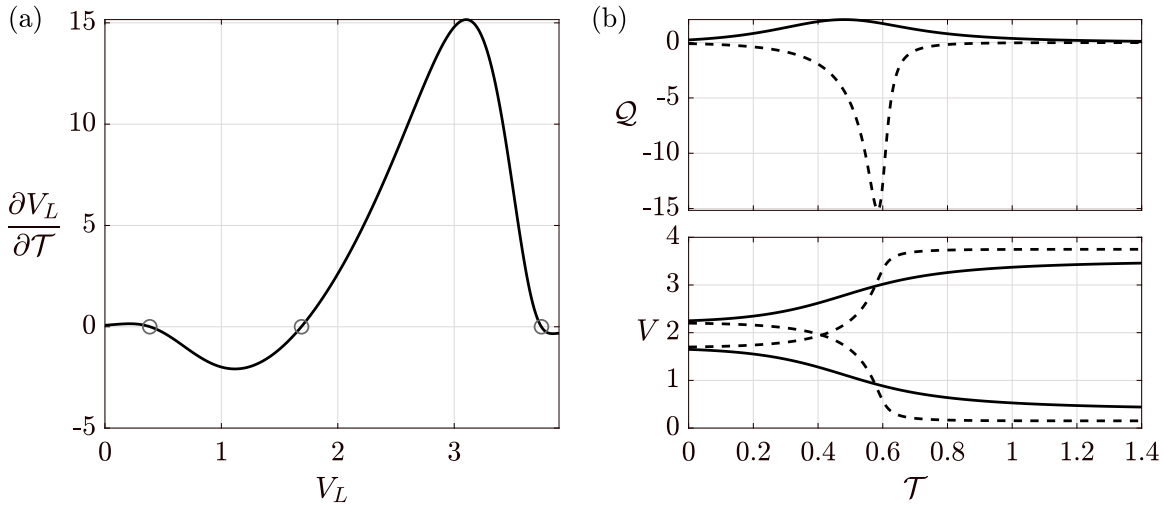


Figure 4.9: Generally there are multiple equilibrium solutions to (4.86). (a) The right-hand side of (4.86) is plotted as a function of V_L with Bo $= 1$, $\alpha_L = 1$ and $\alpha_R = 0.8$. The system has three non-trivial equilibria, at $V_L \approx 0.39, 1.7, 3.7$, as indicated by the circles. The equilibrium $V_L \approx 1.7$ is clearly unstable. (b) The flux and both left and right drop volumes, as functions of time, are shown for the initial conditions $(V_L, V_R) = (1.7, 2.2)$ (dashed lines) and $(1.65, 2.25)$ (solid lines), *i.e.* they have the same total volume.

move away from this equilibrium. In contrast, the other two equilibria, at $V_L \approx 0.39$ and $V_L \approx 3.7$ are stable. In Figure 4.9b we also show some solutions with initial volumes near the unstable equilibrium; a small change in the initial volume (shown in the lower panel) can lead to very different flow rates (shown in the upper panel). Thus, it is important that initial volumes are chosen so as to avoid the unstable equilibrium. Another feature highlighted by Figure 4.9b is that the flux does not necessarily decrease monotonically as it did in the thin-film case.

4.10 Discussion

In this chapter we extended the model of chapter 3 to allow for drops with larger volumes. With this addition we are able to model the full range of volumes used in experiments (see Table 2.1). We were still able to utilise the disparate length scales in the geometry of the device to construct asymptotic solutions which are valid in different regions and over different timescales as the aspect ratio of the conduit width

to length ϵ is decreased. In §4.1 we showed that the asymptotic structure is the same as in the thin-film case: the geometry can be split up into the drop, conduit and junction regions. In the drop and conduit regions we found quasi-steady solutions.

In §4.3 we were able to find an analytic solution for the quasi-steady drop when the Bond number is small, but numerical methods were required to find solutions for Bond numbers of order unity. The numerical solutions showed that there may be multiple steady-state drop profiles satisfying the governing equations for a given volume, *i.e.* nonuniqueness. We made the reasonable assumption that most of these profiles would be unlikely to be encountered in experiments. We then restricted our attention to the upper branch of the pressure-volume curve illustrated in Figure 4.3, the branch on which there is a single lobe.

In §4.4 we showed that the conduit is still thin even when the drops are not. We further showed in §4.5 that the pressure is transmitted straight through the junction region. With these two results we were able to construct a leading-order ODE model for the time-dependent drop volumes analogously to chapter 3, although we were no longer able to find analytic solutions to the ODE.

Now we briefly discuss the possible impacts of what we have ascertained for the use of the device as described in chapters 3 and 4. The main purpose of the drops is to provide a source of fluid which flows through the conduit or to collect fluid at the other end. Controlling the rate of flow means controlling the pressure in each drop. The results in this chapter have identified several parameter regimes which we may want to avoid to allow easy prediction of the pressure. Printing thin drops with a large contact set may be one way to more easily make predictions since the volume and pressure vary linearly in this regime. With a base radius of about 6 mm, volumes of about 20 µl would still be within the thin-film regime in chapter 3. It was also shown that a large enough Bond number Bo would give an interface with a negative height that intersects the drop base. The liquid dewets the substrate in this regime,

i.e. "dry spots" may form as the contact line recedes. Moreover, when the contact angle decreases below the receding contact angle we would expect the contact line to move, though modelling such features is beyond the scope of this thesis. Further, we also deduce that to give an accurate prediction of the flow rate it will be important to use drops possessing a volume beneath the multiple solutions curve of Figure 4.4 and in practice this may represent an important working constraint. Violating this constraint entails in general access to a large number of profiles as predicted by the numerical solution of (4.44) and (4.52), though these are not necessarily all stable, and we anticipate many to result in pinch off.

Chapter 5

Generalisations: networks, corrections, thick conduits and comparisons to data

In this chapter we discuss several generalisations and extensions of the asymptotic models presented in the previous chapters. We begin in §5.1 by considering networks of drops and conduits; some examples of which are shown in Figure 1.2. In chapters 3 and 4 we split the geometry up into several distinct regions and analysed them separately before combining them into a single ODE model for the drainage timescale dynamics of the dumbbell shaped device. We will show that we can use the same components to find systems of ODEs describing the drainage timescale dynamics for a large network of drops, drop-conduit and conduit-conduit (node) junctions. These models are then incorporated into a Graphical User Interface (GUI) to aid in the design of geometries with specific characteristics.

Throughout chapters 3 and 4 we demonstrated, where appropriate, that the leading-order solutions compare favourably with numerical solutions when the conduit aspect ratio is small. In section §5.2 we show how the models can be extended to higher order to incorporate some effects that were not present in the leading-order models, which also generates further novel modelling studies. In §5.2.1 we explore corrections to the drop volumes, noting that in large networks with numerous conduits connecting to a drop, such corrections start becoming necessary even at relatively

small aspect ratios of $\epsilon \approx 0.1$ for example. In §5.2.3 we demonstrate how the flow in the conduit is altered when the Bond number is large and in §5.2.4 we compute the next-order correction to the thin-film velocity, showing how the viscosity ratio affects the flux and velocity profile.

In §5.3 we will analyse an isolated conduit, *i.e.* one that is not explicitly connected to any drop. This will allow us to consider conduits with much higher pressures that could be achieved by pumping liquid into them at much higher rates than have been considered thus far. In §5.4 we compare the model prediction to experimental data. We will see that the fluids used experimentally do not conform to our initial assumptions of standard surface tension boundary conditions and we will show how the models can be modified to incorporate this discrepancy.

5.1 Networks

In the introduction we stated that one of the advantages of the new kind of microfluidic devices described here is that complex patterns of drops and conduits can be easily printed. For example, several network designs are demonstrated by Walsh *et al.* [127], some of which are shown in Figures 1.1 and 1.2. In chapter 3 we developed a model for the dumbbell configuration in the thin-film limit. This model relied on splitting the dumbbell up into separate domains as shown in Figure 3.1 to derive an ODE model on the timescale of drainage. Here we will show how the same technique can be extended to model networks of drops connected by long, narrow and thin conduits (recall that in the context of the thin-film model, thin refers to the height). We will initially focus on a passively driven network in the thin-film limit, before demonstrating how active pumping and the results of chapter 4 can be incorporated. The leading-order drainage timescale models from this chapter and the previous two are then combined into a GUI in which potential network designs can quickly be drawn and the resulting systems of ODEs rapidly solved.

5.1.1 Network geometry

The contact set of a network is defined to be the union of circles (the drop footprints) and rectangles (the conduit footprints) as indicated in Figure 5.1a. We have already defined a junction to be the region where a conduit intersects a drop (see Figure 3.2). We similarly define a node to be the region where multiple conduits intersect one another as shown in Figure 5.1a. We number the nodes by $1, \ldots, n$ and the drops by $n+1, \ldots, n+m$ and label the conduit connecting i to j with $\{i, j\}$, where i and j are labels denoting either a node or a drop. We note that conduit $\{i, j\}$ is the same as conduit $\{j, i\}$, but $\{i, j\}$ is ordered in that i is the starting node relative to the coordinate $x_{i,j}$, highlighted in Figure 5.1b-c. We do not consider the case in which multiple conduits connect the same two objects, so that $\{i, j\}$ denotes a distinct object. Similarly we do not let a conduit connect to the same object at both ends, *i.e.* $\{i, i\}$ is not a valid conduit. As in the original dumbbell case, we define the length of a conduit to be the maximum distance along its straight outer edge. We do not consider conduits whose widths vary along their length here. As before, we require $a^*_{i,j} \ll L_{i,j}$, where $2a^*_{i,j}$ and $L_{i,j}$ are, respectively, the width and length of conduit $\{i, j\}$. We also require that the width of a conduit footprint be much less than the base radius R_i of any drop it is connected to, so $a^*_{i,j} \ll \min(R_i, R_j)$. Although the construction is quite simple we must apply several restrictions to ensure that the footprint is within the framework of our model. The analysis of the junction region and the node analysis presented below is only valid when there are no other nodes or junctions nearby, *i.e.* the distance between every junction and node must be substantially greater than the conduit widths. We also assume that the conduits enter the drops with their centre line making an angle of order unity with the circular outer perimeter of the drop, *i.e.* the conduit need not be exactly perpendicular to the drop but should not be close to tangential. A possible network geometry is illustrated in Figure 5.1 showing how the variables are labelled. In each conduit we also define a local coordinate system with

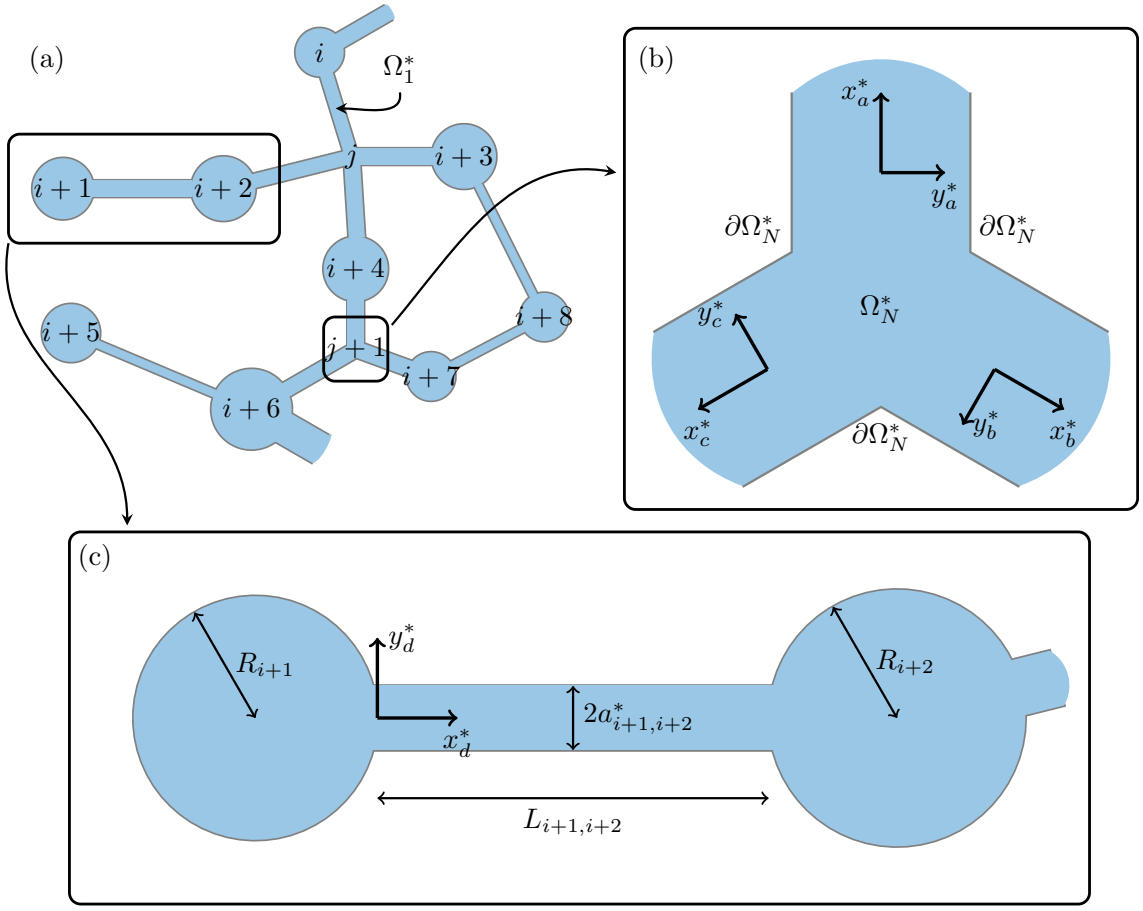


Figure 5.1: (a) The footprint of a network is defined as the union of rectangles and circles; nodes are the regions where the rectangles intersect. (b) The geometry in the node region showing the coordinates along each conduit where $a = j+1,\ i+4$, $b = j+1,\ i+7$ and $c = j+1,\ i+6$. (c) The geometric parameters in the drops and conduits, where $d = i+1,\ i+2$

one axis along the centre of the conduit with the other perpendicular to it, with the origin taken to be at one end of the conduit.

5.1.2 Node asymptotics in the thin-film limit

In the dumbbell model we non-dimensionalised using the length scale of the conduit; here, since there are multiple conduits in a network, there are multiple choices for the length scale L. We assume that all the conduit lengths and widths in the network are of the same order of magnitude. We then define the length scale using the conduit with the largest aspect ratio, where the aspect ratio for conduit $\{i, j\}$ is defined to

be $a^*_{i,j}/L_{i,j}$. Without loss of generality we assume that conduit $\{1,2\}$ has the largest aspect ratio and define $\epsilon = a^*_{1,2}/L_{1,2}$. We further define H_D to be the maximum initial drop height in the network and let $\delta = H_D/L_{1,2}$. The governing equations (2.1)–(2.4) and (2.6)–(2.8) are then rescaled as in §3.2:

$$x^* = L_{1,2}\,x, \quad y^* = L_{1,2}\,y, \quad z^* = \begin{cases} \delta L_{1,2}\,z & \text{for } z^* \in \Gamma_1^*, \\ L_{1,2}\,Z & \text{for } z^* \in \Gamma_2^*, \end{cases} \qquad h^* = \delta L_{1,2}\,h, \tag{5.1}$$

$$t^* = \frac{3L_{1,2}}{U_0}t, \quad \kappa^* = \frac{\delta}{L_{1,2}}\kappa, \quad \boldsymbol{u}_i^* = U_0\,(u_i, v_i, \delta w_i)\,, \tag{5.2}$$

$$p_1^* = \frac{\delta\gamma}{L_{1,2}}\,p_1 + p_{\text{atm}} + \rho_2 g H_O - \rho_1 g L_{1,2} Z, \tag{5.3}$$

where $U_0 = \delta^3\gamma/\mu_1$, Γ_1^* is the fluid in the circuit and Γ_2^* is the overlaying fluid. We begin by considering the case in which $\delta \ll 1$, in this limit the leading-order governing are the same as in §3.2. We recall that the fluid in the overlay only has an effect via the Bond number at leading order, so p_2 does not appear in the thin-film model. We then simplify the notation by defining $p = p_1$. In the remainder of this section we will use subscripts to denote different regions in the network rather than different fluids. The interface height is then governed by

$$\frac{\partial h}{\partial t} = \nabla \cdot \left(h^3 \nabla p\right) \quad \text{for } (x,y) \in \Omega_1, \tag{5.4}$$

where

$$p = -\nabla^2 h - \text{Bo}\,h \quad \text{for } (x,y) \in \Omega_1. \tag{5.5}$$

As in previous chapters Ω_1 denotes the dimensionless footprint of the device, though we do not state explicitly what this geometry is. The interface height is zero on the contact line and there is no flux through the contact line, so we impose the boundary conditions

$$h = 0, \quad \left(h^3 \nabla p\right) \cdot \boldsymbol{\nu} = 0 \quad \text{for } (x,y) \in \partial\Omega, \tag{5.6a,b}$$

where $\boldsymbol{\nu}$ denotes the outward pointing normal on $\partial\Omega$ in the (x,y)-plane. Finally, we prescribe an initial condition for the interface height, as in (3.22).

As with the dumbbell, we split the geometry into distinct regions which can be analysed separately: the drop, conduit, junction and node regions. The first three of these should be familiar from chapter 3 and the analysis remains largely unchanged. We first note that the five timescales that we identified in (3.28) remain the same, although we shall shortly add another for the node region. For $t \gg t_D \sim 1$, the drop relaxation timescale, the interface height h_i and pressure p_i in drop i are given by

$$h_i = \frac{p_i}{\mathrm{Bo}}\left(\frac{J_0\left(\sqrt{\mathrm{Bo}}\, r_i\right)}{J_0\left(\sqrt{\mathrm{Bo}}\,\alpha_i\right)} - 1\right), \quad p_i = \frac{\mathrm{Bo}\, J_0\left(\sqrt{\mathrm{Bo}}\,\alpha_i\right)}{\pi\alpha_i^2 J_2\left(\sqrt{\mathrm{Bo}}\,\alpha_i\right)}\widehat{v}_i, \tag{5.7a,b}$$

where $\alpha_i = R_i/L_{1,2}$ and $\widehat{v}_i$ is the dimensionless volume of drop i. The polar coordinate $r_i = \sqrt{(x-X_i)^2 + (y-Y_i)^2}$ measures the radial distance from the centre of the circular contact set of drop i with origin (X_i, Y_i). This generalises the thin-film dumbbell drop heights (3.31)–(3.33). In §3.3.4 we showed that, for $t \gg t_J \sim \epsilon$, the junction capillary timescale, the pressure is transmitted straight through the junction region. This showed that the pressure at the ends of the conduit is equal to the pressure in the corresponding drop. The same result applies to networks since the asymptotic structure of the junction regions remains the same. That is, in a network, the pressure at the end of a conduit which meets a drop is equal to the pressure in that drop. For $t \gg t_{CL} \sim \epsilon^{-4}$, the conduit relaxation timescale, the interface height $h_{i,j}$ and pressure $p_{i,j}$ in conduit $\{i,j\}$, on assuming that both i and j denote drops, are given by

$$h_{i,j} = \frac{p_{i,j}}{2}\left(\epsilon^2\bar{a}_{i,j}^2 - y_{i,j}^2\right), \quad p_{i,j} = \left(\left(p_j^4 - p_i^4\right)\frac{x_{i,j}}{\overline{L}_{i,j}} + p_i^4\right)^{\frac{1}{4}}, \tag{5.8a,b}$$

where $\bar{a}_{i,j} = a_{i,j}/a_{1,2}$ and $\overline{L}_{i,j} = L_{i,j}/L_{1,2}$, and $x_{i,j}$, $y_{i,j}$ are local conduit coordinates from the conduit starting at drop i and ending at drop j.

As with the junction region in §3.3.4, we will need to determine the local behaviour in the node regions. We consider the illustrative node region shown in Figure 5.1b, which is made up of three intersecting conduits; according to our convention we label

the conduits $\{1, i\}$ for $i = 1, 2, 3$. The height scale in the node region, Ω_N, is set by the conduit height scale so, in the thin-film regime, we rescale with

$$x = x_0 + \epsilon\widetilde{x}, \quad y = y_0 + \epsilon\widetilde{y}, \quad h = \epsilon^2\widetilde{h}, \tag{5.9}$$

where (x_0, y_0) is some origin chosen within Ω_N. As we did for the drop, junction and conduit regions in §3.3.1, we will use a dominant balance argument in the governing equations to find the timescale of relaxation for the node region. Using the scalings given by (5.9) in (5.4), where the pressure scale is O(1) (the same as the drops and conduit), we find the timescale of relaxation in the node region to be given by $t_N \sim 1/\epsilon^2$. We expand $\widetilde{h} \sim \widetilde{h}_0(\widetilde{x}, \widetilde{y}, t) + \epsilon\,\widetilde{h}_1(\widetilde{x}, \widetilde{y}, t)$ and $p \sim p_{N0}(\widetilde{x}, \widetilde{y}, t) + \epsilon\, p_{N1}(\widetilde{x}, \widetilde{y}, t)$ as $\epsilon \to 0$. At leading order for $t \gg t_N \sim 1/\epsilon^2$, the thin-film equation (5.4) gives

$$\nabla \cdot \left(\widetilde{h}_0^3 \nabla p_{N0}\right) = 0 \quad \text{for } (\widetilde{x}, \widetilde{y}) \in \Omega_N. \tag{5.10}$$

As we found for the junction region in §3.3.4, it follows from the boundary conditions being homogeneous Neumann except in the far-field where the pressure tends to that in the adjoining conduits, that $p_{N0}(\widetilde{x}, \widetilde{y}, t) = p_{N0}(t)$ and thus

$$p_{N0}(t) = p_{1,i}(0, t), \quad \text{for } i = 1, 2, 3, \tag{5.11}$$

where $p_{1,i}$ is the pressure in conduit $\{1, i\}$. Recall that the interface height in the thin-film limit is given by (5.5), so that the equation governing the interface height is given by

$$\nabla^2\widetilde{h}_0 = -p_{N0}(t) \quad \text{for } (\widetilde{x}, \widetilde{y}) \in \Omega_N. \tag{5.12}$$

Since the height scales with ϵ^2 in the node, the Bond number Bo does not appear in the leading-order equation (5.12). The interface height is zero on the contact line (as given by (5.6a)) and we match with the conduit solution (given by (5.8a)) in the far-field so the boundary conditions are given by

$$\widetilde{h}_0 = 0 \qquad \text{for } (\widetilde{x}, \widetilde{y}) \in \partial\Omega_N, \tag{5.13}$$

$$\widetilde{h}_0 \sim \frac{p_{1,i}(0,t)}{2}\left(\overline{a}_{1,i}^2 - \widetilde{y}_{1,i}^2\right) \quad \text{as } \widetilde{x}_{1,i} \to \infty \text{ for } i = 1,2,3, \tag{5.14}$$

where the coordinates $(\widetilde{x}_{1,i}, \widetilde{y}_{1,i})$ are the local coordinates in conduit $\{1,i\}$, as illustrated dimensionally in Figure 5.1b. This problem could again be solved via conformal mapping and there are conformal maps similar to (3.53) that could be applied to certain node geometries [67]. However, in general we will be unable to write the map explicitly. Numerical methods for determining conformal maps and solving the Laplace equation on these geometries have been extensively developed [35, 36]. However, we do not need to know the interface height in the node region to find the leading-order drainage timescale behaviour, but we do need to proceed to higher order to close the problem.

At second order for $t \gg 1/\epsilon^2$, conservation of mass, (5.6) and an application of Green's theorem show that

$$\iint_{\Omega_N} \nabla \cdot \left(\widetilde{h}_0^3 \nabla p_{N0}\right) \, \mathrm{d}\widetilde{x}\, \mathrm{d}\widetilde{y} = \int_{\partial\Omega_N} \widetilde{h}_0^3 \nabla p_{N0} \cdot \boldsymbol{n} \, \mathrm{d}s = 0. \tag{5.15}$$

There is no flux through the contact line and the flux through the conduit tends to $\widehat{Q}_{1,i}$ as $\widetilde{x}_i \to \infty$, where $\widehat{Q}_{1,i}$ is given by a similar expression to (3.25b). Thus, the sum of fluxes in the conduits connected to a node must be zero at leading order for $t \gg t_N$. This is true of any network satisfying the restrictions set out above. We thus are able to derive a generalisation of Kirchhoff-type laws which govern the current and voltage in an electrical circuit, which has similarly been applied to flow in networks of pipes [75].

5.1.3 Kirchhoff-type laws for networks

On the timescale of drainage $t_{DD} \sim \epsilon^{-7}$, we can derive an ODE model for the drop volumes as we did in §3.3.6. In a dumbbell circuit the flux in the conduit is given by (3.43), generalising this to conduit $\{i,j\}$ in a network as defined above gives

$$\widehat{Q}_{i,j} \sim -\frac{\overline{a}_{i,j}}{35}\epsilon^7 \frac{\partial}{\partial \widetilde{x}_{i,j}}\left(p_{i,j}^4\right) \quad \text{as } \epsilon \to 0. \tag{5.16}$$

Make the rescaling $\widehat{Q}_{i,j} = \epsilon^7/35\mathcal{Q}_{i,j}$, we thus find that the dimensionless flux is given by

$$\mathcal{Q}_{i,j} = \frac{\overline{a}_{i,j}^7}{\overline{L}_{i,j}} \left({p_i}^4 - {p_j}^4 \right), \tag{5.17}$$

where p_i and p_j are the pressures at the ends of the conduit; if the labels i or j denote a drop the pressure is given by (5.7b). If the labels i or j denote a node the pressure is ultimately found using the Kirchhoff-type laws derived in the previous section. We note that this model is valid for the thin-film limit, where the dimensional drop volumes satisfy $v_i^*/R_i^3 \ll 1$ for $i = n+1, \ldots, n+m$. For drop i we define Π_i to be the set of all drops and nodes directly connected to drop i via a conduit, and similarly we define K_j to be the set of all drops and nodes directly connected to node j. Thus, the ODEs for the thin-film dumbbell problem (3.96) can easily be generalised to account for a more complicated network as follows:

$$\frac{\mathrm{d}\widehat{v}_i}{\mathrm{d}T} = \sum_{l \in \Pi_i} \mathcal{Q}_{i,l}, \tag{5.18}$$

$$\sum_{l \in K_j} \mathcal{Q}_{j,l} = 0, \tag{5.19}$$

for $i = n+1, \ldots, n+m$ and $j = 1, \ldots, n$, where $T = 35\epsilon^{-7}t$. The problem is closed by prescribing an initial volume for each of the n drops. In total there are $n+m$ unknowns; the pressures in the n nodes and in the m drops, while there are n ODEs with n initial conditions and m algebraic equations. In general we cannot find an analytic solution to (5.18), but solving such a system of ODEs can easily be implemented numerically.

We showed in §3.4.1 that active pumping can easily be incorporated into the thin-film dumbbell problem by rewriting one of the boundary conditions for the conduit pressure; we replaced the fixed pressure condition with a fixed flux at $x = 0$. In the network model we additionally allow for the labels of a conduit to denote a pump, with the pumps numbered $n+m+1, \ldots, n+m+k$. For $t \gg t_{CL}$ the pressure in

conduit $\{i, j\}$ is given by

$$p_{i,j} = \left(\frac{\overline{L}_{i,j} \mathcal{Q}_{i,j}}{\overline{a}_{i,j}} \left(1 - \frac{x_{i,j}}{\overline{L}_{i,j}} \right) + p_j^4 \right)^{\frac{1}{4}}, \tag{5.20}$$

if i denotes a pump with flow rate $\mathcal{Q}_{i,j}$. The network is still governed by (5.18) and (5.19), but now the flux in conduit $\{i, j\}$ is given by (5.17) if neither i nor j denotes a pump, otherwise $\mathcal{Q}_{i,j}(T)$ is known and is given by the imposed flow rate of the pump — where we require that any imposed fluxes are not asymptotically large compared to the fluxes that are driven passively.

5.1.4 Numerical validation of the thin-film networks

In this section we compare the numerical solution of (5.18) and (5.19) to the numerical solution of the full thin-film problem given by (3.18) and (3.20)–(3.22) for the network geometries shown in Figure 5.2a and Figure 5.3a. The numerical solutions to the full thin-film problem are found in the same way as in §3.3.7 using COMSOL. In particular we use the geometry with the sharp corners as discussed in §3.3.7. As with the junction regions, the corners of the nodes are expected to smooth out on a short timescale during experiments. For the simple three-drop network shown in Figure 5.2 the drop volumes are in very good agreement with the full numerics as ϵ is decreased, as shown in Figure 5.2b. The geometry in Figure 5.2a corresponds to that shown Figure 1.2a. The conduits do not all have the same width: the upper conduit has a width 1.03 mm and length 7.5 mm, while the lower two conduits have width 0.555 mm and length 10 mm. As described in §5.1.2, we take ϵ to be the largest aspect ratio in the network, which gives $\epsilon \approx 0.069$; the larger aspect ratios in Figure 5.2b correspond to doubling the conduit widths in the network. We further note that the initial drop heights correspond to $\delta \approx 0.16$, which demonstrates that the geometries used experimentally are within the framework of our asymptotic models.

The larger network with the footprint shown in Figure 5.3a corresponds to the one shown in Figure 1.2c. The conduit widths are not equal: the horizontal conduits

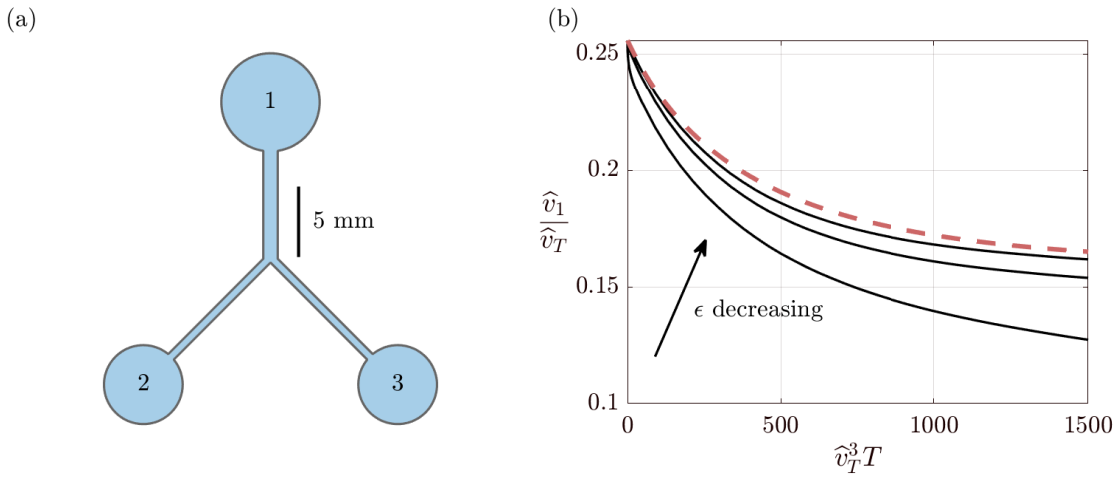


Figure 5.2: Comparison of the drop volumes for solutions to the asymptotic problem (5.18) and (5.19) (dashed lines) to the full numerical problem (3.18) and (3.20)–(3.22) (solid lines) for the geometry shown in (a). The physical parameters are taken from Table 2.1. The two lower drops (2 and 3) both have an initial volume of 11 µl, while the upper drop has an initial volume of 21 µl. (b) The solutions for the volume of drop 2 for $\epsilon \approx 0.27, 0.14, 0.069$.

have width 0.55 mm, while the vertical conduits have width 0.4 mm. The conduit lengths are all 4.5 mm. We recall that the node regions are defined as junctions where conduits meet. As can be seen in Figure 5.3a, there are eight nodes in the network, which gives rise to multiple conduits of length 4.5 mm. This geometry corresponds to $\epsilon \approx 0.061$ and $\delta \approx 0.13$. The higher values of ϵ in Figure 5.3b are obtained by doubling the width of the conduits. We still find good agreement for small values of ϵ, but need to take smaller values than for the simple network of Figure 5.2a for the same level of accuracy. Thus, we still see good agreement for parameters used in experiments. In general, as the size of the network increases smaller values of ϵ are needed before we see such good agreement. The asymptotics predict that drops of the same base radius will tend to the same equilibrium volume, whereas the full numerics show that this is not necessarily the case. This is particularly clear for larger values of ϵ: in Figure 5.3d the volume of drop 3 tends to a noticeably larger equilibrium value than the volumes in drops 1 and 2. In our model, the junction region does not affect the shape or volume of the drop at leading order. The leading-order model works

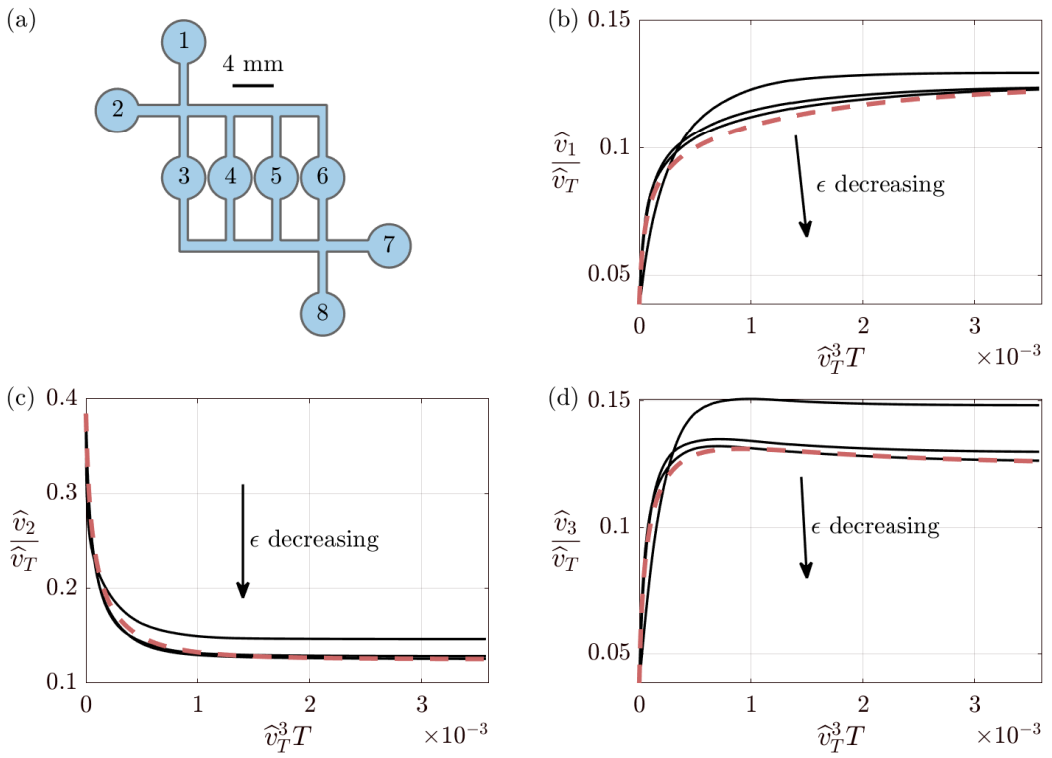


Figure 5.3: Comparison of the drop volumes for solutions to the asymptotic problem (5.18) and (5.19) (dashed lines) to the full numerical problem (3.18) and (3.20)–(3.22) (solid lines) for the geometry shown in (a). The physical parameters are taken from Table 2.1. The left- and rightmost drops (2 and 7) have an initial volume of 10 µl and the remaining drops have an initial volume of 1 µl. (b)–(d) The volumes of drops 1, 2 and 3 respectively for $\epsilon \approx 0.12, 0.061, 0.031$.

well when there is a single junction region for each drop. Since the height scale in the junction region is $O(\epsilon)$, the correction to the drop shape due to a single junction will be small. But with increasing numbers of junction regions this correction eventually will no longer be small. Thus, in Figure 5.3 the topmost drop (with an initial volume of 1 µl) tends to the smallest volume since it is connected to a single conduit with a smaller width than the leftmost drop. Later we will show how we can improve the predictions of the drop volume by finding its next order correction.

5.1.5 Network dynamics

For passively driven thin-film networks the results concerning the maximum shear stresses in a conduit given in §3.3.7 and §3.3.9 will still be applicable, since the model for the conduit is the same. In conduit $\{i, j\}$ the shear stress on the base is given by (3.102):

$$s_{i,j} = \frac{\left(\bar{a}_{i,j}{}^2\epsilon^2 - y^2\right)\left(p_i{}^4 - p_j{}^4\right)}{8\sqrt{p_i{}^4 - \left(p_i{}^4 - p_j{}^4\right)\dfrac{x}{\bar{L}_{i,j}}}}. \tag{5.21}$$

In the dumbbell model, the maximum shear stress occurs at the outlet of a conduit, which can easily be computed for each conduit in a network given the pressure. But unlike the dumbbell geometry, the flow in a conduit may change direction when it is part of a network so that the outlet will not necessarily be at the same end of the conduit for all time. Thus, the conclusion in §3.3.8 that a contact line that is pinned initially (except at any corners as discussed in §3.3.4) remains pinned is no longer valid. Recall that for the dumbbell geometry the minimum contact angle occurs in the conduit and is given, via (3.105), by $\theta_{\min} = \delta\epsilon \min\left(p_L, p_R\right)$. With a dumbbell geometry, on the drainage timescale, the pressures in the outlet and inlet drops will, respectively, increase and decrease monotonically until an equilibrium pressure is reached, thus $\theta_{\min}$ is bounded on the drainage timescale for all time. Since the minimum contact angle depends on both the pressure and conduit width, networks can be constructed in which the minimum contact angle decreases and so may fall below the receding angle. However, the network GUI which shall shortly be discussed easily allows us to check when or if a given geometry and set of initial volumes will fail to satisfy any of our requirements.

As shown in the previous section, networks used experimentally are often within the framework of the thin-film asymptotics of chapter 3 (*i.e.* $\delta \ll 1$ and $\epsilon \ll 1$). In chapter 4 we showed that thick drops (*i.e.* drops whose height is comparable to their base radius, $\delta = \mathrm{O}(1)$) can be incorporated into the dumbbell model by

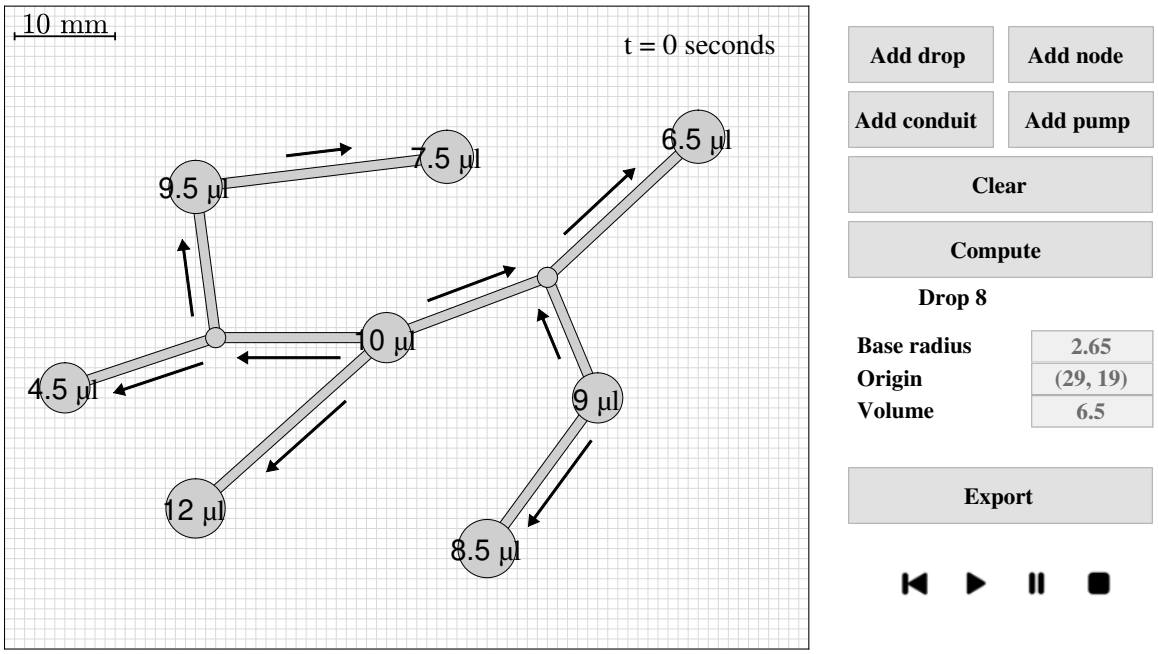


Figure 5.4: The network GUI, created in MATLAB, allows the user to rapidly design and test potential networks.

replacing the linear relationship between drop pressure and volume (given by (3.32)) with the relationship found by solving a system of ODEs (given by (4.14a)–(4.14c), (4.15), (4.17) and (4.18)). We can similarly allow for larger drop volumes in the network model by replacing (5.7b) with the numerical solution of (4.14a)–(4.14c), (4.15), (4.17) and (4.18). In this case, we still assume that the conduit height scales with the width squared (as we found it to in chapter 4), so the analysis of the node and junction regions are unchanged and the Kirchhoff-type laws still apply.

5.1.6 The network GUI

There are innumerable designs that can easily be printed with the new microfluidic devices discussed in this thesis. Walsh *et al.* [127] demonstrate a wide variety (some of which are shown in Figure 1.2), and many of these fall in regimes in which $\epsilon \ll 1$ and/or $\delta \ll 1$. Predicting the dynamics of such a device is, however, far more challenging. As we have seen, the shape of the fluid interface changes over time, as does the flow rate in passively driven conduits. The models that we have developed so

far have the potential to aid in the design of the devices, but computing the solution of the ODEs for the Kirchhoff model can be quite tedious for large networks. To facilitate simpler modelling of networks, the leading-order model has been incorporated into a MATLAB GUI in which the geometry of interest can be rapidly drawn and modified. For each drop and node the set of connected conduits, Π and K are then automatically determined and the system of governing ODEs (5.18) and (5.19) constructed. As in §4.7, for thick drops, we need to compute the pressure for a range of volumes, with interpolation used to determine the pressure as a function of volume. The ODEs are solved with *ODE15s* with a relative tolerance of 10^{-12} and an absolute tolerance of 10^{-12}. An example of the interface is shown in Figure 5.4; drops, conduits, pumps and nodes are added and their proportions easily modified. The footprint of the network and the initial volumes of the drops are sufficient to specify the leading-order system of ODEs and constraints given by (5.18) and (5.19) assuming the fluid parameters are those given in Table 2.1. The initial direction of the flow is indicated by the arrows and warnings are produced to indicate when there are likely to be contact angles that are not within the advancing and receding angles. Knowing that the contact angles will remain pinned is important since we have shown that the flux in a conduit scales with ϵ^7, so small changes to the conduit width can have a large impact on the flow rates, though we have also demonstrated that there is insensitivity to a smoothing of the junction footprint in Figure 3.9.

5.1.7 Further applications

As well as being able to test potential device designs we also note that the description of the network that we have derived has some similarities to a graph [32], where the "nodes" of the graph are the nodes as we have defined them as well as the drops. In particular we will briefly discuss the application of graph theory to the solution of mazes and how microfluidic networks are able to perform the same task. There

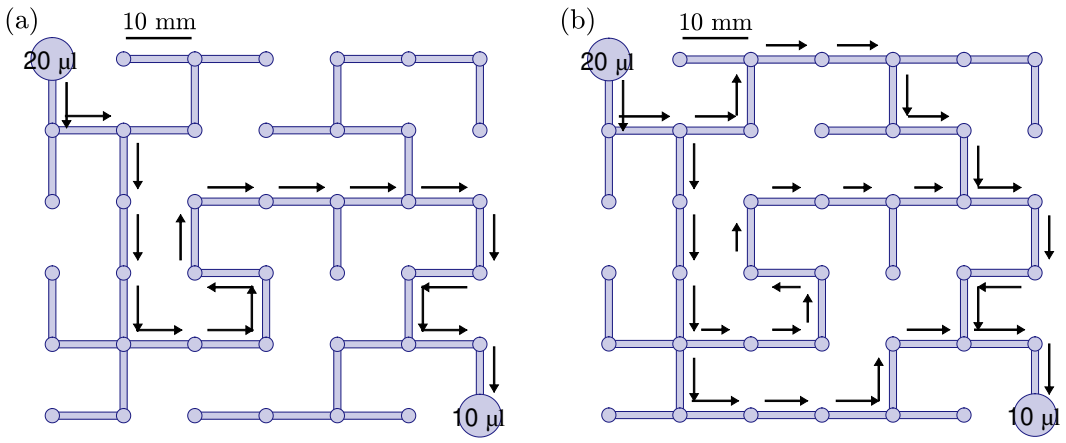


Figure 5.5: Solving mazes using microfluidic networks; the 20 µl drop has the higher pressure and is the "entrance" to the maze, the 10 µl drop is the exit. (a) A maze with lots of dead ends. (b) The same maze with multiple possible routes to the exit.

are numerous algorithms for finding the way through a maze [69]. As the network is drawn in the GUI, arrows next to the conduits indicate the initial direction of flow, for conduits that are connected to two drops at both ends or a pump the flow rate is determined by the drop volumes and/or pump flow rate. To find the initial flow rate in each of the conduits in a network, we need to solve (5.19). If we draw a network consisting of two drops with different initial pressures and a path between them, consisting of nodes and conduits, the solution of (5.19) will only give non-zero fluxes in conduits directly on the path between the drops. In other words, the fluid will flow only through conduits that lead to the "exit" drop. Some examples are illustrated in Figure 5.5. There are 40 nodes and two drops in the examples in Figure 5.5, which means that a 42×42 matrix needs to be inverted to find the path (or paths). As the size of the maze grows this will clearly become very inefficient, though it also suggests that we could solve the maze using the microfluidic devices themselves rather than the model. Such path finding has recently been demonstrated by Soitu *et al.* [110] for the devices studied in this thesis. Though we note the construction differs slightly from that described in §1.1.3; rather than printing the network directly, a layer of

media is first deposited in the Petri dish and then some of it is washed away using FC40 to produce the network shape.

5.1.8 Discussion

In this section we have shown that the leading-order models for the dumbbell circuit, developed in the previous two chapters, can be generalised to model networks. To do this we introduced nodes: conduit-conduit junctions. Asymptotic analysis of this region then showed that, at leading order, the net flux into each node must vanish, giving an algebraic constraint analogous to the conservation of current in DC electric circuits. Since the node region will change shape (and hence volume) as the local pressure changes, we anticipate that the net flux may not vanish at higher order, though this will not be investigated here. Parallels may also be drawn between the fourth power of the pressure in these microfluidic circuits and voltage in electric circuits at least in the thin-film limit. Solution of the resulting system of ODEs and constraints showed good agreement with numerics for small aspect ratios. However, the accuracy of the solution decreases as the number of junction regions increases relative to the number of drops; this will be analysed in more depth in the next section. Finally, by incorporating the reduced network model into a GUI, we were able to rapidly prototype different circuit designs without the need for expensive CFD packages, although, the full numerical modelling of the thin-film networks may be necessary to satisfactorily analyse certain problems. In particular, a valuable direction for future research would be to incorporate transport into the networks, for instance the network in Figure 1.2b delivers different chemical concentrations to the four drops in the centre. Transport in rivulets, via Taylor–Aris dispersion, has been well studied (see, for example, [2, 24, 34]), but not to our knowledge through networks of conduits, nodes and droplets. With the Comsol numerical thin-film model we could easily incorporate transport; in Figure 5.6 we show some streamlines

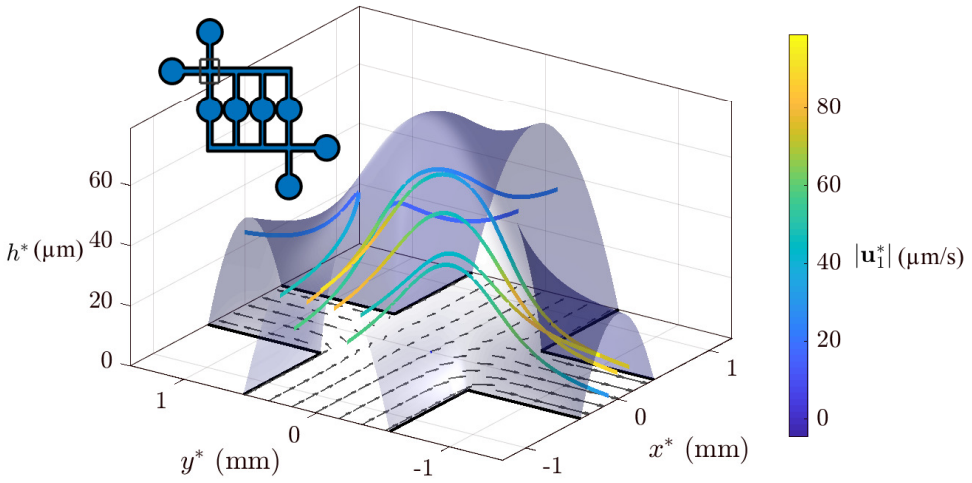


Figure 5.6: Streamlines in a node computed in COMSOL. The arrows on the base of the node show the pressure gradient there.

in the node region computed using the numerical solution shown in Figure 5.3.

5.2 Higher order solutions for the thin-film drop and conduit

In this section we demonstrate how some of our models could be improved by finding higher order corrections. In particular we find the correction in the drop volume due to junctions and the correction due to a large viscosity ratio in the thin-film conduit. We finish the section by considering the impact of large Bond numbers on the dynamics of a thin-film conduit.

5.2.1 Correction to the thin-film drop volume

In Figure 5.3 we showed that in the full numerical solution of the thin-film problem (5.4)–(5.6) the number of conduits connected to a drop can noticeably alter the volume for even moderately small aspect ratios ($\epsilon \approx 0.1$). In this section we will compute the next order correction to the drop volume and show how it depends on the number of conduits connected. We initially consider the geometry consisting of a single drop of base radius R connected to a conduit of length L and width $2a^*$. The geometry

is the same as for passive pumping (illustrated in Figure 2.1d), but we will not be concerned with the flow rate. The leading-order analysis is the same as in §3.3.2, where the relevant contact set in the drop is the circular disc Ω_0 of radius α, with centre $(x, y) = (-\alpha, 0)$. As we noted in §3.3.2, the boundary condition (3.21a) holds on the boundary of the leading-order contact set except at the origin (*i.e.* on $\partial\Omega_0/\{(0,0)\}$). At the origin we matched the drop height with the height in the junction region. To find higher-order solutions in the drop we must expand the solution in the junction region to determine the contribution to the height in its far field. The leading-order height in the junction region was determined in §3.3.4 and is given by (3.59); for convenience we state it again:

$$\widetilde{h}_0 = \frac{2\widetilde{\theta}}{\pi}\,\mathrm{Im}\big(f^{-1}(\omega)\big)\,, \tag{5.22}$$

where $\omega = \widetilde{x} + i\widetilde{y}$ and $\widetilde{\theta}$ is the leading-order contact angle of the drop given by (3.48), which depends on the leading-order pressure:

$$\widetilde{\theta} = \frac{J_1\Big(\sqrt{\mathrm{Bo}}\,\alpha\Big)}{\sqrt{\mathrm{Bo}}\,J_0\Big(\sqrt{\mathrm{Bo}}\,\alpha\Big)}p, \tag{5.23}$$

where p is the pressure in the drop. The mapping $\omega = f(\zeta)$ (originally given in (3.53) and illustrated in Figure 3.5) transforms the upper-half plane to the junction region and is given by

$$f(\zeta) = \frac{2i}{\pi}\left(\sqrt{\zeta^2 - 1} + \sin^{-1}\left(\frac{1}{\zeta}\right)\right). \tag{5.24}$$

The relevant height in the drop region is found by expanding (5.22) as $|\omega| \to \infty$. Expanding the map (5.24) and finding the inverse gives

$$f^{-1}(\omega) = \frac{\pi}{2i}\omega - \frac{i}{\pi\omega} + \mathrm{O}\left(\frac{1}{\omega^3}\right) \quad \text{as } |\omega| \to \infty \text{ for } \frac{\pi}{2} < \arg\omega < \frac{3\pi}{2}; \tag{5.25}$$

substituting this into (5.22) then gives

$$\widetilde{h}_0 \sim -\widetilde{\theta}\,\widetilde{x} + \frac{2\,\widetilde{\theta}\,\widetilde{x}}{\pi^2\,(\widetilde{x}^2 + \widetilde{y}^2)} \quad \text{as } \widetilde{x}^2 + \widetilde{y}^2 \to \infty. \tag{5.26}$$

Recall that the variables in the junction region were rescaled as follows: $h = \epsilon\widetilde{h}$, $x = \epsilon\widetilde{x}$ and $y = \epsilon\widetilde{y}$, so that in the drop region, the height near the junction satisfies

$$h \sim -\widetilde{\theta}\, x + \epsilon^2 \frac{2\,\widetilde{\theta}\, x}{\pi^2\,(x^2+y^2)} \quad \text{as } x^2+y^2 \to 0. \tag{5.27}$$

Thus, we expand $h_i \sim h_{i0}+\epsilon^2 h_{i1}$, $p_i \sim p_{i0}+\epsilon^2 p_{i1}$ and $\widehat{v}_i \sim \widehat{v}_{i0}+\epsilon^2\widehat{v}_{i1}$ as $\epsilon \to 0$, where the subscript $_i$ refers to the position of the drop within the network as illustrated in Figure 5.1, though we begin by considering only a single drop located at $(x,y) = (-\alpha, 0)$ with a single conduit connected at $(x,y) = (0,0)$. The leading-order solutions h_{i0}, p_{i0} and $\widehat{v}_{i0}$ are those found in §3.3.2.

For $t \gg t_D \sim 1$, we find that the $\mathrm{O}(\epsilon^2)$ profile is quasi-steady, with spatially uniform pressure so that p_{i1} is, at most, a function of t. Expanding (3.18) gives the equation for the next order height as

$$\nabla^2 h_{i1} + \mathrm{Bo}\, h_{i1} = -p_{i1} \quad \text{for } (x,y) \in \Omega_0. \tag{5.28}$$

The height is zero on the contact line except at the origin, so that

$$h_{i1} = 0 \quad \text{on } \partial\Omega_D/\{(0,0)\}, \tag{5.29}$$

while matching with the junction region as alluded to above yields

$$h_{i1} \sim -\frac{2\widetilde{\theta}\, x}{\pi^2\,(x^2+y^2)} \quad \text{as } x^2+y^2 \to 0, \text{ with } x<0. \tag{5.30}$$

Finally, the volume correction $\widehat{v}_{i1}$, is given by

$$\widehat{v}_{i1} = \iint_{\Omega_0} h_{i1}\ \mathrm{d}x\ \mathrm{d}y. \tag{5.31}$$

In this form the boundary conditions are difficult to impose, so we make the transformation

$$h_{i1} = \mathcal{H} + \frac{\widetilde{\theta}}{\pi^2}\left(\frac{(x+\alpha)^2+y^2-\alpha^2}{\alpha\,(x^2+y^2)}\right) + \left(\frac{J_0\Big(\sqrt{\mathrm{Bo}\,((x+\alpha)^2+y^2)}\Big)}{J_0\Big(\sqrt{\mathrm{Bo}}\,\alpha\Big)} - 1\right)\frac{p_{i1}}{\mathrm{Bo}}, \tag{5.32}$$

so that the transformed height $\mathcal{H}(x, y, t)$ satisfies

$$\nabla^2\mathcal{H} + \mathrm{Bo}\mathcal{H} = -\frac{\widetilde{\theta}\mathrm{Bo}\left((x+\alpha)^2 + y^2 - \alpha^2\right)}{\pi^2\alpha\left(x^2+y^2\right)} \quad \text{for } (x,y) \in \Omega_0, \tag{5.33}$$

$$\mathcal{H} = 0 \quad \text{on } \partial\Omega_0. \tag{5.34}$$

The volume is now given by

$$\widehat{v}_{i1} = \iint_{\Omega_0} \mathcal{H}\ \mathrm{d}x\ \mathrm{d}y + \frac{\alpha\widetilde{\theta}}{\pi} + \frac{p_{i1}}{\beta} \equiv \widetilde{V} + \frac{\alpha\widetilde{\theta}}{\pi} + \frac{p_{i1}}{\beta}, \tag{5.35}$$

where

$$\beta = \frac{\mathrm{Bo}\, J_0\left(\sqrt{\mathrm{Bo}}\,\alpha\right)}{\pi\alpha^2 J_2\left(\sqrt{\mathrm{Bo}}\,\alpha\right)}. \tag{5.36}$$

We introduce the polar coordinates $x = r\cos\phi - \alpha$ and $y = r\sin\phi$. The governing equation is then given by

$$\mathcal{H}_{rr} + \frac{1}{r}\mathcal{H}_r + \frac{1}{r^2}\mathcal{H}_{\phi\phi} + \mathrm{Bo}\,\mathcal{H} = \mathcal{F}(r,\phi) \quad \text{for } r < 1,\ 0 \le \phi \le 2\pi, \tag{5.37}$$

$$\mathcal{H}(\alpha,\phi) = 0 \qquad \text{for } 0 \le \phi \le 2\pi, \tag{5.38}$$

where the function $\mathcal{F}$ on the right-hand side of (5.37) is defined by

$$\mathcal{F}(r,\phi) = -\frac{\widetilde{\theta}\mathrm{Bo}\left(r^2 - \alpha^2\right)}{\pi^2\alpha\left(r^2 - 2\alpha r\cos\phi + \alpha^2\right)}. \tag{5.39}$$

Thus, we must solve the inhomogeneous Helmholtz equation with zero height on the boundary, the solution of which can be written as a generalised Fourier series [16]

$$\mathcal{H}(r,\phi) = \sum_{m=0}^{\infty}\sum_{n=1}^{\infty} J_m\left(\frac{\lambda_{m,n}}{\alpha}r\right)\left(A_{m,n}\cos m\phi + B_{m,n}\sin m\phi\right), \tag{5.40}$$

where $A_{m,n}$ and $B_{m,n}$ are the coefficients of the series and $\lambda_{m,n}$ is the nth zero of the Bessel function $J_m(x)$. Our main concern is with how the volume of the drop is altered by the junction region. We defined $\widetilde{V}$ to be the integral of (5.40) over the circular contact set, which gives

$$\widetilde{V} = \int_0^{\alpha}\int_0^{2\pi} r\,\mathcal{H}\ \mathrm{d}\phi\,\mathrm{d}r = 2\pi\alpha^2\sum_{n=1}^{\infty}\frac{A_{0,n}}{\lambda_{0,n}}J_1(\lambda_{0,n})\,. \tag{5.41}$$

Thus, we need only determine $A_{0,n}$ to find the volume correction to within a pressure correction term. Substituting (5.40) into the governing equation and using orthogonality gives

$$A_{0,n} = \frac{\alpha^3 \widetilde{\theta} \mathrm{Bo}}{\pi^3 \left(\alpha^2 \mathrm{Bo} - \lambda_{0,n}^2\right) \left[J_1(\lambda_{0,n})\right]^2} \int_0^1 \int_0^{2\pi} \frac{\left(\mathcal{R}^2 - 1\right) \mathcal{R} J_0(\lambda_{0,n} \mathcal{R})}{\mathcal{R}^2 - 2\mathcal{R}\cos\phi + 1} \, \mathrm{d}\phi \, \mathrm{d}\mathcal{R}, \quad (5.42)$$

where $r = \alpha\mathcal{R}$, $n \in \mathbb{N}$ and

$$\widetilde{\theta} = \frac{J_1\left(\sqrt{\mathrm{Bo}}\,\alpha\right)}{\sqrt{\mathrm{Bo}}\, J_0\left(\sqrt{\mathrm{Bo}}\,\alpha\right)} p_{i0}. \quad (5.43)$$

The analysis so far is for a drop with a single conduit connected. In our formulation of the network problem we specified that the distance between conduits connected to the same drop must be much larger than their widths. Given this assumption, each conduit connected to a drop will contribute linearly to the total $\mathrm{O}(\epsilon^2)$ correction. Using the same notation as in §5.1, we let i denote a drop with n connected conduits with dimensionless widths $\bar{a}_{i,j}$ for $j = 1, \ldots, n$. The two-term drop volume is then given by

$$\widehat{v}_i \sim \widehat{v}_{i0} + \epsilon^2 \sum_{j=1}^{n} \bar{a}_{i,j} \widehat{v}_{i1}. \quad (5.44)$$

5.2.2 Numerical validation of the volume correction

We test the validity of (5.44) by comparing it to numerical solutions performed in Comsol. Since (5.44) is quasi-steady, we look for stationary solutions to (5.5) with zero height on the contact line where the pressure is a prescribed constant, $\mathcal{P}$ say. Thus, the interface height is governed by

$$\nabla^2 h + \mathrm{Bo}\, h = -\mathcal{P}. \quad (5.45)$$

The geometries we use for the finite element solution are illustrated in Figure 5.7a, note that the conduit lengths are not drawn to scale. In each case we use the leading-order asymptotic conduit solution (5.8) to fix the height at the ends of the conduit, so

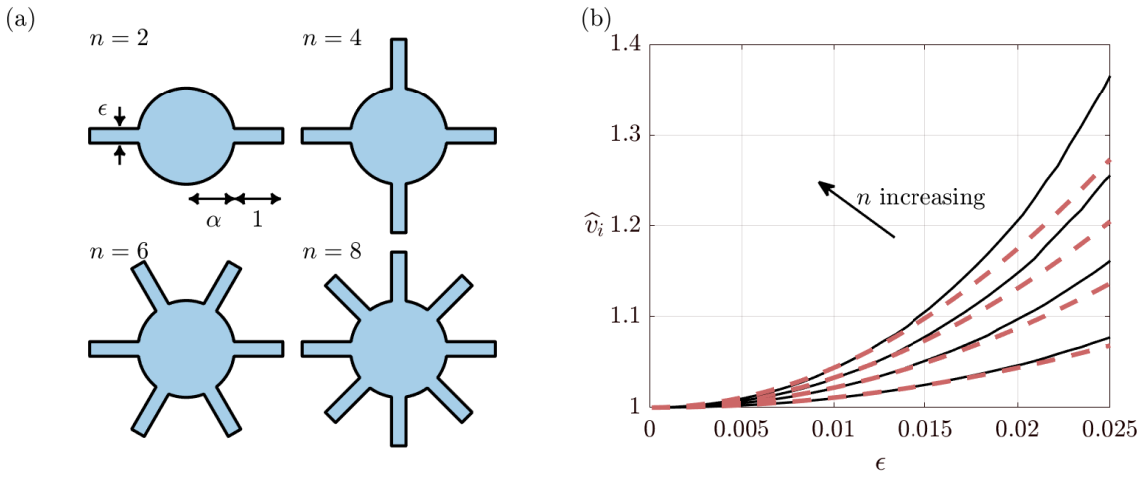


Figure 5.7: (a) The geometries used in the numerical simulations with $n = 2, 4, 6, 8$ conduits. (b) Comparison of the numerical solutions (solid lines) on the domains shown in (a) to (5.44) (dashed lines) for different values of ϵ with $\alpha = 1/8$, Bo $= 256$ and $\mathcal{P} = 1/\beta$, where β is given by (5.36).

that $h = \mathcal{P}/2\left(\epsilon^2\bar{a}_{i,j}^2 - y_{i,j}^2\right)$ at the ends of the conduit not connected to the drop. To compute the coefficients $A_{0,n}$ the integral in (5.42) requires some careful consideration since the denominator tends to zero as $(\mathcal{R}, \phi) \to (1, 0)$. On expanding the integrand we find that it vanishes at $(1, 0)$, so in the vicinity of this point we approximate the integrand with a series solution and then use quadrature (in this case *trapz* in MATLAB) to find the value over the rest of the domain. Solutions of (5.44) are compared to COMSOL solutions in Figure 5.7b for drops with different numbers of connected conduits. We see good agreement as both ϵ and n are decreased. We note that both the finite element and asymptotic solutions show that the drop volume can be altered significantly by the presence of multiple connected conduits. We note that (5.44) is only valid when the distance between the conduits is much greater than their width. With the conduits evenly spaced around the circumference of the drop, as in Figure 5.7a, we require $2\pi\alpha \gg n\epsilon$. For the largest parameters used in Figure 5.7b we find that $2\pi\alpha \approx 0.79$ and $n\epsilon \approx 0.2$. Thus, for larger values of n smaller values of ϵ are needed to see such good agreement, illustrating why small values of ϵ are required when a larger number of conduits are connected to a drop.

5.2.3 Higher order solutions for the thin-film conduit

In chapter 4 we analysed the dumbbell shaped circuit for aspect ratios $\delta = \mathrm{O}(1)$ and $\epsilon \ll 1$. The leading-order, quasi-steady interface height, flux and area of the conduit cross-section were found in §4.4. In this section we will determine the next-order corrections to these solutions. We note that very similar analyses have been carried out for rivulets flowing down an inclined plane [3]. The governing equations are given by (4.5)–(4.11) and we recall that they were rescaled with

$$Y = \epsilon\,\widehat{y}, \quad Z = \begin{cases} \epsilon^2\,\widehat{z} & \text{for } Z \in \Gamma_1, \\ \epsilon\widehat{Z} & \text{for } Z \in \Gamma_2, \end{cases} \qquad H = \epsilon^2\,h_C, \tag{5.46}$$

in the conduit region and expanded as in (4.54). We note the reduced pressure in the overlaying fluid P_2 was shown to be $\mathrm{O}(\epsilon^4)$ so does not appear in the next-order corrections. At $\mathrm{O}(\epsilon)$ the Navier-Stokes equations give

$$\frac{\partial^2 U_{11}}{\partial \widehat{z}^2} = \frac{\partial p_{C1}}{\partial X}, \quad \frac{\partial p_{C1}}{\partial \widehat{y}} = 0, \quad \frac{\partial p_{C1}}{\partial \widehat{z}} = 0 \tag{5.47}$$

for $0 < X < 1$, $0 < \widehat{y} < 1$, $0 < \widehat{z} < h_{C0}$. Thus, p_{C1} is also a function of X and T only, where we recall that T has been scaled with the conduit length relaxation timescale $t^*_{CL} = \mathrm{O}(\epsilon^{-4})$, as defined in §4.1. At $\mathrm{O}(\epsilon)$ the no-slip boundary condition on the base and the tangential component of (4.10) give

$$U_{11} = 0 \qquad \text{on } \widehat{z} = 0, \tag{5.48}$$

$$\frac{\partial U_{11}}{\partial \widehat{z}} = \mu \frac{\partial U_{20}}{\partial \widehat{Z}} - h_{C1} \frac{\partial^2 U_{10}}{\partial \widehat{z}^2} \quad \text{on } \widehat{Z} = 0,\ \widehat{z} = h_{C0}, \tag{5.49}$$

with U_{20} the leading-order contribution to the flow in the X direction in the overlaying fluid. At $\mathrm{O}(\epsilon)$, the normal component of (4.10) gives

$$\frac{\partial^2 h_{C1}}{\partial \widehat{y}^2} = -p_{C1} \quad \text{for } -1 < \widehat{y} < 1, \tag{5.50}$$

where the height is zero on $|\widehat{y}| = 1$ and noting that the Bond number contribution is still negligible. As with the leading-order solution, we find the solution of (5.50)

subject to these boundary conditions to be given by a parabola:

$$h_{C1} = \frac{p_{C1}}{2}\left(1 - \widehat{y}^2\right). \tag{5.51}$$

Using (5.51) we find the solution of (5.47) and (5.49) to be given by

$$U_{11} = \frac{1}{2}\left(\widehat{z}^2 - 2h_{C0}\widehat{z}\right)\frac{\partial p_{C1}}{\partial X} + \left(\mu\frac{\partial U_{20}}{\partial \widehat{Z}}\bigg|_{\widehat{Z}=0} - h_{C1}\frac{\partial p_{C0}}{\partial X} - h_{C0}\frac{\partial p_{C1}}{\partial X}\right)\widehat{z}. \tag{5.52}$$

As we can see, we need only determine the $\widehat{Z}$ derivative of U_{20} on $\widehat{Z} = 0$ to compute U_{11} in the cross-section. Noting the pressure contribution from P_2 is trivial at leading order the governing equation for U_{20} is

$$\widetilde{\nabla}^2 U_{20} = 0 \quad \text{in } \widehat{Z} > 0, \tag{5.53}$$

where $\widetilde{\nabla}^2 = \partial^2/\partial\widehat{y}^2 + \partial^2/\partial\widehat{Z}^2$. Continuity of velocity across the interface (4.7) and the solution for U_{10} at $\widehat{z} = h_{C0}$ given by (4.58) entails

$$U_{20} = -\frac{h_{C0}^2}{2}\frac{\partial p_{C0}}{\partial X} \quad \text{on } \widehat{Z} = 0 \text{ for } |\widehat{y}| \leq 1, \tag{5.54}$$

where h_{C0} is given by (4.61a) and p_{C0} by (4.82). At leading order (4.8) gives

$$U_{20} = 0 \quad \text{on } \widehat{Z} = 0 \text{ for } |\widehat{y}| > 1. \tag{5.55}$$

The overlaying fluid is quiescent on the interface open to the air, so $U_2 \to 0$ as $\widehat{Z} \to \infty$. Combining this with (4.9) gives, at leading order,

$$U_{20} \to 0 \quad \text{as } \widehat{y}^2 + \widehat{Z}^2 \to \infty. \tag{5.56}$$

As we discussed in §3.3.4 a solution to Laplace's equation with Dirichlet boundary data is well known (see (3.80)). The solution of (5.53) with boundary conditions (5.54)–(5.56) can be written as

$$U_{20} = -\frac{\widehat{Z}}{2\pi}\frac{\partial p_{C0}}{\partial X}\int_{-1}^{1}\frac{h_{C0}^2(x,\xi,T)}{\widehat{Z}^2 + (\xi - \widehat{y})^2}\,\mathrm{d}\xi. \tag{5.57}$$

Numerical methods are required to evaluate the integral in (5.57), but there is an analytic expression for the $\widehat{Z}$ derivative on $\widehat{Z}=0$. We find that

$$\left.\frac{\partial U_{20}}{\partial \widehat{Z}}\right|_{\widehat{Z}=0} = \left(\frac{4}{3} - 2\widehat{y}^2 - \widehat{y}\left(1-\widehat{y}^2\right)\log\left(\frac{1+\widehat{y}}{1-\widehat{y}}\right)\right)\frac{p_{C0}^2}{2\pi}\frac{\partial p_{C0}}{\partial X}. \tag{5.58}$$

The next-order flux in the conduit (found by expanding (4.60b)) is then given by

$$\widehat{Q}_1 = -\epsilon^7\left(\int_{-1}^{1}\left(U_{10}(\widehat{z}=h_{C0})\,h_{C1} + \int_0^{h_{C0}} U_{11}\,\mathrm{d}\widehat{z}\right)\,\mathrm{d}\widehat{y}\right), \tag{5.59}$$

$$= -\epsilon^7\left(\frac{4}{105}p_{C0}^3\frac{\partial p_{C1}}{\partial X} + \left(\frac{72\pi p_{C0}^2 p_{C1} - 35\mu p_{C0}^4}{630\pi}\right)\frac{\partial p_{C0}}{\partial X}\right). \tag{5.60}$$

Since the $\mathrm{O}(\epsilon)$ correction to the height, (5.51), has the same form as the leading-order height, expanding (4.60a) gives the next-order cross-sectional area as

$$\widehat{A}_1 = \frac{2}{3}\epsilon^3 p_{C1}. \tag{5.61}$$

At $\mathrm{O}(\epsilon)$ conservation of mass then gives

$$\frac{\partial \widehat{A}_1}{\partial T} + \frac{\partial \widehat{Q}_1}{\partial X} = 0 \quad \text{for } 0<X<1,\, T>0. \tag{5.62}$$

To find the appropriate boundary conditions for (5.62) would require us to analyse the junction region as we did in §4.5. Higher order analysis of the junction region becomes quite complex, so for simplicity we assume that the pressure is fixed at both ends of the conduit. Without loss of generality, we then impose the boundary conditions

$$p_{C1}(0,T) = 0, \quad p_{C1}(1,T) = 0. \tag{5.63}$$

On the drainage timescale $T \gg 1$ we find the quasi-steady solution to (5.62) to be given by

$$p_{C1} = \frac{7\mu}{24\pi}\frac{p_{C0}^5 + \left(p_L^5 - p_R^5\right)X - p_L^5}{p_{C0}^3}. \tag{5.64}$$

The quasi-steady flux is then given by

$$\widehat{Q}_1 = -\mu\epsilon^7\frac{p_L^5 - p_R^5}{90\pi}. \tag{5.65}$$

Thus, for given end pressures, the flow rate in the conduit decreases as the viscosity ratio is increased. This is no longer valid when $\mu = \mathrm{O}(1/\epsilon)$. Since we have assumed that the pressure correction is zero at the ends of the conduit, rather than demonstrate it by expanding the problem in the junction region, we will not incorporate this correction into the model for the drop volume. The correction will, however, be useful in testing the validity of the solutions for isolated conduits.

5.2.4 Large Bond numbers in the thin-film analysis

In chapter 3 we only considered Bond numbers satisfying $\mathrm{Bo} = \mathrm{O}(1)$ so that $\epsilon^2\mathrm{Bo} = \widetilde{\mathrm{Bo}} \ll 1$. This is a reasonable assumption to make given the values stated in Table 2.1. We shall now briefly discuss what happens when this is not the case. We note that the same analysis has been performed for rivulets flowing down an inclined plane [37]. The governing equations in the drop are unchanged, but as we noted in §3.3.2 there is an upper limit on the size of the Bond number given by $\alpha\sqrt{\mathrm{Bo}} < 2.405$. This suggests that we only need consider large negative Bond numbers; these could be achieved with a large increase in the density of the fluid in the circuit, alternatively, if the device was upside down a large increase in the density of the overlaying fluid. In this limit the governing equation in the conduit (3.41) is now given by

$$\frac{\partial^2 h_C}{\partial \widehat{y}^2} = -p_C - \widetilde{\mathrm{Bo}}\, h_C \quad \text{for } -1 < \widehat{y} < 1, \tag{5.66}$$

with the boundary condition $h_C = 0$ on $\widehat{y} = \pm 1$. The solution to (5.66) is given by

$$h_C = \frac{p_C}{\widetilde{|\mathrm{Bo}|}} \left(1 - \frac{\cosh\left(\sqrt{\widetilde{|\mathrm{Bo}|}}\, \widehat{y}\right)}{\cosh\left(\sqrt{\widetilde{|\mathrm{Bo}|}}\right)} \right) \tag{5.67}$$

Some examples are plotted in Figure 5.8a for different values of $\widetilde{\mathrm{Bo}}$; the profiles are very similar to those in the drop region (see Figure 3.3a), but we need much higher Bond numbers to see a similar effect here. The area and flux in the conduit are then

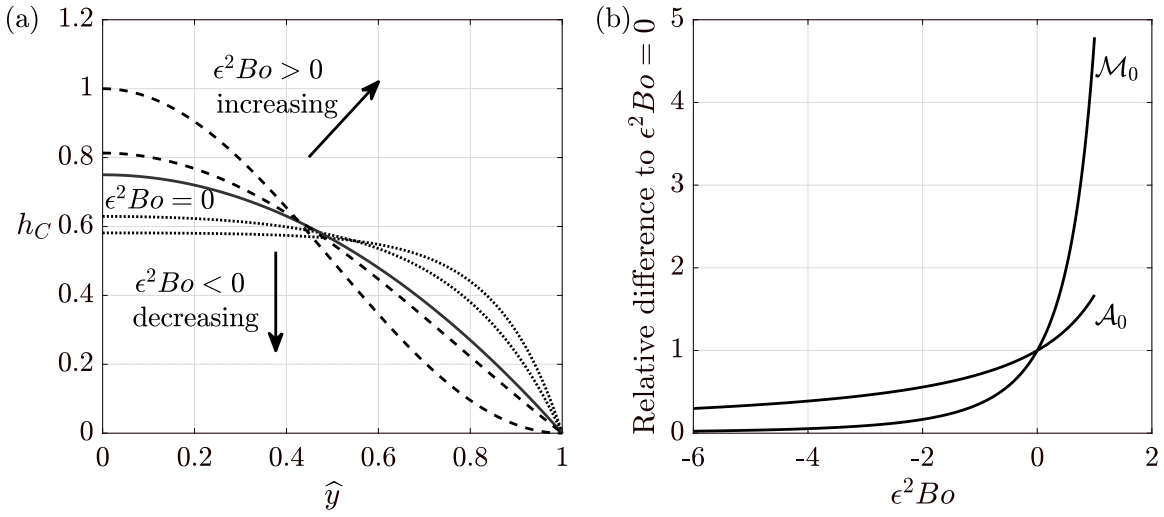


Figure 5.8: (a) Plots of the conduit cross-section profile for $\epsilon^2\mathrm{Bo} = -50$, -20, 0, 4, π^2, with $\widehat{A} = 1$. The profiles corresponding to negative Bond numbers are given by (5.67) (dotted lines). The profiles corresponding to positive Bond numbers are found by replacing the hyperbolic cosines with cosines and multiplying by -1 in (5.67) (dashed lines). For $\mathrm{Bo} = 0$ the profile is given by (3.42) (solid line). (b) The relative difference in $\mathcal{A}_0$ and $\mathcal{M}_0$ compared to the values in (3.43) as a function of the Bond number.

found to be given by

$$\widehat{A} \sim \mathcal{A}_0\,\epsilon^3 p_C, \quad \widehat{Q} \sim -\mathcal{M}_0\,\epsilon^7 \frac{\partial}{\partial x}\big(p_C^4\big) \quad \text{as } \epsilon \to 0, \tag{5.68}$$

where the constants $\mathcal{A}_0$ and $\mathcal{M}_0$ are given by

$$\mathcal{A}_0 = \frac{2\left(\sqrt{|\widetilde{\mathrm{Bo}}|} - \tanh\left(\sqrt{|\widetilde{\mathrm{Bo}}|}\right)\right)}{|\widetilde{\mathrm{Bo}}|^{3/2}}, \tag{5.69}$$

$$\mathcal{M}_0 = \frac{9\sqrt{|\widetilde{\mathrm{Bo}}|}\,\mathrm{sech}\left(\sqrt{|\widetilde{\mathrm{Bo}}|}\right)^2 - \tanh\left(\sqrt{|\widetilde{\mathrm{Bo}}|}\right)\left(4\,\mathrm{sech}\left(\sqrt{|\widetilde{\mathrm{Bo}}|}\right)^2 + 11\right) + 6\sqrt{|\widetilde{\mathrm{Bo}}|}}{12\,|\widetilde{\mathrm{Bo}}|^{7/2}}. \tag{5.70}$$

In Figure 5.8b we plot $3/2\mathcal{A}_0$ and $35\mathcal{M}_0$, *i.e.* the relative difference in area and flux compared to the model with $\epsilon^2\mathrm{Bo} \ll 1$. We can see that large negative Bond numbers are associated with small flow rates and large positive Bond numbers with larger flow rates. The solutions for $\widetilde{\mathrm{Bo}} > 0$ are given by replacing the hyperbolic functions with

their trigonometric counterparts and flipping the signs in (5.67), (5.69) and (5.70). The conduit relaxation problem (3.26) then generalises to

$$\frac{\mathcal{A}_0}{\epsilon^4 \mathcal{M}_0} \frac{\partial p_C}{\partial t} = \frac{\partial^2}{\partial x^2} \left(p_C^4 \right) \quad \text{for } 0 < x < 1. \tag{5.71}$$

Making the rescaling $t = (\mathcal{A}_0/\mathcal{M}_0)\, \epsilon^{-4} \tau$ gives the same governing equation as we found for the small Bond number case (see (3.89)). Thus, only the timescale is changed and the analysis from chapter 3 is still applicable. Nonetheless finding the solution in the junction region when $\epsilon^2 \mathrm{Bo} = \mathrm{O}(1)$ is far more challenging and will not be discussed here.

5.2.5 Discussion

Although we have focused on the leading-order models throughout this thesis (and will continue to do so) it is informative to extend the models to higher order. The differences between the equilibrium drop volumes for the full numerical and leading-order solutions shown in Figure 5.3 can be better understood by analysing the next-order solutions in the drop region. It may be valuable in the future to incorporate higher order drop and conduit corrections into the network GUI illustrated in Figure 5.4, though this will also require analysing the junction region to higher order than we have done in this thesis.

5.3 Analysis of a long, thick conduit

In this section we model a long conduit without considering the drops at either end. Instead we shall impose the pressure or liquid flux at either end. This analysis will mostly be applicable in the active flow case, where fluid is pumped into the conduit. As we saw in the previous chapters, where the flow was driven passively, the height of the conduit was much smaller than the width. In this section we shall investigate what happens when the height of the conduit is comparable to its width by imposing

a suitably high flux or pressure at the inlet. Imposing the flow rate via a pump allows for greater control over the dynamics (as we showed for the thin-film case in §3.4). As with the previous sections (§5.2.3 and §5.2.4), we note that the majority of the following analysis has been done for rivulets on an inclined plane, although without the overlaying liquid [92, 120].

5.3.1 Geometry and governing equations

The contact set of the conduit is defined by $\Omega_C^* = \{(x^*, y^*) : \ 0 < x^* < L, \ |y^*| < a^*(x^*)\}$, where the function a^* varies slowly along the conduit length and we define $a^*(0) = a_0$. We denote by Γ_1^* and Γ_2^* the regions containing the conduit and the overlay respectively. There are three length scales to consider in the conduit: its length L (x^*-scale), its width $2a^*$ (y^*-scale) and its maximum height H_C (z^*-scale) above the base as shown in Figure 5.9. As in previous chapters, our most important assumption is that the conduit is long compared to its width, *i.e.* $\epsilon = a_0/L \ll 1$. In this chapter we further assume that $a_0 \sim H_C$. The components of velocity are scaled to balance the terms in the incompressibility condition (2.1b). We nondimensionalise the governing equations (2.1)–(2.4) and (2.6)–(2.8) by scaling

$$\begin{gathered} x^* = L\,X, \quad y^* = \epsilon L\,Y, \quad z^* = \epsilon L\,Z, \quad h^* = \epsilon L\,H, \quad a^* = \epsilon L\,a \\ t^* = \frac{L}{U_0}\,T, \quad \kappa^* = \frac{1}{\epsilon L}\kappa, \quad \boldsymbol{U}_i = U_0\,(U_i, \epsilon\,V_i, \epsilon\,W_i)\,, \\ p_i^* = \frac{\gamma}{\epsilon L}\,P_i + p_{\mathrm{atm}} + \rho_2 g H_O - \rho_i g L Z. \end{gathered} \tag{5.72}$$

The appropriate pressure scale, $\gamma/(\epsilon L)$, is found from a dominant balance in the normal stress boundary condition and similarly the velocity scale $U_0 = \epsilon\gamma/\mu_1$ is found by balancing the momentum equations. We drop the asterisks from Ω_C^*, Γ_{Ci}^* and S_{Ci}^* to denote the corresponding dimensionless footprints, domains and interfaces. The governing equations (2.1) are now given by

$$\epsilon^2 \mathrm{Re}_3 \left(\frac{\partial U_i}{\partial T} + (\boldsymbol{U}_i \cdot \boldsymbol{\nabla}) U_i\right) - \frac{\nu_i}{\nu_1}\left(\epsilon^2 \frac{\partial^2 U_i}{\partial X^2} + \widetilde{\nabla}^2 U_i\right) = -\frac{\rho_1}{\rho_i}\frac{\partial P_i}{\partial X}, \tag{5.73a}$$

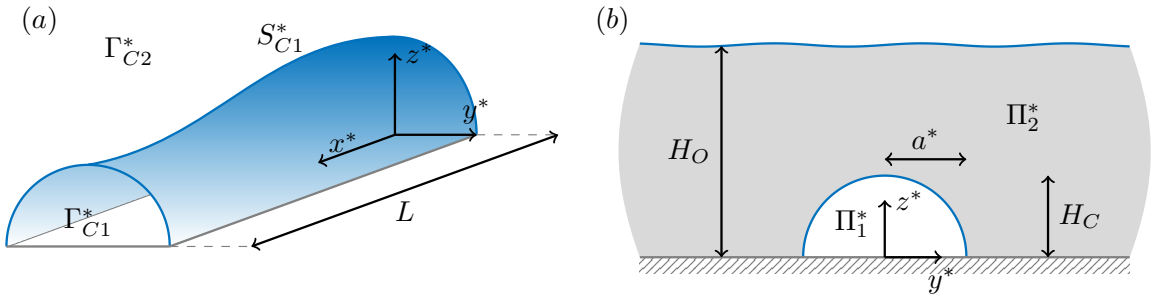


Figure 5.9: (a) The geometry of the conduit showing the different fluid regions, Γ^*_{C1}, Γ^*_{C2}, and the dividing interface S^*_{C1}. (b) The cross-section of the conduit, Π^*_1, Π^*_2 and the relevant length scales.

$$\epsilon^4 \mathrm{Re}_3 \left(\frac{\partial V_i}{\partial T} + (\boldsymbol{U}_i \cdot \boldsymbol{\nabla}) V_i \right) - \frac{\nu_i}{\nu_1} \left(\epsilon^4 \frac{\partial^2 V_i}{\partial X^2} + \epsilon^2 \widetilde{\nabla}^2 V_i \right) = -\frac{\rho_1}{\rho_i} \frac{\partial P_i}{\partial Y}, \tag{5.73b}$$

$$\epsilon^4 \mathrm{Re}_3 \left(\frac{\partial W_i}{\partial T} + (\boldsymbol{U}_i \cdot \boldsymbol{\nabla}) W_i \right) - \frac{\nu_i}{\nu_1} \left(\epsilon^4 \frac{\partial^2 W_i}{\partial X^2} + \epsilon^2 \widetilde{\nabla}^2 W_i \right) = -\frac{\rho_1}{\rho_i} \frac{\partial P_i}{\partial Z}, \tag{5.73c}$$

for $(X, Y, Z) \in \Gamma_{Ci}$, $i = 1, 2$ where $\widetilde{\nabla}^2 = \partial^2/\partial Y^2 + \partial^2/\partial Z^2$ and $\mathrm{Re}_3 = U_0 L/\nu_1$. The incompressibility condition is

$$\boldsymbol{\nabla} \cdot \boldsymbol{U}_i = 0 \quad \text{for } (X, Y, Z) \in \Gamma_{Ci},\ i = 1, 2. \tag{5.74}$$

The kinematic condition (2.2) and continuity of velocity (2.3) on the interface are now given by

$$\boldsymbol{U}_i \cdot \mathbf{n} = \widehat{v}_n \qquad \text{on } S_{C1} \text{ for } i = 1, 2, \tag{5.75}$$

$$\boldsymbol{U}_1 = \boldsymbol{U}_2 \qquad \text{on } S_{C1}. \tag{5.76}$$

where $\mathbf{n}$ is the unit normal to S_{C1} and $\widehat{v}_n$ is the velocity of the free boundary S_{C1} in that direction. There is no-slip on the base of the device so

$$\boldsymbol{U}_i = \mathbf{0} \quad \text{on } Z = 0 \text{ for } (X, Y) \in \Omega_{Ci},\ i = 1, 2. \tag{5.77}$$

The dynamic boundary condition on the interface becomes

$$\widehat{\boldsymbol{\sigma}}_2 \cdot \mathbf{n} - \widehat{\boldsymbol{\sigma}}_1 \cdot \mathbf{n} = -\left(\kappa + \epsilon^2 \mathrm{Bo}\, Z\right) \mathbf{n} \quad \text{on } S_{C1}. \tag{5.78}$$

The rescaled stress tensor is given by

$$\widehat{\boldsymbol{\sigma}}_i = -P_i\mathbf{I} + \frac{\mu_i}{\mu_1}\boldsymbol{\tau}_i, \tag{5.79}$$

where

$$\boldsymbol{\tau}_i = \epsilon \begin{bmatrix} 2\,\epsilon\,(U_i)_X & \epsilon^2\,(V_i)_X + (U_i)_Y & \epsilon^2\,(W_i)_X + (U_i)_Z \\ \epsilon^2\,(V_i)_X + (U_i)_Y & 2\,\epsilon\,(V_i)_Y & \epsilon\,((W_i)_Y + (V_i)_Z) \\ \epsilon^2\,(W)_X + (U_i)_Z & \epsilon\,((W_i)_Y + (W_i)_Z) & 2\,\epsilon\,(W)_Z \end{bmatrix}. \tag{5.80}$$

A similar expression to (5.78) can also be derived for the dynamic condition on the free surface open to the atmosphere.

5.3.2 The leading-order problem

Throughout we shall assume that $\epsilon^2\mathrm{Re}_3 \ll 1$. As shown in Table 2.2 the Reynolds number can potentially be quite large; as much as 10^5. Although $\epsilon \in [0.005, 0.5]$, there may be Reynolds numbers for which this analysis is not applicable. The leading-order problem in the conduit is given by

$$\widetilde{\nabla}^2 U_1 = -\frac{\partial P_1}{\partial X}, \quad \frac{\partial P_1}{\partial Y} = 0, \quad \frac{\partial P_1}{\partial Z} = 0 \quad \text{in } \Gamma_{C1}, \tag{5.81}$$

$$\mu\widetilde{\nabla}^2 U_2 = -\frac{\partial P_2}{\partial X}, \quad \frac{\partial P_2}{\partial Y} = 0, \quad \frac{\partial P_2}{\partial Z} = 0 \quad \text{in } \Gamma_{C2}, \tag{5.82}$$

where $\mu = \mu_2/\mu_1$ is the ratio of the fluid viscosities. Hence, $P_1 = P_1(X,T)$ and $P_2 = P_2(X,T)$ at leading order, *i.e.* the pressure in each fluid depends only on the distance X along the conduit and time T. There is no-slip for either fluid on the substrate and on the interface S_{C1} the fluid velocities are equal so that

$$U_1 = 0 \quad \text{on } Z = 0 \text{ for } (X,Y) \in \Gamma_{C1}, \tag{5.83}$$

$$U_2 = 0 \quad \text{on } Z = 0 \text{ for } (X,Y) \in \Gamma_{C2}, \tag{5.84}$$

$$U_1 = U_2 \quad \text{on } S_{C1}. \tag{5.85}$$

The tangential component of (2.2) then gives, at leading order,

$$\frac{\partial U_1}{\partial n} = \mu \frac{\partial U_2}{\partial n} \quad \text{on } S_{C1}. \tag{5.86}$$

We define Π_i to be the cross-section of the device in a YZ-plane for $i = 1, 2$ (see Figure 5.9). The dimensions of the container are much larger than those of the conduit, so we assume that in each cross-section the area of Π_1 is much less than that of Π_2. Further assuming that the flow in Π_2 is driven solely by the flow in the conduit and is quiescent far from the conduit, the relevant far-field conditions are

$$(U_2, V_2, W_2) \to 0, \quad P_2 \to 0 \quad \text{as } X^2 + Y^2 + Z^2 \to \infty. \tag{5.87}$$

The last follows from the pressure being hydrostatic in Γ_{C2} away from the conduit with the perturbations to H_O being small. Then, since P_2 depends only on X and T as shown by (5.82), we have $P_2 = 0$. Assuming that the interface height is single-valued, the normal component of (5.78) is given by

$$P_1(X,T) = -\frac{\partial}{\partial Y}\left(\frac{\dfrac{\partial H}{\partial Y}}{\sqrt{1+\left(\dfrac{\partial H}{\partial Y}\right)^2}}\right) + \widetilde{\mathrm{Bo}}\, H \quad \text{for } -a < Y < a \text{ and } 0 < X < 1. \tag{5.88}$$

where H is the height of the interface and $\widetilde{\mathrm{Bo}} = \epsilon^2 \mathrm{Bo}$. The height is zero on the contact line so we impose

$$H = 0 \quad \text{on } |Y| = a. \tag{5.89}$$

The X dependence comes from conservation of mass. Since the pressure P_1 has no Y or Z dependence at leading order we can simplify (5.81) and (5.82) with the scaling

$$U_i = -\frac{\partial P_1}{\partial X}\,\overline{U}_i \quad \text{for } i = 1, 2. \tag{5.90}$$

Thus, in each cross-section, the leading-order system is given by

$$\widetilde{\nabla}^2 \overline{U}_1 = 1 \quad \text{in } \Pi_1, \tag{5.91}$$

$$\widetilde{\nabla}^2\overline{U}_2 = 0, \quad \text{in } \Pi_2. \tag{5.92}$$

With no-slip on the base

$$\overline{U}_i = 0 \quad \text{on } \Pi_i \cap \{Z = 0\}. \tag{5.93}$$

On the interface we have

$$\frac{\partial \overline{U}_1}{\partial n} = \mu \frac{\partial \overline{U}_2}{\partial n}, \quad \overline{U}_1 = \overline{U}_2 \quad \text{on } S_{C1}. \tag{5.94}$$

and in the far-field we have

$$\overline{U}_2 \to 0 \quad \text{as } Y, Z \to \infty. \tag{5.95}$$

The flux and area in the conduit are defined as

$$\mathcal{Q}\Big(P_1; \widetilde{\mathrm{Bo}}, \mu\Big) = \iint_{\Pi_1} \overline{U}_1 \, \mathrm{d}Y \, \mathrm{d}Z, \tag{5.96}$$

$$\mathcal{A}\Big(P_1; \widetilde{\mathrm{Bo}}\Big) = \iint_{\Pi_1} \mathrm{d}Y \, \mathrm{d}Z, \tag{5.97}$$

so that conservation of mass in the conduit (2.14) gives the evolution of the interface in the X-direction as

$$\frac{\partial \mathcal{A}}{\partial T} = \frac{\partial}{\partial X}\left(\mathcal{Q}\frac{\partial P_1}{\partial X}\right). \tag{5.98}$$

Intriguingly, (5.98) is only well posed when $\mathcal{A}$ and $\mathcal{Q}$ are both monotonically increasing (or decreasing) functions of P_1, otherwise we would have a backward diffusion equation with pathological behaviour that does not make physical sense. There are several choices for the boundary conditions that may be imposed on (5.98); we could prescribe the pressure at $X = 0$ and $X = 1$ as in chapters 3 and 4; we could also prescribe the liquid flux at $X = 0$ and $X = 1$ or indeed a mixture of these; for comparisons with data it may also be more appropriate to prescribe the conduit height at either end. An initial condition is also required: specifying the pressure P_1 at $T = 0$ will be sufficient. There are several limiting cases which will allow us to find asymptotic solutions.

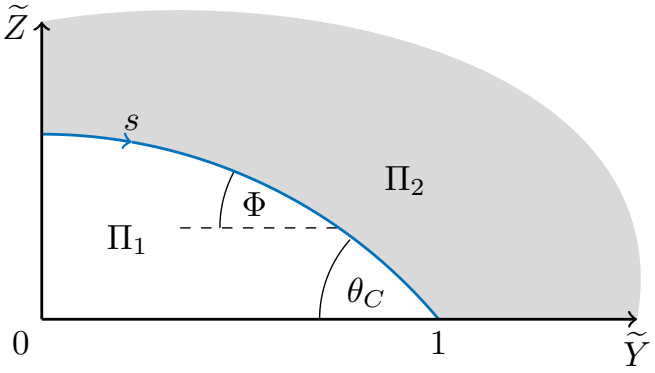


Figure 5.10: The coordinate system for the conduit cross-section: s is the arc length from the top of the profile, θ_C is the contact angle and Φ is the angle the curve makes with the horizontal. The regions inside and outside of the conduit are denoted Π_1 and Π_2 respectively.

5.3.3 Zero Bond number: circular cross-sections

As shown in Table 2.1 we would typically expect $\widetilde{\mathrm{Bo}} = \epsilon^2 \mathrm{Bo}$ to be small so we begin by considering the limit $\widetilde{\mathrm{Bo}} \to 0$. In this limit solutions to (5.88) will be circular arcs. The variables are rescaled with the conduit width $a(X)$ as follows

$$Y = a\,\widetilde{Y}, \quad Z = a\,\widetilde{Z}, \quad H = a\,\widetilde{H}, \quad P_1 = \frac{\widetilde{P}_1}{a}. \tag{5.99}$$

Then (5.88) becomes

$$\widetilde{P}_1(X,T) = -\frac{\partial}{\partial \widetilde{Y}}\left(\frac{\dfrac{\partial \widetilde{H}}{\partial \widetilde{Y}}}{\sqrt{1+\left(\dfrac{\partial \widetilde{H}}{\partial \widetilde{Y}}\right)^2}}\right) \quad \text{for } -1 < \widetilde{Y} < 1 \text{ and } 0 < X < 1, \tag{5.100}$$

subject to the boundary condition

$$\widetilde{H} = 0 \quad \text{on } |\widetilde{Y}| = 1. \tag{5.101}$$

In much the same way as we did for the drop profile in §4.3.3, we introduce the new variables s measuring the distance from the apex of the profile and Φ measuring the angle with the horizontal as illustrated in Figure 5.10. Then the solution to (5.100)

with the boundary condition (5.101) can be written parametrically as

$$\widetilde{Y} = \frac{\sin\Phi}{\widetilde{P}_1}, \quad \widetilde{H} = \frac{\cos\Phi - \cos\theta_C}{\widetilde{P}_1}, \quad \text{for } -\theta_C < \Phi < \theta_C, \tag{5.102}$$

where $\theta_C(X,T)$ is the contact angle for the cross-section. The leading-order pressure in the conduit can be written in terms of the contact angle via

$$\widetilde{P}_1(X,T) = \sin\theta_C. \tag{5.103}$$

Assuming the contact angle is in the range $0 < \theta_C < \pi$, (*i.e.* the angle is constrained only by the solid base) (5.103) shows that different contact angles may have the same pressure. For the thick conduit problem, it will be more convenient to work with the contact angle instead of the pressure. Making the rescaling $\mathcal{A} = a(X)^2\,\widetilde{\mathcal{A}}$, the area of the circular cross-section in terms of θ_C is given by

$$\widetilde{\mathcal{A}}(\theta_C) = 2\int_0^1 \mathrm{d}Y\,\widetilde{H} = 2\int_0^{\theta_C} \mathrm{d}\Phi\frac{\mathrm{d}Y}{\mathrm{d}\Phi}\widetilde{H} = \frac{2\theta_C - \sin(2\theta_C)}{2\sin^2\theta_C}. \tag{5.104}$$

5.3.4 Leading-order flow problem

We now want to find the flow in a cross-section given by (5.102). Since the interface cross-section is a circular segment, we can derive a solution via a conformal map as we shall now describe. In each cross-section the conduit is a circular arc forming part of a circle of radius R_0 centred at $(0, Z_0)$, where

$$R_0 = \frac{1}{\sin\theta_C}, \quad Z_0 = -\frac{\cos\theta_C}{\sin\theta_C}. \tag{5.105}$$

The upper half $(\widetilde{Y}, \widetilde{Z})$-plane can be then be mapped to a strip in the (τ, σ)-plane using a bipolar transformation [43] defined by

$$\widetilde{Y} = \frac{\sinh\tau}{\cosh\tau - \cos\sigma}, \quad \widetilde{Z} = \frac{\sin\sigma}{\cosh\tau - \cos\sigma}. \tag{5.106}$$

Lines in τ-σ space are transformed into circles in $\widetilde{Y}$-$\widetilde{Z}$ space as shown in Figure 5.11. The interface is then given by $\sigma = \beta = \pi - \theta_C$ in τ-σ space. The velocity is rescaled

with the conduit width and the leading-order problem in the conduit transformed to Laplace's equation via

$$\overline{U}_1 = a^2 \left(\mathcal{U}_1 + f(\tau, \sigma; \theta_C) \right), \quad \overline{U}_2 = a^2 \, \mathcal{U}_2, \tag{5.107}$$

where

$$f(\tau, \sigma; \theta_C) = \frac{R_0}{4} - \frac{\widetilde{Y}^2 + (\widetilde{Z} - Z_0)^2}{4}. \tag{5.108}$$

Then the leading-order problem in the transformed domain is now given by

$$\widetilde{\nabla}^2 \mathcal{U}_1 = 0 \quad \text{for } \beta < \sigma < \pi, \tag{5.109}$$

$$\widetilde{\nabla}^2 \mathcal{U}_2 = 0 \quad \text{for } 0 < \sigma < \beta, \tag{5.110}$$

for $-\infty < \tau < \infty$, with the boundary conditions

$$\mathcal{U}_1 + f(\tau, \pi, \theta_C) = 0 \qquad \text{on } \sigma = \pi, \tag{5.111}$$

$$\mathcal{U}_2 = 0 \qquad \text{on } \sigma = 0, \tag{5.112}$$

$$\mathcal{U}_1 = \mathcal{U}_2 \qquad \text{on } \sigma = \beta, \tag{5.113}$$

$$\frac{\partial \mathcal{U}_1}{\partial \sigma} + \left. \frac{\partial f}{\partial \sigma} \right|_{\sigma=\beta} = \mu \frac{\partial \mathcal{U}_2}{\partial \sigma} \quad \text{on } \sigma = \beta, \tag{5.114}$$

$$\mathcal{U}_1 \to 0 \qquad \text{as } \tau \to \infty \tag{5.115}$$

$$\mathcal{U}_2 \to 0 \qquad \text{as } \tau \to \infty \tag{5.116}$$

We could solve this problem with a Fourier transform, but the resulting expressions are unwieldy for quadrature. It will be easier to truncate the domain to $-\mathcal{L} < \tau < \mathcal{L}$ and impose the boundary condition

$$\mathcal{U}_1 = \mathcal{U}_2 = 0 \quad \text{on } \tau = \pm \mathcal{L}; \tag{5.117}$$

we recover in the limit $\mathcal{L} \to \infty$ our original problem. Since $\mathcal{U}_1$ and $\mathcal{U}_2$ are symmetric about $\tau = 0$, the solution to (5.109) and (5.110) can be written as a standard Fourier series on the domain $0 < \tau < \mathcal{L}$:

$$\mathcal{U}_1 = \sum_{n=1}^{\infty} \left[A_n \sinh\left(K_n \left(\sigma - \pi\right)\right) + B_n \cosh\left(K_n (\sigma - \pi)\right) \right] \cos\left(K_n \tau\right), \tag{5.118}$$

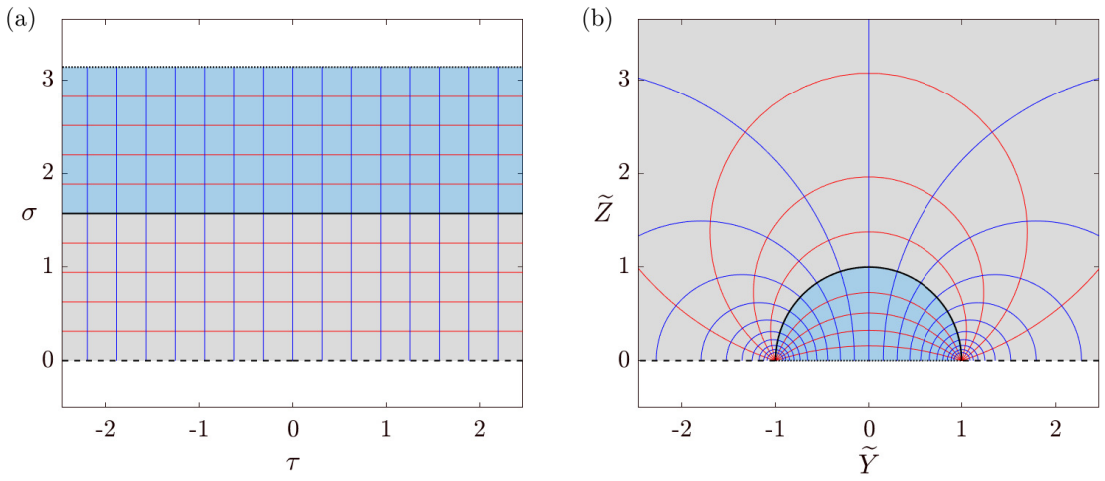


Figure 5.11: (a) In τ-σ space the fluid interface is a straight line with the infinite strips, bounded by $0 < \sigma < \beta$ and $\beta < \sigma < \pi$, mapping to the overlay and circuit cross-section respectively. (b) The transformed coordinates given by (5.106), constant values of σ are transformed to circles in Y-Z space. The shading represents the same region.

$$\mathcal{U}_2 = \sum_{n=1}^{\infty} C_n \sinh\left(K_n \sigma\right) \cos\left(K_n \tau\right), \tag{5.119}$$

where

$$K_n = \frac{(2n-1)\pi}{2\mathcal{L}}. \tag{5.120}$$

To find the coefficients A_n, B_n and C_n we first write $f(\tau, \pi, \theta_C)$ and $\frac{\partial f}{\partial \sigma}\big|_{\sigma=\alpha}$ as a Fourier cosine series:

$$f(\tau, \pi, \theta_C) = \frac{1}{2(\cosh\tau + 1)} = \sum_{n=1}^{\infty} f_n \cos\left(K_n \tau\right), \tag{5.121}$$

$$\left.\frac{\partial f}{\partial \sigma}\right|_{\sigma=\beta} = \frac{1}{2(\cosh\tau + \cos\theta_C)\sin\theta_C} = \sum_{n=1}^{\infty} \zeta_n \cos\left(K_n \tau\right), \tag{5.122}$$

where the coefficients are given by

$$f_n = \frac{2}{\mathcal{L}} \int_0^{\mathcal{L}} \frac{\cos\left(K_n \tau\right)}{2(\cosh\tau + 1)} \, \mathrm{d}\tau, \tag{5.123}$$

$$\zeta_n = \frac{2}{\mathcal{L}} \int_0^{\mathcal{L}} \frac{\cos\left(K_n \tau\right)}{2(\cosh\tau + \cos\theta_C)\sin\theta_C} \, \mathrm{d}\tau. \tag{5.124}$$

The integrals for the coefficients f_n and ζ_n cannot be evaluated analytically, so they need to be found numerically. We use trapezoidal numerical integration implemented

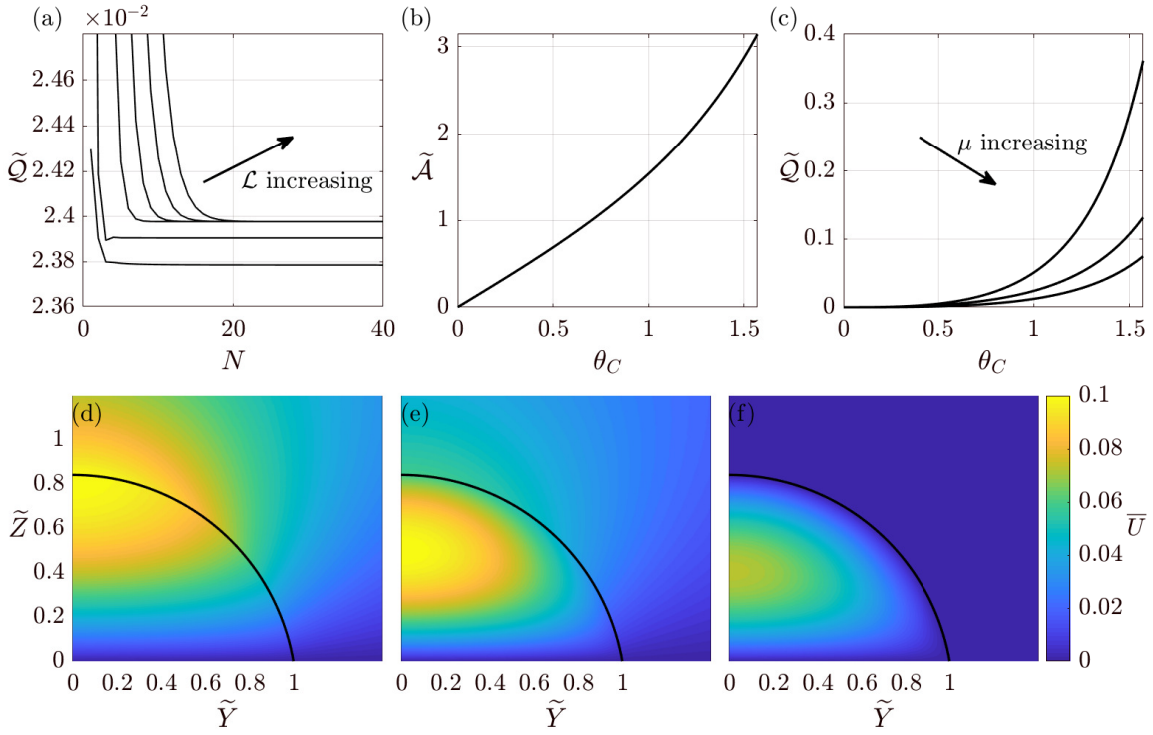


Figure 5.12: (a) The convergence of the Fourier series solution for the flux (5.128) as a function of N for $\mathcal{L} = 3, 4, 10, 15, 20, 25$, with $\mu = 4$ and $\theta_C = 1$. (b) The cross-sectional area (5.104) as a function of the contact angle. (c) The flux given by (5.128) as a function of θ_C for $\mu = 0, 4, 1000$. (d)–(f) The velocity in the cross-section of the conduit $\overline{U}_1$ and overlay $\overline{U}_2$ given by (5.118) and (5.119) with $\theta_C = 1.4$, $\mathcal{L} = 20$, and $N = 100$, where the viscosity ratio μ is given by $\mu = 0$ in (d), $\mu = 4$ in (e) and $\mu = 1000$ in (f). We note that the velocity outside of the conduit is effectively zero in (f).

with the MATLAB function *trapz*. In terms of f_n and ζ_n, the coefficients in (5.118) and (5.119) are given by

$$B_n = -f_n, \tag{5.125}$$

$$C_n = \frac{2K_nB_n + 2\zeta_n \sinh(K_n\theta_C)}{K_n\left[(\mu+1)\sinh(K_n\pi) + (\mu-1)\sinh(K_n(2\theta_C - \pi))\right]}, \tag{5.126}$$

$$A_n = \frac{K_n\left(B_n \sinh(K_n\theta_C) + \mu C_n \cosh(K_n(\theta_C - \pi))\right) - \zeta_n}{K_n \cosh(K_n\theta_C)}. \tag{5.127}$$

We rescale the flux in the conduit $\mathcal{Q}$ with $\mathcal{Q} = a(X)^2\,\widetilde{\mathcal{Q}}$, then (5.96) is written as

$$\widetilde{\mathcal{Q}}(\theta_C;\mu) = 2\int_\beta^\pi \int_0^{\mathcal{L}} \frac{\overline{U}_1}{(\cosh\tau - \cos\sigma)^2}\,\mathrm{d}\tau\,\mathrm{d}\sigma. \tag{5.128}$$

We are unable to evaluate (5.128) analytically, so we use quadrature via the MATLAB function *trapz* to perform the numerical evaluation. Truncating the Fourier series to the first N terms leaves us with two parameters that we must specify: N and $\mathcal{L}$. We note that the line $\tau = \mathcal{L}$ is transformed to the circle $\left(\widetilde{Y} - Y_{\mathcal{L}}\right)^2 + \widetilde{Z}^2 = R_{\mathcal{L}}^2$, where

$$R_{\mathcal{L}} = \frac{1}{\sinh \mathcal{L}}, \quad Y_{\mathcal{L}} = \frac{\cosh \mathcal{L}}{\sinh \mathcal{L}}. \tag{5.129}$$

The radius of this circle rapidly tends to zero as $\mathcal{L} \to \infty$. Figure 5.12a shows the convergence of the integral in (5.128) as N and $\mathcal{L}$ are increased for the parameter values $\mu = 4$ and $\Phi = 1$ and a uniform grid size of 0.01. As we increase the size of the domain more terms in the Fourier series are required for the solution to converge. We then construct a lookup table for $\widetilde{\mathcal{Q}}$ by evaluating the integral in (5.128) for different values of θ_C and μ. Interpolation can then be used to find $\widetilde{\mathcal{Q}}$ for any $0 < \theta_C < \pi$ and $\mu > 0$ as illustrated in Figure 5.12c. In Figure 5.12d–f we plot the velocity profile in the conduit cross-section for $\mu = 0, 4, 1000$. As the viscosity ratio is increased the maximum velocity moves from the interface to the middle of the conduit.

Conservation of mass (5.98) in terms of the contact angle θ_C is given by

$$\frac{\partial \mathcal{A}}{\partial T} = \frac{\partial}{\partial X}\left(\mathcal{Q}(\theta_C;\mu)\ \frac{\partial}{\partial X}\left(\frac{\sin\theta_C}{a}\right)\right) \quad \text{for } 0 < X < 1. \tag{5.130}$$

As detailed in §5.3.2 there are several possible boundary conditions that we could impose on (5.130). To illustrate the framework, we impose the flux at the inlet and the contact angle at the outlet:

$$\mathcal{Q}(\theta_C;\mu)\ \frac{\partial}{\partial X}\left(\frac{\sin\theta_C}{a}\right)\Bigg|_{X=0} = \mathcal{Q}_0, \quad \theta_C(1,T) = \theta_O. \tag{5.131}$$

To close the problem we prescribe an initial condition of the form

$$\theta_C(X,0) = \widetilde{\theta}_C(X) \quad \text{for } 0 < X < 1. \tag{5.132}$$

In experiments incorporating active flows, a drop is typically printed at the end of the conduit to act as a reservoir. In chapter 3 our main motivation for determining the

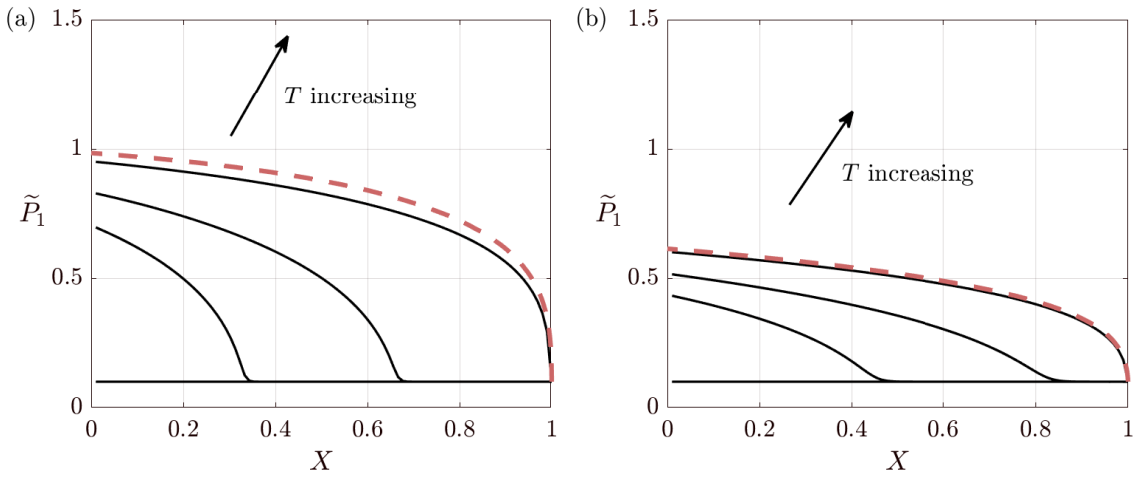


Figure 5.13: Numerical solutions of (5.130) and (5.132) with the initial condition $\widetilde{P}_1(X,0) = 0.1$ for (a) $\mathcal{Q}_0 = 0.01$, where the solid lines show the solution at $T = 0, 92, 194, 500$, and (b) $\mathcal{Q}_0 = 0.001$, where the solid lines show the solution at $T = 0, 18, 39, 100$. The dashed red line shows the steady state solution.

volumes of the drops was to determine the characteristics of the flow in the conduit. When the flux is imposed by an external pump the leading-order flow in the conduit is not affected by the presence of the drop.

5.3.5 Incorporating gravity into the cross-section

When $\widetilde{\mathrm{Bo}} = \mathrm{O}(1)$ we will be unable to find an analytic solution for the profile of the conduit in each cross-section. Instead we must rely on numerical methods. The problem is reformulated in the same way as Figure 5.10, where s is the distance from the apex of the profile and Φ is the angle with the horizontal. In these coordinates, (5.88) gives the system of equations

$$\frac{\mathrm{d}\Phi}{\mathrm{d}s} = a^2\widetilde{\mathrm{Bo}}\,\widetilde{H} + \widetilde{P}_1, \tag{5.133a}$$

$$\frac{\mathrm{d}\widetilde{Y}}{\mathrm{d}s} = \cos\Phi, \tag{5.133b}$$

$$\frac{\mathrm{d}\widetilde{H}}{\mathrm{d}s} = -\sin\Phi, \tag{5.133c}$$

for $0 < s < s^*$, where s^* corresponds to the point where the fluid boundary meets the base. The pressure $\widetilde{P}_1$ and total arc length s^* need to be determined as part

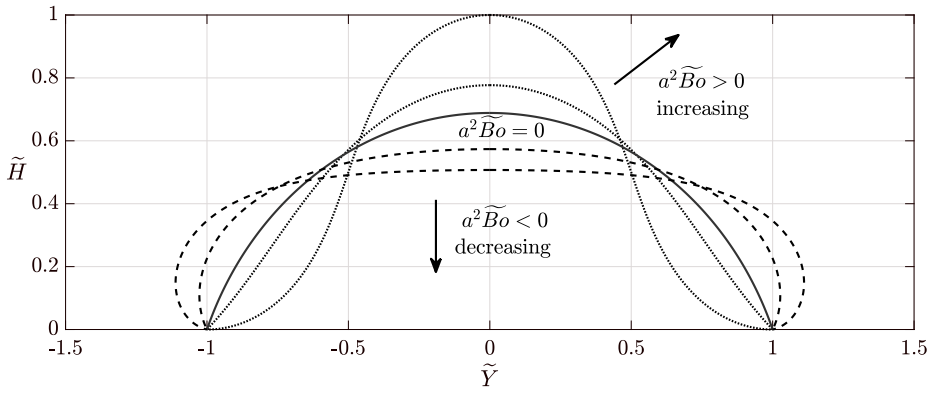


Figure 5.14: Numerical solutions of (5.133) and (5.134) for $a^2\widetilde{\mathrm{Bo}} = -15,\ -8,\ 0,\ 3,\ 5.1962$ for a fixed area $\widetilde{\mathcal{A}} = 1$. For clarity, dashed lines have been used for profiles with $a^2\widetilde{\mathrm{Bo}} < 0$, dotted lines have been used for $a^2\widetilde{\mathrm{Bo}} > 0$ and the solid line shows the profile for $a^2\widetilde{\mathrm{Bo}} = 0$.

of the solution, so we need to specify five boundary conditions. The profile in the cross-section is symmetric with no cusps so the angle with the horizontal is zero at the apex and the angle with the horizontal at the base of the interface is defined to be the contact angle θ_C. The height of the interface is zero at $\widetilde{Y} = 1$ so the relevant boundary conditions are

$$\Phi(0) = 0, \quad \Phi(s^*) = \theta_C, \quad \widetilde{Y}(0) = 0, \quad \widetilde{Y}(s^*) = 1, \quad \widetilde{H}(s^*) = 0. \tag{5.134}$$

The area of the cross-section is then given by

$$\widetilde{\mathcal{A}} = 2\int_0^{s^*} \widetilde{H}\,\cos\Phi\,\mathrm{d}s. \tag{5.135}$$

The system (5.133) together with the boundary conditions (5.134) can be solved numerically. We will use the same numerical method as we did for the drop profiles in §4.3, *i.e.* the MATLAB function *BVP5C*. Fortunately, this system is easier to solve since there is no singularity at the origin as there was for the axisymmetric drop profile in §4.3.3. The area is then computed numerically via (5.97) using *trapz* in MATLAB. Figure 5.14 shows some solutions of (5.133) and (5.134) for a range of values of $a^2\widetilde{\mathrm{Bo}}$ with a fixed area $\widetilde{\mathcal{A}} = 1$. As we might expect, the Bond number has a similar effect on the profile in the cross-section as it did on the drops (see §4.3.3): for

large positive Bond numbers the edges of the conduit are flattened and as the Bond number is increased the fluid is pulled downwards. We also find that, for positive Bond numbers, there may be multiple solutions for a given cross-sectional area, as we found for the drop volumes in §4.3.4. However, after imposing the reasonable constraints that the height and pressure be everywhere positive, we find that there is at most a single profile with a given area for any $a^2\widetilde{\mathrm{Bo}}$ as illustrated in Figure 5.15b. We further note that there is an upper limit on the Bond number beyond which the interface height may become negative; this value is computed numerically and we find it to be $a^2\widetilde{\mathrm{Bo}}_C \approx 5.1962$. In Figure 5.15a we plot the pressure given by (5.133) as a function of the contact angle θ_C for a range of Bond numbers and in Figure 5.15 we plot the corresponding cross-sectional area given by (5.135). The exact solutions (*i.e.* when $\mathrm{Bo} = 0$) determined in §5.3.3 are indicated by the dashed red lines. The area increases monotonically with $\theta_C < \pi$. For positive Bond numbers, the constraints set out above impose an upper limit on the area.

5.3.6 Flow in the conduit

When $\widetilde{\mathrm{Bo}} = \mathrm{O}(1)$ there are no transformations that can be easily utilised to simplify the problem of finding the velocity in each cross-section. We shall use a finite element method to solve (5.91)–(5.94) on the geometries given by (5.133) and (5.134). We must first define a finite domain for the overlaying fluid, namely

$$\widetilde{\Pi}_2 = \Pi_2 \cap \{\left(\widetilde{Y}, \widetilde{Z}\right) : |\widetilde{Y}| < \mathcal{N}, 0 < \widetilde{Z} < \mathcal{N}\}, \tag{5.136}$$

where $\mathcal{N}$ is a suitably large number. We then impose the far-field boundary condition on $\widetilde{Y} = \pm\mathcal{N}$ and $\widetilde{Z} = \mathcal{N}$; as $\mathcal{N} \to \infty$ we recover the original problem. The problem to be solved numerically for the velocities $\overline{U}_1\left(\widetilde{Y}, \widetilde{Z}\right)$ and $\overline{U}_2\left(\widetilde{Y}, \widetilde{Z}\right)$ is then given by

$$\widetilde{\nabla}^2\overline{U}_1 = 1 \quad \text{in } \Pi_1, \tag{5.137}$$

$$\widetilde{\nabla}^2\overline{U}_2 = 0 \quad \text{in } \widetilde{\Pi}_2. \tag{5.138}$$

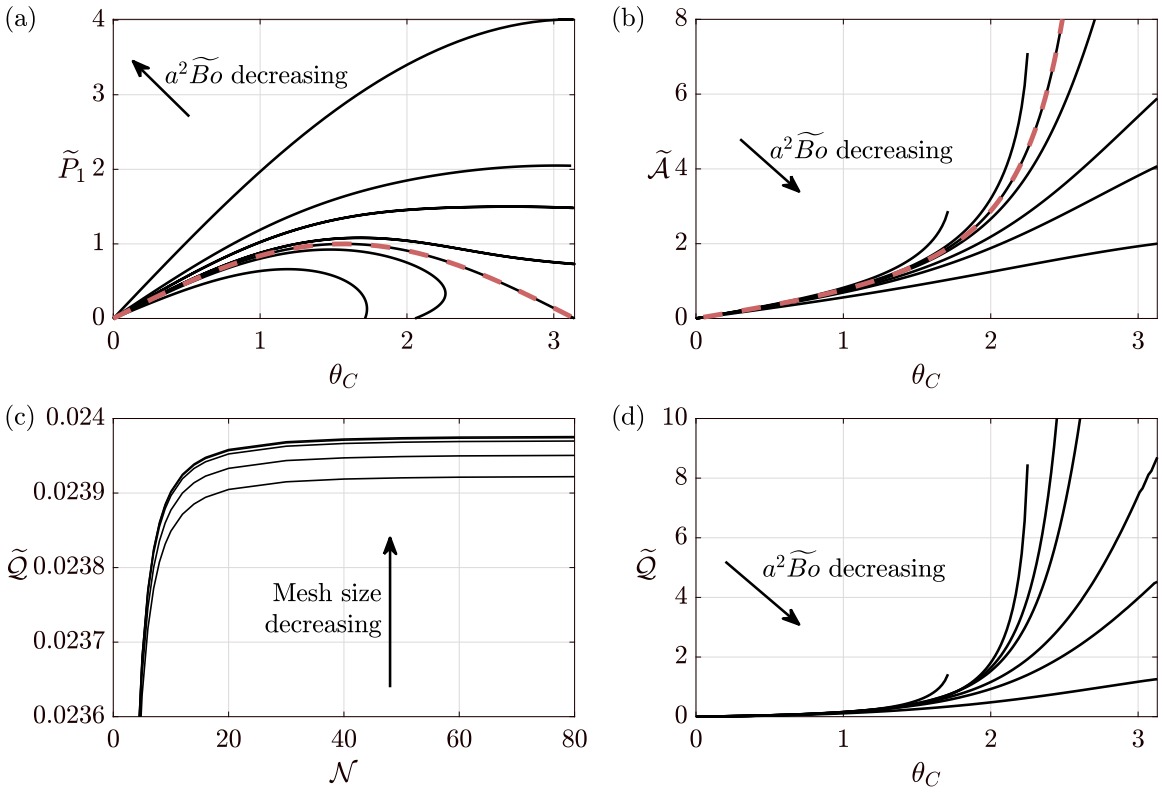


Figure 5.15: (a) Pressure and (b) area of a conduit cross-section as a function of contact angle θ_C given by (5.133)–(5.135) for $a^2\widetilde{\mathrm{Bo}} = -4, -1, -0.5, -0.1, 0, 0.1, 0.5$. The dashed red lines show the exact solution when $a^2\widetilde{\mathrm{Bo}} = 0$ given by (5.103) in (a) and by (5.104) in (b). (c) The convergence of the COMSOL solution as $\mathcal{N}$ is increased and the mesh size is decreased for $\theta_C = 1$, $\mu = 4$ and $a^2\widetilde{\mathrm{Bo}} = 0$. (d) The flux in each cross-section given by (5.96) corresponding to the solutions in (a) and (b), with $\mu = 4$.

With zero velocity on the edges of the domain

$$\overline{U}_1\left(\widetilde{Y}, 0\right) = 0 \quad \text{for } |\widetilde{Y}| < 1, \tag{5.139}$$

$$\overline{U}_2\left(\widetilde{Y}, 0\right) = 0 \quad \text{for } 1 < |\widetilde{Y}| < \mathcal{N}, \tag{5.140}$$

$$\overline{U}_2\left(\pm\mathcal{N}, \widetilde{Z}\right) = 0 \quad \text{for } 0 < \widetilde{Z} > \mathcal{N}, \tag{5.141}$$

$$\overline{U}_2\left(\widetilde{Y}, \mathcal{N}\right) = 0 \quad \text{for } 0 < \widetilde{Z} < \mathcal{N}. \tag{5.142}$$

The boundary conditions on the interface are unchanged: (5.94) gives

$$\frac{\partial \overline{U}_1}{\partial n} = \mu \frac{\partial \overline{U}_2}{\partial n}, \quad \overline{U}_1 = \overline{U}_2 \quad \text{on } S_{C1}. \tag{5.143}$$

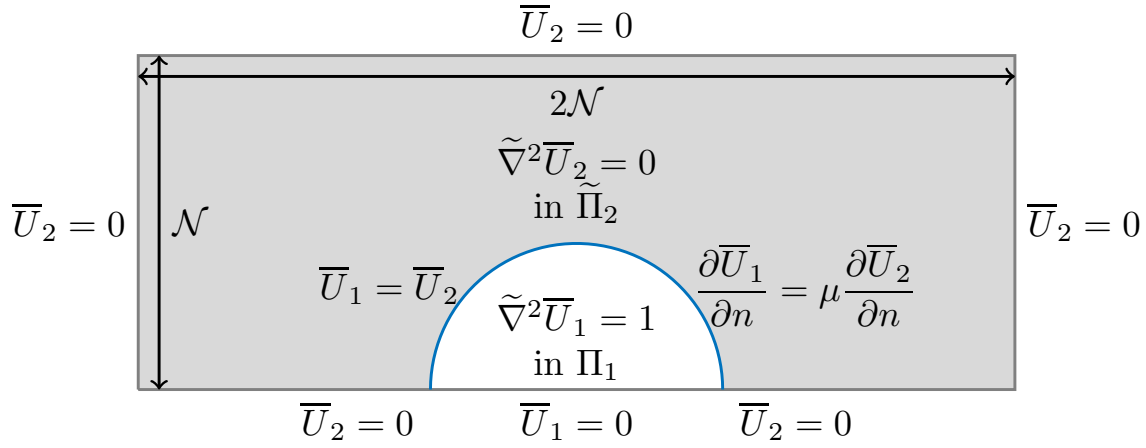


Figure 5.16: The geometry and governing equations for the finite element problem in the conduit cross-section, where the interface S_{C1} between Π_1 and $\widetilde{\Pi}_2$ is found by solving (5.133) and (5.134)

The numerical problem is summarised in Figure 5.16. Solutions of the Laplace and Poisson equations with Dirichlet and Neumann boundary conditions are easily found numerically in COMSOL, once we have used the numerical solution of (5.133) and (5.134) to define the boundary S_{C1} with a suitably large value of $\mathcal{N}$ for the far-field boundary. The integral in (5.96) for the flux is also computed in COMSOL and we use this to test the convergence of the solution as $\mathcal{N}$ increases and the mesh size decreases. An example of the convergence of the flux is shown in Figure 5.15c for $\theta_C = 1$ and $\widetilde{\text{Bo}} = 0$, with viscosity ratio of $\mu = 4$ (as in Table 2.1).

Solutions to the mass conservation equation (5.98) are found in a similar way to the solutions in §5.3.3. We first compute $\widetilde{P}_1$, $\widetilde{\mathcal{A}}$ and $\widetilde{\mathcal{Q}}$ numerically for a range of values of θ_C and $a^2\widetilde{\text{Bo}}$. We can then use interpolation to approximate the values for any θ_C and $a^2\widetilde{\text{Bo}}$ in an appropriate range. We would again like to know when (5.98) is well posed. Figure 5.15a, b and d show $\widetilde{P}_1$, $\widetilde{\mathcal{A}}$ and $\widetilde{\mathcal{Q}}$ as functions of θ_C for a range of Bond numbers. For a fixed value of $a^2\widetilde{\text{Bo}}$ we still find that $\widetilde{\mathcal{A}}$ and $\widetilde{\mathcal{Q}}$ are monotonic increasing functions for $0 < \theta_C < \pi$ and thus conservation of mass (5.98) is still well posed. As in §5.3.4 we would also like to impose an upper limit on the contact angle. We find this upper value by considering where the pressure gradient with respect to

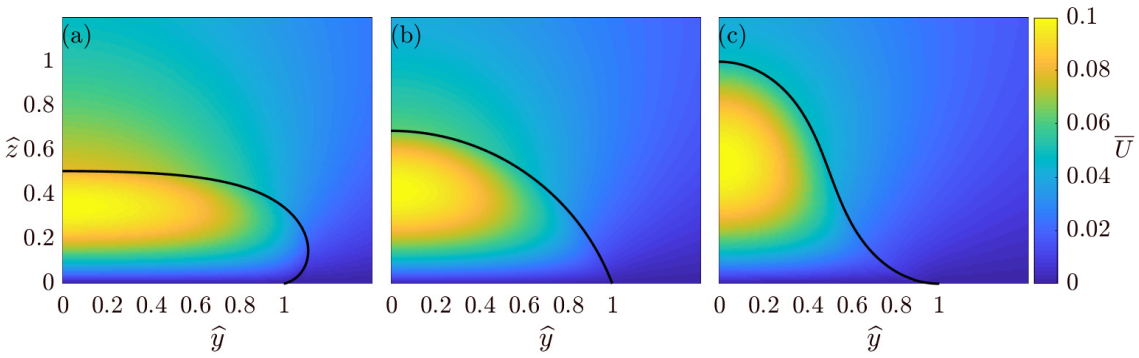


Figure 5.17: Plots of the conduit interface cross-section given by (5.133) and (5.134) (thick black lines) and the corresponding velocity profiles given by (5.137)–(5.143) for (a) $a^2\widetilde{\mathrm{Bo}} = -15$; (b) $a^2\widetilde{\mathrm{Bo}} = 0$ and (c) $a^2\widetilde{\mathrm{Bo}} = 5.1962$ with $\mu = 4$ and $\mathcal{A} = 1$.

θ_C changes sign. We can see in Figure 5.15a, the location of the maximum in $\widetilde{P}_1$ as a function of θ_C depends on the value of $a^2\widetilde{\mathrm{Bo}}$. As $a^2\widetilde{\mathrm{Bo}}$ is increased the maximum occurs for smaller values of θ_C.

5.3.7 Discussion

In this section we considered the flow in an isolated conduit in which the vertical and transverse length scales were comparable in size. Unlike the thin conduit case, the viscosity ratio μ appears at leading order in the governing equations. Hence, the velocity maximum is no longer on the interface, but instead lies somewhere between the centre of the conduit and the interface, with larger values of μ moving it neared to the centre. We also considered the effect of gravity in the conduit; for the Bond number to appear in the leading-order equations we required $\mathrm{Bo} = \mathrm{O}(1/\epsilon^2)$ and, for example, we observed significant changes in the cross-sectional shape of the conduit and demonstrated how an upper limit on the contact angle could be investigated. However, as shown in Table 2.2, this may be outside the range of values typically used.

5.4 Comparison to experimental data

In this section we attempt to validate the modelling thus far by comparing some of our predictions for the conduit flow to recent experimental data. Two experimental runs were carried out with a conduit of width 900 µm and length 10 mm by Prof. Walsh and his collaborators in the Department of Engineering Science at the University of Oxford. Fluid was pumped in at one end with flow rates of $Q_0 = 3.125\,\mathrm{nl\,s^{-1}}$ or $Q_0 = 50\,\mathrm{nl\,s^{-1}}$ with a drop at the other end acting as a reservoir. The maximum height of the interface and the velocity in a cross-section were both measured. The corresponding Bond number Bo and aspect ratio ϵ were about 0.065 and 0.045 respectively. The maximum height of the conduit interface did not exceed 90 µm in either experiment, which is consistent with our deductions in both chapter 3 and chapter 4 that the conduit height scales with $\epsilon^2 L$. We compare the data to the thin-film model with active pumping discussed in §3.4.1. The pressure in the conduit is given by (3.111) and using the cross-sectional height (3.42) we find the maximum height along the length of the conduit to be

$$h_{\max} = \frac{1}{2}\left(\mathscr{Q}_0\,(1-x) + p_R^4\right)^{\frac{1}{4}}, \tag{5.144}$$

where $\mathscr{Q}_0 = 105\mu_1/(\delta^4\epsilon^7\gamma L^2)Q_0$ with μ_1 the dynamic viscosity of the fluid in the conduit, $\delta = H_D/L$, $\epsilon = a_0/L$, γ the surface tension of the fluid-fluid interface and Q_0 the imposed flux. As shown by (5.144), the pressure at the end of the conduit ($x = 1$) is given by $p_R = 2\,h_{\max}$, where the maximum interface height $h_{\max}$ can be measured experimentally far more easily than the pressure. We have used the simplest model here, without incorporating the junction region, so the last few data points where the height increases as the conduit joins the drop are not included. The interface height given by (5.144) shows very good agreement with the experimental data away from the junction region for both flow rates as shown in Figure 5.18.

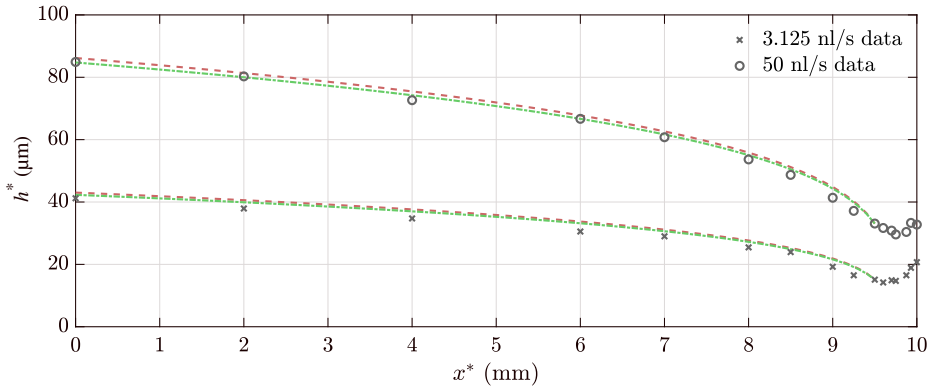


Figure 5.18: Comparison of the maximum conduit interface height given by (5.144) (red dashed lines) with experimental data for different imposed flow rates. The flow is from left to right and the final six data points for each experiment are not included in the comparison since they are in the junction region. The solid green lines show the interface height with interface elasticity, as derived later (see (5.175) where the parameter value $\mathscr{E} = 3.4$ has been used).

The velocity of the fluid in the conduit was also measured during the experiments using Particle Image Velocimetry (PIV), in which the velocities of small particles placed in the fluid are measured and assumed to follow the flow. The measurements of the velocity in a cross-section were taken in a conduit with a flow rate of $3.125\,\mathrm{nl\,s^{-1}}$ at a point where the maximum height of the interface was approximately 42 µm. The velocity data is shown in Figure 5.19a with the location of the interface indicated by the dashed line. The location of this interface was found by fitting (5.102) to the data, which gave the contact angle as approximately 10°. The maximum velocity in the experimental data is closer to the middle of the conduit and approaches zero at the interface. With our model this would only happen as $\mu \to \infty$ as illustrated in Figure 5.19b; the height of the maximum velocity above the conduit base is shown as a function of μ. This was computed using the Fourier series model (5.118), since the viscosity ratio does not appear in the leading-order models of chapters 3 and 4. With this model and the parameter values in Table 2.2 we would predict the maximum velocity to be about 34 µm above the base of the conduit, as illustrated by the dashed lines in Figure 5.19b. Thus, the no shear boundary condition on the free surface (see

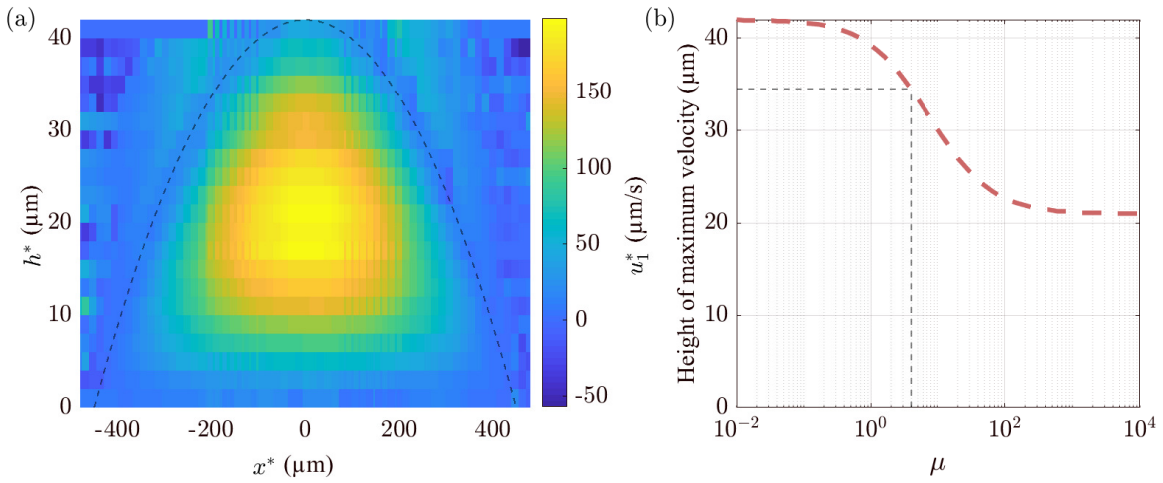


Figure 5.19: (a) The velocity in the conduit measured using PIV. The dashed line shows the location of the interface found by fitting (5.102) to data. (b) The height of the velocity maximum as a function of the viscosity ratio μ computed with (5.118).

(2.6)–(2.8)) is not consistent with the PIV data shown in Figure 5.19a, which suggests there is no-slip on the interface.

5.5 An elastic interface

The models that we have presented so far in this thesis have been based on fairly standard assumptions about the behaviour of the fluids involved, e.g. they are Newtonian and have constant surface tension. While these assumptions seem sensible for a circuit made purely from water, these free surface devices are particularly useful in studying the behaviour of cells [127] and as such a culture medium is required to stimulate cell growth and proliferation. A standard culture media to use is foetal bovine serum (FBS), the composition of which will vary from batch to batch [49, 123] and the exact properties of FBS are thus poorly characterised in general. But experimental observations by our collaborators suggest that some of the proteins in the FBS absorb onto the interface with the FC40 and form a membrane which reduces the fluid velocity to zero on the interface. Such complex interfaces are common in biological processes [45]. A similar phenomena is seen on the surface of milk [17, 100]. This

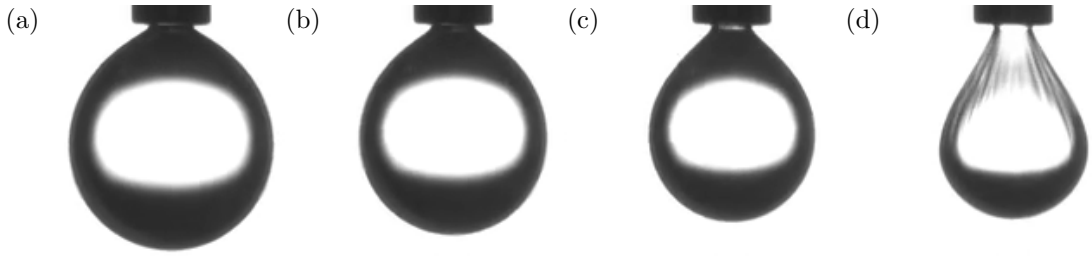


Figure 5.20: The water serum mixture used in the devices forms wrinkles on its surface as demonstrated by sucking fluid out of a suspended drop. In (a)-(c) the decreasing volume causes the drop to shrink but in (d) the elastic properties of the surface cause it to wrinkle. Unpublished figures kindly supplied by Prof. Walsh.

membrane can be observed, for instance, by sucking fluid out of a drop suspended on the end of a pipette. As the drop is deflated the membrane causes wrinkles to form on the surface as shown in Figure 5.20d. This is also clear evidence that we cannot model the boundary between the two fluids simply as a constant surface tension fluid interface but instead we should additionally incorporate elasticity into the mechanics of the interface, which thus behaves as an elastic membrane under tension. This will support higher pressures in the conduit and assuming no-slip on the interface move the maximum velocity toward the centre of the conduit as seen in the experimental data. However, there is no evidence to suggest that the Cauchy stress tensor deviates from that of a Newtonian fluid.

5.5.1 A preliminary model incorporating an elastic interface

Fully deriving a new model incorporating the elastic membrane is beyond the scope of this thesis. Instead we demonstrate how the existing thin-film model can be modified to account for an elastic membrane. Two modifications are made to the model of chapter 3: (i) the velocity is assumed to be zero on the interface and (ii) the pressure is modelled with the Föppl-von Kármán equation (5.148), which has been used extensively to model fluid flows constrained by elastic membranes [27, 93, 102].

With no-slip on the interface (now an elastic membrane) the thin-film velocity

(3.19) becomes

$$u_1 = \left(z^2 - hz\right)\frac{\partial p_1}{\partial x}, \quad v_1 = \left(z^2 - hz\right)\frac{\partial p_1}{\partial y}. \tag{5.145a,b}$$

Making the further rescaling $t = 4\widehat{t}$ we arrive at the same Reynolds lubrication equation from chapter 3:

$$\frac{\partial h}{\partial \widehat{t}} = \nabla \cdot \left(h^3 \nabla p_1\right) \quad \text{for } (x, y) \in \Omega_1, \tag{5.146}$$

where we again consider only the dumbbell setup illustrated in Figure 3.1. We still impose zero height on and flux through the contact line giving

$$h = 0, \quad \left(h^3 \nabla p_1\right) \cdot \boldsymbol{\nu} = 0 \quad \text{for } (x, y) \in \partial\Omega, \tag{5.147a,b}$$

where $\boldsymbol{\nu}$ denotes the outward pointing normal on $\partial\Omega$ in the (x, y)-plane. Instead of deriving the pressure using the stress balance condition (2.6), we assume that the pressure satisfies the Föppl-von Kármán equation

$$p_1 = E\nabla^4 h - \nabla^2 h - \mathrm{Bo}\, h \quad \text{for } (x, y) \in \Omega_1, \tag{5.148}$$

where E is a dimensionless number measuring the importance of flexural rigidity compared to surface tension. We define E to be

$$E = \frac{D}{\gamma L^2}, \tag{5.149}$$

where D is the flexural rigidity of the membrane. An additional boundary condition is now required on the contact line, and natural boundary conditions on the consideration of energy minimisation give

$$\nabla^2 h = 0 \quad \text{on } \partial\Omega, \tag{5.150}$$

i.e. there is zero bending moment on the contact line. To close the problem an initial condition $\mathscr{H}(x, y)$ is prescribed for the interface height at time $\widehat{t} = 0$, *i.e.*

$$h(x, y, 0) = \mathscr{H}(x, y) \quad \text{for } (x, y) \in \Omega_1. \tag{5.151}$$

Based on experimental observations we anticipate that surface tension dominates in the drop regions and the elasticity only has an effect in the conduit, so that $E = O(\epsilon^2)$, at least for the systems studied experimentally. The timescales derived in (3.28) remain the same when surface tension dominates in the drop regions, so we have

$$\widehat{t}_J \sim \epsilon, \quad \widehat{t}_D \sim 1, \quad \widehat{t}_{CW} \sim \frac{1}{\epsilon^2}, \quad \widehat{t}_{CL} \sim \frac{1}{\epsilon^4}, \quad \widehat{t}_{DD} \sim \frac{1}{\epsilon^7}. \tag{5.152a–e}$$

5.5.2 Quasi-steady conduit solution

We let $E = \epsilon^2 \mathscr{E}$, then we recover the same leading-order governing equations in the drop region as in §3.3.2 and the same results apply here. Thus, we begin with an analysis of the conduit region, as in §3.3.3 we rescale with

$$y = \epsilon\, \widehat{y}, \quad h = \epsilon^2\, h_C. \tag{5.153}$$

Expanding $p_1 \sim p_C(x, \widehat{y}, t)$ as $\epsilon \to 0$ in (5.4) then gives

$$\frac{\partial h_C}{\partial \widehat{t}} = \epsilon^4 \frac{\partial}{\partial x}\left(h_C^2 \frac{\partial p_C}{\partial x}\right) + \epsilon^2 \frac{\partial}{\partial \widehat{y}}\left(h_C^2 \frac{\partial p_C}{\partial \widehat{y}}\right). \tag{5.154}$$

Similarly to our analysis of the original thin-film conduit, when $\widehat{t} \gg \widehat{t}_{CW} \sim \epsilon^{-2}$, the pressure is spatially uniform in each x-plane at leading order once the system is quasi-steady as then the last term dominates with solutions of the form $\partial p_C/\partial \widehat{y} \sim h_C^{-2}$ excluded as they are singular. Analogously expanding (5.148) then gives

$$\mathscr{E}\left(\epsilon^4 \frac{\partial^4 h_C}{\partial x^4} + 2\epsilon^2 \frac{\partial^2}{\partial x^2}\frac{\partial^2 h_C}{\partial \widehat{y}^2} + \frac{\partial^4 h_C}{\partial \widehat{y}^4}\right) - \epsilon^2 \frac{\partial^2 h_C}{\partial x^2} - \frac{\partial^2 h_C}{\partial \widehat{y}^2} - \epsilon^2 \mathrm{Bo}\, h_C = p_C \tag{5.155}$$

for $-1 < \widehat{y} < 1$. At leading order, the governing equation is therefore given by

$$\mathscr{E}\frac{\partial^4 h_C}{\partial \widehat{y}^4} - \frac{\partial^2 h_C}{\partial \widehat{y}^2} = p_C \quad \text{for } -1 < \widehat{y} < 1. \tag{5.156}$$

Equation (5.156) is the beam equation and has also been used to model flows under elastic membranes [55]. On the edges of the conduit the boundary conditions (5.147a) and (5.150) give

$$h_C = 0, \quad \frac{\partial^2 h_C}{\partial \widehat{y}^2} = 0 \quad \text{on } \widehat{y} = \pm 1 \text{ for } 0 < x < 1. \tag{5.157}$$

The solution to (5.156) and (5.157) is then given by

$$h_C = \left[\frac{1-\widehat{y}^2}{2} - \mathscr{E}\left(1 - \frac{\cosh\left(\widehat{y}/\sqrt{\mathscr{E}}\right)}{\cosh\left(1/\sqrt{\mathscr{E}}\right)}\right)\right] p_C. \tag{5.158}$$

The limit $\mathscr{E} \to 0$ corresponds to the original problem without elasticity given by (3.42). The flux along and cross-sectional area of, the conduit are defined to be

$$\widehat{A}\,(x,t) = \int_{-1}^{1} h_C \,\mathrm{d}y, \quad \widehat{Q}\,(x,t) = \int_{-1}^{1}\int_{0}^{h_C} u_1 \,\mathrm{d}z\,\mathrm{d}y. \tag{5.159a,b}$$

With the cross-sectional height given by (5.158) we can update the area and flux as follows

$$\widehat{A} = \epsilon^3 \frac{2\,\mathscr{A}(\mathscr{E})}{3} p_C, \quad \widehat{Q} = -\epsilon^7 \frac{\mathscr{F}(\mathscr{E})}{70}\frac{\partial}{\partial x}\left(p_C^4\right), \tag{5.160a,b}$$

where the functions $\mathscr{A}(\mathscr{E})$ and $\mathscr{F}(\mathscr{E})$ are given by

$$\mathscr{A}(\mathscr{E}) = 3\mathscr{E}^{3/2}\frac{\sinh(1/\sqrt{\mathscr{E}})}{\cosh(1/\sqrt{\mathscr{E}})} - 3\mathscr{E} + 1, \tag{5.161}$$

$$\begin{aligned}\mathscr{F}(\mathscr{E}) = 1 &- \left(7 - \frac{35}{2}\mathscr{E} + \frac{3395}{8}\mathscr{E}^2\right)\mathscr{E} \\ &+ \left(105 + \frac{21385}{48}\mathscr{E} + \frac{35}{3\cosh^2(1/\sqrt{\mathscr{E}})}\mathscr{E}\right)\mathscr{E}^{5/2}\tanh(1/\sqrt{\mathscr{E}}) \\ &+ \left(\frac{35}{4} - \frac{525}{16}\mathscr{E}\right)\mathscr{E}^2\frac{1}{\cosh^2(1/\sqrt{\mathscr{E}})}.\end{aligned} \tag{5.162}$$

The behaviour of both (5.161) and (5.162) are not immediately obvious but can easily be described: we find that both functions tend to one as $\mathscr{E} \to 0$ and tend monotonically to zero as $\mathscr{E}$ is increased. Thus, increasing the elasticity $\mathscr{E}$ results in a decrease in cross-section area and flux in the conduit. We note that in the zero elasticity limit the flux is half that given by (3.43b). The fluxes do not match in this limit because the velocities have different boundary conditions on the interface; zero slip for the elastic interface and zero shear for the fluid interface, and the non-dimensionalisation timescales differ by a factor of four.

5.5.3 Elasticity in the junction region

The inclusion of elasticity now makes it much harder to undertake a complete analysis of the junction region. However, our main motivation for analysing the junction region is to determine the appropriate boundary conditions in the conduit region, and as in both the thin and thick film chapters we will show that

$$p_{JL}(t) = p_L(t) = p_C(0,t), \tag{5.163}$$

where p_{JL} is the pressure in the left-hand junction region. In the junction region there is a transition from the drop, where surface tension is dominant, to a region where surface tension and elasticity are comparable. We rescale in the junction region as in (3.44):

$$x = \epsilon\widetilde{x}, \quad y = \epsilon\widetilde{y}, \quad h = \epsilon\widetilde{h}. \tag{5.164}$$

The relevant geometry is the same as in Figure 3.4 and we expand $h \sim h_0 + \epsilon h_1$, $p_1 \sim p_{JL}$. For $\widehat{t} \gg \widehat{t}_J \sim \epsilon$, the evolution equation (5.146) gives

$$\nabla \cdot \left(h_0^3 \nabla p_{JL}\right) = 0. \tag{5.165}$$

Expanding (5.148), we find the leading-order problem for the interface height to be

$$\mathscr{E}\nabla^4\widetilde{h}_0 - \nabla^2\widetilde{h}_0 = 0, \tag{5.166}$$

At leading order the boundary conditions are identical to the ones given in Figure 3.4a: the height is zero on the contact line $\partial\Omega_J$, tends to zero in the conduit and matches with the drop solution as $\widetilde{x}^2 + \widetilde{y}^2 \to \infty$ for $\widetilde{x} < 0$. Moreover, we need an additional condition to close the problem, given by (5.150); so that the boundary conditions on the contact line are given by

$$\widetilde{h}_0 = 0, \quad \nabla^2\widetilde{h}_0 = 0 \quad \text{on } \partial\Omega_J. \tag{5.167}$$

We note that the original thin-film solution for the leading-order junction interface (3.59) also satisfies the governing equation (5.166) with the boundary conditions

shown in Figure 3.4a with the inclusion of (5.167). The next-order term in the expansion of (5.148) is given by

$$\mathscr{E}\nabla^4\widetilde{h}_1 - \nabla^2\widetilde{h}_1 = p_{JL}. \tag{5.168}$$

The boundary conditions shown in Figure 3.4b remain largely unchanged. Since any corrections to the drop shape due to the elastic interface will be $\mathrm{O}(\epsilon^2)$, as $E = \mathrm{O}(\epsilon^2\mathscr{E})$, the far-field condition in the drop is unchanged, as are the conditions on the contact line. Only the far-field condition in the conduit is affected by the elasticity and via (5.152) is now given by

$$\widetilde{h}_1 \to \left[\left(\frac{1-\widetilde{y}^2}{2}\right) - \mathscr{E}\left(1 - \frac{\cosh\left(\widetilde{y}/\sqrt{\mathscr{E}}\right)}{\cosh\left(1/\sqrt{\mathscr{E}}\right)}\right)\right] p_C \quad \text{as } \widetilde{x} \to \infty. \tag{5.169}$$

Expanding (5.150) on the drop contact line, (3.45), and the conduit contact line, $|\widetilde{y}| = 1$ gives the final boundary conditions

$$\nabla^2\widetilde{h}_1 = 0 \qquad \text{on } |\widetilde{y}| = 1 \text{ for } \widetilde{x} \geq 0. \tag{5.170}$$

$$\nabla^2\widetilde{h}_1 = -\left(\frac{\widetilde{y}^2-1}{2\alpha_L}\right)\frac{\partial}{\partial\widetilde{x}}\left(\nabla^2\widetilde{h}_0\right) \quad \text{on } \widetilde{x} = 0 \text{ for } |\widetilde{y}| \geq 1. \tag{5.171}$$

The pressure is transmitted straight through the junction region at leading order for the same reasons as in §3.3.4, with $\nabla p_{JL} = 0$ in (5.165), so that the pressure is simply a function of time $p_{JL}(t)$. Solving for $\widetilde{h}_1$ may be possible using conformal mapping techniques, but we do not pursue it here.

Thus, we can derive a new ODE on the drainage timescale for the dumbbell with an elastic interface. Since the flux given by (5.160b) has the same dependence on the pressure as in both (3.43b) and (4.61c) we deduce that, for $\widehat{t} \gg \widehat{t}_{CL}$, the pressure in a passively driven conduit is given by

$$p_C = \left(\left(p_R^4 - p_L^4\right)x + p_L^4\right)^{\frac{1}{4}}, \tag{5.172}$$

where $p_L\left(\widehat{t}\right)$ and $p_R\left(\widehat{t}\right)$ are the pressures at the bases of the left- and right-hand drops respectively. If we then rescale time with $\widehat{t} = 70/(\mathscr{F}(\mathscr{E})\beta_R^4\widehat{v}_T^3)\,\epsilon^{-7}T_E$ in the volume

ODEs (3.27) we get the same governing equation that we found in the thin-film case (see (3.96) and (3.97)):

$$\frac{\mathrm{d}\mathcal{V}_L}{\mathrm{d}T_E} = (1-\mathcal{V}_L)^4 - \alpha^4\mathcal{V}_L^4, \tag{5.173}$$

where $\alpha = \beta_L/\beta_R$ and $\mathcal{V}_L = \widehat{v}_L/\widehat{v}_T$ is the leading-order rescaled drop volume. The solution of this ODE has been discussed at length in the latter sections of chapter 3 and will not be analysed further here. However, we note that the timescales are different in the original thin film ODE (3.97) and the ODE we have derived above, in particular

$$T_E = \frac{\mathscr{F}(\mathscr{E})}{8}T. \tag{5.174}$$

Thus, we conclude from this preliminary analysis that the main effect of elasticity on the drainage timescale is to reduce the flow rate in the conduit and consequently the equilibration time.

5.5.4 Returning to the experimental data

The experimental data shown in Figure 5.18 and Figure 5.19a used active pumping so we must update (5.144) using the elastic interface model that we have just discussed. Using (5.158) the maximum height along the conduit is now given by

$$h_{\max} = \left[\frac{1}{2} - \mathscr{E}\left(1 - \operatorname{sech}\left(\frac{1}{\sqrt{\mathscr{E}}}\right)\right)\right]\left(\mathscr{Q}_0\left(1-X\right) + P_R^4\right)^{\frac{1}{4}}, \tag{5.175}$$

where we must now rescale the flux with $\mathscr{Q}_0 = 840\mu_1/(\delta^4\epsilon^7\mathscr{F}(\mathscr{E})\gamma L^2)Q_0$. Fitting (5.175) to the data then allows us to estimate the bending stiffness of the membrane; we find a value of $\mathscr{E} \approx 3.4$ for the experimental data shown in Figure 5.18. As shown in Figure 5.18, we get similarly accurate results for the maximum interface height to the original model when we set $\mathscr{E} = 3.4$ in (5.175), though now the model also has the velocity maximum along the conduit near the centre of the cross-section as predicted by (5.145) and as seen in the data (see Figure 5.19a). Recalling that $E = \epsilon^2\mathscr{E}$, where E is given by (5.149), we find the dimensional bending stiffness of the

membrane to be approximately $D = 1.8 \times 10^{-8}\,\mathrm{kgm^2/s^2}$. For comparison, a thin sheet of aluminium foil (that you might find in a typical kitchen) has a bending stiffness of about $2.6 \times 10^{-8}\,\mathrm{kgm^2/s^2}$ [117]. The bending stiffness could also be estimated by looking at the pattern of wrinkles illustrated in Figure 5.20d and comparing them with theoretical predictions [66, 125]. However, such analysis is beyond the scope of this preliminary investigation.

5.5.5 Discussion

In this section we have shown how the two models that have been developed in this thesis compare to experimental data. While the thin-film model showed good agreement with the data for the interface height we found that the velocity measurements in the conduit suggested that the interface was behaving as an elastic solid. This is due to the use of the cell culture medium foetal bovine serum (FBS). By modelling the pressure in the lubrication equation (3.20) with the Föppl-von Kármán equation and imposing no-slip boundary conditions on the interface we were able to explain this discrepancy, though a thorough derivation of the governing equations incorporating the elastic interface is still needed. The Föppl-von Kármán equation introduced a new physical variable that needed to be estimated from the data: the bending stiffness D. The properties of FBS may vary with different batches [49, 123] and it is not clear how much variation we would expect to see in D. We anticipate that the original models that we derived will still be applicable when water is used in the devices in place of FBS. It may also be possible to replace the serum with a cell medium that has more consistent properties [123].

5.6 Summary

In this chapter we demonstrated several ways in which the asymptotic model for the simple dumbbell geometry could be extended. We began by showing how networks

of drops and conduits could be modelled by adding another region — a node — in addition to the drop, junction and conduit regions. This allowed us to derive a generalisation of Kirchhoff's laws and subsequently a system of ODEs with algebraic constraints governing the flow in the network on the drainage timescale. This system of equations was then incorporated into a GUI to allow for rapid device design. The network model retains much of the simplicity of earlier models but has a far greater range of application. One shortcoming is that the presence of multiple junctions connected to a single drop can lead to large discrepancies in the drops volumes. In §5.2 we discussed the impact of introducing higher order terms into our asymptotic models. In particular we showed how we could account for the differences in equilibrium drop volume caused by the junction regions in the network model. In §5.3 we analysed an isolated conduit. Without the assumption that there are fluid drops at either end of the conduit we were able to consider much higher flow rates. Finally, in §5.4, we showed that the nature of the particular fluids used for cell-based experiments means that the standard Navier-Stokes equations and fluid-fluid boundary conditions were unable to capture the full behaviour of the system. We then developed a preliminary model using the Föppl-von Kármán equation in place of the Laplace-Young equation for the pressure in the thin-film limit.

Chapter 6

Concluding remarks and future work

6.1 Conclusions

In this thesis we have presented a model for a novel microfluidic device in which the fluid is constrained primarily by the interfacial properties of two immiscible fluids. This has several advantages over traditional microfluidic devices, in particular for biological applications: it avoids use of PDMS and its potential biocompatibility concerns, it is simple to construct and fluids can be easily added and removed. We began by presenting the governing equations in chapter 2. The fluids were assumed to obey the incompressible Navier-Stokes equations with the usual kinematic and dynamic boundary conditions with constant surface tension. We initially focused on the simple dumbbell-shaped design shown in Figure 1.1 and represented schematically in Figure 3.1. Several dimensionless parameters were identified showing that the problem would be amenable to asymptotic analysis. Of particular importance are the two aspect ratios ϵ: the ratio of conduit width to length and δ: the ratio of drop height to conduit length, both of which are typically small in experiments.

In chapter 3 we analysed the regime in which $\delta, \epsilon \ll 1$ and were able to utilise the much simpler lubrication equations. Five timescales were identified for the relaxation of different regions of the device, each depending on the aspect ratio ϵ. The drop,

conduit and junction regions were analysed separately and quasi-steady solutions were found in each. In §3.3.2 we showed that the leading-order drop height is described by a Bessel function and that the Bond number imposes an upper limit on how big the quasi-static drops can be given the thin film assumption. In §3.3.3 we found that the interface of the conduit cross-section is a parabola. To model the full device it was necessary to analyse the region connecting the drops to the conduit. The key result was to show that at leading order the pressure is transmitted straight through the junction allowing us to construct an ODE model on the drainage timescale which had an analytic solution. Nonetheless, the profile of the junction region was also determined making extensive use of the theory of complex variables. We were then able to form a composite solution for the dumbbell geometry, illustrated in Figure 3.11. Numerical validation in §3.3.7 showed excellent agreement as ϵ was decreased for both the time dependent ODE model and the quasi-steady composite model. We then went on to characterise the key determinants of conduit fluxes, their decay in time and the scale of the shear stress in the resulting flows. Finally, we considered two methods of altering the flow characteristics; replacing one of the drops with a pump to impose a flux in the conduit and printing conduits of varying width to gain more control over the distribution of shear stresses in the conduit.

In chapter 4 we considered the case in which $\delta = \mathrm{O}(1)$. Our main interest was in determining how the drop pressure varies with the volume and Bond number. There exist parameter regimes in which the drop pressure is not a single-valued function of the drop volume, although most of these profiles are not expected to be stable to small perturbations. The non-linear relationship between drop pressure and volume also allowed for the existence of multiple steady states which we briefly considered. We also found that with a large enough Bond number our solutions were no longer valid, though this regime could easily be avoided experimentally (it would require drops with a much larger base radius than are typically used).

In the final research chapter we considered several extensions and modifications to the models developed in chapters 2 to 4. We began by showing how the basic dumbbell geometry considered in earlier chapters could be extended to allow for more complex network geometries. To do this we introduced the node region. Asymptotic analysis of this region showed that we could construct an ODE model with a set of algebraic constraints for the network, analogous to Kirchhoff's laws for electric circuits. Validation of this model by comparison to numerics showed good agreement for small aspect ratios, although the equilibrium drop volume deviated from the numerics as the number of conduits connected to the drop was increased. In the next section we explained the reduction in accuracy of the asymptotic model by finding the next order correction in the drop region. We further found the corrections due to the upper fluid and due to large Bond numbers in the thin conduit. Our analysis of passive flows showed that the conduits are thin, *i.e.* the vertical length scale is much less than the horizontal length scales. In the next section we considered isolated conduits with comparable width and height scales. In a further study, we then compared experimental data with our modelling predictions, which demonstrated that surface tension interface conditions are not adequate for free surface microdevices designed for biological studies due to the use of foetal bovine serum as a medium, which displays elasticity in its interfacial properties. Preliminary investigation in the thin-film limit has shown that modelling the interface as an elastic sheet with surface tension and zero-slip can more closely match the data. However, this is a first, initial, study and there is extensive scope for a further detailed investigation of the relevant equations based on no-slip elastic membrane interface conditions with surface tension as indicated by experimental observation.

6.2 Future work

There are several ways in which the models presented in this thesis could be extended, such as including transport [2, 24, 34], the most important next step is to fully derive the appropriate governing equations that take account of the elastic nature of the interface. Modelling of elastic interfaces between fluids has been studied in various contexts, for instance in the modelling of lipid bilayers [53], or flow under elastic membranes [93]. Many of the most relevant models deal with elastic membranes on fluid drops [6, 66, 125]. The same modelling assumptions should extend to the conduit. It is hoped the small elastic modulus and larger length scale of the drops will mean that the original drop modelling will be sufficient to predict the pressure in the drops. The exact composition and mechanical properties of the interface are not well-classified. It seems that the velocity approaches zero on the interface, which suggests the FC40 will not play such an important role in the dynamics. Once the new model is formally derived one could seek to analyse the same properties as with the original model, e.g. the interface shape, flow rate and shear stress.

While the focus of this thesis has been on the flow in such devices recent development of Freestyle Fluidics has focused on applications in which the fluid is not flowing [107, 108, 109]. The ease with which circuits can be drawn with the new device also allows the easy construction of something analogous to microtiter plates, in which several hundred fluid drops on a Petri dish are used as small test tubes. In these experiments the drops are created by first dispensing a layer of cell medium into the Petri dish and overlaying it with FC40. A stylus is then used to reshape the fluid by drawing lines through the medium, which displaces it, causing drops to form; this results in drops with square bases rather than the round ones covered in this thesis.

We hope that the theoretical work undertaken in this thesis will help increase the uptake of this new class of microfluidic device across a wide range of different disciplines.

Bibliography

[1] T. Ahmed, T.S. Shimizu, R. Stocker, A. Libchaber, A. Groisman, A. Levchenko, K.H. Lee, H.J. Kim, J. Brody, and N.L. Jeon. Microfluidics for bacterial chemotaxis. *Integr. Biol.*, **2**(11-12):604, 2010.

[2] F.H.H. Al Mukahal, B.R. Duffy, and S.K. Wilson. Advection and Taylor–Aris dispersion in rivulet flow. *Proc. R .Soc .A*, **473**(2207), 2017.

[3] R.F. Allen and C.M. Biggin. Longitudinal flow of a lenticular liquid filament down an inclined plane. *Phys. Fluids*, **17**:287–291, 1974.

[4] A. Alrifaiy, O.A. Lindahl, and K. Ramser. Polymer-based microfluidic devices for pharmacy, biology and tissue engineering. *Polymers*, **4**(4):1349–1398, 7 2012.

[5] E.Y. Arashiro and N.R. Demarquette. Use of the pendant drop method to measure interfacial tension between molten polymers. *Mater. Res.*, **2**(1):23–32, 1999.

[6] C. Balemans, M.A. Hulsen, and P.D. Anderson. Modeling of complex interfaces for pendant drop experiments. *Rheol. Acta*, **55**(10):801–822, 2016.

[7] O.A. Basaran and L.E. Scriven. Axisymmetric shapes and stability of pendant and sessile drops in an electric field. *J. Colloid Interface Sci.*, **140**(1):10–30, 1990.

[8] F. Bashforth and J.C. Adams. *An Attempt to Test the Theories of Capillary Action*. University Press, 1883.

[9] H. Becker and C. Gärtner. Polymer microfabrication technologies for microfluidic systems. *Anal. Bioanal. Chem.*, **390**(1):89–111, 2008.

[10] M.C. Bélanger and Y. Marois. Hemocompatibility, biocompatibility, inflammatory and in vivo studies of primary reference materials low-density polyethylene and polydimethylsiloxane: a review. *J. Biomed. Mater. Res.*, **58**(5):467–77, 2001.

[11] J.D. Berry, M.J. Neeson, R.R. Dagastine, D.Y.C. Chan, and R.F. Tabor. Measurement of surface and interfacial tension using pendant drop tensiometry. *J. Colloid Interface Sci.*, **454**:226–237, 2015.

[12] S.B. Berry, J.J. Lee, J. Berthier, E. Berthier, and A.B. Theberge. Open channel droplet-based microfluidics. In *22nd International Conference on Miniaturized Systems for Chemistry and Life Sciences, MicroTAS 2018*, **2**, pages 1093–1096. Chemical and Biological Microsystems Society, 3 2018.

[13] E. Berthier and D.J. Beebe. Flow rate analysis of a surface tension driven passive micropump. *Lab Chip*, **7**(11):1475–1478, 2007.

[14] E. Berthier, E.W.K. Young, and D. Beebe. Engineers are from PDMS-land, biologists are from polystyrenia. *Lab Chip*, **12**(7):1224–1237, 2012.

[15] J. Berthier, K.A. Brakke, and E. Berthier. *Open Microfluidics*. Wiley, 2016.

[16] N. Bleistein. *Mathematical Methods for Wave Phenomena*. Academic Press, 1984.

[17] J.V. Boyd, J.R. Mitchell, L. Irons, P.R. Musselwhite, and P. Sherman. The mechanical properties of milk protein films spread at the air-water interface. *J. Colloid Interface Sci.*, **45**(3):478–486, 1973.

[18] S.N. Calver, E.A. Gaffney, E.J. Walsh, W.M. Durham, and J.M. Oliver. On the thin-film asymptotics of surface tension driven microfluidics. *J. Fluid Mech.*, **901**:A6, 2020.

[19] A.K. Chesters. An analytical solution for the profile and volume of a small drop or bubble symmetrical about a vertical axis. *J. Fluid Mech.*, **81**(4):609–624, 1977.

[20] E. Chmela, M.T. Blom, J.G.E. Gardeniers, A. Van den Berg, and R. Tijssena. A pressure driven injection system for an ultra-flat chromatographic microchannel. *Lab Chip*, **2**(4):235–241, 2002.

[21] I. Cimrák, M. Gusenbauer, and T. Schrefl. Modelling and simulation of processes in microfluidic devices for biomedical applications. *Comput. Math. with Appl.*, **64**(3):278–288, 2012.

[22] COMSOL Multiphysics® v. 5.4. *COMSOL Multiphysics Reference Manual*. Stockholm, 2018.

[23] COMSOL Multiphysics® v. 5.4. *MEMS Module User's Guide*. Stockholm, 2018.

[24] A.A. Darhuber, J.Z. Chen, J.M. Davis, and S.M. Troian. A study of mixing in thermocapillary flows on micropatterned surfaces. *Philos. Trans. R. Soc. A Math. Phys. Eng. Sci.*, **362**(1818):1037–1058, 2004.

[25] A.A. Darhuber, J.M. Davis, S.M. Troian, and W.W. Reisner. Thermocapillary actuation of liquid flow on chemically patterned surfaces. *Phys. Fluids*, **15**:1295, 2003.

[26] A.A. Darhuber, S.M. Troian, and W.W. Reisner. Dynamics of capillary spreading along hydrophilic microstripes. *Phys. Rev. E - Stat. Physics, Plasmas, Fluids, Relat. Interdiscip. Top.*, **64**(3):8, 8 2001.

[27] B. Davidovitch, R.D. Schroll, D. Vella, M. Adda-Bedia, and E.A. Cerda. Prototypical model for tensional wrinkling in thin sheets. *Proc. Natl. Acad. Sci. U. S. A.*, **108**(45):18227–32, 2011.

[28] S.H. Davis. Moving contact lines and rivulet instabilities. Part 1. The static rivulet. *J. Fluid Mech.*, **98**(2):225, 1980.

[29] P.-G. de Gennes, F. Brochard-Wyart, and D. Quéré. *Capillarity and Wetting Phenomena: Drops, Bubbles, Pearls, Waves*. Springer, 2004.

[30] T.E. De Groot, K.S. Veserat, E. Berthier, D.J. Beebe, and A.B. Theberge. Surface-tension driven open microfluidic platform for hanging droplet culture. *Lab Chip*, **16**(2):334–344, 2016.

[31] O.I. Del Río and A.W. Neumann. Axisymmetric drop shape analysis: Computational methods for the measurement of interfacial properties from the shape and dimensions of pendant and sessile drops. *Journal of Colloid and Interface Science*, **196**(2):136–147, 1997.

[32] R. Diestel. *Graph Theory*. Springer-Verlag, 5 edition, 2017.

[33] J.A. Diez, A.G. González, and L. Kondic. On the breakup of fluid rivulets. *Phys. Fluids*, **21**(8):082105, 2009.

[34] K.D. Dorfman and H. Brenner. Generalized Taylor-Aris dispersion in discrete spatially periodic networks: Microfluidic applications. *Phys. Rev. E*, **65**, 2002.

[35] T.A. Driscoll. Algorithm 756; a MATLAB toolbox for Schwarz-Christoffel mapping. *ACM Trans. Math. Softw.*, **22**(2):168–186, 1996.

[36] T.A. Driscoll and L.N. Trefethen. *Schwarz-Christoffel Mapping*. Cambridge University Press, 2002.

[37] B.R. Duffy and H.K. Moffatt. Flow of a viscous trickle on a slowly varying incline. *Chem. Eng. J. Biochem.*, **60**(1-3):141–146, 1995.

[38] B.R. Duffy and H.K. Moffatt. A similarity solution for viscous source flow on a vertical plane. *Eur. J. Appl. Math.*, **8**(1):37–47, 1997.

[39] J. Eggers. Drop formation - an overview. *ZAMM Zeitschrift fur Angew. Math. und Mech.*, **85**:400–410, 2005.

[40] D. Ericksо and D. Li. Microscale flow and transport simulation for electrokinetic and lab-on-chip applications. In *BioMEMS Biomed. Nanotechnol.*, **4**, pages 277–300. Springer US, 2007.

[41] D. Erickson. Towards numerical prototyping of labs-on-chip: modeling for integrated microfluidic devices. *Microfluid. Nanofluidics*, **1**(4):301–318, 2005.

[42] S.V. Ermakov, S.C. Jacobson, and J.M. Ramsey. Computer simulations of electrokinetic transport in microfabricated channel structures. *Anal. Chem.*, **70**(21):4494–4504, 1998.

[43] R.T. Farouki and H.P. Moon. Bipolar and Multipolar Coordinates. In *The Mathematics of Surfaces IX*, pages 348–371. Springer London, 2000.

[44] S. Fordham. On the calculation of surface tension from measurements of pendant drops. *Proc. R. Soc. London A Math. Phys. Eng. Sci.*, **194**(1036):1–16, 1948.

[45] G.G. Fuller and J. Vermant. Complex fluid-fluid interfaces: rheology and structure. *Annu. Rev. Chem. Biomol. Eng.*, **3**(1):519–543, 2012.

[46] C.F. Gauss. *Principia Generalia Theoriae Figurae Fluidorum in Statu Aequilibrii*. Gottingae, 1877.

[47] A. Gökaltun, Y.B. Kang, M.L. Yarmush, O.B. Usta, and A. Asatekin. Simple surface modification of poly(dimethylsiloxane) via surface segregating smart polymers for biomicrofluidics. *Sci. Rep.*, **9**(1), 2019.

[48] A. Gökaltun, M.L. Yarmush, A. Asatekin, and O.B. Usta. Recent advances in nonbiofouling PDMS surface modification strategies applicable to microfluidic technology. *Technology (Singap. World Sci.)*, **5**(1):1–12, 2017.

[49] D. Gospodarowicz and J.S. Moran. Growth factors in mammalian cell culture. *Annu. Rev. Biochem.*, **45**(1):531–558, 1976.

[50] J. Graham-Eagle and S. Pennell. Contact angle calculations from the contact/maximum diameter of sessile drops. *Int. J. Numer. Methods Fluids*, **32**(7):851–861, 2000.

[51] M. Hajirahimi, F. Mokhtari, and A.H. Fatollahi. Exact identities for sessile drops. *Appl. Math. Mech. (English Ed.)*, **36**(3):293–302, 2015.

[52] S. Halldorsson, E. Lucumi, R. Gómez-Sjöberg, and R.M.T. Fleming. Advantages and challenges of microfluidic cell culture in polydimethylsiloxane devices. *Biosens. Bioelectron.*, **63**:218–231, 2015.

[53] W. Helfrich. Elastic properties of lipid bilayers: theory and possible experiments. *Zeitschrift fur Naturforsch. - Sect. C J. Biosci.*, **28**(11):693–703, 1973.

[54] D.M. Henderson, W.G. Pritchard, and L.B. Smolka. On the pinch-off of a pendant drop of viscous fluid. *Phys. Fluids*, **9**(11):3188–3200, 1997.

[55] I.J. Hewitt, N.J. Balmforth, and J.R. De Bruyn. Elastic-plated gravity currents. *Eur. J. Appl. Math.*, **26**(1):1–31, 2015.

[56] L.M. Hocking and M.J. Miksis. Stability of a ridge of fluid. *J. Fluid Mech.*, **247**:157–177, 1993.

[57] D. Holmes and S. Gawad. The application of microfluidics in biology. *Methods Mol. Biol.*, **583**:55–80, 2010.

[58] K.M. Huang, T.Y. Tsou, C.W. Chang, and Y.C. Liao. Stability analysis of printed liquid elbows. *Langmuir*, **33**(2):645–651, 2017.

[59] C. Iliescu, H. Taylor, M. Avram, J. Miao, and S. Franssila. A practical guide for the fabrication of microfluidic devices using glass and silicon. *Biomicrofluidics*, **6**(1):16505–1650516, 2012.

[60] A. Javadi, M. Habibi, F.S. Taheri, S. Moulinet, and D. Bonn. Effect of wetting on capillary pumping in microchannels. *Scientific Reports*, **3**, 2013.

[61] K. Javadi, H. Moezzi-Rafie, V. Goodarzi-Ardakani, A. Javadi, and R. Miller. Flow physics exploration of surface tension driven flows. *Colloids Surfaces A Physicochem. Eng. Asp.*, **518**:30–45, 2017.

[62] J. Ju, J.Y. Park, K.C. Kim, H. Kim, E. Berthier, D.J. Beebe, and S.H. Lee. Backward flow in a surface tension driven micropump. *J. Micromechanics Microengineering*, **18**, 2008.

[63] T.M. Keenan and A. Folch. Biomolecular gradients in cell culture systems. *Lab Chip*, **8**(1):34–57, 2008.

[64] J. Kierzenka and L.F. Shampine. A BVP solver that controls residual and error. *J. Numer. Anal. Ind. Appl. Math.*, **3**(1-2):27–41, 2008.

[65] R.M. Kirby, G.E. Karniadakis, O. Mikulchenko, and K. Mayaram. An integrated simulator for coupled domain problems in MEMS. *J. Microelectromechanical Syst.*, **10**(3):379–391, 2001.

[66] S. Knoche, D. Vella, E. Aumaitre, P. Degen, H. Rehage, P. Cicuta, and J. Kierfeld. Elastometry of deflated capsules: elastic moduli from shape and wrinkle analysis. *Langmuir*, **29**(40):12463–12471, 2013.

[67] H. Kober. *Dictionary of Conformal Representations*. Cambridge University Press, 1953.

[68] F. Kratz and J. Kierfeld. Pendant drop tensiometry: a machine learning approach. *J. Chem. Phys.*, **153**(9), 2020.

[69] N. Kumar and S. Kaur. A review of various maze solving algorithms based on graph theory. *Int. J. Sci. Res.*, **6**(12):2–6, 2019.

[70] R.K. Lade, E.J. Hippchen, C.W. Macosko, and L.F. Francis. Dynamics of capillary-driven flow in 3D printed open microchannels. *Langmuir*, **33**(12):2949–2964, 2017.

[71] A. Lawal and R.A. Brown. The stability of an inclined pendent drop. *J. Colloid Interface Sci.*, **89**(2):332–345, 1982.

[72] A. Lawal and R.A. Brown. The stability of inclined sessile drops. *J. Colloid Interface Sci.*, **89**(2):346–352, 1982.

[73] N. Le Grand, A. Daerr, and L. Limat. Shape and motion of drops sliding down an inclined plane. *J. Fluid Mech.*, **541**:293–315, 2005.

[74] Y. Lee, I. Seder, and S.J. Kim. Influence of surface tension-driven network parameters on backflow strength. *RSC Adv.*, **9**(18):10345–10351, 2019.

[75] E. Marušić-Paloka. Fluid flow through a network of thin pipes. *Comptes Rendus l'Académie des Sci. - Ser. IIB - Mech.*, **329**(2):103–108, 2001.

[76] M. Mehling and S. Tay. Microfluidic cell culture. *Curr. Opin. Biotechnol.*, **25**:95–102, 2014.

[77] D.H. Michael and P.G. Williams. Equilibrium and stability of axisymmetric pendant drops. *Proc. R. Soc. Lond. A*, **351**(1664):117–127, 1976.

[78] D.H. Michael and P.G. Williams. Equilibrium and stability of sessile drops. *Proc. R. Soc. London A Math. Phys. Eng. Sci.*, **354**(1676):127–136, 1977.

[79] O.S. Mills. Tables for use in the measurement of interfacial tensions between liquids with small density differences. *Br. J. Appl. Phys.*, **4**(8):247–252, 1953.

[80] V. Narayanamurthy, Z.E. Jeroish, K.S. Bhuvaneshwari, P. Bayat, R. Premkumar, F. Samsuri, and M.M. Yusoff. Advances in passively driven microfluidics and lab-on-chip devices: a comprehensive literature review and patent analysis. *RSC Adv.*, **10**(20):11652–11680, 2020.

[81] P.N. Nge, C.I. Rogers, and A.T. Woolley. Advances in microfluidic materials, functions, integration, and applications. *Chem. Rev.*, **113**(4):2550–2583, 2013.

[82] S.B.G. O'Brien. On the shape of small sessile and pendant drops by singular perturbation techniques. *J. Fluid Mech.*, **233**:519, 1991.

[83] S.B.G. O'Brien. Asymptotics of a sequence of pendant drops. *SIAM J. Appl. Math.*, **62**(5):1569–1580, 2002.

[84] S.B.G. O'Brien, B.H.A.A. van den Brule, and H.J. Kent. Shape of a small sessile drop and the determination of contact angle. *J. Chem. Soc. Faraday Trans.*, **87**(10):1579, 1991.

[85] J.R. Ockendon. *Applied Partial Differential Equations*. Oxford University Press, 2003.

[86] I.L. Omocea, I.-R. Damian, C. Patrascu, and C. Balan. Formation and break-up of pendant drops in a viscous liquid. *Energy Procedia*, **112**:204–209, 2017.

[87] A. Oron, S.H. Davis, and S.G. Bankoff. Long-scale evolution of thin liquid films. *Rev. Mod. Phys.*, **69**(3):931–980, 1997.

[88] A.L. Paguirigan and D.J. Beebe. Microfluidics meet cell biology: bridging the gap by validation and application of microscale techniques for cell biological assays. *BioEssays*, **30**(9):811–821, 2008.

[89] A.L. Paguirigan and D.J. Beebe. From the cellular perspective: exploring differences in the cellular baseline in macroscale and microfluidic cultures. *Integr. Biol.*, **1**(2):182, 2009.

[90] F. Pan, S. Altenried, M. Liu, D. Hegemann, E. Bülbül, J. Moeller, W.W. Schmahl, K. Maniura-Weber, and Q. Ren. A nanolayer coating on polydimethylsiloxane surfaces enables a mechanistic study of bacterial adhesion influenced by material surface physicochemistry. *Mater. Horizons*, 2020.

[91] C. Paterson, S.K. Wilson, and B.R. Duffy. Pinning, de-pinning and re-pinning of a slowly varying rivulet. *Eur. J. Mech. - B/Fluids*, **41**:94–108, 2013.

[92] C.A. Perazzo and J. Gratton. Navier-Stokes solutions for parallel flow in rivulets on an inclined plane. *J. Fluid Mech.*, **507**(507):367–379, 2004.

[93] D. Pihler-Puzović, A. Juel, G.G. Peng, J.R. Lister, and M. Heil. Displacement flows under elastic membranes. Part 1. Experiments and direct numerical simulations. *J. Fluid Mech.*, **784**:487–511, 2015.

[94] C. Pozrikidis. Stability of sessile and pendant liquid drops. *J. Eng. Math.*, **72**:1–20, 2012.

[95] G. Qiu, Z. Gai, Y. Tao, J. Schmitt, G.A. Kullak-Ublick, and J. Wang. Dual-functional plasmonic photothermal biosensors for highly accurate severe acute respiratory syndrome coronavirus 2 detection. *ACS Nano*, 2020.

[96] B.E. Rapp. *Microfluidics: Modeling, Mechanics and Mathematics*. Elsevier, 2016.

[97] K. Ren, Y. Chen, and H. Wu. New materials for microfluidics in biology. *Curr. Opin. Biotechnol.*, **25**:78–85, 2014.

[98] P.J. Resto, E. Berthier, D.J. Beebe, and J.C. Williams. An inertia enhanced passive pumping mechanism for fluid flow in microfluidic devices. *Lab Chip*, **12**(12):2221–2228, 2012.

[99] S.W. Rienstra. The shape of a sessile drop for small and large surface tension. *J. Eng. Math.*, **24**:193–202, 1990.

[100] S. Rouimi, C. Schorsch, C. Valentini, and S. Vaslin. Foam stability and interfacial properties of milk protein–surfactant systems. *Food Hydrocoll.*, **19**(3):467–478, 2005.

[101] E.K. Sackmann, A.L. Fulton, and D.J. Beebe. The present and future role of microfluidics in biomedical research. *Nature*, **507**(7491):181–189, 2014.

[102] A. Sahu, A. Glisman, J. Tchoufag, and K.K. Mandadapu. Geometry and dynamics of lipid membranes: the Scriven-Love number. *Phys. Rev. E*, **101**(5), 2020.

[103] L.F. Shampine. Vectorized adaptive quadrature in MATLAB. *Journal of Computational and Applied Mathematics*, **211**(2):131–140, 2008.

[104] L.F. Shampine and M.W. Reichelt. The MATLAB ode suite. *SIAM Journal of Scientific Computing*, **18**(1):1–22, 1997.

[105] C. Sheridan. Coronavirus and the race to distribute reliable diagnostics. *Nat. Biotechnol.*, **38**(4):382–384, 2020.

[106] J.H. Snoeijer, N. Le Grand-Piteira, L. Limat, H.A. Stone, and J. Eggers. Cornered drops and rivulets. *Phys. Fluids*, **19**(4):042104, 2007.

[107] C. Soitu, C. Deroy, A.A. Castrejón-Pita, P.R. Cook, and E.J. Walsh. Using fluid walls for single-cell cloning provides assurance in monoclonality. *SLAS Technol.*, **25**(3):267–275, 2019.

[108] C. Soitu, A. Feuerborn, C. Deroy, A.A. Castrejón-Pita, P.R. Cook, and E.J. Walsh. Raising fluid walls around living cells. *Sci. Adv.*, **5**(6), 2019.

[109] C. Soitu, A. Feuerborn, A.N. Tan, H. Walker, P.A. Walsh, A.A. Castrejón-Pita, P.R. Cook, and E.J. Walsh. Microfluidic chambers

using fluid walls for cell biology. *Proc. Natl. Acad. Sci. U. S. A.*, **115**(26):E5926–E5933, 2018.

[110] C. Soitu, N. Stovall-Kurtz, C. Deroy, A.A. Castrejón-Pita, P.R. Cook, and E.J. Walsh. Jet-Printing Microfluidic Devices on Demand. *Adv. Sci.*, **7**(23):2001854, 2020.

[111] H. Somaweera, A. Ibraguimov, and D. Pappas. A review of chemical gradient systems for cell analysis. *Anal. Chim. Acta*, **907**:7–17, 2016.

[112] N.A. Stathopoulos and J.D. Hellums. Shear stress effects on human embryonic kidney cellsin Vitro. *Biotechnol. Bioeng.*, **27**(7):1021–1026, 1985.

[113] C.E. Stauffer. The measurement of surface tension by the pendant drop technique. *J. Phys. Chem.*, **69**(6):1933–1938, 1965.

[114] H.A. Stone, A.D. Stroock, and A. Ajdari. Engineering flows in small devices: microfluidics toward a lab-on-a-chip. *Annu. Rev. Fluid Mech*, **36**(1):347–382, 2004.

[115] P.T. Sumesh and R. Govindarajan. The possible equilibrium shapes of static pendant drops. *J. Chem. Phys.*, **133**(14):144707, 2010.

[116] F. Sun, A. Ganguli, J. Nguyen, R. Brisbin, K. Shanmugam, D.L. Hirschberg, M.B. Wheeler, R. Bashir, D.M. Nash, and B.T. Cunningham. Smartphone-based multiplex 30-minute nucleic acid test of live virus from nasal swab extract. *Lab Chip*, **20**(9):1621–1627, 2020.

[117] K. Suzuki, Y. Matsuki, K. Masaki, M. Sato, and M. Kuroda. Tensile and microbend tests of pure aluminum foils with different thicknesses. *Mater. Sci. Eng. A*, **513**:77–82, 2009.

[118] W. Thomson. Capillary attraction: II. *Nature*, **34**(874):290–294, 1886.

[119] M.W. Toepke and D.J. Beebe. PDMS absorption of small molecules and consequences in microfluidic applications. *Lab Chip*, **6**(12):1484, 2006.

[120] G.D. Towell and L.B. Rothfeld. Hydrodynamics of rivulet flow. *AIChE J.*, **12**(5):972–980, 1966.

[121] M. Tress, S. Karpitschka, P. Papadopoulos, J.H. Snoeijer, D. Vollmer, and H.-J. Rgen Butt. Shape of a sessile drop on a flat surface covered with a liquid film. *Soft Matter*, **13**:3760, 2017.

[122] Y. Tsoumpas, S. Dehaeck, A. Rednikov, and P. Colinet. Effect of Marangoni flows on the shape of thin sessile droplets evaporating into air. *Langmuir*, **31**(49):13334–13340, 2015.

[123] J. van der Valk, D. Brunner, K. De Smet, Å. Fex Svenningsen, P. Honegger, L.E. Knudsen, T. Lindl, J. Noraberg, A. Price, M.L. Scarino, and G. Gstraunthaler. Optimization of chemically defined cell culture media - replacing fetal bovine serum in mammalian in vitro methods. *Toxicol. Vitr.*, **24**(4):1053–1063, 2010.

[124] J.L. Vazquez. *The Porous Medium Equation: Mathematical Theory*. Oxford University Press, 2007.

[125] D. Vella, A. Ajdari, A. Vaziri, and A. Boudaoud. Wrinkling of pressurized elastic shells. *Phys. Rev. Lett.*, **107**(17):174301, 2011.

[126] G.M. Walker and D.J. Beebe. A passive pumping method for microfluidic devices. *Lab Chip*, **2**(3), 2002.

[127] E.J. Walsh, A. Feuerborn, J.H.R. Wheeler, A.N. Tan, W.M. Durham, K.R. Foster, and P.R. Cook. Microfluidics with fluid walls. *Nat. Commun.*, **8**(1):816, 2017.

[128] G.M. Whitesides. The origins and the future of microfluidics. *Nature*, **442**(7101):368–373, 2006.

[129] Y. Xia and G.M. Whitesides. Soft lithography. *Annu. Rev. Mater. Sci.*, **28**(12):153–184, 1998.

[130] D. Yang, M. Krasowska, C. Priest, M.N. Popescu, and J. Ralston. Dynamics of capillary-driven flow in open microchannels. *J. Phys. Chem. C*, **115**:18761–18769, 2011.

[131] S.H. Yun, L.M. Cabrera, J.W. Song, N. Futai, Y.C. Tung, G.D. Smith, and S. Takayama. Characterization and resolution of evaporation-mediated osmolality shifts that constrain microfluidic cell culture in poly(dimethylsiloxane) devices. *Anal. Chem.*, **79**(3):1126–1134, 2007.

[132] B. Zhao, J.S. Moore, and D.J. Beebe. Surface-directed liquid flow inside microchannels. *Science*, **291**(5506):1023–1026, 2001.

[133] X. Zhou, D. Liu, R. Zhong, Z. Dai, D. Wu, H. Wang, Y. Du, Z. Xia, L. Zhang, X. Mei, and B. Lin. Determination of SARS-coronavirus by a microfluidic chip system. *Electrophoresis*, **25**(17):3032–3039, 2004.